LOW AND INTERMEDIATE REYNOLDS NUMBER FLOWS IN MULTIPARTICLE SYSTEMS

by

MICHAEL J. GLUCKMAN

A dissertation submitted to the Graduate Faculty in Engineering in partial fulfillment of the requirement for the degree of Doctor of Philosophy, the City University of New York.

1971

This manuscript has been read and accepted for the Graduate Faculty in Engineering in satisfaction of the dissertation requirement for the degree of Doctor of Philosophy.

March 10, 1971
date

Chairman of Examining Committee

10 March 1971
date

Executive Officer

Latif Jiji

Arthur Squires

Sheldon Weinbaum

Robert Pfeffer, Chairman

Supervisory Committee

The City University of New York

TO

JANET

Without her encouragement, willing perseverance,
and cooperation this work would have been impossible.

ACKNOWLEDGMENTS

I take this opportunity to express my sincere thanks and appreciation to Professor R. Pfeffer for his continuing and helpful guidance throughout the course of this work as well as during the entire course of my graduate studies. His constant interest and encouragement made the performance of this work an extremely pleasant and educational experience for me. I also sincerely thank Professor S. Weinbaum for his unfailing interest, his many important contributions, and the large amount of time that he devoted to guiding, evaluating, and polishing this work.

Appreciation is due Professor C. M. Tchen for his helpful suggestions, especially those devoted to the three sphere quasi-steady state problem and Professor S. Katz for his valuable suggestions in the area of creeping flows past arbitrary bodies of revolution. Personal thanks are expressed to Dean A. X. Schmidt and Professor A. M. Squires for their interest and encouragement throughout the course of this work.

I acknowledge with thanks the support provided by the St. Regis Paper Company.

Sincere appreciation is expressed to Mrs. N. Hobesil for the time and talent that she devoted to the preparation of all of the illustrations in this dissertation.

TABLE OF CONTENTS

TABLE OF CONTENTS (Continued)

TABLE OF CONTENTS (Continued)

LIST OF FIGURES

LIST OF FIGURES (Continued)

LIST OF FIGURES (Continued)

NOMENCLATURE

The principal symbols are shown below. Symbols for quantities having only temporary significance are not shown, but are clearly defined in the text. A certain amount of duplication of symbols occurs, in which cases all pertinent definitions are given and in some cases are followed by equation numbers in parenthesis which correspond to the particular definitions.

a ..... Radius of sphere or cylinder

a ..... Major axis of prolate spheroid

a ..... Minor axis of oblate spheroid

a/b ..... Aspect ratio of spheriods

A ..... Area

A_n, A'_n ..... Constants (2.5)

A_1, A_2 ..... Local Constants (A.43)

b ..... Distance between objects

b ..... Minor axis of prolate spheroid

b ..... Major axis of oblate spheroid

B_n, B'_n ..... Constants (2.5)

c ..... Distance between objects

c ..... Distance between foci of spheroid

C_n, C'_n ..... Constants (2.5)

C_D ..... Drag coefficient (4.15)

d ..... Distance between objects

D_n, D'_n ..... Constants (2.5)

e ..... Constant (5.18)

f ..... Constant (5.18)

NOMENCLATURE (Continued)

$f(Re)$ ..... Function of Reynolds Number (4.16), (4.17)

F ..... Drag force

F_c ..... Drag force on cylinder (3.6)

F_o ..... Drag force on cone (3.10)

Fr ..... Froude Number (4.39), (4.42)

F_s ..... Drag force on sphere (3.5)

F_1, F_2 ..... Shape factors (A.45)

g ..... Gravitational constant

$\tilde{g}$ ..... Dimensionless gravity (4.39)

g ..... Constant (5.18)

h ..... Length of cylinder

h ..... Constant (5.18)

h_η, h_ξ ..... Metrical coefficients

H_n ..... Gegenbauer functions of the second kind (2.5)

I_n ..... Gegenbauer functions of the first kind (2.5)

k ..... Configuration parameter (4.18)

K ..... Settling factor (3.8)

L ..... Porosity (6.6)

m ..... Constant controlling doublet strength (A.9), (A.19)

M ..... Number of boundary points on each generating arc

M ..... Mass of sphere

M' ..... Mass of displaced fluid

N ..... Total number of objects in an array

p ..... Fluid pressure

p, q ..... Spheroidal coordinates

NOMENCLATURE (Continued)

p_e ..... Pressure at edge of boundary layer (A.29)

P_n ..... Legendre functions of the first kind

Q_n ..... Legendre functions of the second kind

r ..... Radial distance

r_n ..... Cylinder radius

r_n ..... Radius of cone base

r_o ..... Local radius of curvature of body

r_s ..... Sphere radius

r_1 ..... Defined by (A.55)

R ..... Defined in Figure A.3

Re ..... Reynolds Number (4.39)

R_e ..... Defined in Figure A.3

Re_1 ..... Local Reynolds Number (6.4)

R_o ..... Defined in Figure A.3

t ..... Time

$\tilde{t}$ ..... Dimensionless time (4.39)

$\tilde{t}_s$ ..... Dimensionless short time (4.47)

$\tilde{t}_\infty$ ..... Dimensionless long time (4.48)

$\tilde{t}^*_s$ ..... Dimensionless experimental short time (4.50)

$\tilde{t}^*_\infty$ ..... Dimensionless experimental long time (4.51)

T ..... Kinetic energy of fluid (4.21)

u ..... Local fluid velocity (rotational)

U ..... Reference velocity

$\tilde{U}$ ..... Dimensionless velocity (4.39)

U_c ..... Settling velocity of cylinder

U_e ..... Inviscid tangential velocity

U_1 ..... Local inviscid velocity (6.4)

U_s ..... Settling velocity of sphere of radius r_s

U_t ..... Terminal settling velocity of sphere

v_r ..... Velocity in the r direction

v_θ ..... Velocity in the θ direction

$\overline{V}$ ..... Velocity vector

V_e ..... Inviscid normal velocity

w ..... Fourier transform variable

X, Y ..... Cartesian coordinates

X_o, Y ..... Boundary layer coordinates

X* ..... Stretched boundary layer coordinate (5.1)

Z ..... Complex plane

α_n ..... Constants (2.29)

γ ..... Local curvature (A.36)

δ ..... Boundary layer thickness

δ^* ..... Displacement thickness (5.15)

∇ ..... Nabla operator

∇^2 ..... Laplace operator

ε ..... Local angle of curvature (A.36)

ζ ..... cos θ

θ ..... Spherical coordinate

θ ..... Momentum thickness (5.16)

θ_o ..... Angular distance from forward stagnation point

θ* ..... Stretched angular coordinate (5.2)

θ_1^* ..... Defined by (A.55)

λ ..... Particle interaction parameter (2.23)

Λ ..... Shape factor (5.20)

μ ..... Fluid viscosity

ν ..... Kinematic viscosity

$\tilde{\nu}$ ..... Dimensionless kinematic viscosity (4.39)

ξ, η ..... Spheroidal coordinates (2.33), (2.34)

ρ ..... Fluid density

$\tilde{\rho}$ ..... Dimensionless density (4.39)

ρ_s ..... Solid density

τ ..... Shear stress

ϕ ..... Velocity potential

ψ ..... Stream function

Ψ ..... Sphericity (3.9)

ω ..... Vorticity

ω ..... Complex potential function (A.2)

Subscripts

B ..... Basset force

D ..... Drag

e ..... End object

f.s.p. ..... Forward stagnation point

j ..... Particle number in an array

o ..... At the origin or on the boundary

p ..... Potential (irrotational)

NOMENCLATURE (Continued)

s ..... Short time

V.M. ..... Virtual mass

w ..... Wall

∞ ..... Free stream value

∞ ..... Long time

LOW AND INTERMEDIATE REYNOLDS NUMBER FLOWS IN MULTIPARTICLE SYSTEMS

by

MICHAEL J. GLUCKMAN

ABSTRACT

The thesis presents new approaches to three classes of problem, (a) streaming motions in closely spaced multiparticle systems, (b) flow past single obstacles whose boundaries do not conform to special natural coordinate systems, and (c) extension of the creeping motion theory to the intermediate Reynolds Number region $1 \lesssim Re \lesssim 200$, for which no really satisfactory treatment presently exists.

In the realm of low Reynolds Number hydrodynamics in multiparticle systems, a new procedure has been developed for treating multiple body interaction phenomena in an unbounded, incompressible viscous fluid. This new procedure, termed the multipole truncation technique, treats all interactions simultaneously to the same order. It exhibits rapid convergence characteristics even when the particles are touching one another and enables the boundaries of the submerged objects to be described to any desired degree of accuracy by controlling the degree of truncation.

This procedure, when applied to axisymmetric systems containing up to 101 spheres and up to 15 prolate or oblate spheroids, demonstrated five figure convergence for all spacings if only the first ten multipoles are retained in the solution. These solutions indicated large drag reduction effects in the central sections of each chain; these effects being greatest for objects of low aspect ratio; i.e., oblate spheroids.

The multipole procedure has been extended to include axisymmetric creeping motion flows past bodies of revolution of arbitrary shape. The complex shape, not having a natural coordinate system, is represented by a number of touching oblate spheroids of low aspect ratio. In the limit of vanishing aspect ratio, this representation approaches the exact boundaries of the desired shape. For illustrative purposes, this procedure was applied to the settling of short cylinders and cones. Predicted drag forces were found to be in remarkable agreement with experimental data where available.

The extreme flexibility of the multipole procedure has been further demonstrated by application to the quasi-steady problem of three spheres settling along their line of centers in the range $0<Re\leq 10$. The numerical results obtained are in good agreement with qualitative experimental observations.

For intermediate Re flow in the range $1\ll Re\ll 200$, a modification to Prandtl's boundary layer theory has been presented to enable the investigation of flow separation and wake formation for steady flow past two dimensional or axisymmetric bodies. This new procedure does not require that the boundary layer thickness be small compared to the local radius of curvature and is achieved by means of a streamwise coordinate stretching technique. Application to 2-D flow past a cylinder and axisymmetric flow past a sphere for the prediction of separation angles as a function of Re produced results that were in excellent agreement with numerical solutions of the complete Navier Stokes equations of motion as well as with experimental observations. Approximate solutions for flow parallel to two cylinders or spheres indicated very minor effects of the second object on separation from the first object.

However, for flow normal to three cylinders it was found that separation from the central cylinder was suppressed as the cylinder spacing decreased.

CHAPTER 1

INTRODUCTION

1.1 PRELIMINARY REMARKS

The slow motion of an incompressible fluid relative to assemblages of submerged particles has long been of interest in the areas of sedimentation theory, filtration, flow through packed and fluidized beds, the study of suspension viscosities and other applications of two phase flow. In the more than 100 years that have elapsed since the pioneering paper of Stokes (62) on the creeping motion past a sphere a somewhat staggering literature has evolved. For example, the recent text on this subject by Happel and Brenner (1) has a bibliography of nearly 500 references. Three problem areas which have received widespread attention over the years but relatively limited success are: (a) streaming motions in closely spaced multiparticle systems, (b) the near field flow past single obstacles whose boundaries do not conform to special natural coordinate systems and (c) the extension of the creeping motion theory to the intermediate Re region, $1 \ll Re \lesssim 60$ for the two-dimensional flow past a cylinder and $1 \ll Re \lesssim 130$ for the three-dimensional motion past a sphere, where the flow remains steady near the body and a wake separation bubble forms.

Nearly all flow problems in category (a) have heretofore been treated using the method of reflections first introduced by Smoluchowski (2), (3) or the point force approximation technique developed by Burgers (4), (5), (6). The method of reflections is an iterative procedure in which the flow past the object of interest is first computed in the absence of all other boundaries and then corrected for the disturbance or reflection produced by the zeroth order solution for all other objects in the flow. Higher order reflections can also be computed in the same

manner. The point force approximation technique requires that the disturbance produced by a submerged object be replaced by one or more point forces located at the foci of the object. Since point forces radiate with equal intensity in all directions the angular dependence of disturbances of one object in the presence of others cannot be taken into account. Therefore, the accuracy of the point force representation quickly diminishes as the objects approach one another.

The method of reflections used by itself or in conjunction with the point force approximation is satisfactory for dilute systems but involves an enormous amount of labor because of very slow convergence characteristics for closely spaced systems of two or more objects. No practical previous theoretical technique had been devised for treating the latter class of problems.

There are, however, three special exceptions to the above generalization concerning flow in closely spaced multiparticle systems. For example, Stimson and Jeffery (7) utilized a coordinate transformation procedure to map the exact solution for flow past a single perfect sphere in spherical coordinates into the exact solution for flow past two perfect spheres in bipolar coordinates. Secondly, Wang and Skalak (8) made use of the property of periodicity to develop an analytical solution to the problem of slow viscous flow past an infinite chain of equally spaced spheres along the axis of rotation of a cylindrical tube. Finally, Wakiya (9) utilized a technique of inner and outer expansions to obtain an approximate solution to the problem of slow viscous flow past two spheroids having any orientation to each other as well as to the free stream flow direction.

A similar state of the art exists for flow problems in category (b). While Happel and Brenner (1) present a formalism for treating

arbitrary shaped bodies which is based on introducing 21 unknown scalar resistance coefficients, the requirement that these coefficients must be determined experimentally renders this technique ineffective for obtaining numerical solutions in the absence of experimental data. As a practical matter no previous analytical technique was available for treating such common shapes as a short cylinder or a cone.

For problems in category (c) a great deal of effort based on Oseen's classic treatise (63) has been directed toward determining the flow past objects at Reynolds numbers in the vicinity of unity. No successful theoretical attempts have yet been made which venture further than this into the realm of $1<Re<130$ where a growing abundance of numerical Navier-Stokes solutions are becoming available. The formation of a steady wake bubble and its dependence on Re in this range have been subjects of keen interest for many years.

Experimental observations of flows through packed beds have indicated that drag and pressure drop data can be predicted relatively well by models based on the creeping motion equations for flows in the range $1\leq Re\leq 50$ depending on the porosity of the system even though these Reynolds Numbers are considerably outside the range of validity of the creeping motion equations. Leclair and Hamielec (13) showed by numerically solving the Navier-Stokes equation for a unit cell surrounding a single sphere in an assemblage of spherical particles, that wake formation around the test sphere is suppressed due to interactions with the surrounding particles. Their analysis suffers due to the fact that a questionable boundary condition of zero vorticity at the edge of the unit cell was used. Therefore, it is apparent that there is need for a simple procedure which can be employed to investigate the effects of multiple particle interactions on wake suppression in the intermediate Re range.

Such a technique would be extremely valuable in providing a better understanding of the fluid dynamical behavior of packed beds, solid-liquid heterogeneous reaction systems and flows past tube banks in the intermediate Re range.

1.2 AIM AND SCOPE OF THE DISSERTATION

To describe the basic concepts for treating flows in categories (a) and (b) efforts were confined to the axially symmetric motion past any number of bodies of revolution of arbitrary shape. These basic ideas should apply equally well to the general three-dimensional motions. The new approach for treating the multiparticle flow problems, which has been termed the multipole truncation technique, is based on two hypotheses. The first is that the disturbance due to any number of objects conforming to special natural boundaries, for example, spheres and spheroids, can be exactly constructed from infinite series of multilobular disturbances placed at the geometric center of each object. The second is that accurate representations of the entire flow can be obtained from finite truncations of the series in which the disturbances due to all particles are treated simultaneously at all orders of truncation. Convergence of the solution is thus many times more rapid than by using an iterative procedure such as the method of reflections. Solutions for the flow field and drag will be presented for as many as 101 spheres and 15 spheroids in a line. As a further demonstration of the power of the technique, the unsteady problem of three spheres falling along their line of centers will be presented for Re in the range $0<R<10$. The solutions, which are the first obtained for a strong interaction three-body problem in fluid mechanics, exhibit an intriguing behavior because of the existence of two time scales, a short time characteristic of the

initial transient motion during which acceleration forces are large and a long time characteristic of the changes in sphere spacing due to sphere interaction effects.

For problems in category (b) it is shown that the disturbance due to an arbitrary body of revolution can be constructed as a limiting process from the fundamental solutions for contiguous oblate spheroids. It is demonstrated that in the limit of vanishing aspect ratio the entrained eddies between adjacent spheroids disappear yielding the exact solution for the flow past an arbitrary body of revolution. The first theoretical solutions for short cylinders and cones have been obtained and are in excellent agreement with available experimental data.

The approach to problems in category (c) was that it might be possible, as in the high Reynolds number limit, to find new simplifying features that would reduce these steady intermediate Reynolds number flows to a mathematically tractable form. The data from numerical studies were carefully scrutinized and a number of simplifying hypotheses tested. A new theory was formulated based on the straining of the stream-wise coordinate along the displacement arc of an enlarged body due to vorticity diffusion effects. The theory provides an interesting contrast to the normal coordinate straining of Prandtl boundary layer theory. The theory has been used to obtain solutions for the position of flow separation as a function of Re for the flow past both cylinders and spheres. These results exhibit remarkable agreement with Takami and Keller's (12) numerical Navier-Stokes solutions for the flow past a cylinder for $7<Re<60$ and at lower values predict almost exactly the experimentally observed Reynolds number for incipient separation. The agreement of the results with experimental and numerical solutions for a sphere is also good over the entire range $1<Re<130$. The effect of

wake suppression by adding additional cylinders or spheres around the test particle was also investigated.

CHAPTER 2

AXISYMMETRIC FLOW PAST ASSEMBLAGES OF SPHERES AND SPHEROIDS

2.1 INTRODUCTION

A comprehensive review of the literature pertaining to the low Reynolds Number motion of an incompressible viscous fluid relative to assemblages of submerged particles conducted by Happel and Brenner (1), indicated that two approaches - the method of reflections and the point force approximation - have been used extensively for treating multi-particle slow flow problems. The method of reflections, developed by Smoluchowski (2) and (3) and used by Burgers (14), Kynch (15) and Happel and Brenner (1), is an iterative approximation technique. For the first reflection, perturbations resulting from the velocity field due to one particle being reflected from the boundary of a second particle are utilized to correct the zeroth order velocity field of the second particle calculated in the absence of the first particle. The nth order reflection is then the correction required to satisfy the no slip boundary conditions at the surface of each object caused by the disturbance field of the $(n-1)^{th}$ reflection of all other particles. This technique allows multiple particle interaction problems to be handled and has been shown to converge to the exact solution for the two-sphere problem. The convergence characteristics are strongly dependent on the ratio of sphere spacing 2d to sphere diameter 2a. When this ratio d/a is large (i.e. dilute system) a single reflection describes the particle interactions adequately. For concentrated systems ($d/a \rightarrow 1$) higher order interaction effects become significant and the leading term in the iterative series solution becomes a poor description of particle interaction effects and generates a series with very slow convergence characteristics.

The point force approximation technique developed by Burgers (4), (5) and (6) and used by McNown and Lin (16), Tchen (17), Broersma (18) and Tam (19), requires that the disturbance produced by a submerged object be replaced by one or more point forces located at the foci of the object. This technique approximates the exact viscous no slip boundary condition by requiring that the velocity over the surface of the sphere vanish in some average sense. This approximate technique has also been used in conjunction with the method of reflections to describe multiple particle interaction problems by Burgers (5) and (6) and Kynch (15). Since point forces radiate with equal intensity in all directions the angular dependence of disturbances on the boundaries of one spherical object in the presence of others cannot be taken into account. This angular dependence grows in importance as the angle subtended by the test sphere relative to the origins of the other spheres increases. Therefore, the accuracy of the point force representation quickly diminishes as the spheres approach one another.

The techniques described above must in general be used when more than two objects are present except for the special case of the flow relative to an infinite chain of equally spaced spheres along their line of centers. Because of the perfect periodicity existing in such an infinite chain this latter problem can be viewed as the flow past a single sphere in a cell with periodic boundary conditions, e.g. Wang and Skalak (8). The numerous two-sphere problems treated in the literature form an important class of exact solutions that provide valuable insight into the convergence characteristics of the method of reflections and the accuracy of the point force approximation. These exact solutions all depend on mapping the solution for a single sphere into spherical bipolar coordinates. This technique was first used by Stimson and

Jeffery (7), for two spheres translating along their line of centers, and was extended to the asymmetric case by Dean and O'Neill (19). Further extensions of this problem have been reported by Goldman, Cox and Brenner (20), slow motion of two identical arbitrarily oriented spheres and by Davis (21), translation and rotation of two unequal spheres.

The object of the present study is to develop a new technique for handling concentrated systems of particles which is capable of satisfying the no slip boundary conditions more accurately than the point force approximation technique and which also converges more rapidly than does the method of reflections. The new method is based on the concept that the disturbance due to each submerged object can be represented by an infinite series of multipoles with one or more focal points, where each multipole series has a different origin. The strength of each multipole is determined so as to satisfy the no slip boundary conditions along the surface of all interacting particles simultaneously. To satisfy the boundary conditions exactly along a finite surface, multipoles of all orders must be retained in the same sense that a complete Fourier series is required to represent any well behaved function over a finite interval. However, since each multipole that is used to represent a submerged object allows the exact no slip boundary conditions to be satisfied at two discrete points on each object, solutions of any order of accuracy can be obtained depending on the order of the multipoles retained in the solution. The technique is, therefore, one of truncation rather than an iterative procedure as in the method of reflections. Furthermore, since all particles are treated simultaneously to the same order, the effect of other particles are considered even in the lowest order truncation. It shall be shown that the lowest order

truncation solution for the drag on each particle using the new technique is considerably more accurate than the first reflection solution in the method of reflections when the particles are close together and as good a solution as the point force approximation when the particles are far apart. This improvement in accuracy over the method of reflections increases as one goes to corresponding higher order corrections in each method.

The multipole representation technique can be used to describe the motion past any number of spherical objects, by placing a multipole series at the focal point of each sphere. This reasoning is easily extended to oblate and prolate spheroids. The characteristic length between foci is then used to stretch or compress the lobes of each multipole originating from the geometrical center of each spheroid. In principle an arbitrary axisymmetric object can be represented by an infinite array of oblate spheroids of vanishing aspect ratio. From a practical point of view a good approximation to flow past complex shapes can be obtained using other objects, e.g., a long cylinder is well approximated by a string of prolate spheroids placed end to end. The present chapter is restricted to the axisymmetric flow past spheres and spheroids in order to demonstrate the simplicity and utility of the multipole approach. Low Reynolds Number flows past axisymmetric bodies of revolution of arbitrary shape will be discussed in the next chapter.

2.2 FORMULATION FOR MULTIPLE SPHERES

In this section, a general description and discussion of the multipole representation technique will be presented and applied to a general solution for slow viscous incompressible flow past a finite chain of equally spaced spheres.

By omitting the inertial terms, $\rho\bar{V}\cdot\nabla\bar{V}$ the steady state Navier-Stokes equations reduce to the well-known creeping motion or Stokes equations i.e.

$$\nabla^2\bar{V} = \frac{1}{\mu}\nabla p \tag{2.1}$$

To obtain an equation in a single dependent variable, one introduces the stream function, defined in spherical coordinates as,

$$V_r = -\frac{1}{r^2\sin\theta}\frac{\partial\psi}{\partial\theta} \quad ; \quad V_\theta = \frac{1}{r\sin\theta}\frac{\partial\psi}{\partial r} \tag{2.2}$$

and takes the curl of (2.1) which results in the biharmonic equation

$$\nabla^2(\nabla^2\psi) = 0 \tag{2.3}$$

where $$\nabla^2 = \frac{\partial^2}{\partial r^2} + \frac{(1-\mu^2)}{r^2}\frac{\partial^2}{\partial\mu^2}$$

and $$\mu = \cos\theta$$

The stream function ψ is related to the vorticity ω as follows:

$$\nabla^2\psi = 2\omega$$

The general solution to (2.3), presented by Sampson (22), Savic (23), and Haberman and Sayre (24), is based on the linearity of (2.3) and contains two basic summations:

$$\psi = \psi_1 + \psi_2 \tag{2.4}$$

where ψ_1 contains the irrotational solutions $\nabla^2\psi_1 = 0$ and ψ_2 contains the rotational solutions $\nabla^2\psi_2 = 2\omega$;

$$\psi = \sum_{n=0}^{\infty} \left[A_n r^n + B_n r^{-n+1} + C_n r^{n+2} + D_n r^{-n+3} \right] I_n(\xi)$$

$$+ \sum_{n=2}^{\infty} \left[A'_n r^n + B'_n r^{-n+1} + C'_n r^{n+2} + D'_n r^{-n+3} \right] H_n(\xi) \qquad (2.5)$$

where the terms $A_n r^n$, $B_n r^{-n+1}$, $A'_n r^n$, and $B'_n r^{-n+1}$ belong to ψ_1 and the terms $C_n r^{n+2}$, $D_n r^{-n+3}$, $C'_n r^{n+2}$, and $D'_n r^{-n+3}$ belong to ψ_2. Here $I_n(\xi)$ and $H_n(\xi)$ are Gegenbauer functions of the first and second kind respectively, related to Legendre functions as follows:

$$I_n(\xi) = \frac{P_{n-2}(\xi) - P_n(\xi)}{2n-1} \qquad n \geq 2 \qquad (2.6)$$

$$H_n(\xi) = \frac{Q_{n-2}(\xi) - Q_n(\xi)}{2n-1} \qquad n \geq 2$$

where $I_0(\xi) = 1$; $I_1(\xi) = -\xi$; $H_0(\xi) = -\xi$; $H_1(\xi) = -1$

The condition of uniform flow at infinity in the direction of the negative x axis requires that:

$$\psi \to \tfrac{1}{2} U r^2 \sin^2\theta \quad \text{as} \quad r \to \infty \qquad (2.7)$$

This condition plus the fact that the functions of the second kind ($H_n(\xi)$) become infinite along the axis $\xi = \pm 1$ results in the following evaluation of some of the constants in (2.5):

$$C_n = A'_n = B'_n = C'_n = D'_n = 0 \text{ for all } n$$
$$A_2 = U; \; A_n = 0 \text{ for } 3 \leq n < \infty \qquad (2.8)$$

Application of (2.7) and (2.8) to (2.5) results in the following general form for the stream function in spherical coordinates:

$$\psi = \tfrac{1}{2} U r^2 \sin^2\theta + \sum_{n=2}^{\infty} \left[B_n r^{-n+1} + D_n r^{-n+3} \right] I_n(\xi) \tag{2.9}$$

Sampson has shown that for flow past a single perfect sphere

$$B_n = D_n = 0 \text{ for } n > 2$$

(2.9) therefore reduces to the well-known single sphere result

$$\psi = \tfrac{1}{2} U r^2 \sin^2\theta + \tfrac{1}{2} \sin^2\theta \left[\frac{B_2}{r} + D_2 r \right]$$

Finally B_2 and D_2 are determined by applying the no slip boundary conditions to equations (2.2) evaluated at r = a.

The force exerted by the fluid on a spherical boundary r = constant is shown in Happel and Brenner (1) to be

$$F = -\mu \pi \int_0^{\pi} r^3 \sin^3\theta \frac{\partial}{\partial r} \left[\frac{\nabla^2 \psi}{r^2 \sin^2\theta} \right] r \, d\theta \tag{2.10}$$

Performing this integration on (2.9) and making use of the orthogonality of the Gegenbauer function $I_n(\xi)$ i.e.

$$\int_{-1}^{+1} \frac{I_m(\xi) I_n(\xi)}{1-\xi^2} \, d\xi = \begin{cases} 0 & \text{for } m \neq n \\ \dfrac{2}{n(n-1)(2n-1)} & \text{for } m = n \end{cases} \tag{2.11}$$

results in,

$$F = 4\pi \mu D_2 \tag{2.12}$$

i.e. the drag on a single sphere is represented by the leading term in

the infinite series solution for the rotational part of the flow.

It is possible to extend Sampson's results for flow past a single sphere to the case of flow past any finite number of equally spaced spheres along their line of centers. The geometry of the system being considered is shown in Figure 2.1. From the linearity of the governing equation of motion (2.3) it is possible to write the solution to the stream function for flow past N spheres as follows:

$$\psi = \sum_{j=-\frac{(N-1)}{2}}^{\frac{(N-1)}{2}} \psi_j \qquad \text{for } N \text{ odd} \tag{2.13a}$$

where the origin is taken for convenience on the center sphere. For N even the origin is taken on the sphere closest to the center of the chain, i.e.

$$\psi = \sum_{j=-\frac{(N-2)}{2}}^{\frac{N}{2}} \psi_j \qquad \text{for } N \text{ even} \tag{2.13b}$$

where ψ_j is represented by (2.9), i.e.

$$\psi_j = \tfrac{1}{2} U r_o^2 \sin^2\theta_o + \sum_{n=2}^{\infty} \left[B_{nj} r_j^{-n+1} + D_{nj} r_j^{-n+3} \right] I_n(\xi_j) \tag{2.14}$$

Here r_j and ξ_j are measured from the origin of each sphere considered separately. Combining (2.13) and (2.14) yields the following solution for the stream function for flow past N spheres

$$\psi = \tfrac{1}{2} U r_o^2 \sin^2\theta_o + \sum_{j=-\frac{(N-1)}{2}}^{\frac{(N-1)}{2}} \sum_{n=2}^{\infty} \left[B_{nj} r_j^{-n+1} + D_{nj} r_j^{-n+3} \right] I_n(\xi_j) \tag{2.15}$$

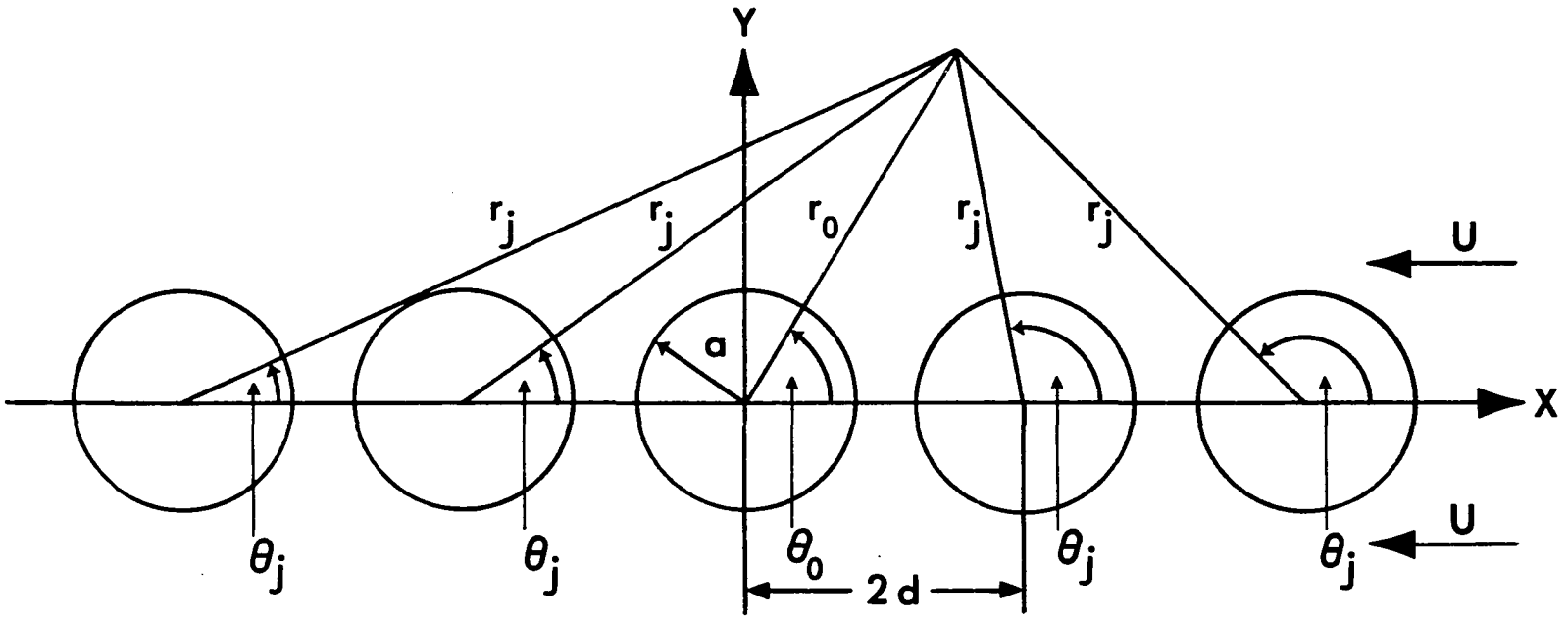

Figure 2.1 – GEOMETRY OF THE MULTIPLE SPHERE SYSTEM

In order to apply (2.15), the r_j and $\mathcal{S}_j$ terms must be written in terms of a single coordinate system, i.e.:

$$r_j = \left[(x-2j\alpha)^2 + y^2\right]^{1/2}$$

$$\mathcal{S}_j = \frac{(x-2j\alpha)}{r_j} \qquad -\frac{(N-1)}{2} \leq j \leq \frac{(N-1)}{2}$$

Examination of the complete expression for the stream function (2.15) indicates that a double series expansion which is infinite in one dimension and can be large in the other dimension is required to represent the exact solution. The basic problem is to determine the constants in this two-dimensional series expansion so as to satisfy the no slip viscous boundary conditions along the surfaces of spheres considered simultaneously. A better insight into the flow representation of (2.15) can be had by examining the Gegenbauer functions of the first kind, i.e. $I_n(\mathcal{S})$. Figure 2.2 demonstrates the form taken by I_2 (cos θ) through I_5(cos θ). It can be seen from this figure that Gegenbauer functions of the first kind represent, conceptually, disturbances emanating from a single focal point. These disturbances are symmetrical about both axes and increase in complexity as the order of the Gegenbauer function increases. In general, $I_n(\mathcal{S}_j)$ represents a disturbance which will have 2n-2 lobes distributed symmetrically about the x axis. The term multipole has been coined to describe a single term in the inner series in (2.15). Thus, each multipole has associated with it two constants, B_{nj} and D_{nj} which are related to the intensity of the multipoles. These multipoles are somewhat akin to Burgers' point forces in

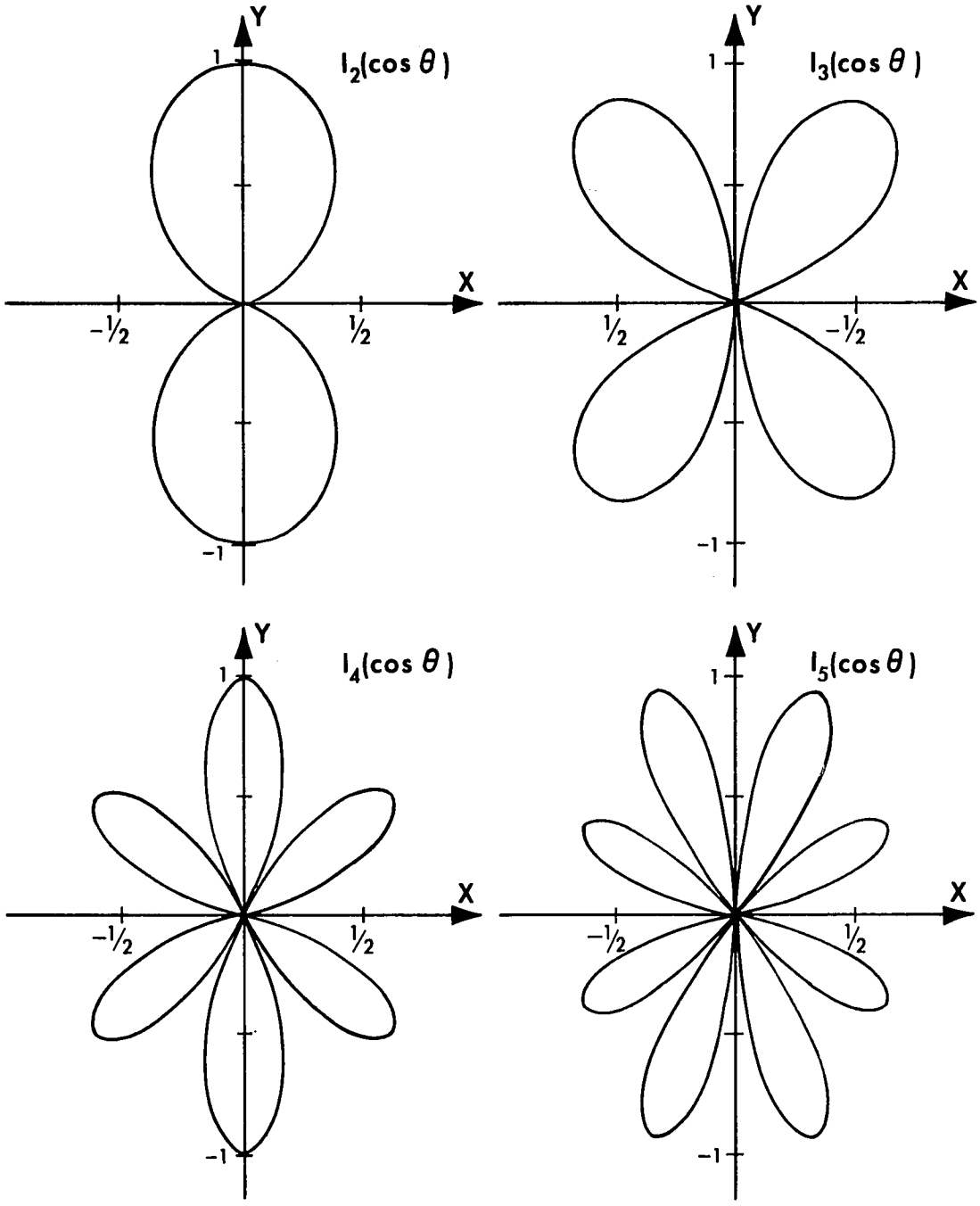

Figure 2.2 - GEGENBAUER FUNCTIONS

that they represent disturbances radiating from a single focal point. They differ from point forces in that their intensity varies as a function of the polar angle θ_j.

Further examination of these multipoles in the context in which they appear in equation (2.15) leads to certain rather interesting conclusions. Each compound term or multipole in the inner series expansion for the solution to the stream function contains two constants operating on $I_n(\mathcal{S}_j)$. Now, for flow past spherical objects, the no slip boundary conditions on the surface of each object result in two equations for each discrete point on the semi-circular arc of radius a that revolves about the x axis to form the sphere, i.e. at $r_j = a$ and $\theta_j = \theta_j$.

$$\left.\begin{aligned} V_{r_j} &= 0 = \frac{\partial \psi}{\partial \theta_j} \\ V_{\theta_j} &= 0 = \frac{\partial \psi}{\partial r_j} \end{aligned}\right\} \qquad (2.16)$$

The two arbitrary constants in each multipole thus provide the freedom to satisfy the boundary conditions (2.16) at one point along the generating arc of each sphere. If the boundary conditions are to be satisfied over the entire surface of each sphere (i.e. at an infinite number of points on the generating arc), an infinite number of terms of multipoles would be required to represent the disturbance due to each submerged sphere.

The question of greatest practical importance is how many multipoles are required to represent each sphere in the chain to produce a result having the desired accuracy. The answer to this question is complex and will be the object of careful examination in subsequent

sections where detailed comparisons with the known exact solution for two spheres are presented. One anticipates that the constants in each multipole will be a function of the dimensionless spacing d/a and that in the limit as $d/a \to \infty$ all the higher order coefficients should become vanishingly small. This must occur if the multipole representation (2.15) is to reduce to the exact solution for a single sphere.

Returning to the equation for the stream function (2.15) and using the boundary conditions (2.16), we shall now present in general form the solution to the problem of axisymmetric flow past an arbitrary number of equally spaced spherical objects. If a system of N spheres is spaced evenly along the x axis as depicted in Figure 2.1 and the boundary conditions are satisfied at M points along the generating arc of each of the N spheres, then a set of 2 x N x M homogeneous simultaneous linear algebraic equations results for the 2 x N x M unknown constants B_{nj} and D_{nj}. The general solution for all of the required constants in (2.15) can be represented as follows. Using (2.2), (2.15), (2.16) and the differential form for $I_n(\beta)$, i.e.

$$\frac{dI_n(\beta)}{d\beta} = -P_{n-1}(\beta) \tag{2.17}$$

it can be shown that:

$$V_{tjm} = A'_{jm} + \sum_{q=1}^{N} \sum_{n=2}^{M+1} \left[B'_{nqm} B_{nq} + D'_{nqm} D_{nq} \right] = 0$$

$$V_{0jm} = A''_{jm} + \sum_{q=1}^{N} \sum_{n=2}^{M+1} \left[B''_{nqm} B_{nq} + D''_{nqm} D_{nq} \right] = 0 \tag{2.18a}$$

for $1 \leq m \leq M$

$$A'_{jm} = -U\cos\theta_{jm}$$

$$B'_{nqm} = \frac{1}{r_{jm}^2 \sin\theta_{jm}}\left[(n-1)r_{qm}^{-n}\frac{\partial r_{qm}}{\partial\theta_{jm}} I_n(\beta_{qm}) + r_{qm}^{-n+1} P_{n-1}(\beta_{qm})\frac{\partial \beta_{qm}}{\partial\theta_{jm}}\right]$$

$$D'_{nqm} = \frac{1}{r_{jm}^2 \sin\theta_{jm}}\left[(n-3)r_{qm}^{-n+2}\frac{\partial r_{qm}}{\partial\theta_{jm}} I_n(\beta_{qm}) + r_{qm}^{-n+3} P_{n-1}(\beta_{qm})\frac{\partial \beta_{qm}}{\partial\theta_{jm}}\right]$$

(2.18b)

$$A''_{jm} = U\sin\theta_{jm}$$

$$B''_{nqm} = \frac{1}{r_{jm}\sin\theta_{jm}}\left[(-n+1)r_{qm}^{-n}\frac{\partial r_{qm}}{\partial r_{jm}} I_n(\beta_{qm}) - r_{qm}^{-n+1} P_{n-1}(\beta_{qm})\frac{\partial \beta_{qm}}{\partial r_{jm}}\right]$$

$$D''_{nqm} = \frac{1}{r_{jm}\sin\theta_{jm}}\left[(-n+3)r_{qm}^{-n+2}\frac{\partial r_{qm}}{\partial r_{jm}} I_n(\beta_{qm}) - r_{qm}^{-n+3} P_{n-1}(\beta_{qm})\frac{\partial \beta_{qm}}{\partial r_{jm}}\right]$$

(2.18) when written in matrix form becomes

$$\begin{vmatrix} B'_{2,1,1} & D'_{2,1,1} & B'_{3,1,1} & D'_{3,1,1} & \cdots & D'_{M+1,N,1} \\ B'_{2,1,2} & D'_{2,1,2} & B'_{3,1,2} & D'_{3,1,2} & \cdots & D'_{M+1,N,1} \\ \vdots & \vdots & \vdots & \vdots & & \vdots \\ B'_{2,1,M} & D'_{2,1,M} & B'_{3,1,M} & D'_{3,1,M} & \cdots & D'_{M+1,N,M} \\ B''_{2,1,1} & D''_{2,1,1} & B''_{3,1,1} & D''_{3,1,1} & \cdots & D''_{M+1,N,1} \\ B''_{2,1,2} & D''_{2,1,2} & B''_{3,1,2} & D''_{3,1,2} & \cdots & D''_{M+1,N,2} \\ \vdots & \vdots & \vdots & \vdots & & \vdots \\ B''_{2,1,M} & D''_{2,1,M} & B''_{3,1,M} & D''_{3,1,M} & \cdots & D''_{M+1,N,M} \end{vmatrix} \begin{vmatrix} B_{2,1} \\ D_{2,1} \\ \vdots \\ D_{M+1,\frac{N-1}{2}} \\ B_{2,\frac{N+1}{2}} \\ D_{2,\frac{N+1}{2}} \\ \vdots \\ D_{M+1,N} \end{vmatrix} = \begin{vmatrix} -A'_{1,1} \\ -A'_{1,2} \\ \vdots \\ -A'_{N,M} \\ -A''_{1,1} \\ -A''_{1,2} \\ \vdots \\ -A''_{N,M} \end{vmatrix} \qquad (2.19)$$

This linear set of simultaneous algebraic equations can be solved by any of the standard matrix reduction techniques (such as the Crout method) to yield the B_{nj} and D_{nj} constants required in equation (2.15) for the stream function.

The drag force exerted by the fluid on each sphere in the array can be determined from:

$$F_j = -\mu\pi \int_0^{\pi} r_j^3 \sin^3\theta_j \frac{\partial}{\partial r_j}\left[\frac{\nabla^2\psi}{r_j^2 \sin^2\theta_j}\right] r_j \, d\theta_j \qquad (2.20)$$

Performing the above integration and using the orthogonality properties of the Gegenbauer functions results in the simple relationship:

$$F_j = 4\pi\mu D_{2j} \qquad (2.21)$$

Equation (2.21) demonstrates just as for the case of a single sphere that only the first multipole contributes to the drag forces exerted on each submerged sphere. It is important to note that (2.20) requires that r_j be constant and independent of θ_j. Therefore, the integration is performed over the generating arc of a perfect sphere, even when the zero streamline is distorted and does not conform to the desired spherical shape.

2.3 SOLUTIONS FOR TWO SPHERES

Solutions using the multipole representation technique to axisymmetric slow viscous flow past two spheres along their line of centers will be presented in this section. This two-sphere problem was chosen since the exact solutions presented by Stimson and Jeffery (7) provide a convenient means for evaluating the truncated multipole representation

technique. The solutions for the flow past submerged objects can be presented graphically by plotting streamline patterns and also by calculating the drag force on each object. Streamline patterns, although descriptive, are extremely tedious to obtain and will, therefore, only be shown for representative cases.

Happel and Brenner (1) describe a convenient coefficient for comparing the drag on a sphere in an array to the drag on a single sphere. The well-known Stokes result for the drag force on a single sphere is:

$$F = 6\pi\mu Ua \tag{2.22}$$

Based on (2.22) λ is defined as follows:

$$F_j = 6\pi\mu Ua\lambda_j \tag{2.23}$$

where j represents the particular sphere in the chain (see Figure 2.1). Referring back to equation (2.21), the drag force exerted on a submerged sphere is represented by:

$$F_j = 4\pi\mu D_{2j} \tag{2.21}$$

Combining (2.21) and (2.23) produces:

$$\lambda_j = \frac{D_{2j}}{1.5Ua} \tag{2.24}$$

In all of the two sphere problems considered herein, the sphere radius and the free stream velocity U have been normalized to unity. Also, for the case of two spheres, the drag forces on each of the spheres are equal due to symmetry and, therefore, the subscript j will be dropped from λ, i.e. for two spheres:

$$\lambda = \frac{D_2}{1.5} \tag{2.25}$$

In writing a program to determine the B_{nj} and D_{nj} constants in equation (2.15), some practical hints gleaned from the experience of the author should prove to be useful. The no slip boundary conditions presented in the previous section are represented by

$$V_{rj} = 0 = \frac{\partial \psi}{\partial \theta_j}$$
$$V_{\theta j} = 0 = \frac{\partial \psi}{\partial r_j} \qquad (2.26)$$

Differentiation of the stream function with respect to each sphere individually is tedious as there is a different origin for each sphere and each r_j and θ_j are functions of all the other r_j's and θ_j's. For this reason it is simpler to use a rectangular coordinate system which has common coordinates for each sphere. The velocities V_{rj} and $V_{\theta j}$ are orthogonal and in the same plane. Therefore, all other velocities originating from the same point as V_{rj} and $V_{\theta j}$ in the same plane must be zero. In particular, V_x and V_y must be identically zero. A simpler set of boundary conditions, equivalent to the above would, therefore, be:

$$V_x = 0 = \frac{\partial \psi}{\partial y}$$
$$V_y = 0 = \frac{\partial \psi}{\partial x} \qquad \text{on} \quad r_j = a \qquad (2.27)$$

Secondly, when specifying the number of points along the boundary of each sphere where the conditions (2.27) must be exactly satisfied, it is desirable to specify an odd number of points. The reason for this is as follows. The first point that should be specified should always be the highest point on the generating arc (i.e. the point $r_j = a$, $\theta_j = \pi/2$). This point is most advantageous as the drag on the sphere

is a strong function of the projected area of the sphere normal to the direction of flow and the above mentioned point provides the best single estimate of this projected area. The argument is valid for all low aspect ratio objects, e.g. the drag on a flat disc is only 15.2% lower than the drag on a sphere of the same diameter. If more points along the generating arc are to be specified, they should occur as mirror image pairs about the line $\theta_j = \pi/2$ in order to satisfy the geometric symmetry of the boundary about this line. The particular technique used for spacing these points along each boundary was to divide the half arc of the sphere into equal segments.

A practical difficulty arises from the specification of the first point, i.e. $\phi = 0^o$ or $\theta_j = \pi/2$. Referring to equations (2.2) and (2.15) V_{rj} can be represented as follows:

$$V_{rj} = -U\cos\theta_j + \sum_j \sum_n \left[B_{nj} r_j^{-n-1} + D_{nj} r_j^{-n+1}\right] P_{n-1}(\cos\theta_j) \qquad (2.28)$$

It can be seen that if $\theta_j = \pi/2$, the trivial solution of 0 - 0 will result when n = 2, as $P_1(\cos\theta_j) = \cos\theta_j$. Thus, one of the algebraic equations in the set (2.19) is lost with the result that one of the elements of the principal diagonal will be equal to zero thereby rendering a solution impossible. In order to overcome this difficulty, the top point can be considered to be a combination of two points that are very close together, i.e. $\phi = \pm\alpha$. The technique used for choosing α is to solve a number of problems in which the boundary conditions are exactly satisfied at only the two points $\phi = \pm\alpha$ on each sphere and noting the largest value of α for which convergence to a prescribed accuracy is obtained. These results are presented in Table 2.1. Examination of Table 2.1 indicates that λ converges to five significant

figures for all sphere spacings where $|\alpha| \leq 1^{o}$. Therefore, in all subsequent multiple sphere problems presented in this study ϕ for the first two points was taken as 1^{o} and these first two points were considered to be the single high point required.

Table 2.1

Convergence Trials for Choosing ϕ for Two Spheres

Number of Points = M	Spacing = d/a	ϕ	λ
2	1	10^{o}	.65994
2	1	5^{o}	.66113
2	1	3^{o}	.66139
2	1	2^{o}	.66147
2	1	1^{o}	.66152
2	1	0.1^{o}	.66152
2	2	10^{o}	.74991
2	2	5^{o}	.75047
2	2	3^{o}	.75059
2	2	2^{o}	.75062
2	2	1^{o}	.75065
2	2	0.1^{o}	.75065
2	4	10^{o}	.84587
2	4	5^{o}	.84599
2	4	3^{o}	.84602
2	4	2^{o}	.84603
2	4	1^{o}	.84604
2	4	0.1^{o}	.84604
2	8	10^{o}	.91481
2	8	5^{o}	.91483
2	8	3^{o}	.91483
2	8	2^{o}	.91483
2	8	1^{o}	.91483
2	8	0.1^{o}	.91483

A fundamental question that remains unanswered at this point is how many multipoles (or at how many points on the generating arc at which the no slip condition is exactly satisfied) are required for each sphere in order that a solution of prescribed accuracy will result.

The accuracy of the truncation is principally a function of d/a. Thus, the convergence characteristics of the two sphere problem were examined over the entire range of spacings, i.e., $1 \leq d/a < \infty$. This problem was handled using the multipole technique satisfying the no-slip boundary conditions at varying numbers of points along the generating arc of each sphere. The drag results are shown in Table 2.2. The data of Table 2.2 are represented graphically in Figure 2.3 by plotting the absolute percentage change in λ from the converged solution against the spacing with the number of boundary points as parameter.

A number of interesting conclusion can be drawn based on the above data. In the most difficult case (i.e. spheres touching) convergence to five significant figures is obtained when the boundary conditions are satisfied at nine equally spaced points on each generating arc. This rapid convergence for the case of two spheres touching is in dramatic contrast to the results of applying the method of reflections to this same problem. Faxén and Dahl (25) carried computations based on the method of reflections to the ninth power and obtained an equation for λ. Happel and Brenner (1) employed an empirical procedure based on the assumption that the last terms in Dahl's expression represent a slowly converging geometric series and obtained the following expression for λ.

$$\lambda = \sum_{n=0}^{9} (-1)^n \alpha_n \left(\frac{a}{d}\right)^n \qquad (2.29)$$

Numerical values for α_n are listed by Happel and Brenner (1). When (a/d) = 1, λ calculated from (2.29) is 0.48, representing an error of 25.6%. Happel and Brenner then assumed that for terms in λ in (2.29) corresponding to $n > 9$, α_n = constant = 1/3. They then carried the summation in (2.29) to infinity and obtained a λ of 0.647 representing

Table 2.2

Approach to Exact Solution for Flow Past 2 Spheres

Number of Points = M	Spacing = d/a	λ
1	1	.66152
3	1	.64411
5	1	.64487
7	1	.64514
9	1	.64515
11	1	.64515
1	2	.75065
3	2	.74244
5	2	.74226
7	2	.74226
1	3	.80851
3	3	.80477
5	3	.80472
7	3	.80472
1	4	.84604
3	4	.84414
5	4	.84412
7	4	.84412
1	8	.91484
3	8	.91454
5	8	.91454
1	16	.95530
3	16	.95525
5	16	.95525

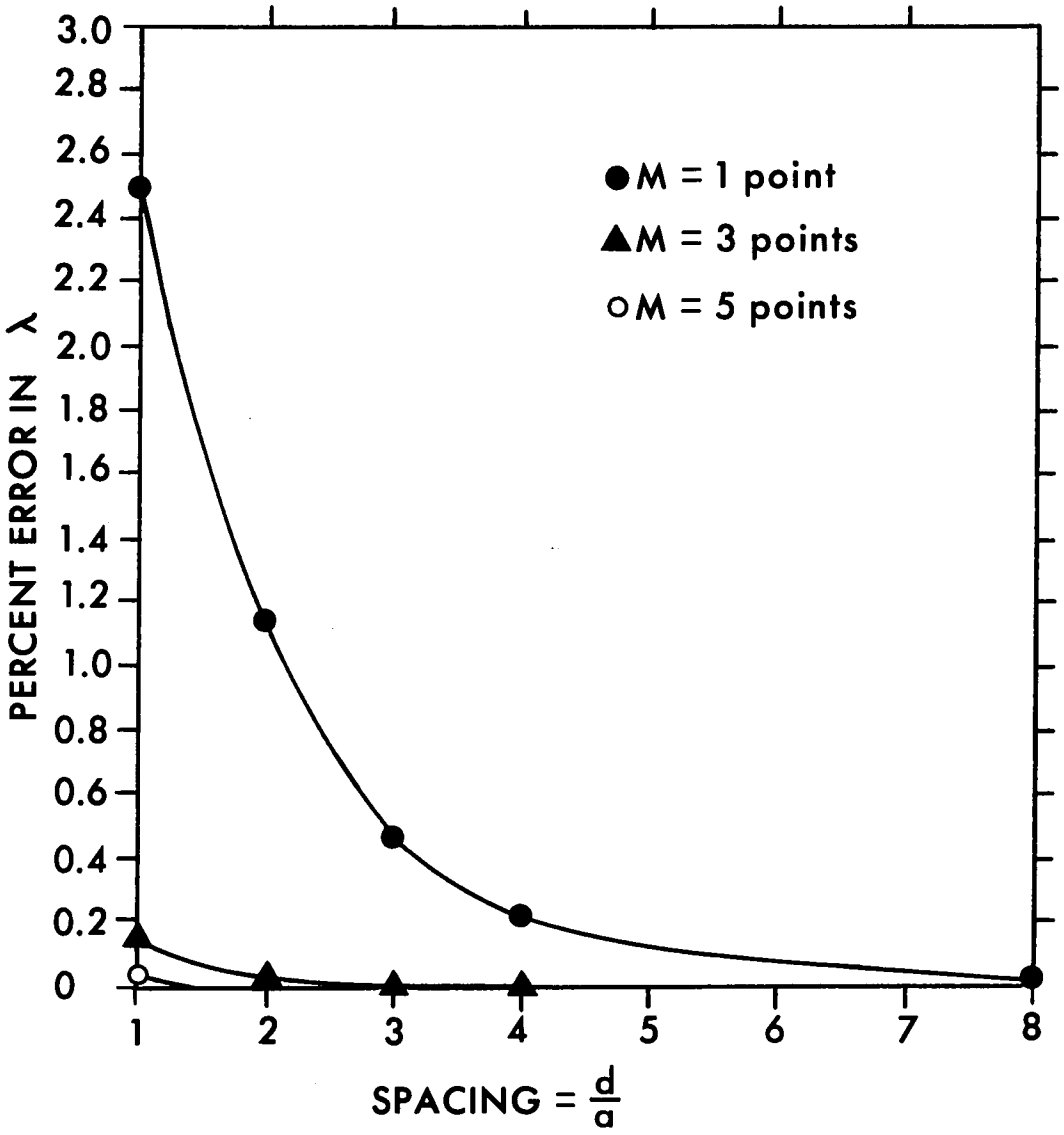

Figure 2.3 - ERROR IN λ VS. d/a AND M FOR SPHERES

an error of 0.31%. It should be noted that the maximum error resulting from the application of the multipole technique to two touching spheres is 2.5% when only one point on each generating arc is used (see Figure 2.3). This greatly improved accuracy occurs because the truncation procedure involves simultaneous interactions, even when the lowest order truncation is used. Table 2.2 indicates that for each case of two touching spheres, convergence to five significant figures is obtained when the boundary conditions are satisfied at nine points along the generating arc of each sphere. For all other cases where $d/a \geq 2$, convergence was attained when only five points on each generating arc were used to satisfy the no slip condition. The relative rates of convergence of this technique are demonstrated graphically in Figure 2.3. It is obvious that for any sphere spacing, convergence increases rapidly with increasing numbers of points.

The streamline patterns in Figure 2.4 indicate certain interesting features. For the case where the two spheres are touching and only one point on each generating arc is used to satisfy the no slip condition it can be seen that the actual solid boundary (represented by the zero streamline) is grossly distorted from the desired spherical shapes (represented by the broken lines). However, the distorted boundary has the same projected area normal to the direction of flow as the true spherical boundary. This accounts for the fact that the drag on the grossly distorted boundary is only 2.5% different from the drag on two perfect spheres. This important feature indicates that if drag results are desired, satisfying the boundary conditions at only one point on the generating arc of each sphere will result in a maximum error of 2.5% whereas if velocity fields are required, a larger number

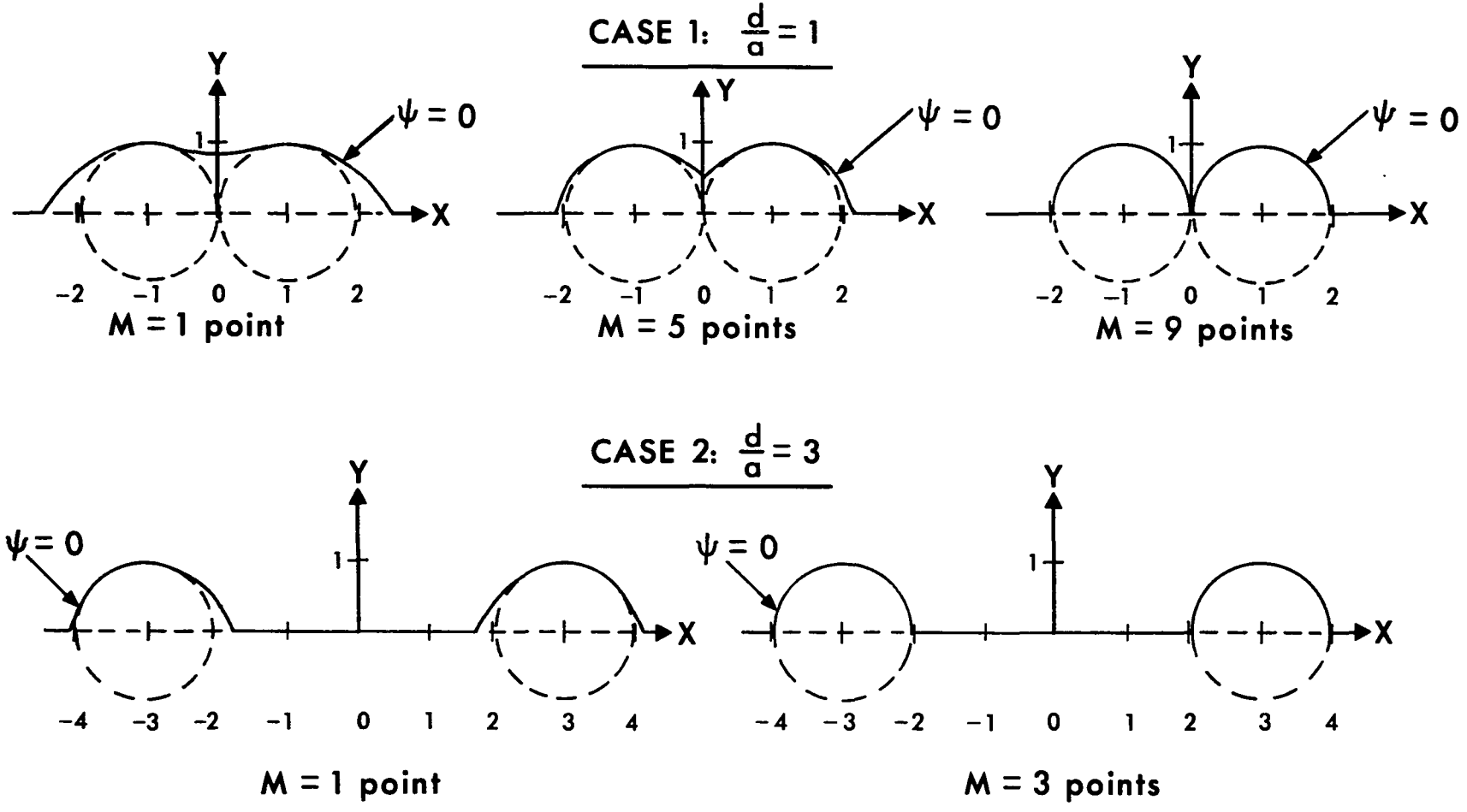

Figure 2.4 - ZERO STREAMLINES VS. d/a AND M FOR SPHERES

of points on each boundary must be used to eliminate large errors.

It has been demonstrated that rapid convergence on a solution is possible for all sphere spacings using the new multipole representation technique. The question yet to be answered is whether the solution obtained actually represents the true solution. To this end, a number of solutions to the two sphere problem at various spacings using the multipole technique are compared with the exact solution of Stimson and Jeffery (7) in Table 2.3.

These data demonstrate that the solution obtained on convergence using the multipole technique is in fact the exact solution as obtained by Stimson and Jeffery. It is of interest to note that the problem of two touching spheres d/a = 1 represents a degenerate case of the exact solution presented by Stimson and Jeffery, i.e.

$$\lambda_{sj} = \frac{2}{3}\sinh\alpha \sum_{n=1}^{\infty} \frac{n(n+1)}{(2n-1)(2n+3)} \left[1 - \frac{4\sinh^2(n+\frac{1}{2})\alpha - (2n+1)^2\sinh^2\alpha}{2\sinh(2n+1)\alpha + (2n+1)\sinh 2\alpha}\right] \quad (2.30)$$

where α is defined as follows:

$$\cosh\alpha = \frac{d}{a}$$

Faxén (26) developed an integral technique for treating the limiting case of equation (2.30) when d/a = 1. The result of applying Faxén's method to the problem of two touching spheres is reported by Goldman, Cox and Brenner (20) as $\lambda_{sj} = 0.6451408$. This result is in fairly close agreement with the equivalent converged solution for λ calculated by the multipole technique and reported in Table 2.2, i.e. $\lambda = 0.64515$.

2.4 SOLUTIONS FOR MULTIPLE SPHERES

In the previous section solutions to the axisymmetric flow past two spheres based on the multipole truncation technique have been

Table 2.3

Comparison of 2 Sphere Solutions with

Exact Results of Stimson and Jeffery

Number of Points = M	Spacing = d/a	λ	λ_{Exact}
1	1.1276260	.67493	.65963
3		.65932	
5		.65946	
7		.65961	
9		.65963	
1	1.5430806	.71431	.70245
3		.70272	
5		.70245	
7		.70245	
1	2.3524096	.77408	.76778
3		.76789	
5		.76778	
7		.76778	
1	3.7621957	.83843	.83620
3		.83622	
5		.83620	
7		.83620	
1	6.1322895	.89221	.89158
3		.89159	
5		.89158	
7		.89158	
1	10.067662	.93096	.93079
3		.93079	
5		.93079	

presented and were shown to be in agreement with the exact solutions presented by other workers. This section will examine the solutions to the problem of axisymmetric flow past finite chains of spheres. To the best of the authors' knowledge exact solutions for finite chains of three or more spheres do not exist in the literature. This is due to the fact that for assemblages of more than three settling spheres, orientations other than sedimentation along the line of centers appear to represent more stable configurations. Slack and Matthews (27) have shown experimentally that clusters containing no more than six spheres will tend to arrange themselves in the same horizontal plane at the vertices of a regular polyhedron. The purpose of considering linear chains of more than three spheres is to demonstrate the application and convergence characteristics of this new technique for systems containing three or more spheres rather than to infer that such chains represent stable settling configurations.

Solutions to flow past chains containing 3, 5, 7, 9, 11, 13, 15 and 101 equally spaced spheres where the boundary conditions are satisfied at one or more points on each generating arc have been obtained. The results of the preceding section for two spheres provide a qualitative guide to the accuracy of these solutions. The maximum error to be expected in λ_j (when the spheres are touching and the boundary conditions are satisfied at only the $\theta_j = \pi/2$ point on the generating arc) will be approximately 2½%. This maximum error will be greatly reduced if more than one point is chosen, e.g. for three points on each generating arc the probable error when the spheres are touching will be 0.16%.

In order to handle the 15 sphere problem utilizing only the two lowest order multipoles, 60 linear simultaneous equations need to be

solved as the uppermost point is actually two points $\phi = \pm 1^{o}$ and this involves four velocity boundary conditions for each sphere. Although this is accomplished very rapidly with the use of a computer, the storage capacity required is rather high. In order to increase the number of spheres from 15 to say 101 requires that 404 simultaneous equations be solved. This is not difficult but requires the use of complex overlaying techniques to accommodate the entire coefficient matrix in core (i.e. 163, 216 words of storage or 652,864 bytes are required).

The drag correction factor λ_j was determined for chains containing various numbers of spheres at different sphere spacings in the range $1 \leq d/a \leq 16$ with the boundary conditions satisfied at both one and three points on each generating arc. The results for $d/a = 2$ are plotted in Figure 2.5. The values for λ_j for the central spheres in a 101 sphere chain are also shown. It is estimated that the error in λ_j in Figure 2.5 where the boundary conditions are satisfied at one point on each generating arc will be approximately 1.1% based on the results of the previous section. Although the drag correction factor λ_j has a discrete value for each object, the values have been connected by solid lines to indicate each individual chain. It can be seen that as the chain length is increased the drag on the central sphere decreases indicating a shielding effect. As the ends of any chain are approached the relative drag on adjacent spheres changes rapidly demonstrating the importance of end effects. As the length of the chain increases the drag on the spheres located in the central portion of the chain changes very slowly. In the limit of an infinite chain the drag on each sphere would be the same.

The broken lines indicate the drag on the nth sphere in any chain.

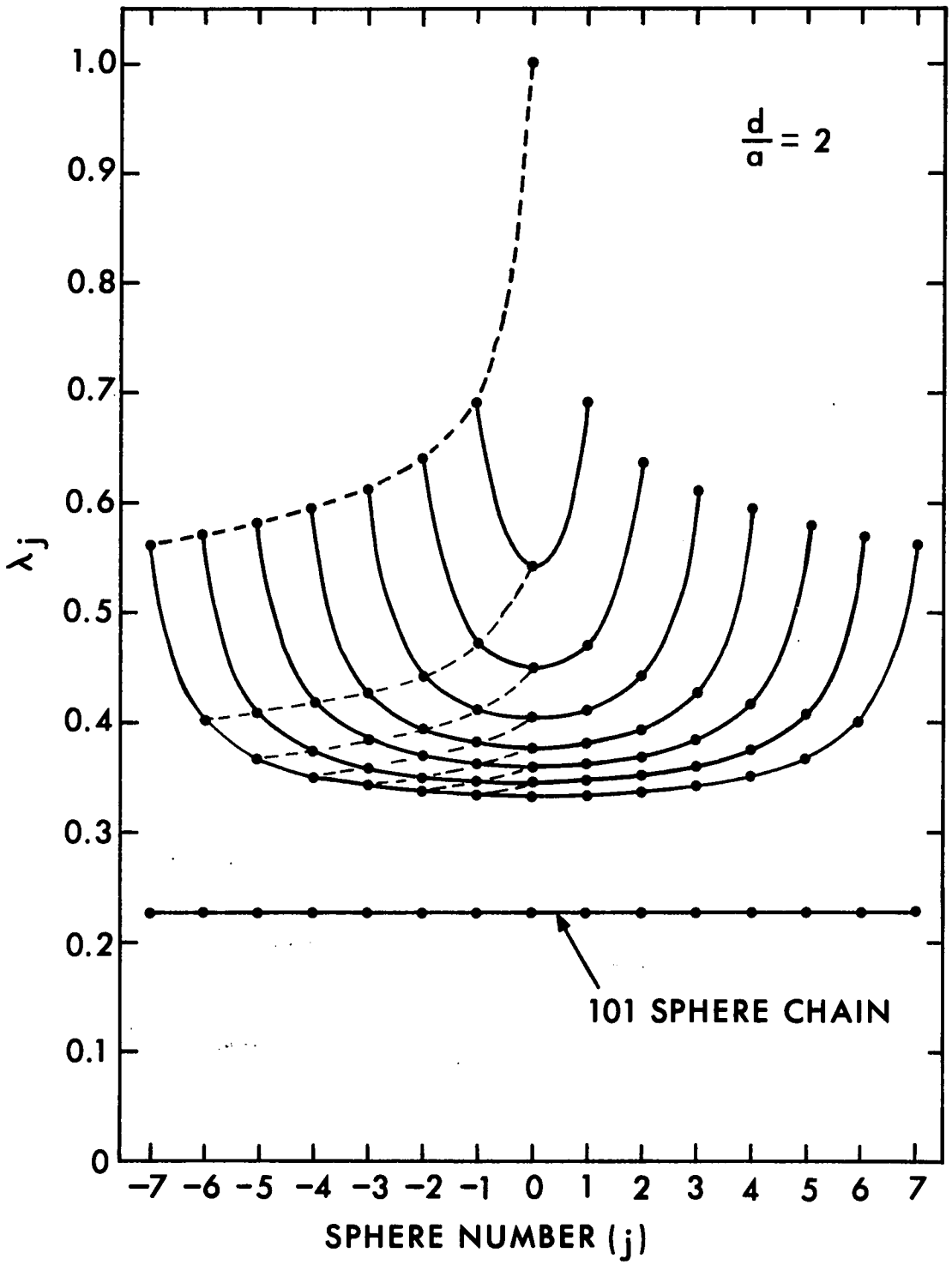

Figure 2.5 - λ_j FOR CHAINS OF SPHERES

It can be seen that as the chain length increases the broken lines tend to become horizontal once again demonstrating the relatively strong shielding characteristics exhibited by a chain of spheres.

All of the above results apply only to a spacing (d/a) of two. In order to determine the effect of sphere spacing on λ_j, curves of λ_j vs. sphere number with d/a as a parameter were plotted for a chain of seven spheres in Figure 2.6. These results demonstrate that as the spacing increases the end effects will decrease. Also, as the spheres get closer together the drag on each sphere in the chain will be reduced.

Figure 2.7 represents plots of the drag correction factor λ_j vs. the sphere number in a chain containing 101 spheres at spacings (d/a) of 1, 2 and 4. For all cases the boundary conditions were satisfied at one point ($\theta_j = \pi/2$) on each sphere with probable errors of 2½% for the case of d/a = 1 and 0.2% for d/a = 4. This figure indicates that the drag on all of the spheres in the center section of the chain changes very little with position. However, it is interesting to note the extent of the end effects exhibited by long finite chains as shown in Figure 2.7.

Finally, if equations (2.15) and (2.24) are used to determine the drag on each sphere in a chain of infinite extent in an unbounded fluid (using the property of perfect periodicity, i.e. $B_{nj} = B_n$ and $D_{nj} = D_n$), it is found that λ_j approaches zero as the number of spheres in the chain becomes very large. This paradoxical result is in contrast to the results of Wang and Skalak (8) who considered the case of an infinite chain of spheres moving along the axis of a circular cylinder. These workers found that for the case of an infinite chain of touching spheres having a ratio of sphere diameter to cylinder diameter of 0.1 the correction to the Stokes drag would be 0.473. This zero drag is in

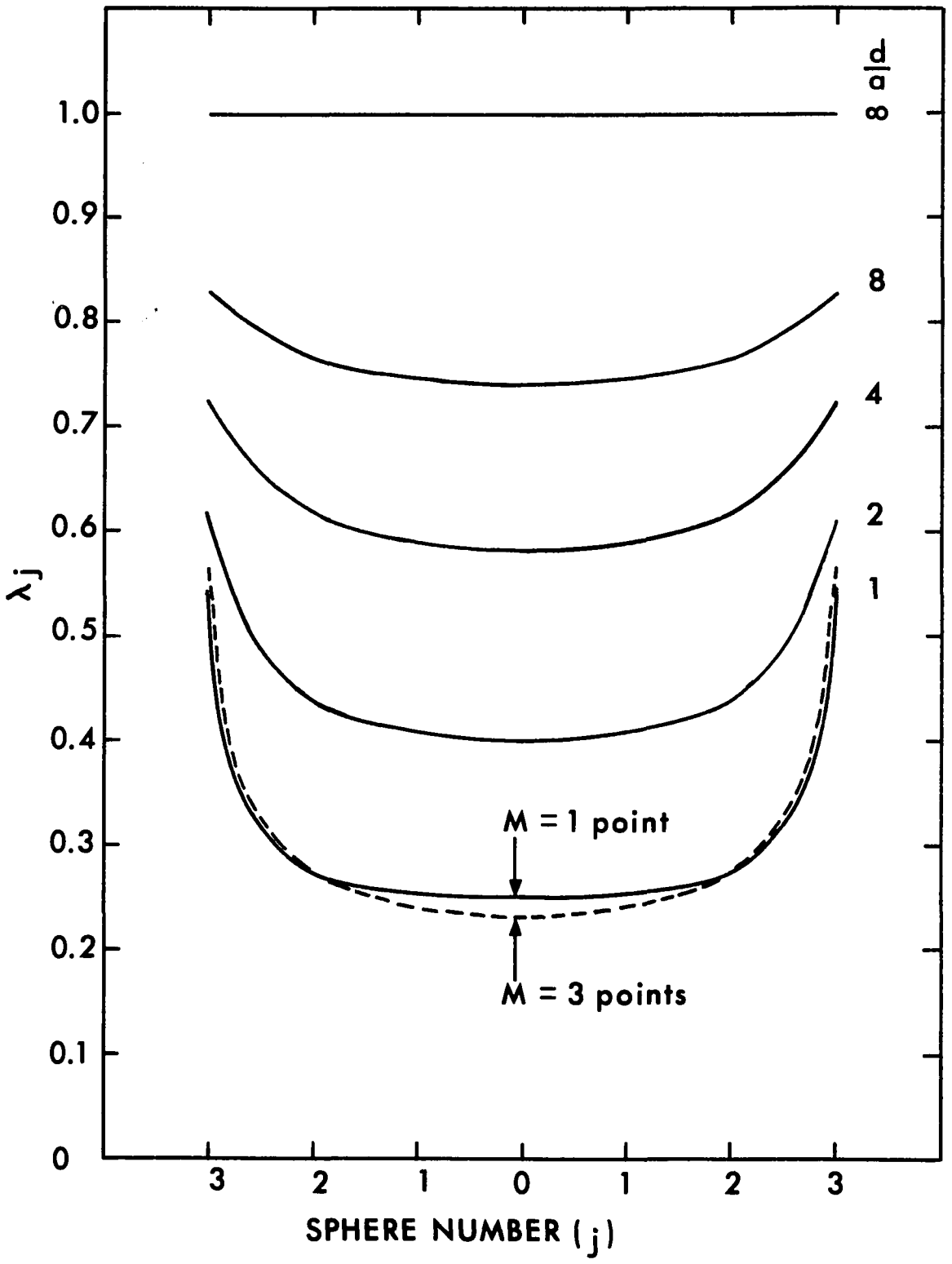

Figure 2.6 - λ_j FOR 7 SPHERE CHAINS

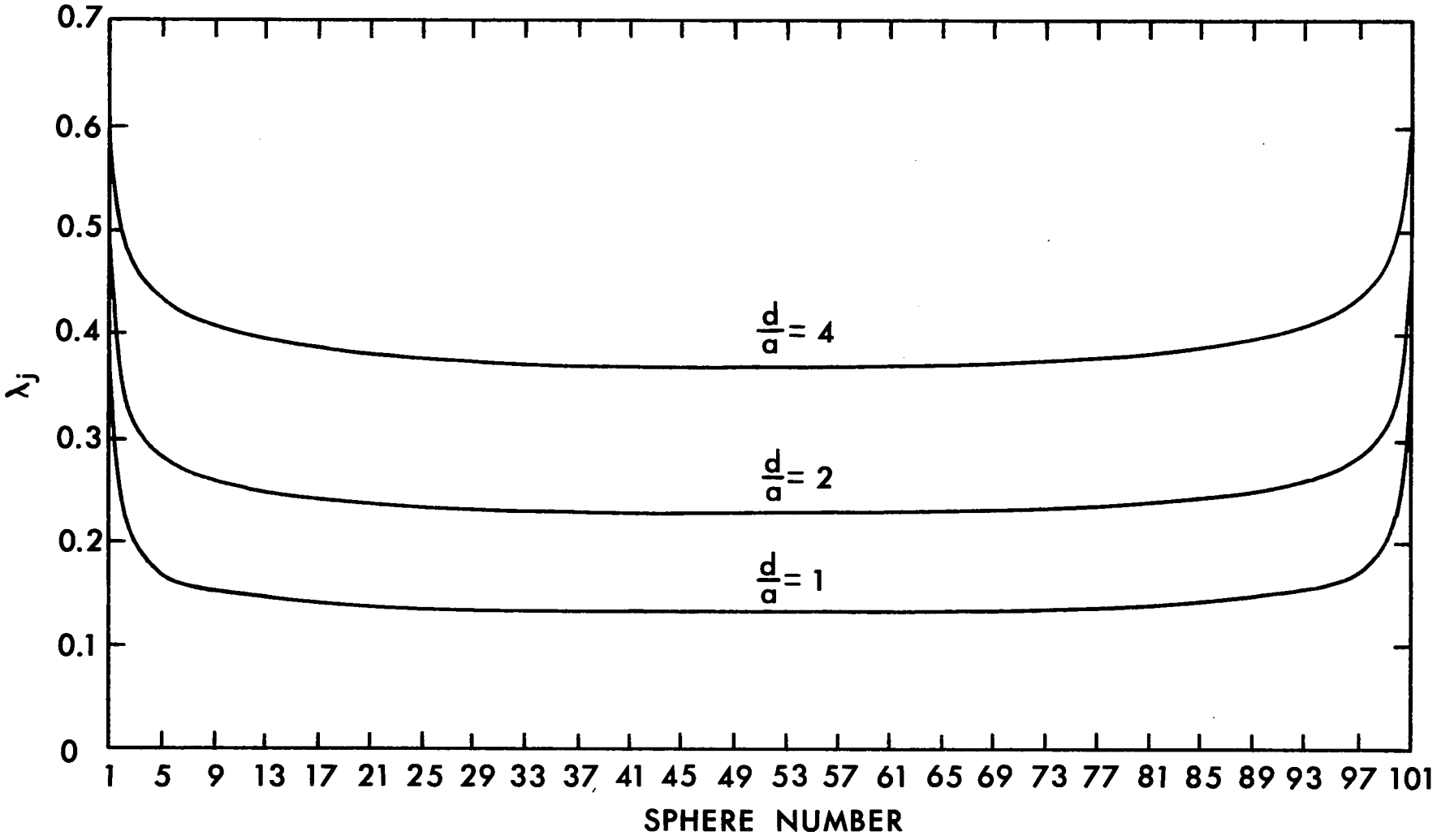

Figure 2.7 - λ_j FOR 101 SPHERE CHAINS

accord with Burgers approximate formula for calculating the drag force per unit length on long cylinders:

$$\frac{F}{h} \approx \frac{2\pi\mu U}{L_n\left(\frac{h}{r_n}\right)-0.72} \tag{2.31}$$

where h = cylinder length

r_n = cylinder radius

It can be seen from (2.31) that as h tends to infinity the drag force per unit length on the cylinder approaches zero.

2.5 FORMULATION FOR MULTIPLE SPHEROIDS

In this section the formulation of a general solution for creeping motion past a finite chain of equally spaced bifocal objects will be presented. An important class of objects in this category are prolate (ovary) spheroids and oblate (planetary) spheroids. (It should be kept in mind that oblate spheroids are only bifocal in a meridian plane as the locus of their foci form a circular ring about their minor axis.) The formulation of the general solution in spheroidal coordinates to the creeping motion equations (2.1) has been presented by Sampson (22):

$$\begin{aligned}\psi = {} & 2c^2 U I_2(p) I_2(q) + \left[D_2 p + B_2 H_2(p) + D_4 H_4(p)\right] I_2(q) \\ & + \left[D_3 + B_3 H_3(p) + D_5 H_5(p)\right] I_3(q) \\ & + \sum_{n=4}^{\infty} \left[D_n H_{n-2}(p) + B_n H_n(p) + D_{n+2} H_{n+2}(p)\right] I_n(q)\end{aligned} \tag{2.32}$$

where U = free stream velocity

D_n, B_n = constants

$I_n(q)$ = Gegenbauer functions of the first kind defined in section 2.4

$H_n(p)$ = Gegenbauer functions of the second kind defined in section 2.4

The p and q are related to the appropriate bifocal coordinate transformations (also see Figure 2.8). For prolate spheroids the coordinate transformation used is:

$$X + iY = c\cosh(\xi + i\eta)$$

$$X = c\cosh\xi\cos\eta \;; \qquad Y = c\sinh\xi\sin\eta$$

$$p = \cosh\xi = \frac{R_1 + R_2}{2c} \;; \qquad q = \cos\eta = \frac{R_2 - R_1}{2c} \tag{2.33}$$

$$R_1 = \left[(x-c)^2 + Y^2\right]^{1/2} \;; \qquad R_2 = \left[(x+c)^2 + Y^2\right]^{1/2}$$

$$\frac{x^2}{a^2} + \frac{y^2}{b^2} = 1 \;; \qquad c^2 = a^2 - b^2$$

while for oblate spheroids the coordinate transformation used is:

$$X + iY = c\sinh(\xi + i\eta)$$

$$X = c\sinh\xi\cos\eta \;; \qquad Y = c\cosh\xi\sin\eta$$

$$p = i\sinh\xi = i\left[\left(\frac{R_1+R_2}{2c}\right)^2 - 1\right]^{1/2} \;; \quad q = \cos\eta = \left[1 - \left(\frac{R_2-R_1}{2c}\right)^2\right]^{1/2} \tag{2.34}$$

$$R_1 = \left[x^2 + (y-c)^2\right]^{1/2} \;; \qquad R_2 = \left[x^2 + (y+c)^2\right]^{1/2}$$

$$\frac{x^2}{a^2} + \frac{y^2}{b^2} = 1 \;; \qquad c^2 = a^2 - b^2$$

It can be shown that the first term in (2.32) represents the free stream contribution to the stream function,

$$2c^2 U I_2(p) I_2(q) = \tfrac{1}{2} U Y^2 \tag{2.35}$$

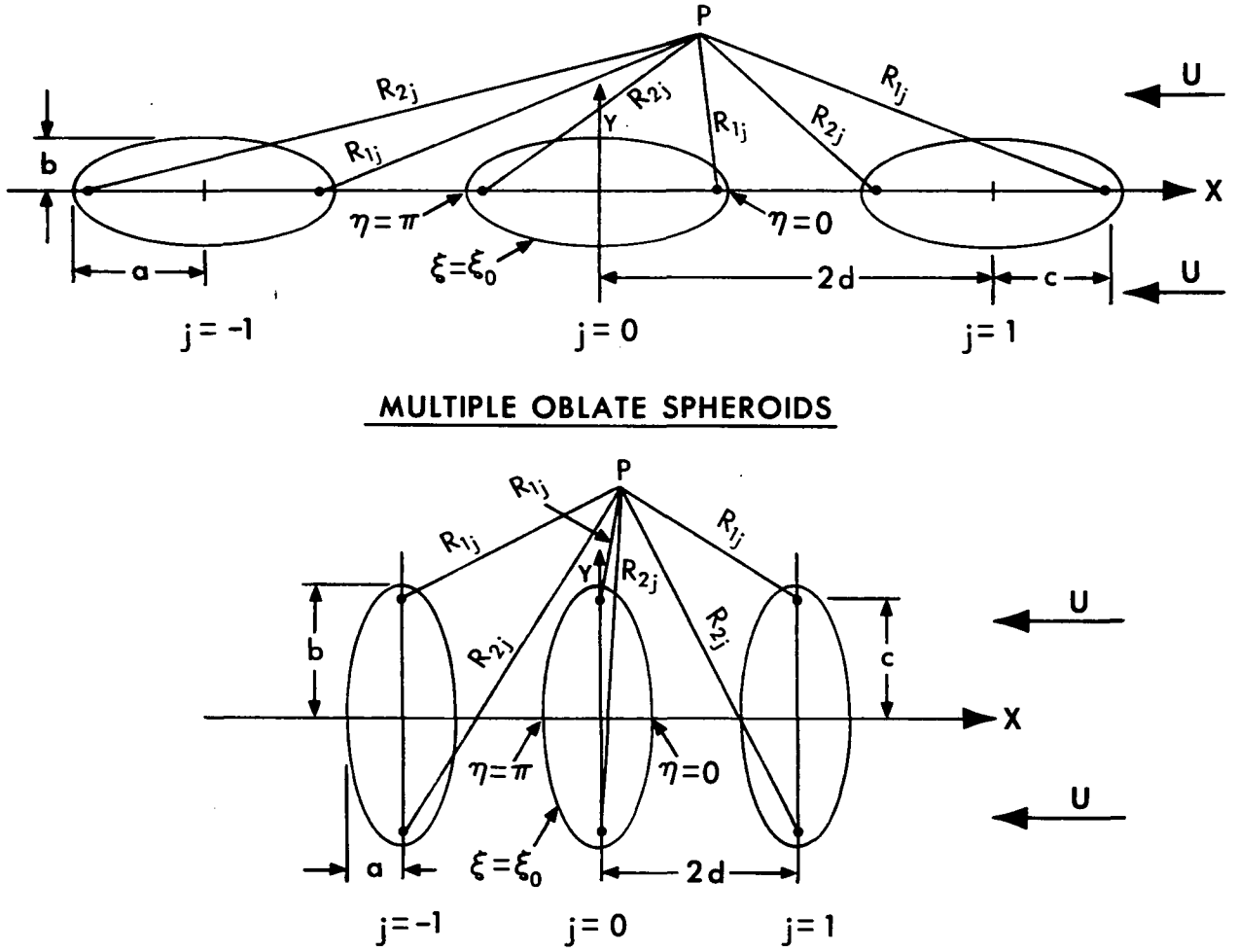

Figure 2.8 - GEOMETRY OF MULTIPLE OBLATE AND PROLATE SPHEROIDAL SYSTEMS

Sampson applied (2.32) to the problem of flow past a single spheroid and showed that the following results needed to be true to produce finite velocities in the far flow field:

$$B_3 = B_4 = B_5 = ... = B_n = D_3 = D_4 = ... = D_n = 0 \qquad (2.36)$$

The remaining constants B_2 and D_2 are determined by applying the no slip boundary conditions,

$$V_p = 0 = \frac{\partial \psi}{\partial q} \quad ; \quad V_q = 0 = \frac{\partial \psi}{\partial p} \quad \text{on} \quad p = p_o \qquad (2.37)$$

where p_o is the surface of the spheroid. Equation (2.32) subject to (2.36) and (2.37) reduces to the solution for the flow past a single spheroid:

$$\psi = 2c^2 U I_2(q)\left[I_2(p) - \frac{p + (p_o^2+1) H_2(p)}{2\left(\frac{p_o^2+1}{4} L_n \frac{p_o+1}{p_o-1} - \frac{p_o}{2}\right)}\right] \qquad (2.38)$$

The above solution for a single spheroid is the same as that proposed by Payne and Pell (28) and Happel and Brenner (1).

In order to extend Sampson's results for flow past a single spheroid to the case of multiple spheroids, the linearity of the biharmonic equation is used,

$$\psi = \sum_{j=-\frac{(N-1)}{2}}^{\frac{(N-1)}{2}} \psi_j \qquad (2.39)$$

where ψ_j is represented by (2.32). Figure 2.8 shows the geometry of the system.

Applying (2.39) to (2.32) one obtains the general form of the solution for the stream function for flow past N spheroids.

$$\Psi = 2c^2 U I_2(p) I_2(q) + \sum_{j=\frac{-(N-1)}{2}}^{\frac{(N-1)}{2}} \Big\{ \Big[D_{2j} P_j + B_{2j} H_2(p_j) + D_{4j} H_4(p_j) \Big] I_2(q_j)$$

$$+ \Big[D_{3j} + B_{3j} H_3(p_j) + D_{5j} H_5(p_j) \Big] I_3(q_j) + \tag{2.40}$$

$$\sum_{n=4}^{\infty} \Big[D_{nj} H_{n-2}(p_j) + B_{nj} H_n(p_j) + D_{n+2,j} H_{n+2}(p_j) \Big] I_n(q_j) \Big\}$$

where p_j and q_j are defined using (2.33) and (2.34) for each spheroid. For prolate spheroids:

$$p_j = \frac{R_{1j} + R_{2j}}{2c} \quad ; \quad q_j = \frac{R_{2j} - R_{1j}}{2c}$$

and (2.41)

$$R_{1j} = \left[(x - c - 2jd)^2 + Y^2 \right]^{1/2} \quad ; \quad R_{2j} = \left[(x + c - 2jd)^2 + Y^2 \right]^{1/2}$$

For oblate spheroids:

$$p_j = i \left[\left(\frac{R_{1j} + R_{2j}}{2c} \right)^2 - 1 \right]^{1/2} \quad ; \quad q_j = \left[1 - \left(\frac{R_{2j} - R_{1j}}{2c} \right)^2 \right]^{1/2}$$

and (2.42)

$$R_{1j} = \left[(x - 2jd)^2 + (Y - c)^2 \right]^{1/2} \quad ; \quad R_{2j} = \left[(x - 2jd)^2 + (Y + c)^2 \right]^{1/2}$$

As for the case of multiple spheres, equation (2.40) contains a a double series expansion which is infinite in one dimension and can be large in the other. Examination of equation (2.40) indicates that the multipole truncation technique described in section 2.2 for multiple spheres is equally valid and readily applied to multiple spheroids. Each term in the inner summation can be interpreted as a multilobular

disturbance emanating from the geometric center of the spheroid with its amplitude related to the B_{nj} and D_{nj} coefficients and its angular dependence given by the Gegenbauer function $I_n(q_j)$. The multilobular function $I_n(\cos \gamma_j)$ differs from the $I_n(\cos \theta_j)$ used in (2.15) for describing spheres in that the angular coordinate θ_j allows the lobes of the Gegenbauer functions to conform to natural spherical coordinates whereas the q_j coordinate stretches or compresses the lobes so as to conform to natural spheroidal coordinates. This transformation from θ_j to γ_j is shown in Figure 2.9 for the function $I_2(\cos \gamma)$ for aspect ratios a/b of 5.0, 1.0 and 0.2. It can be seen that for a/b = 1.0, $I_2(\cos \gamma) = I_2(\cos \theta)$, i.e. the case of a perfect sphere. As the aspect ratio increases above 1.0 an elongation in the x direction occurs and the lobes conform to prolate spheroids. For aspect ratios less than 1.0 compression in the x direction provides lobes that conform to oblate spheroidal cross sections. Similar results are obtained for the higher order $I_n(q_j)$ and represent a stretching of the diagrams shown in Figure 2.2. All the logic developed in section 2.2 concerning the use of the multipole truncation technique for flow past spheres can be applied to the flow past spheroids. Each multipole contains two arbitrary constants B_{nj} and D_{nj} and thus provides freedom to satisfy the no slip boundary conditions at one point along the generating arc of each spheroid. To satisfy exactly the no slip conditions over the entire surface of each spheroid would require the use of an infinite number of multipoles. For any point m on the generating arc of a spheroid in a chain containing N spheroids the no slip boundary conditions can be represented as follows for $\rho_{jm} = \rho_{ojm}$ and $\gamma_{jm} = \gamma_{ojm}$ where M is the total number of points on each generating arc where the no slip boundary conditions are to be satisfied.

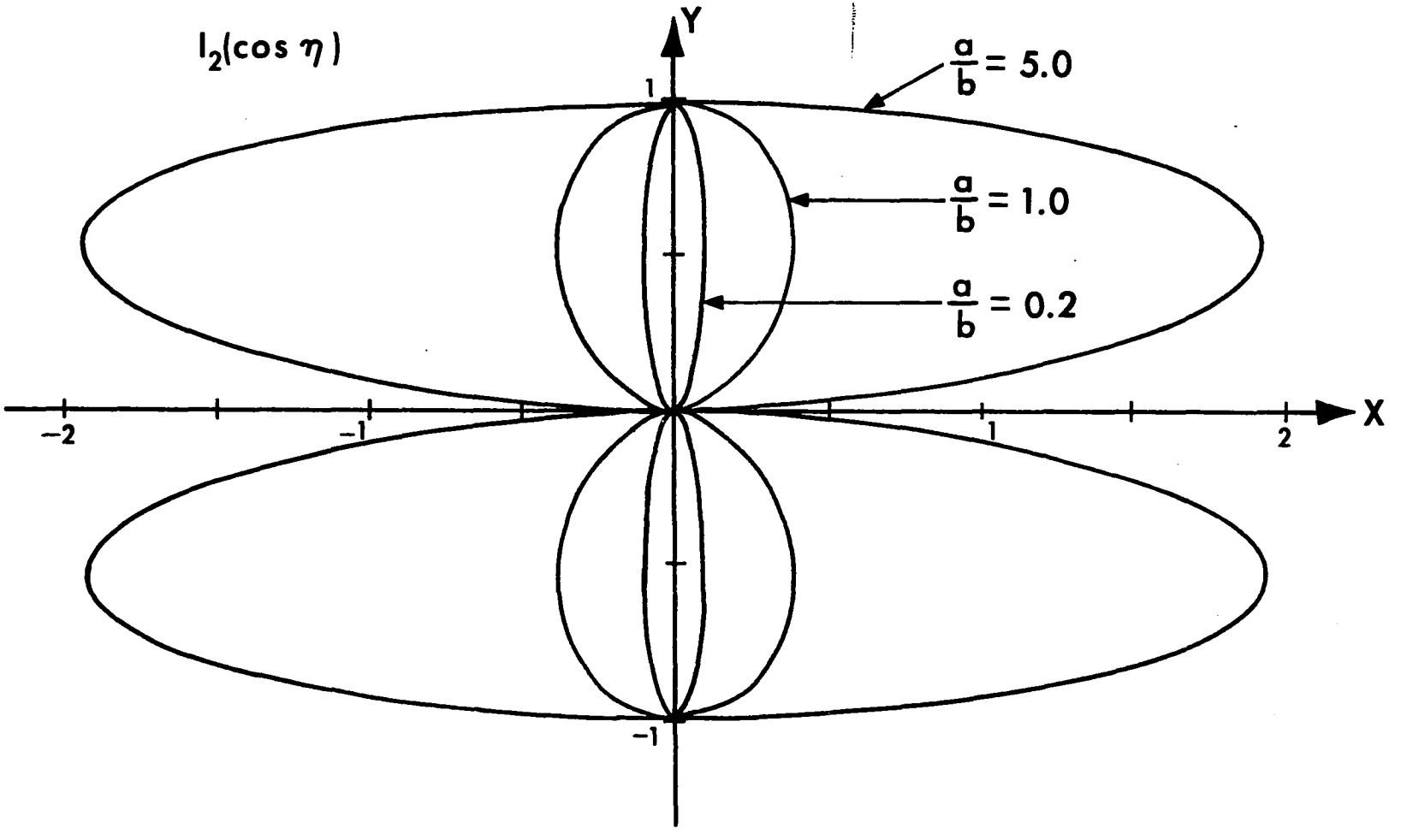

Figure 2.9 - EFFECT OF LOBE STRETCHING ON I_2 ($\cos\eta$)

$$V_{pjm} = 0 = A'_{jm} + \sum_{s=1}^{N} \left\{ \left[D'_{2,s,m} D_{2,s} + B'_{2,s,m} B_{2,s} \right] \right.$$

$$\left. + \left[D'_{3,s,m} D_{3,s} + B'_{3,s,m} B_{3,s} \right] + \sum_{n=4}^{M+1} \left[D'_{n,s,m} D_{n,s} + B'_{n,s,m} B_{n,s} \right] \right\} \quad (2.43a)$$

$$V_{qjm} = 0 = A''_{jm} + \sum_{s=1}^{N} \left\{ \left[D''_{2,s,m} D_{2,s} + B''_{2,s,m} B_{2,s} \right] \right.$$

$$\left. + \left[D''_{3,s,m} D_{3,s} + B''_{3,s,m} B_{3,s} \right] + \sum_{n=4}^{M+1} \left[D''_{n,s,m} D_{n,s} + B''_{n,s,m} B_{n,s} \right] \right\}$$

for $1 \leq m \leq M$

$$A'_{jm} = -2c^2 U I_2(p_{jm}) P_1(q_{jm})$$

$$B'_{n,s,m} = -Q_{n-1}(p_{sm}) I_n(q_{sm}) \frac{\partial p_{sm}}{\partial q_{jm}} - H_n(p_{sm}) P_{n-1}(q_{sm}) \frac{\partial q_{sm}}{\partial q_{jm}}$$

$$D'_{2,s,m} = I_2(q_{sm}) \frac{\partial p_{sm}}{\partial q_{jm}} - p_{sm} P_1(q_{sm}) \frac{\partial q_{sm}}{\partial q_{jm}}$$

$$D'_{3,s,m} = -P_2(q_{sm}) \frac{\partial q_{sm}}{\partial q_{jm}}$$

$$D'_{n,s,m} = -\left[Q_{n-3}(p_{sm}) I_n(q_{sm}) + Q_{n-1}(p_{sm}) I_{n-2}(q_{sm}) \right] \frac{\partial p_{sm}}{\partial q_{jm}}$$
$$- \left[H_{n-2}(p_{sm}) P_{n-1}(q_{sm}) + H_n(p_{sm}) P_{n-2}(q_{sm}) \right] \frac{\partial q_{sm}}{\partial q_{jm}} \quad (2.43b)$$

$$A''_{jm} = -2c^2 U P_1(p_{jm}) I_2(q_{jm})$$

$$B''_{n,s,m} = -Q_{n-1}(p_{sm}) I_n(q_{sm}) \frac{\partial p_{sm}}{\partial p_{jm}} - H_n(p_{sm}) P_{n-1}(q_{sm}) \frac{\partial q_{sm}}{\partial p_{jm}}$$

$$D''_{2,s,m} = I_2(q_{sm}) \frac{\partial p_{sm}}{\partial p_{jm}} - p_{sm} P_1(q_{sm}) \frac{\partial q_{sm}}{\partial p_{jm}}$$

$$D''_{3,s,m} = -P_2(q_{sm}) \frac{\partial q_{sm}}{\partial p_{jm}}$$

$$D''_{n,s,m} = -\left[Q_{n-3}(p_{sm}) I_n(q_{sm}) + Q_{n-1}(p_{sm}) I_{n-2}(q_{sm}) \right] \frac{\partial p_{sm}}{\partial p_{jm}}$$
$$- \left[H_{n-2}(p_{sm}) P_{n-1}(q_{sm}) + H_n(p_{sm}) P_{n-3}(q_{sm}) \right] \frac{\partial q_{sm}}{\partial p_{jm}}$$

It can be seen that (2.43a) and (2.43b) are the equivalent equations in spheroidal coordinates to (2.18a) and (2.18b) in spherical coordinates. Therefore, the solution to slow viscous flow past N submerged spheroids where the boundary conditions are satisfied at M points on each generating arc is represented explicitly by the matrix equation (2.19) where each element is given by (2.43b).

It is of interest to note that equation (2.40) reduces to the solution for flow past equally spaced multiple spheres as the distance between the foci of the spheroids approaches zero. The proof will be outlined for the case of prolate spheroids ($p_j = \cosh \xi_j$) with the free stream contribution in (2.40) represented as $\frac{1}{2}Ur_o^2 \sin^2 \theta_o$. A similar proof could be presented for the case of oblate spheroids. Consider the repeating term in (2.40)

$$R_{nj} = D_{nj} H_{n-2}(p_j) + B_{nj} H_n(p_j) + D_{n+2,j} H_{n+2}(p_j) \tag{2.44}$$

using the recurrence relationship:

$$H_{n+2}(p_j) = \frac{(p_j^2 - \varepsilon_n)}{\delta_n} H_n(p_j) - \frac{\xi_n}{\delta_n} H_{n-2}(p_j) \tag{2.45}$$

where

$$\xi_n = \frac{(n-2)(n-3)}{(2n-1)(2n-3)} \quad ; \quad \xi_0 = \xi_1 = 0$$

$$\delta_n = \frac{(n+1)(n+2)}{(2n-1)(2n+1)}$$

$$\varepsilon_n = \frac{2n^2 - 2n - 3}{(2n+1)(2n-3)}$$

results in

$$R_{nj} = E_{nj} H_{n-2}(p_j) + F_{nj} H_n(p_j) + G_{nj} p_j^2 H_n(p_j) \tag{2.46}$$

where

$$E_{nj} = D_{nj} - \frac{\varepsilon_n}{\delta_n} D_{n+2,j}$$

$$F_{nj} = B_{nj} - \frac{\varepsilon_n}{\delta_n} D_{n+2,j}$$

$$G_{nj} = \frac{D_{n+2,j}}{\delta_n}$$

As $r_j = [(x-2jd)^2 + y^2]^{\frac{1}{2}}$ it is simple to show that as $c \to 0$, $p_j \to r_j/c$, i.e. $H_n(p_j) \to H_n(r_j/c)$. For large values of the argument, the asymptotic behavior of Gegenbauer functions of the second kind can be deduced from their relationship to the hypergeometric function:

$$H_n(p) = 2^{-n} \frac{(n-2)!\,\pi^{1/2}}{(n-\frac{1}{2})!} p^{-n+1} F\left[\frac{n-1}{2}, \frac{n}{2}, n-\tfrac{1}{2}, (p^{-2})\right] \qquad (2.47)$$

ie. $H_n\left(\frac{r_j}{c}\right) \to M_n \left(\frac{r_j}{c}\right)^{-n+1}$ as $c \to 0$

as $F\left[\frac{n-1}{2}, \frac{n}{2}, n-\tfrac{1}{2}, (p^{-2})\right] \to 1$ as $c \to 0$

where M_n is a constant and can therefore be combined with c to produce:

$$H_n\left(\frac{r_j}{c}\right) \to M_n' r_j^{-n+1} \quad \text{as} \quad c \to 0 \qquad (2.48)$$

Combining (2.48) with (2.46) results in:

$$R_{nj} \to E_{nj}' r_j^{-n+3} + F_{nj}' r_j^{-n+1} \quad \text{as} \quad c \to 0$$

Using this result with (2.48) in (2.40) produces:

$$\psi = \tfrac{1}{2} U r_o^2 \sin^2\theta_o + \sum_j \left\{ \left[D'_{2j} r_j + B'_{2j} r_j^{-1} \right] I_2(\eta_j) + \left[D'_{3j} + B'_{3j} r_j^{-2} \right] I_3(\eta_j) + \sum_{n=4}^{\infty} \left[E'_{nj} r_j^{-n+3} + F'_{nj} r_j^{-n+1} \right] I_n(\eta_j) \right\}$$

It can be seen that this is identical in form to (2.15), the solution to the stream function for flow past multiple spheres.

Finally one wishes to determine the drag force exerted by the fluid on each submerged spheroid. In this case instead of using the integral relationship to determine Fj, a technique developed by Payne and Pell (28) will be used. Provided that the fluid at infinity is at rest the above authors have shown that the drag on a submerged object can be represented as follows:

$$F_j = 8\pi\mu \lim_{r_j \to \infty} \frac{r_j \psi}{r_j^2 \sin^2\theta_j} \tag{2.49}$$

If the fluid at infinity is not at rest, (2.49) can easily be modified to represent the drag force

$$F_j = 8\pi\mu \lim_{r_j \to \infty} \frac{r_j (\psi - \psi_\infty)}{r_j^2 \sin^2\theta_j} \tag{2.50}$$

For the case of prolate spheroids

$$r_j = c\left(\cosh^2\xi_j \cos^2\eta_j + \sinh^2\xi_j \sin^2\eta_j\right)^{1/2} \tag{2.51}$$

as $r_j \to \infty$, $r_j \to c\cosh\xi_j \to c e^{\xi_j}$ i.e. $\cosh\xi \to \sinh\xi$ $\xi \gg 1$

also $r_j^2 \sin^2\theta_j = y^2 = c^2 \sinh^2\xi_j \sin^2\eta_j$

as $r_j \to \infty$, $r_j^2 \sin^2\theta_j \to c^2 e^{2\xi_j} \sin^2\eta_j$

i.e., $$\frac{r_j}{r_j^2 \sin^2\theta_j} \to \frac{1}{c\, e^{\xi_j} \sin^2\eta_j} \quad \text{for} \quad \xi_j >> 1$$

Using the fact that

$$\psi_\infty = 2c^2 U I_2(p_0) I_2(q_0) \tag{2.52}$$

(2.50) reduces to

$$F_j = 8\pi\mu \lim_{ce^{\xi_j}\to\infty} \frac{(\psi - \psi_\infty)}{c e^{\xi_j} \sin^2\eta_j} \tag{2.53}$$

It has already been demonstrated that for large arguments, the asymptotic behavior of Gegenbauer functions of the second kind can be represented as follows:

$$H_n(p_j) \to p_j^{-n+1} \quad \text{as} \quad p_j \to \infty$$

$$H_n(p_j) \to \frac{1}{e^{n\xi_j - \xi_j}} \quad \text{as} \quad r_j \to \infty \tag{2.54}$$

Applying (2.54) and (2.40) to (2.53) it can be seen that the only multipole in (2.40) that contributes to the drag is the first one.

$$\frac{p_j I_2(q_j)}{c e^{\xi_j} \sin^2\eta_j} \to \frac{\frac{1}{2} e^{\xi_j} \sin^2\eta_j}{c e^{\xi_j} \sin^2\eta_j} \to \frac{1}{2c} \quad \text{as} \quad \xi_j \to \infty$$

$$\frac{I_3(q_j)}{c e^{\xi_j} \sin^2\eta_j} \to 0 \; ; \quad \frac{H_2(p_j) I_2(q_j)}{c e^{\xi_j} \sin^2\eta_j} \to \frac{1}{2c e^{2\xi_j}} \to 0 \quad \text{as} \quad \xi_j \to \infty \tag{2.55}$$

Using (2.55) the following result for the drag on each object is obtained:

$$F_j = \frac{4\pi\mu D_{2,j}}{C} \tag{2.56}$$

Thus, as was the case for submerged spheres, the drag is determined by the intensity of the first order multipole in the expression for the stream function. This intensity of course depends implicity on the higher order multipoles as D_{2j} is just one element of the set of matrix equations that are solved simultaneously. By adopting similar techniques it can be shown that (2.56) applies to the case of oblate spheroids as well as to prolate spheroids.

In order to be able to compare drag results for spheroids with the Stokes drag for a single sphere, the following argument is proposed. Consider a sphere having a radius equal to the axis dimension of the spheroid normal to the direction of flow. This would be represented by the minor axis of a prolate spheroid or the major axis of an oblate spheroid -- in both cases represented by the symbol b in this study. The drag on a perfect sphere of radius b as represented by Stokes formula would be:

$$F = 6\pi\mu U b \tag{2.57}$$

If, once again, λ_j is used to represent the correction to the Stokes drag on a single sphere in terms of the drag force on a spheroid, (2.57) can be modified as follows:

$$F_j = 6\pi\mu U b \lambda_j \tag{2.58}$$

Solving (2.58) and (2.56) simultaneously results in the following expression for λ_j

$$\lambda_j = \frac{D_{2j}}{1.5cbU} \tag{2.59}$$

2.6 SOLUTIONS FOR MULTIPLE PROLATE SPHEROIDS

Creeping motion solutions for flow past two spheroids have been formulated by Wakiya (9). Although these general solutions were formulated for any orientation of the spheroids, they were not solved for the axisymmetric case and cannot therefore be used as a source of comparison for the results presented in this section.

Before presenting solutions for flow past prolate spheroids some of the practical aspects of solving equations (2.43) will be discussed. The major numerical difficulty is that ill conditioning can occur in the matrix equation (2.19) if any of the p_j arguments become large or if high order multipoles are required to satisfy the boundary conditions at many points on each generating arc as the absolute values of Gegenbauer functions of the second kind $H_n(p_j)$ become extremely small for large arguments as well as for high orders. When ill conditioning exists, instead of using a direct matrix reduction technique one employs an iterative matrix reduction scheme (i.e., corrections to original solution computed from residual vectors) utilizing double precision arithmetic. A second difficulty which is not immediately obvious is associated with the generation of Gegenbauer and Legendre functions of the second kind using recurrence relationships of the form:

$$Q_n(p) = \frac{(2n-1)\,p\,Q_{n-1}(p) - (n-1)\,Q_{n-2}(p)}{n}$$

and (2.60)

$$H_n(p) = \frac{Q_{n-2}(p) - Q_n(p)}{(2n-1)}$$

Even the use of double precision arithmetic produces errors in $H_{10}(10)$ computed from the above of $0(10^{15})$. Therefore, when the absolute value of either $Q_n(p)$ or $H_n(p)$ is less than 10^{-9}, the values of these functions should be calculated directly from their asymptotic behavior rather than the above recurrence relationships. The asymptotic behavior of these functions for $p \gg 1$ is given by

$$Q_n(p) = \frac{n!}{1.3.5.7.\ldots.(2n+1)}\,p^{-n-1}$$

$$H_n(p) = \frac{(n-2)!}{1.3.5.7.\ldots.(2n-1)}\,p^{-n+1} \qquad (2.61)$$

A third difficulty discussed previously for multiple spheres, is that the equations (2.43) reduce to trivial form at $\phi = 0$, the point located vertically above the geometric center of the spheroid. This uppermost point must again be represented by two points on the generating arc of each spheroid where the no slip conditions are to be satisfied, and chosen such that the solution for these two points converges to the solution for a single point. The results of these particular convergence trials will not be presented in detail. It is sufficient to state that in all cases examined the value of the

angle $\phi = \pm\alpha$ in degrees required to produce convergence to five significant figures was equal in magnitude to the ratio of major to minor axis

$$\alpha = \frac{a}{b}$$

In order to show that equation (2.40) converges to the exact solution for the flow past a single prolate spheroid, solutions were obtained for two prolate spheroids having a spacing to major axis ratio of 10,000. The boundary conditions were satisfied at only the uppermost point on each generating arc. These results based on the two lowest order multipoles are compared with the exact solutions of Happel and Brenner (1) in Table 2.4. All results in this section will be stated in terms of the drag correction factor λ_j defined by (2.59).

Table 2.4

Comparison of Drag Results for 1 Prolate Spheroid from (2.40) with Exact Results of Happel and Brenner (1)

Aspect Ratio = a/b	Spacing = d/a	λ Equation (2.40)	λ Happel & Brenner
1.01	10,000	1.002	1.002
1.10	10,000	1.020	1.020
1.50	10,000	1.102	1.102
2.00	10,000	1.204	1.204
5.00	10,000	1.785	1.785
10.00	10,000	2.647	2.647
100.00	10,000	13.895	13.895

Table 2.4 demonstrates that in the limit of one prolate spheroid, equation (2.40) agrees with the exact solution to four significant digits. We next examine the convergence characteristics of truncated multipole solutions for flow past two prolate spheroids at various spacings where the boundary conditions are satisfied at increasing numbers of points along the generating arc of each spheroid. The

locations of these boundary points were chosen by dividing the η coordinate into equal parts. These results are tabulated in Table 2.5 and are presented graphically in Figure 2.10. The streamlines have also been plotted in Figure 2.11 for certain cases of particular interest.

Table 2.5 and Figure 2.10 indicate that convergence to five significant figures is rapidly attained in all cases - even when the spheroids are touching. Except for the case of two spheroids touching where seven points were required for five digit convergence, only five points on each object resulted in convergence to five significant figures for all other spacings. From Figure 2.10 it can be seen that the relative errors in λ_j are almost the same as those for the two sphere problem (see Figure 2.3). The distortions of the zero streamline for two touching spheroids (a/b = 2) and for two spheroids having a d/a ratio of three (see Figure 2.11) are similar but of smaller magnitude to the distortions in the case of two spheres (see Figure 2.4). This result is not unexpected because as the aspect ratio increases the objects become extended in the flow direction and in the limit of infinite aspect ratio the boundaries will be parallel to the free stream streamlines.

Finally, drag results for flow past chains consisting of from one to fifteen prolate spheroids have been plotted in Figure 2.12. The spheroids considered for this case had an aspect ratio of five and a spacing parameter (d/a) of two. The drag correction factor λ_j for each spheroid in every chain has been plotted against the spheroid number j as was done in section 2.4 for chains of spheres (see Figure 2.5). The boundary conditions were satisfied at only one point on each object indicating a probable maximum error of 0.6% based on the

Table 2.5

Convergence of Drag Results for 2 Prolate Spheroids

Aspect Ratio = a/b	Spacing = d/a	No. of Boundary Points = M	λ
2.0	1.0	1	0.8669
2.0	1.0	3	0.8452
2.0	1.0	5	0.8441
2.0	1.0	7	0.8442
2.0	1.0	9	0.8442
2.0	2.0	1	0.9876
2.0	2.0	3	0.9813
2.0	2.0	5	0.9812
2.0	3.0	1	1.0480
2.0	3.0	3	1.0458
2.0	3.0	5	1.0458
2.0	4.0	1	1.0825
2.0	4.0	3	1.0815
2.0	4.0	5	1.0815
2.0	8.0	1	1.1397
2.0	8.0	3	1.1396
2.0	8.0	5	1.1396
2.0	16.0	1	1.1709
2.0	16.0	3	1.1709
5.0	1.0	1	1.4076
5.0	1.0	3	1.3752
5.0	1.0	5	1.3705
5.0	1.0	7	1.3700
5.0	1.0	9	1.3700
5.0	1.0	11	1.3700
5.0	2.0	1	1.5727
5.0	2.0	3	1.5676
5.0	2.0	5	1.5675
5.0	2.0	7	1.5675
5.0	2.0	9	1.5675
5.0	3.0	1	1.6380
5.0	3.0	3	1.6365
5.0	3.0	5	1.6364
5.0	3.0	7	1.6364
5.0	4.0	1	1.6726
5.0	4.0	3	1.6719
5.0	4.0	5	1.6719
5.0	8.0	1	1.7270
5.0	8.0	3	1.7269
5.0	8.0	5	1.7269
5.0	16.0	1	1.7554
5.0	16.0	3	1.7554

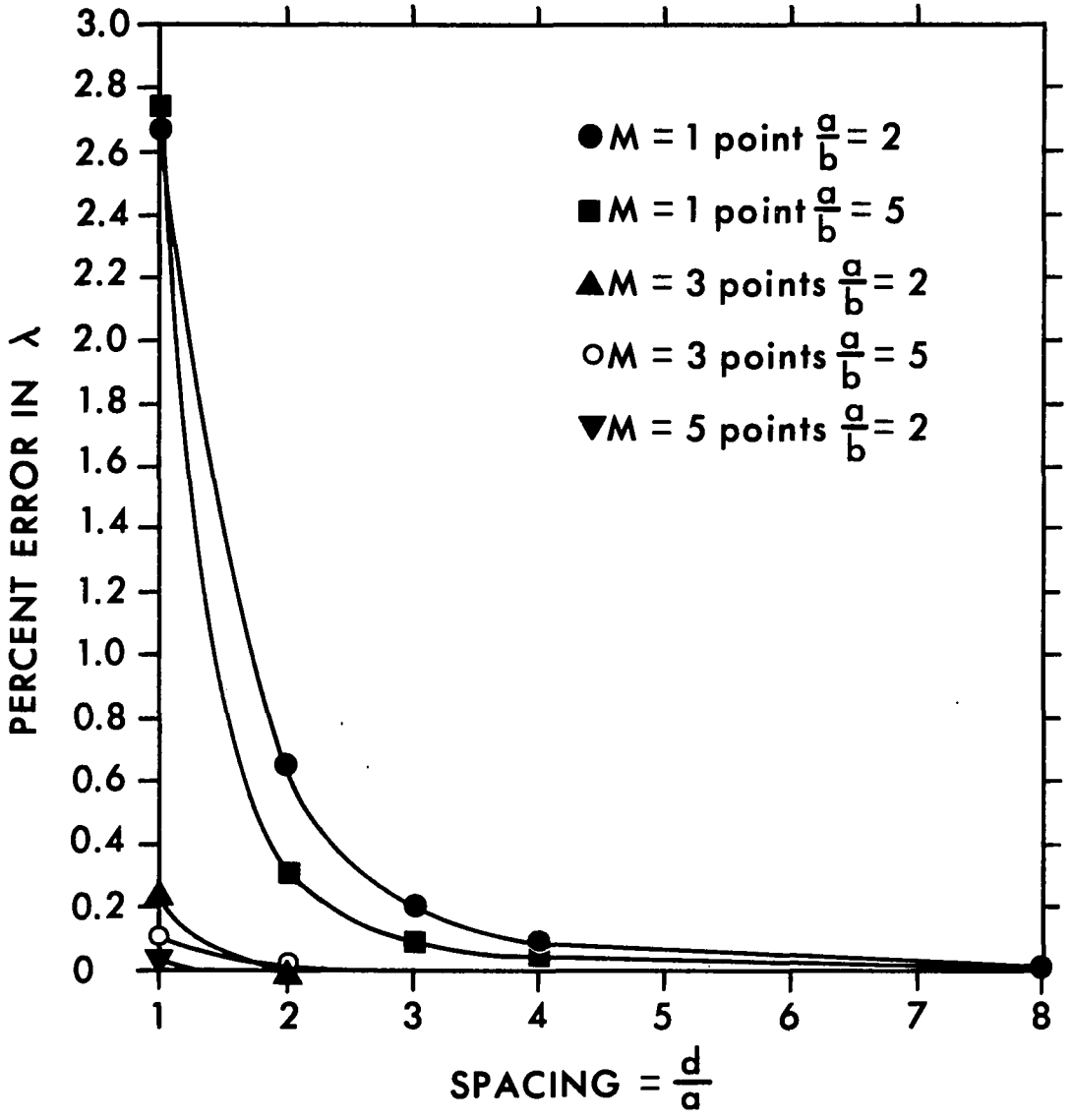

Figure 2.10 - ERROR IN λ VS. d/a AND M FOR PROLATE SPHEROIDS

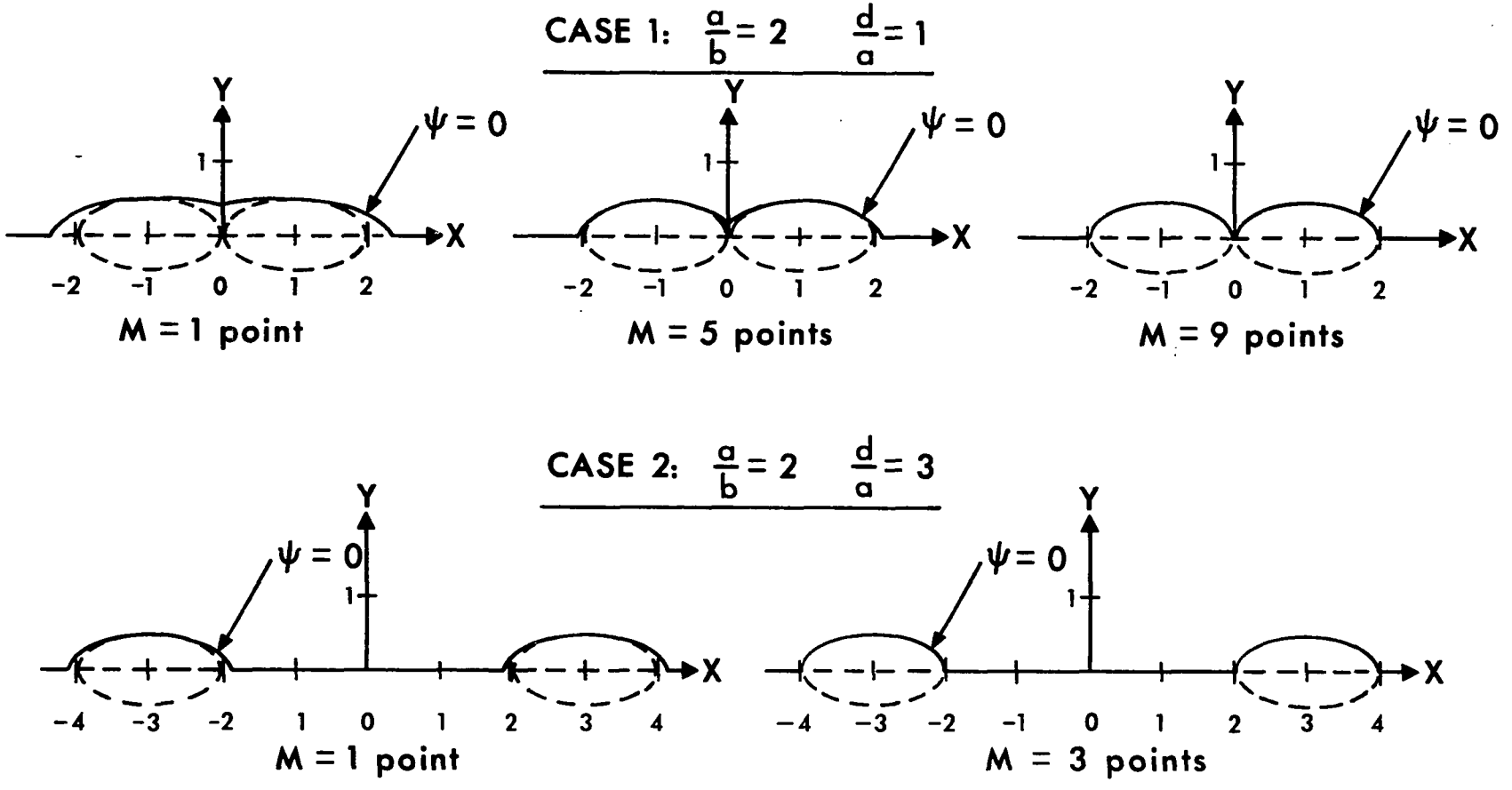

Figure 2.11 - ZERO STREAMLINES VS. d/a AND M FOR PROLATE SPHEROIDS

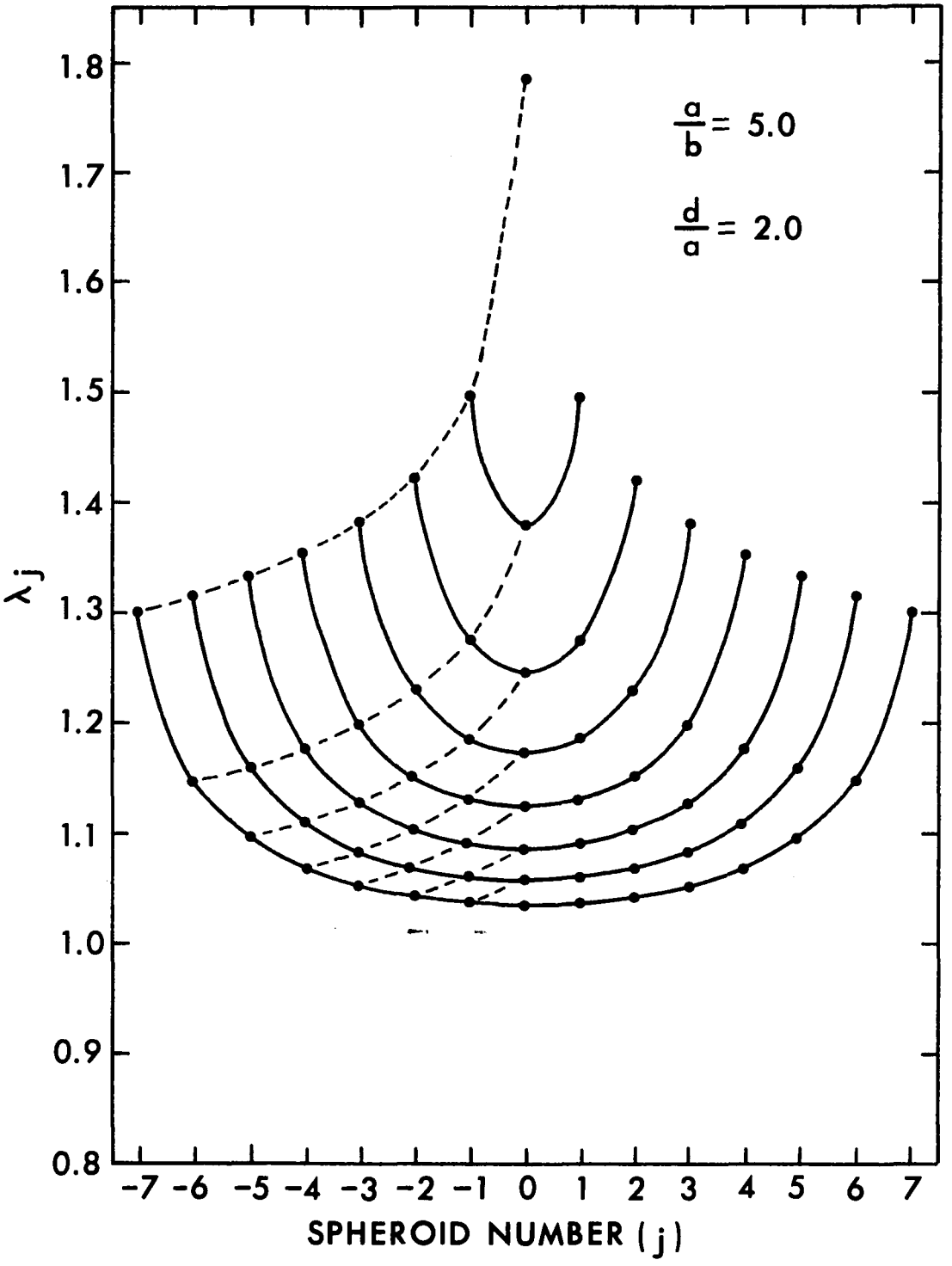

Figure 2.12 - λ_j FOR CHAINS OF PROLATE SPHEROIDS

two spheroid results presented in Figure 2.10.

The solid curves have been drawn to show the change in drag between spheroids within one chain. Comparing these curves with the equivalent drag results for spheres in Figure 2.5, it can be seen that for the case of prolate spheroids less shielding exists within any single chain than in an equivalent chain of spheres. The broken curves in Figure 2.12 demonstrate the change in drag on the jth spheroid in a chain as more spheroids are added to the chain. These curves are of greater slope than those for spheres (Figure 2.5) once again indicating the weaker shielding characteristics exhibited by a chain of prolate spheroids. As the results in Figure 2.12 were all obtained for spheroids having a spacing parameter (d/a) of two the drag on each spheroid in a seven spheroid chain is plotted in Figure 2.13 for different particle spacings. Comparing these results with the equivalent results for spheres in Figure 2.6 one again observes the weaker shielding effects of prolate spheroids. This comparison also indicates that the interactions between prolate spheroids in a chain will approach zero at smaller values of the spacing parameter than can be expected in the case of spheres.

2.7 SOLUTIONS FOR MULTIPLE OBLATE SPHEROIDS

All of the precautionary measures discussed in section 2.6 to be adopted when applying equation (2.40) to the case of prolate spheroids apply when (2.40) is used to solve flow problems past oblate spheroids. In addition, it must be kept in mind that for oblate spheroids the coordinate axis p_j is purely imaginary and, therefore, the Gegenbauer and Legendre functions of the second kind need to be determined using double precision complex arithmetic.

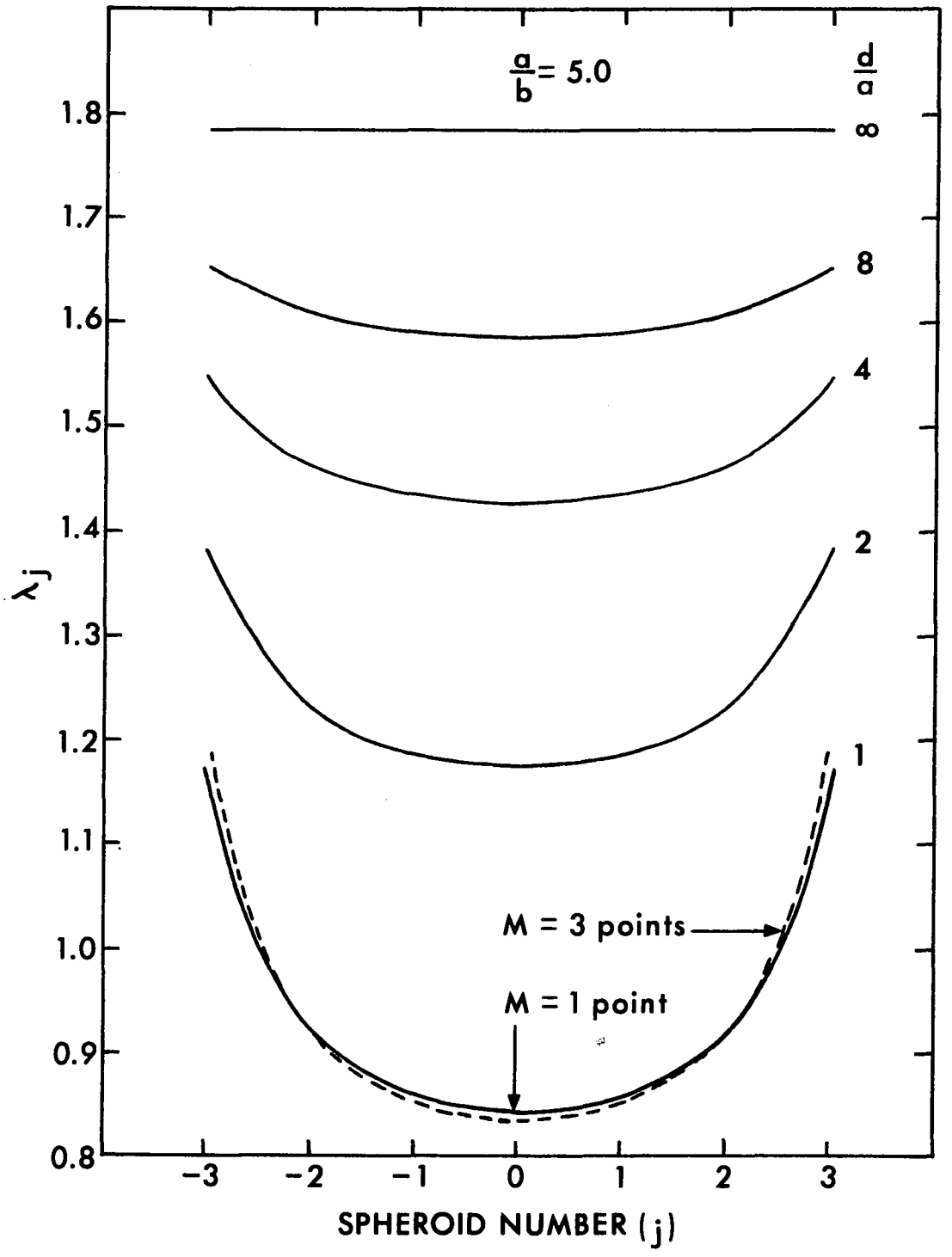

Figure 2.13 - λ_j FOR CHAINS CONTAINING 7 PROLATE SPHEROIDS

Results for flow past a single oblate spheroid were obtained from equation (2.40) by considering two oblate spheroids having a spacing parameter (d/a) of 10,000. The boundary conditions were satisfied at the uppermost point on each generating arc and the results are compared with the exact solutions of Happel and Brenner (1) in Table 2.6. These results demonstrate that truncated solutions based on the lowest order multipoles agree to four significant digits with the exact solution for the limiting case of flow past a single oblate spheroid for all values of $0.01 \leq a/b \leq 1.0$.

Table 2.6

Comparison of Drag Results for 1 Oblate Spheroid from (2.40) with Exact Solutions of Happel and Brenner (1)

Aspect Ratio = a/b	Spacing Parameter = d/a	λ Equation (2.40)	λ_{Exact} Happel & Brenner
0.99	10,000	.9980	.9980
0.90	10,000	.9801	.9801
0.70	10,000	.9415	.9415
0.50	10,000	.9053	.9053
0.20	10,000	.8615	.8615
0.10	10,000	.8525	.8525
0.01	10,000	.8489	.8489

Results showing the convergence of the solution for flow past two oblate spheroids at various spacings where the boundary conditions were satisfied at increasing numbers of points along the generating arc of each spheroid, are tabulated in Table 2.7 and presented graphically in Figure 2.14. Streamlines have been plotted in Figure 2.15 for some cases of interest. The locations of points along the generating arc where the boundary conditions are to be satisfied are determined by dividing the angle γ into equal parts as was done for the case of prolate spheroids. Also from symmetry $\lambda_1 = \lambda_2 = \lambda$.

Table 2.7

Convergence Results for Flow Past 2 Oblate Spheroids

Aspect Ratio = a/b	Spacing = d/a	No. of Points = M	λ
0.2	1	1	0.4829
0.2	1	3	0.4672
0.2	1	5	0.4699
0.2	1	7	0.4696
0.2	1	9	0.4697
0.2	1	11	0.4697
0.2	2	1	0.5146
0.2	2	3	0.5007
0.2	2	5	0.5015
0.2	2	7	0.5015
0.2	3	1	0.5410
0.2	3	3	0.5293
0.2	3	5	0.5295
0.2	3	7	0.5295
0.2	4	1	0.5644
0.2	4	3	0.5548
0.2	4	5	0.5548
0.2	8	1	0.6394
0.2	8	3	0.6351
0.2	8	5	0.6351
0.2	16	1	0.7217
0.2	16	3	0.7207
0.2	16	5	0.7207
0.5	1	1	0.5516
0.5	1	3	0.5358
0.5	1	5	0.5374
0.5	1	7	0.5375
0.5	1	9	0.5375
0.5	2	1	0.6103
0.5	2	3	0.6001
0.5	2	5	0.6001
0.5	3	1	0.6571
0.5	3	3	0.6504
0.5	3	5	0.6504
0.5	4	1	0.6939
0.5	4	3	0.6897
0.5	4	5	0.6897
0.5	8	1	0.7771
0.5	8	3	0.7762
0.5	8	5	0.7762
0.5	16	1	0.8349
0.5	16	3	0.8348
0.5	16	5	0.8348

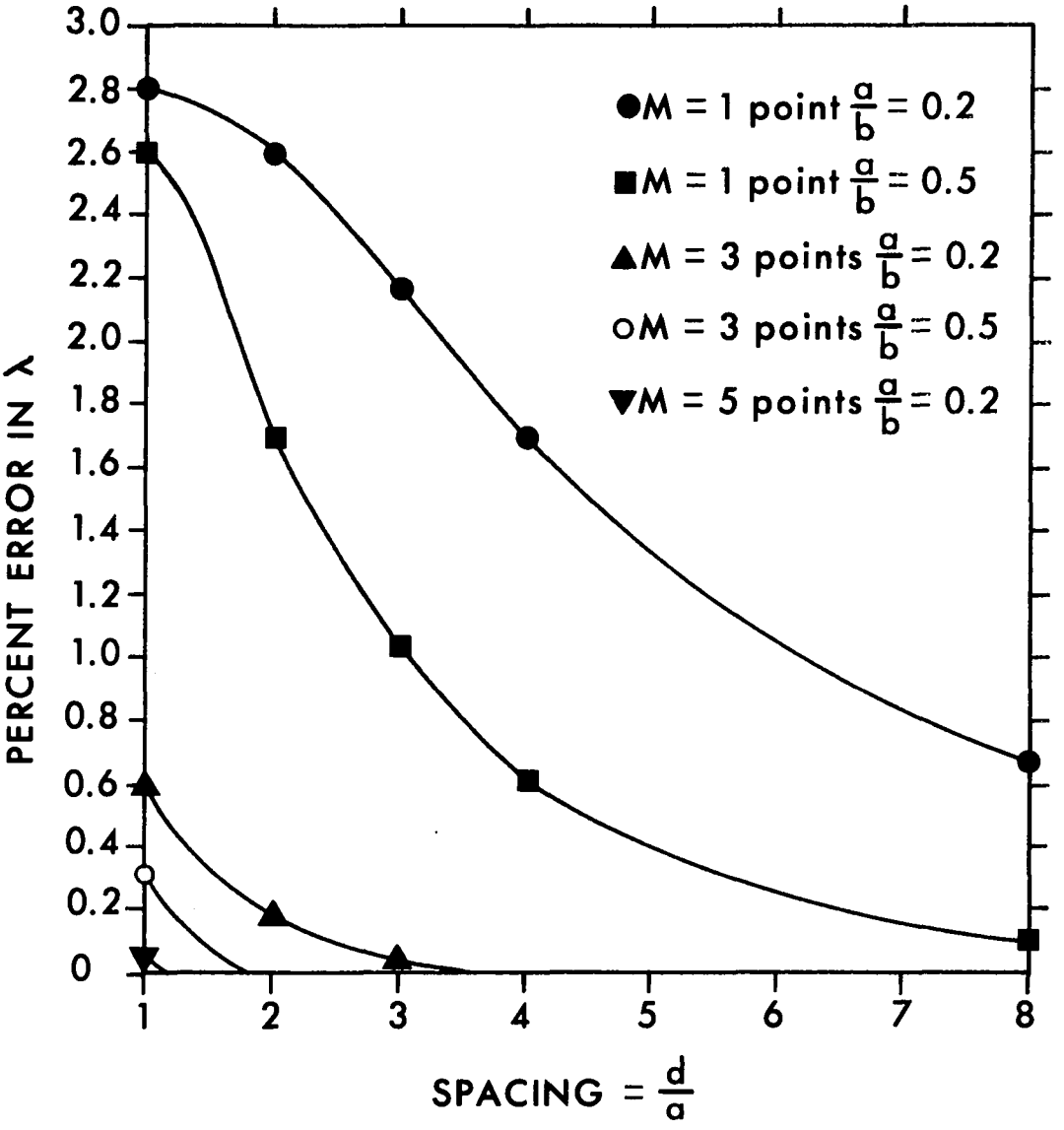

Figure 2.14 - ERROR IN λ VS. d/a AND M FOR OBLATE SPHEROIDS

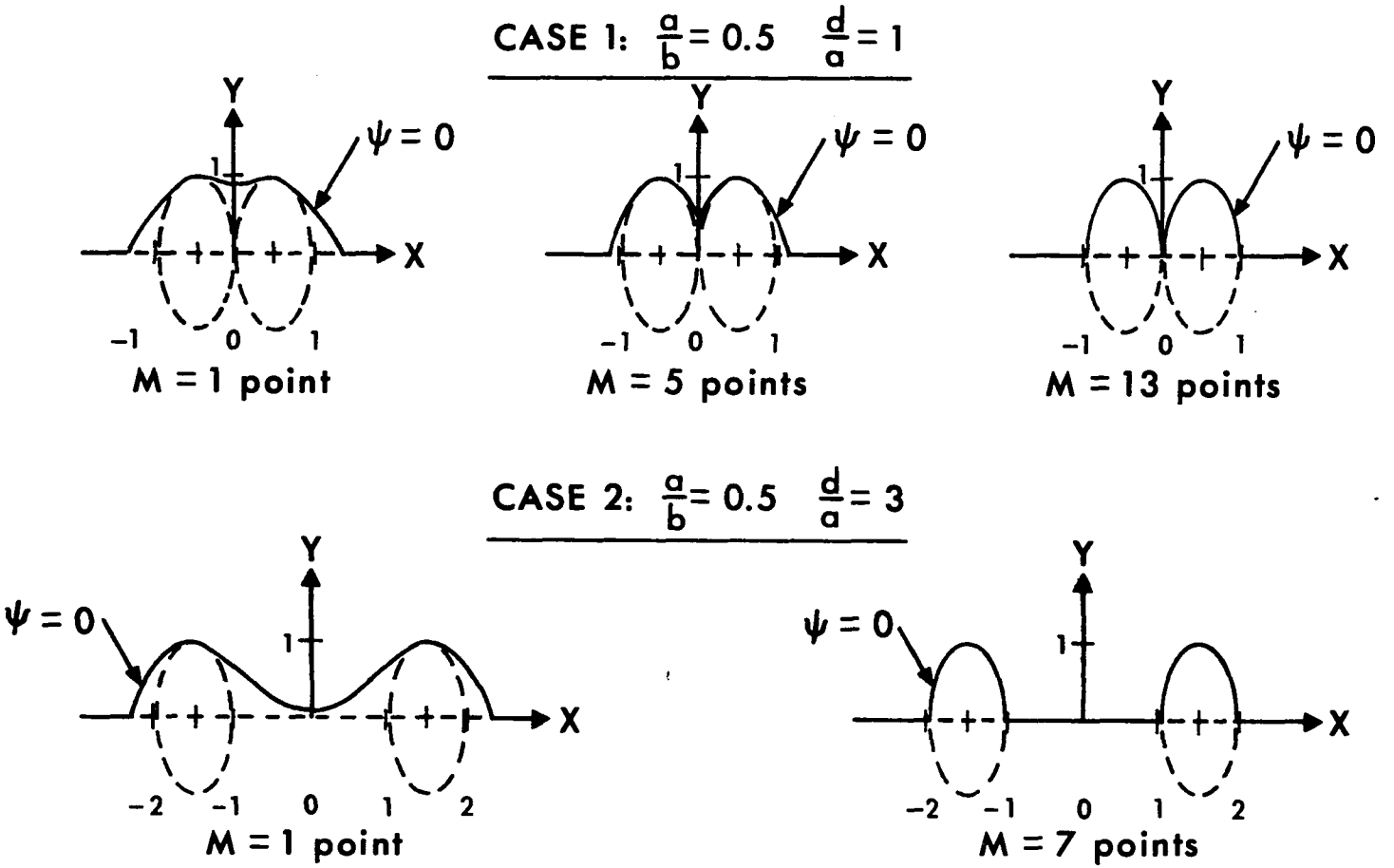

Figure 2.15 - ZERO STREAMLINES VS. d/a AND M FOR OBLATE SPHEROIDS

Table 2.7 and Figure 2.14 indicate that as for the equivalent cases of flow past spheres and prolate spheroids convergence to five significant figures is rapidly attained with two oblate spheroids - even when they are touching - as the number of multipoles is increased. It can be seen that convergence to five significant figures is achieved when the boundary conditions are satisfied at only five points on the generating arc of each spheroid except for the case of two touching spheroids where nine points on each generating arc are required for convergence to four significant figures. Comparing the error in λ shown in Figure 2.14 with the equivalent curves for spheres (Figure 2.3) and prolate spheroids (Figure 2.10) it can be seen that these errors in all three cases for touching objects are approximately equal. However, as the object spacing increases, errors in λ decrease most rapidly for prolate spheroids and least rapidly for oblate spheroids. Distortions of the zero streamline for two touching oblate spheroids ($a/b = 0.5$) and for two spheroids having a d/a ratio three (Figure 2.15) are greater than the equivalent distortions observed for either spheres or prolate spheroids (Figures 2.4 and 2.11 respectively). This result is in agreement with the previous observation that streamline distortions are greater for spheres than for prolate spheroids when the boundary conditions are satisfied at only one point on the generating arc of each object, i.e. as the aspect ratio decreases the objects become extended in a direction normal to the flow thereby requiring more terms in the series (or higher order multipoles) to describe their boundaries accurately.

Drag results for flow past chains consisting of from one to fifteen oblate spheroids have been plotted in Figure 2.16. These spheroids all have an aspect ratio of 0.2 and a spacing parameter (d/a) of two. As was done for chains of spheres (Figure 2.5) and

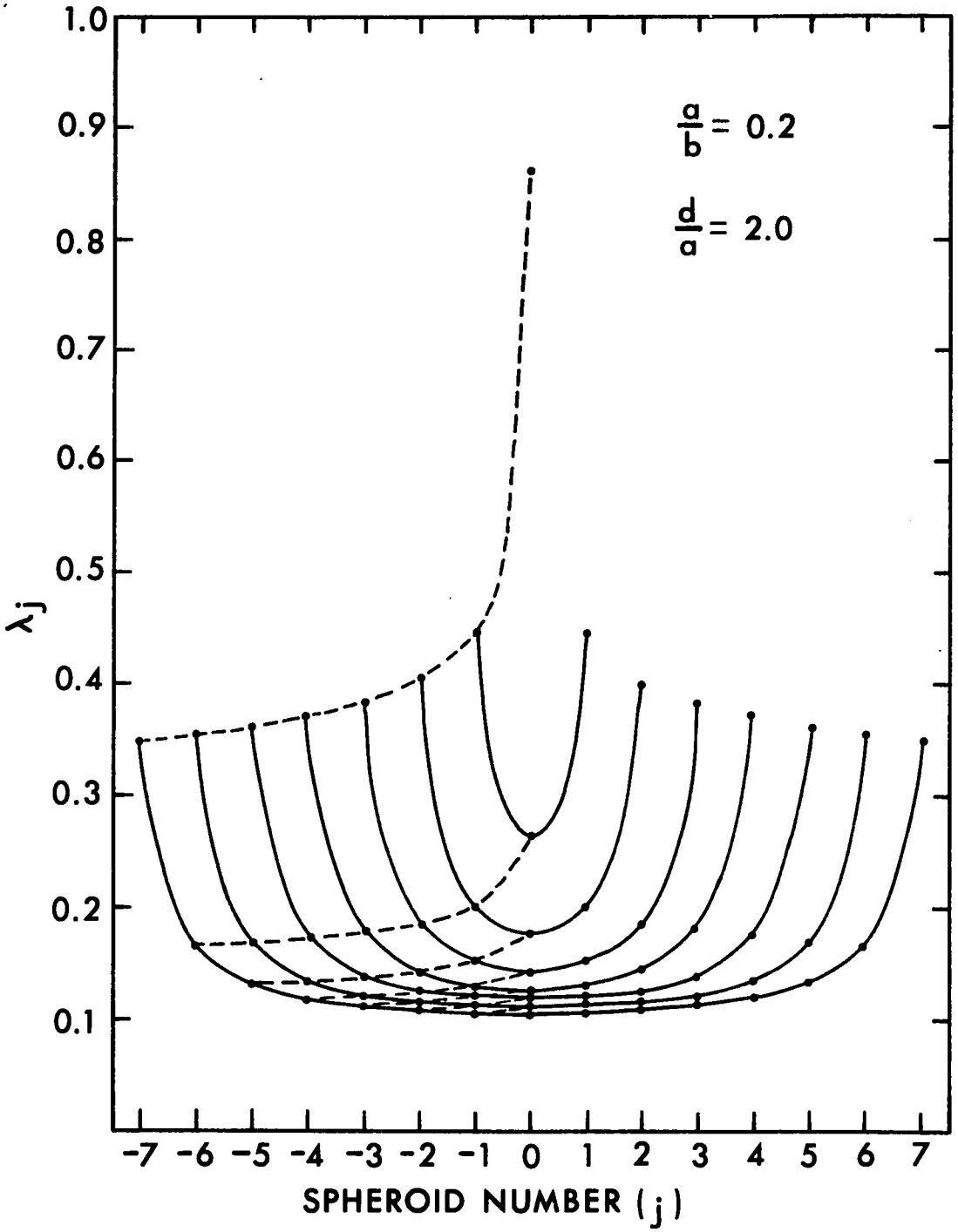

Figure 2.16 - λ_j FOR CHAINS OF OBLATE SPHEROIDS

chains of prolate spheroids (Figure 2.12) the drag correction factor λ_j for each oblate spheroid has been plotted against the spheroid number j in Figure 2.16. The boundary conditions were satisfied at only the uppermost point on each spheroid. The percentage error to be expected can be deduced from Figure 2.14.

The solid curves showing the change in drag between spheroids in any chain indicate a much stronger shielding effect in a chain of oblate spheroids than was observed for the cases of prolate spheroids or spheres. This assertion is implemented by the almost horizontal nature of the broken curves representing the change in drag on the jth spheroid in a chain as more spheroids are added to the chain. The results presented in Figure 2.16 were all obtained for spheroids having a spacing parameter (d/a) of two and, therefore, the drag on each spheroid in a seven spheroid chain is plotted in Figure 2.17 for different particle spacings. Comparing these results with the equivalent results for prolate spheroids (Figure 2.13) and spheres (Figure 2.6) indicates the stronger shielding effects of oblate spheroids. It can also be seen from the relatively slow approach of the λ_j curves to the value for a single oblate spheroid that the interactions between oblate spheroids in a chain will approach zero at larger values of the spacing parameter than can be expected in either the case of chains of prolate spheroids or chains of spheres.

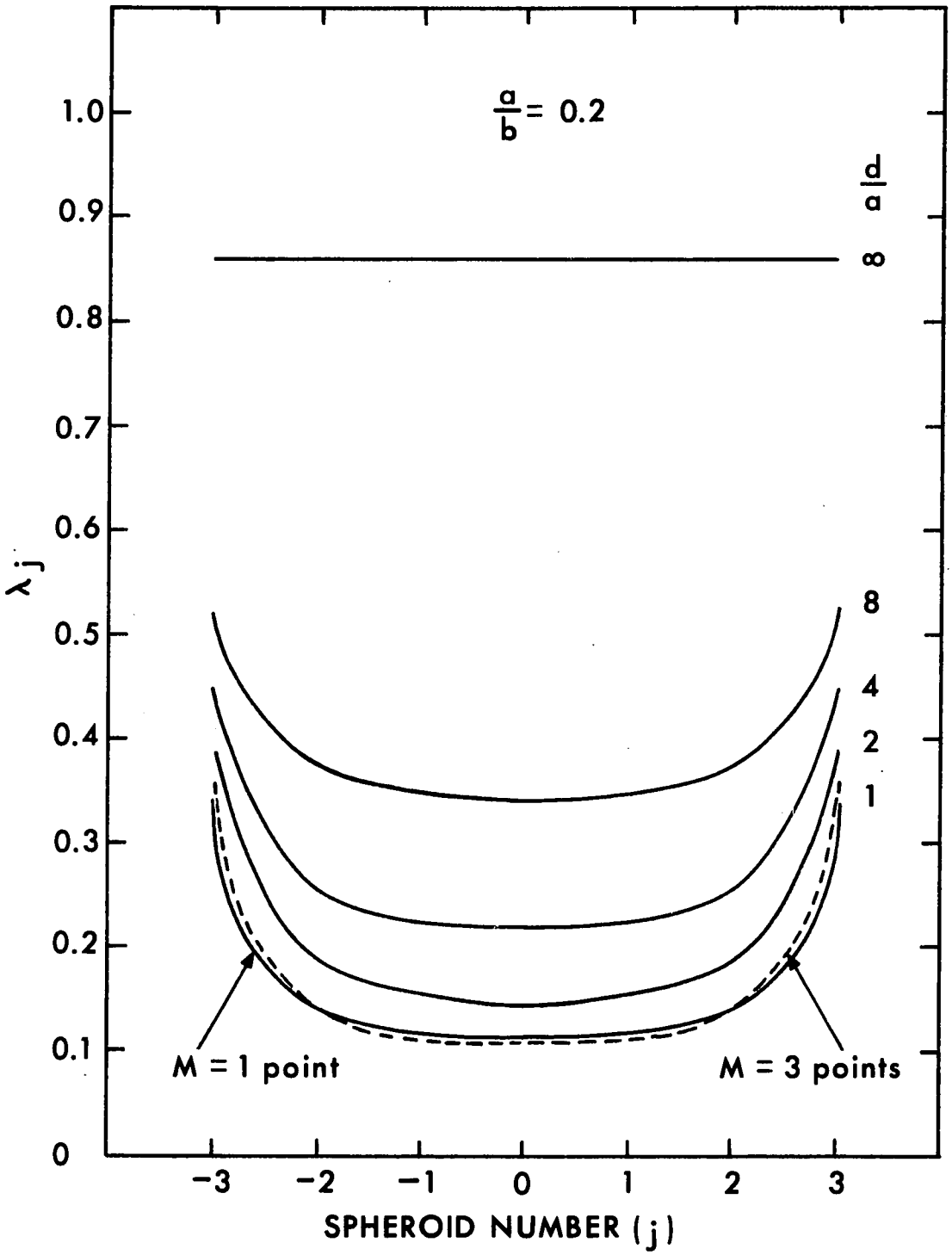

Figure 2.17 - λ_j FOR CHAINS CONTAINING 7 OBLATE SPHEROIDS

CHAPTER 3

AXISYMMETRIC FLOW PAST BODIES OF REVOLUTION OF ARBITRARY SHAPE

3.1 INTRODUCTION

The existing literature contains a number of techniques that can be applied in theory to the problem of slow viscous incompressible flow past a body of revolution of arbitrary shape. One such technique developed by Brenner (see Happel & Brenner (1)) depends upon three fundamental second-rank tensors which are intrinsic geometrical properties of the body. Complete characterization of the resistances due to translation and rotation requires a knowledge of 21 independent scalar resistance coefficients. Geometric symmetry of the particle reduces the number of required coefficients; e.g., bodies of revolution require two scalar components of the translational tensor, two components of the rotational tensor and one component of the coupling tensor. In most cases, the requirement of experimental determination of a number of resistance coefficients renders this technique ineffective for obtaining numerical solutions in the absence of experimental data.

A second technique, the method of reflections developed by Smoluchowski (2 and 3) can be applied in principle if the particle under consideration can be represented by a number of bodies of more standard configuration such as spheres or spheroids thereby enabling velocity field interactions to be evaluated at simply described boundaries. If this technique is employed, the bodies used to represent the disturbance generated by the desired shape would have to be in close proximity in order to approximate the desired boundary. However, it has been shown that the series solution generated by the method of reflections converges very slowly for close particle spacing and is tedious to apply if more than two

objects are present in the flow field (see Happel & Brenner (1)). Therefore, practical considerations preclude the use of the method of reflections for describing the creeping motion past non-simple axisymmetric geometries.

A third technique, the point force approximation developed by Burgers (4), approximates the disturbance produced by an arbitrary axisymmetric body by a system of forces distributed along the axis of the body. Instead of satisfying the no-slip boundary conditions all along the body surface, the technique requires that the mean value of the velocity vanish on the surface approximating the surface of the body. Burgers (4) used this technique to model flow past long finite cylinders by placing a force $f(\xi)d\xi$ at every element $d\xi$ of the axis. By assuming a simple polynomial form for $f(\xi)$ and integrating over the length of the cylinder Burgers was able to develop an approximate solution for the drag force on a long cylinder neglecting terms in the expansion for $f(\xi)$ of order greater than four. This analysis cannot be applied to short cylinders or other axisymmetric bodies of low aspect ratio due to the importance of end effects in these situations and the inability of the point force approximation to account for these end effects to any degree of accuracy.

Sampson (22) and Happel and Brenner (1) have shown how the complete infinite series solution to the creeping motion equations can be truncated in order to obtain a first approximation to a boundary that is only slightly distorted from the perfect spherical shape. The limitation of very small distortions from the perfect spherical shape, however, precludes the use of this type of analysis for a majority of arbitrary axisymmetric shapes.

It is evident that the techniques described above are rather limited in their applicability to the general problem of axisymmetric viscous creeping motion. The shortcomings of previous solution techniques is manifest when one considers that there are no known solutions for the flow past such common bodies of revolution as short circular cylinders and right circular cones.

The new solution technique presented herein is an extension of the multipole truncation technique developed, discussed and demonstrated in the previous chapter to describe creeping flow along the line of centers of any finite number of submerged axisymmetric objects having natural coordinate systems such as spheres and spheroids.

It has been shown that for these simple geometries the disturbance due to each object including the effect of particle interactions can be represented exactly by infinite series of multipoles with origins at the geometric centers of each object. The strengths of the multipoles are determined by satisfying the no-slip boundary conditions along the surfaces of all interacting particles treated simultaneously. Furthermore, it was demonstrated that approximate solutions could be obtained to any order of accuracy by truncating the multipole series and satisfying the no-slip boundary conditions at discrete points along the generating arc of each object. Rapid convergence of the solution procedure was observed even in the most extreme case of objects touching, in contrast to the poor convergence characteristics of the series solution in the method of reflections for close particle spacings.

The rapid convergence characteristics of the multipole truncation technique in concentrated systems mentioned above provides the rationale for treating axisymmetric flow problems past complex bodies of revolution

that do not possess a simple natural coordinate system. One might anticipate that for complex geometries the disturbance produced by each object should be represented by a continuous distribution of multipoles distributed along the axis of symmetry of the object, in contrast to the point or concentrated distribution for analytically simple objects with boundaries conforming to natural coordinates. Some insight into the difficulty of obtaining an analytical expression for the axial distribution of disturbances that will produce a desired boundary shape is gleaned from the equivalent problem in axially symmetric potential theory. Even for this simpler problem analytical expressions for the required axial source-sink distribution are only possible within the framework of a linearized theory in which the boundary conditions are not satisfied at the actual surface of the object but at corresponding points along the axis of symmetry.

The above difficulties call for a different approach in which a continuous distribution of axial disturbances might be approximated by a finite array of discrete point disturbances each represented by a multipole series. In this approach complex bodies of revolution are constructed by the linear superposition of point disturbances representing contiguous simpler bodies whose boundaries do conform to natural coordinates. Intuitively, one might expect that the oblate spheroid is the basic element in such a construction because in the limit of vanishing aspect ratio each oblate spheroid shrinks to a disk of infinitesimal thickness. Thus, provided the lateral dimensions of each oblate spheroid can be adjusted to coincide with the boundaries of the desired body one might well suspect that the discrete point disturbances representing each oblate spheroid should reduce in this limit to a continuous distribution

of axial disturbances and that this axial distribution will satisfy the exact boundary value problem of interest. However, the convergence of the solution in the limit as the minor axis dimension becomes infinitesimal and the manner in which the no-slip boundary conditions are satisfied are both somewhat subtle because of the existence of an entrained flow with standing eddies between adjacent spheroids. These topics will be discussed in depth in the body of this chapter.

3.2 USE OF MULTIPOLES

It has been hypothesized in the introduction that the boundaries of complex bodies of revolution may be approximated by a number of touching oblate spheroids having considerably lower aspect ratios than the desired object and having major axis dimensions that allow them to conform to the desired boundaries. Convergence of this procedure to the desired solution will be discussed later. At this point, the solution to the creeping motion equations for axisymmetric incompressible viscous flow past multiple oblate spheroids will be summarized from Chapter 2.

The steady state Navier-Stokes equations reduce to the creeping motion equations by omission of the inertial terms:

$$\nabla^2 \bar{v} = \frac{1}{\mu} \nabla p \tag{2.1}$$

or

$$\nabla^2 (\nabla^2 \psi) = 0 \tag{2.3}$$

where the stream function ψ is defined as follows in oblate spheroidal coordinates:

$$V_\xi = -\frac{h_\eta}{\gamma}\frac{\partial \psi}{\partial \eta} \quad ; \quad V_\eta = \frac{h_\xi}{\gamma}\frac{\partial \psi}{\partial \xi} \tag{3.1}$$

for

$$h_\xi = h_\eta = \frac{1}{c(\cosh^2\xi - \sin^2\eta)^{1/2}} \tag{3.2}$$

$y = c \cosh\xi \sin\eta$

ξ, η = oblate spheroidal coordinates as shown in Figure 3.1

$c^2 = a^2 - b^2$

The general solution to equation (2.3) for flow parallel to N equally spaced axisymmetric disturbances is presented in Chapter 2.

$$\psi = 2c^2 U I_2(p_0) I_2(q_0) + \sum_{j=-\frac{(N-1)}{2}}^{\frac{(N-1)}{2}} \Big\{ \left[D_{2j} p_j + B_{2j} H_2(p_j) + D_{4j} H_4(p_j) \right] I_2(q_j)$$

$$+ \left[D_{3j} + B_{3j} H_3(p_j) + D_{5j} H_5(p_j) \right] I_3(q_j) +$$

$$\sum_{n=4}^{\infty} \left[D_{nj} H_{n-2}(p_j) + B_{nj} H_n(p_j) + D_{n+2,j} H_{n+2}(p_j) \right] I_n(q_j) \Big\} \tag{2.40}$$

where:

$$p_j = i \sinh \xi_j = i\left[\left(\frac{R_{1j} + R_{2j}}{2c} \right)^2 - 1 \right]^{1/2} \quad ; \quad q_j = \cos\eta_j = \left[1 - \left(\frac{R_{2j} - R_{1j}}{2c} \right)^2 \right]^{1/2} \tag{2.42}$$

$$R_{1j} = \left[(x - 2jd)^2 + (y - c)^2 \right]^{1/2} \quad ; \quad R_{2j} = \left[(x - 2jd)^2 + (y + c)^2 \right]^{1/2}$$

$I_n(q_j)$ = Gegenbauer function of the first kind

$H_n(p_j)$ = Gegenbauer function of the second kind

D_{nj}, B_{nj} = constants

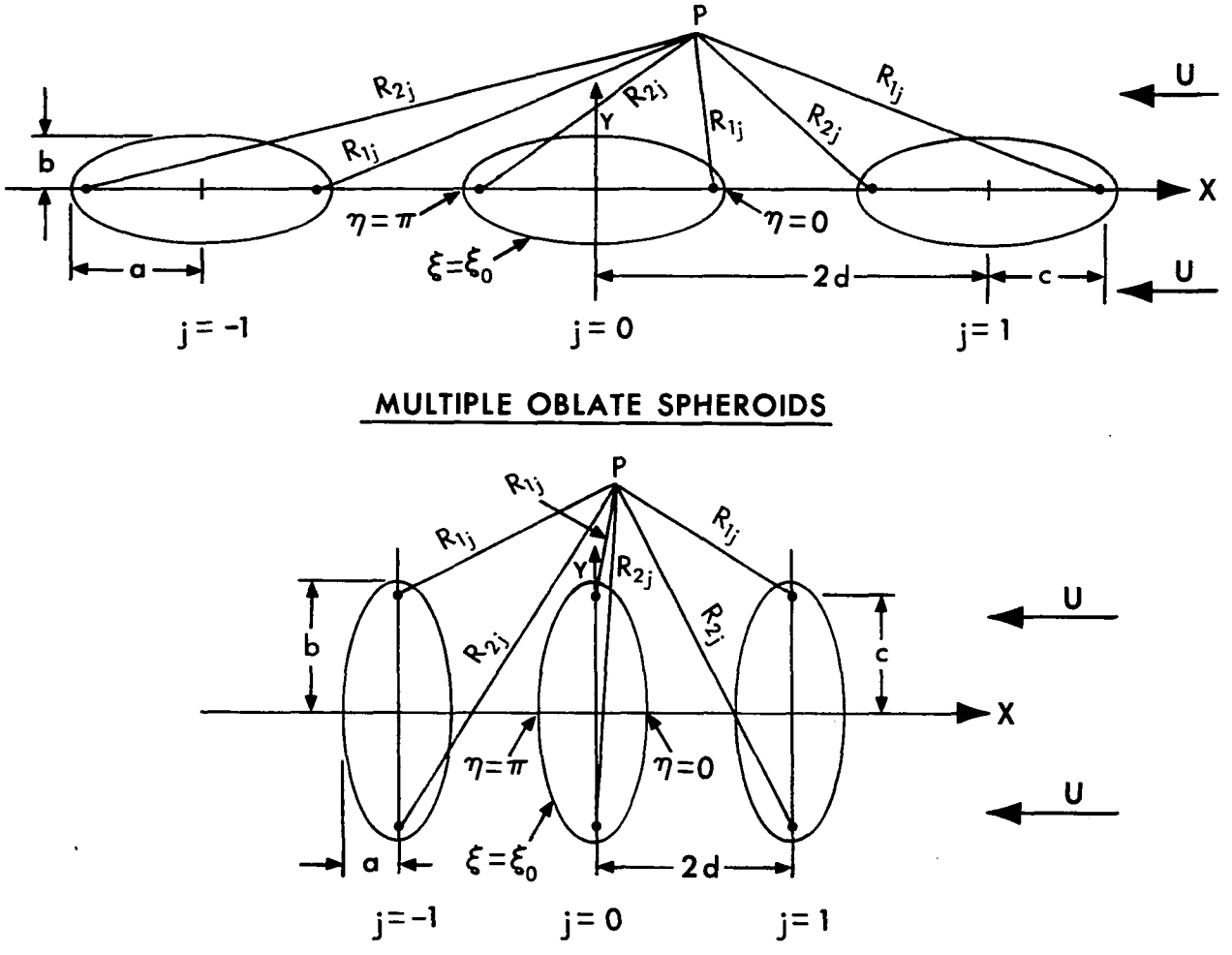

Figure 3.1 - GEOMETRY OF MULTIPLE OBLATE AND PROLATE SPHEROIDAL SYSTEMS

If one wished to determine the flow past N equally spaced oblate spheroids the constants D_{nj} and B_{nj} would be determined by satisfying the no-slip boundary conditions over the surfaces of each spheroid:

$$V_{p_j} = 0 = \frac{\partial \psi}{\partial q_j} \quad ; \quad V_{q_j} = 0 = \frac{\partial \psi}{\partial p_j} \tag{2.37}$$

where if one lets $a = a_j$ and $b = b_j$ the spheroids need not be of the same shape.

If the boundary conditions (2.37) are to be satisfied at all points along the generating arc of each spheroid then all the B_{nj} and D_{nj} constants in the infinite series solution (2.40) must be determined. However, it is demonstrated in Ch. 2 that rapidly converging solutions can be obtained to any order of accuracy for all spheroid spacings by truncating the series solution (2.40) and satisfying the no-slip boundary conditions (2.37) at judiciously chosen discrete points along the generating arc of each spheroid. For example, it is shown that solutions for the drag accurate to four significant digits can be obtained for the most severe case of touching spheroids by retaining only the first 8 terms in the series. The term multipole is introduced in Chapter 2 to describe each $I_n(q_j)$ term in (2.40) together with its coefficient. The two B_{nj} and D_{nj} constants in each multipole provide the freedom to satisfy the no-slip boundary condition at one point on the generating arc of the spheroid. The interaction between spheroids and the intensity of the multipoles is determined by the simultaneous solution of the linear system of algebraic relations that result for the truncated array of B_{nj} and D_{nj} coefficients.

In Chapter 2 attention was confined to studying the flow past multiple spheroids since the boundary conditions (2.37) or their discrete point counterpart are strictly appropriate only to this case. The fundamental problem here is to show just how the boundary conditions (2.37) are related to the no-slip boundary conditions for an arbitrary body of revolution, and to determine the limiting behavior of the solutions to (2.40) and (2.37) for touching spheroids as their aspect ratio approaches zero. The basic hypothesis that an arbitrary body of revolution can be constructed from a line array of oblate spheroids of varying aspect ratio obviously depends on this limiting behavior. To obtain a better insight into the precise nature of the boundary value problem it will first be necessary to examine in detail the behavior of the multipoles in spheroidal coordinates.

An introductory description of the physical significance of the multipoles and their relationship to the Gegenbauer functions of the first kind, i.e., $I_n(q_j)$ is given in Chapter 2. Figure 2.2 shows the first four Gegenbauer functions of the series for a perfect sphere (aspect ratio = a/b = 1). It can be seen that these functions represent multilobular disturbances emanating from the origin and having 2n-2 lobes. In Figure 3.2 the effects of changing the aspect ratio (a/b) on the individual lobes and their angular dependence can be seen. As all of these functions are symmetrical about both the x and y axes, only the first quadrant is shown for illustrative purposes.

Examination of Figure 3.2 allows a number of interesting conclusions to be drawn concerning the general characteristics of multipoles of various orders. All functions of even order possess a central lobe together with side lobes (except for I_2). Both the attitude of the side

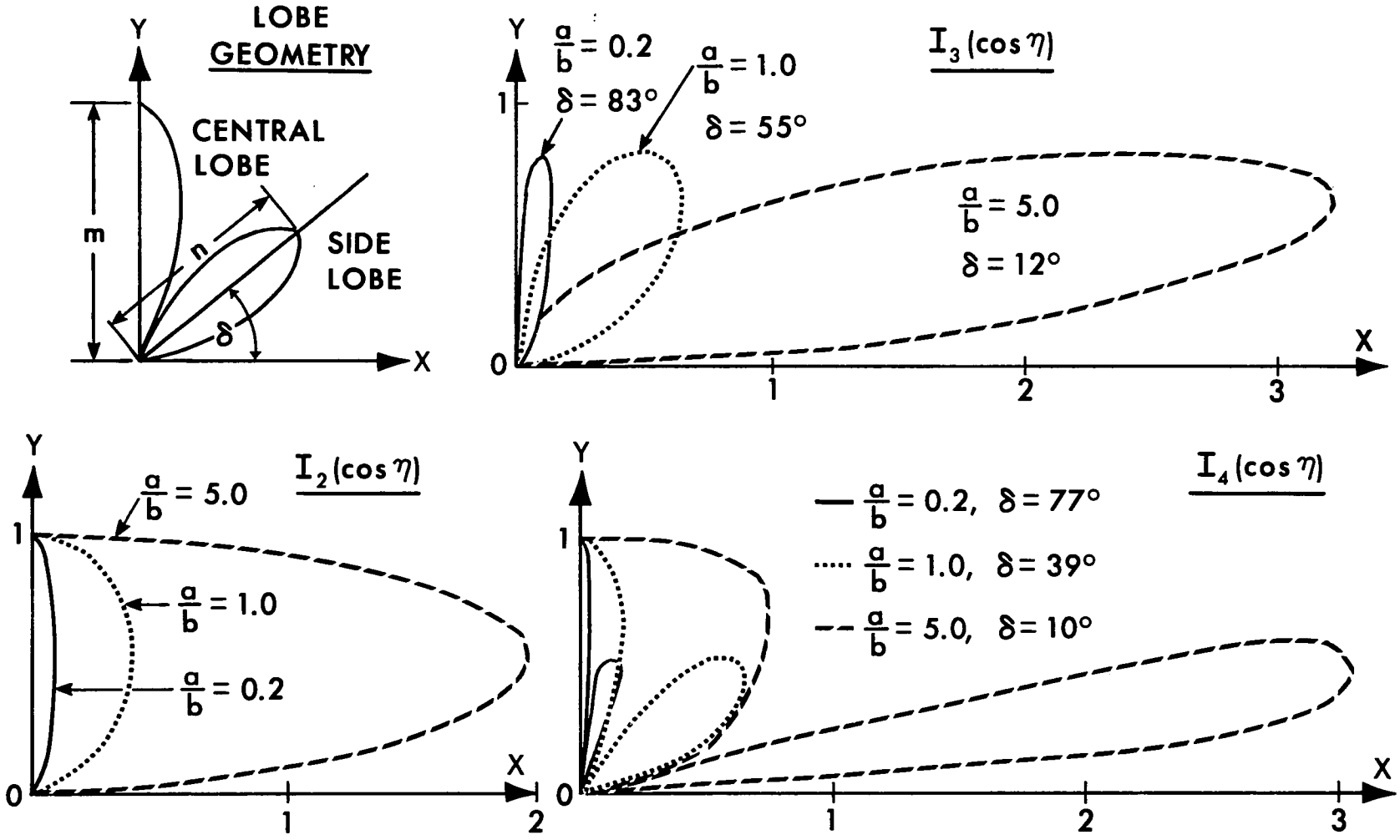

Figure 3.2 - GEGENBAUER FUNCTIONS FOR ASPECT RATIOS $0.2 \leq a/b \leq 5.0$

lobes and the length of a side lobe referred to the length of the central lobe (n/m) are only functions of the aspect ratio a/b.

One notes that the attitude of the side lobes is a very sensitive function of a/b and rapidly approaches $\theta_j = \pi/2$ as the a/b ratio of the oblate spheroids decrease while the length ratio n/m of successive side lobes quickly diminishes as one proceeds away from the central lobe. These features are of particular importance when one tries to satisfy viscous boundary conditions along a complex surface that departs significantly from the natural boundaries of the oblate spheroids used to construct it.

Suppose, for example, one represents a right circular cylinder by a line array of oblate spheroids having a common major axis dimension equal to the cylinder radius. One would find little difficulty in trying to satisfy a boundary condition at the $\theta = \pi/2$ point above each spheroid since such points lie on the natural boundaries of each spheroid. Also, only the even ordered multipoles would contribute a disturbance along the $\theta = \pi/2$ line since only these multipoles possess a central lobe.

Suppose next the multipole series for each oblate spheroid is truncated and a sufficient number of discrete point boundary conditions is prescribed in a close neighborhood of $\theta_j = \pi/2$ to determine the intensity of all disturbances due to the central lobes in the truncated solution. The intensity of disturbances due to all side lobes of the even ordered multipoles will then also be determined since they are related to the central lobes solely through the aspect ratio a/b of the oblate spheroids. The amplitudes of these side disturbances, therefore, naturally conform to an oblate spheroid of the specific aspect ratio chosen and contradict all other boundary shapes. Suppose then that

boundary conditions are prescribed along the cylinder surface at points further removed from the $\theta_j = \pi/2$ line of each spheroid. These boundary conditions might be satisfied by the addition of higher order multipoles. However, the B_{nj} and D_{nj} coefficients would have to be large since the n/m ratios of the side lobes used to satisfy these boundary conditions rapidly decreases as the departure from $\theta_j = \pi/2$ increases. The addition of higher order multipoles would, therefore, cause large changes in the solution in the vicinity of the central lobes. Similar arguments to these can also be made for multipoles of odd order except that these multipoles do not possess central lobes.

In summary, any attempt to satisfy directly the no-slip boundary conditions on a complex body of revolution at points differing significantly from the boundaries of the elemental oblate spheroids used to construct it by introducing higher order terms in the multipole series for each spheroid will lead to a diverging solution in which the higher order B_{nj} and D_{nj} coefficients grow increasingly large. The technique for solving the viscous boundary value problem for an arbitrary body of revolution using contiguous oblate spheroids is described in the remainder of this section using an inductive approach. The discussion will also use the example of a short finite cylinder; however, the solution technique and convergence characteristics will apply equally well to axisymmetric bodies of any shape.

In accord with the basic hypothesis the disturbance due to the cylinder is replaced by the disturbance due to a finite number of multipole series distributed, as yet in an undetermined manner, along the axis of rotation of the cylinder. If the multipole series were equally spaced the disturbance would be formally given by equation (2.40). Each multi-

pole series is written in a local oblate spheroidal coordinate system and referred to a common origin through a suitable translation. Just how the discrete point boundary value problem should be prescribed is not known and will be determined essentially through a series of numerical experiments. To do this the convergence characteristics of the multipole representation in spheroidal coords., will be examined in two parts: (i) convergence to the desired boundary in the central section of the cylinder and (ii) convergence to the boundaries representing the ends of the cylinder.

Consider first the central portion of the cylinder. Figures 3.3a and 3.3b refer to the previous solutions in Chapter 2 for the flow past finite chains of equally spaced oblate spheroids. Figure 3.3a is obtained by requiring that the no-slip boundary conditions be satisfied at only the $\theta_j = \pi/2$ point on each oblate spheroid. As previously shown, this solution requires that only the two lowest order multipoles be retained in the representation of each spheroid. The zero streamline conforms to the surfaces of the oblate spheroids only in the vicinity of the $\theta_j = \pi/2$ points as insufficient multipoles have been used to force the zero streamline to conform to the exact boundaries of the spheroids. However, the interesting point is that the zero streamline approaches rather closely the desired boundary of the cylinder.

One's first inclination to improve this situation might be to prescribe the no-slip boundary conditions at additional intermediate points along the surface of the cylinder by introducing higher order multipoles. However, one finds for the reasons outlined in the previous discussion of multipoles that this is a diverging procedure when the boundary points do not conform to the natural boundaries of the oblate spheroids used in

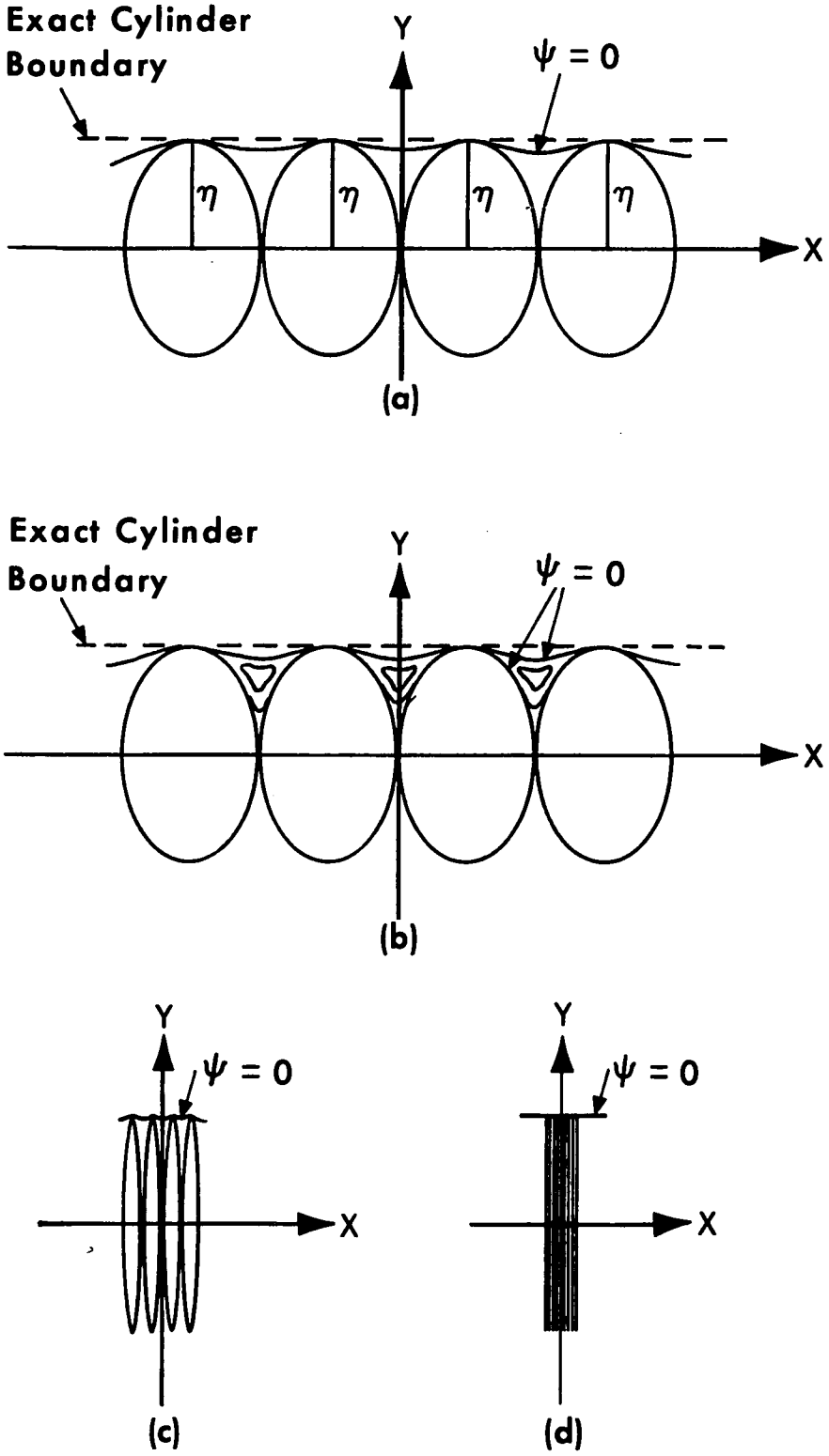

Figure 3.3 - ZERO STREAMLINE FOR CENTRAL SECTIONS OF CYLINDER

the construction. Instead an alternate path is taken which at first glance might appear to be counterproductive. Rather than taking additional points along the cylinder surface, the no-slip boundary conditions are satisfied at more points along the generating curves of each oblate spheroid. The treatment of these points using higher order multipoles does not lead to a divergent solution for the higher order B_{nj} and D_{nj} constants since these boundary points are natural to the local coordinate system used for each spheroid.

The results for such a higher order truncated solution are shown in Figure 3.3b. One zero streamline follows the boundaries of the oblate spheroids as dictated by the boundary conditions specified. However, a stationary or entrained eddy is also created in the space between adjacent spheroids. This results in the existence of a second zero streamline which conforms closely to the desired boundary of the cylinder. The circulatory flows in the regions bounded by the two zero streamlines is in an opposite sense to the bulk stream flow. The stagnation point or eye of the eddy is to all practical purposes symmetrically located between neighboring spheroids. This will, of course, change if spheroids of varying aspect ratio are used. As more and more spheroids are introduced to represent a cylinder of fixed length the aspect ratio of each spheroid decreases and the stationary eddies between adjacent spheroids become increasingly small, Figure 3.3c. Finally, in the limit of zero aspect ratio, Figure 3.3d, these eddies become vanishingly small and have zero circulation. The result is a zero streamline which conforms exactly to the horizontal boundary of the cylinder and along which the no-slip boundary conditions are satisfied.

The ends of the cylinder are considered next where a sharp turning of the zero streamline is required. If the no-slip boundary conditions

are satisfied at only the $\eta_j = \pi/2$ point on the generating curve of the end oblate spheroid in a finite chain of touching spheroids, the resulting zero streamline will exhibit major distortions from both the boundary of the end spheroid and the cylinder end as shown in Figure 3.4a. If the no-slip boundary conditions are satisfied at more points along the generating curve of the end oblate spheroid by adding higher order multipoles in the description of the end spheroid the streamline can be forced to conform to the outer boundary of the end spheroid as shown in Figure 3.4b. A stationary eddy forms in the region between the two end spheroids as described previously for interior spheroids while the shape of the zero streamline approximating the cylinder sides is not significantly altered.

One concludes from the above results that higher order multipoles are required only in regions of large boundary curvature and that regions where the boundary shape is slowly varying are well represented by the lowest order multipoles provided that the no-slip boundary conditions are satisfied at the uppermost point of the elemental spheroids in these regions. Furthermore, the effect of the higher order multipoles appears to decay rapidly and consequently does not significantly influence the behavior of the multipoles describing the other spheroid. As noted before, oblate spheroids exhibit very strong shielding characteristics particularly at low-aspect ratios. In view of these properties convergence to the desired end boundary for the cylinder should be achieved by simply decreasing the aspect ratio of just the end oblate spheroid as demonstrated in Figure 3.4c.

The results represented in Figures 3.3 and 3.4 when combined show that the zero streamline does indeed converge to the exact boundary value

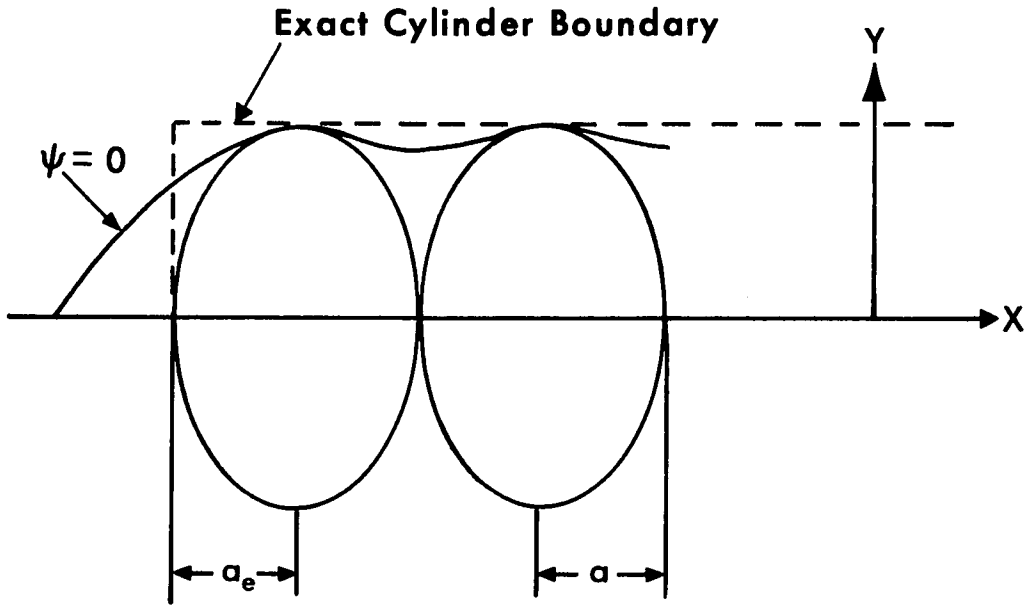

(a) M = 1 point $a_e = a$

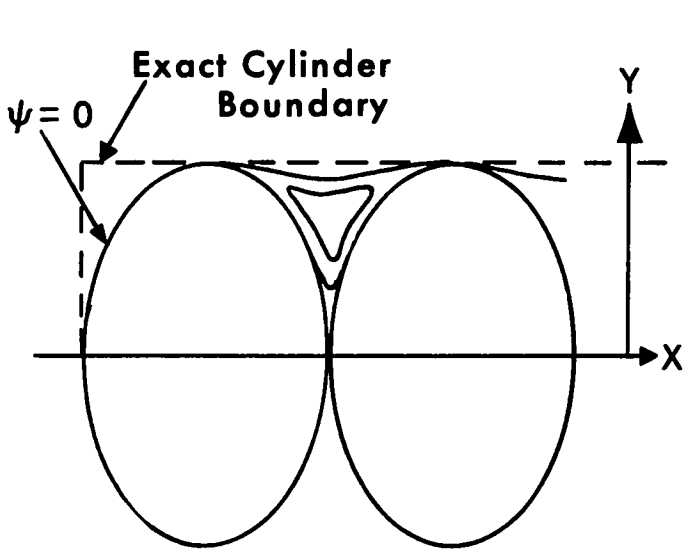

(b) M = 15 points $a_e = a$

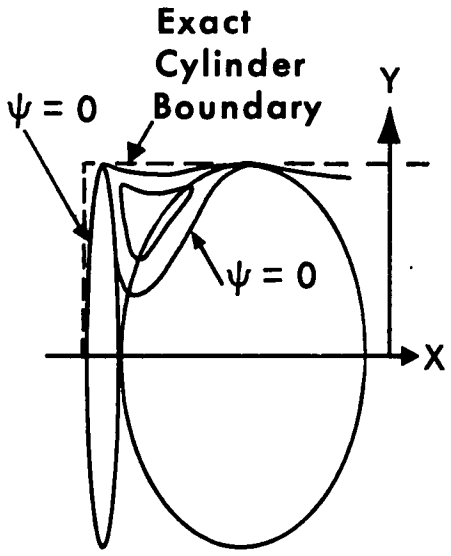

(c) M = 15 points $a_e < a$

Figure 3.4 - ZERO STREAMLINE FOR ENDS OF CYLINDER

problem both in the interior and at the ends of the cylinder in the limit as the aspect ratio of the elemental spheroids is reduced to zero. This same line of reasoning can be employed to demonstrate convergence of solutions obtained by the above technique to any other complex axisymmetric boundary shape.

Finally, it should be pointed out that in order to compute the drag on the cylinder the Laplacian of the stream function needs to be integrated over the surface of the cylinder according to the following

$$F_c = \mu \pi \int y^3 \frac{\partial}{\partial n}\left(\frac{\nabla^2 \psi}{y^2}\right) \delta S \tag{3.3}$$

(refer to Figure 3.1)

where n = outward normal from surface

δS = element of surface

To perform this integration over the exact surface of the cylinder in oblate spheroidal coordinates would be extremely tedious since the orthogonality relationships of the Gegenbauer functions in spheroidal coordinates only apply when integrated over a closed surface for which p_j is a constant. Therefore, in order to simplify drag calculations the following approximate technique is proposed.

The drag force on the cylinder can be approximated by:

$$F_c = \sum_{j=1}^{N} F_j \tag{3.4}$$

where F_j = drag force on the j^{th} spheroid. The F_j are obtained as described in Ch. 2 by carrying out the integration (3.3) over the surface of each oblate spheroid. The errors resulting from this approach can be described qualitatively with the aid of Figure 3.5. Considering only

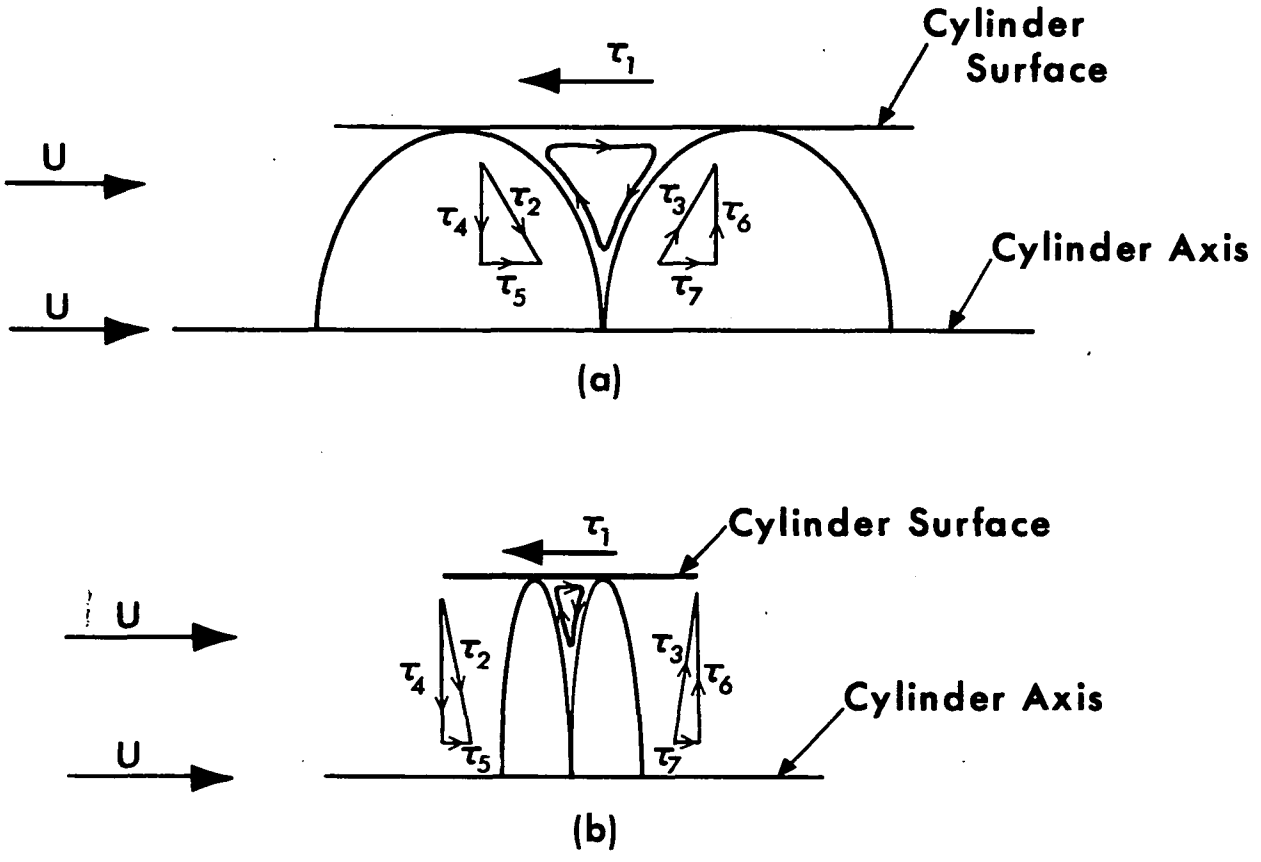

Figure 3.5 - FLOW BETWEEN CYLINDER WALL AND SPHEROIDAL BOUNDARIES

two spheroids it can be seen that the desired drag force on the horizontal cylinder surface is derived from the stress τ_1. However, the integration procedure described above employs the values of the shearing stresses τ_2 and τ_3. These stresses have vertical and horizontal components τ_4, τ_5 and τ_6, τ_7 respectively. τ_4 and τ_6 result in oppositely directed lift forces whereas τ_5 and τ_7 are additive and represent thrust forces in the opposite direction to the required drag force. It can be seen by comparing Figures 3.5a and 3.5b that the magnitude of these thrust forces continuously decreases as the aspect ratios of the two spheroids is decreased and that in the limit of vanishing aspect ratio should approach zero. Thus, if only a few oblate spheroids of relatively high aspect ratio are used to represent a short cylinder, the drag calculated using (3.3) and (3.4) will be lower than the actual drag on the cylinder. However, as the number of spheroids used to represent the cylinder is increased, the computed drag should increase and approach the actual drag on the cylinder. The extent of the error introduced by this approximation and the convergence of this procedure will be demonstrated by numerical results in the following section.

3.3 RESULTS FOR SHORT FINITE CYLINDERS AND CONES

The techniques described in the previous section will now be applied to calculate the drag on short finite cylinders and cones. The convergence characteristics of this new solution procedure will be demonstrated and the solutions compared with existing experimental data when available.

It has been pointed out by Happel & Brenner (1) that no previous theoretical treatment is available for creeping motion relative to cylinders with aspect ratios of less than approximately five. However, a

large amount of experimental data exists in this area. Before comparing the results for flow past short cylinders computed as described above with experimental results, the method used for describing settling rates will be outlined.

The settling factor K is defined as the ratio of the terminal settling velocity of the body under consideration to the settling velocity of a perfect sphere having the same volume as the object. The Stokes law drag force acting on the sphere having the same volume as the cylinder is

$$F_s = 6\pi\mu U_s r_s \tag{3.5}$$

where U_s is the settling velocity of the sphere and r_s is its radius. The drag force on the cylinder can be related to the Stokes drag on a sphere having the same radius as the cylinder by introducing a multiplication factor λ which depends only on the geometry of the total flow configuration. Thus,

$$F_c = 6\pi\mu U_c r_n \lambda \tag{3.6}$$

where U_c = settling velocity of cylinder

r_n = radius of cylinder

From (3.5) and (3.6), $F_c = F_s$ if

$$\frac{U_c}{U_s} = \frac{(r_s/r_n)}{\lambda} \tag{3.7}$$

where if the sphere and cylinder are to have equal volumes, $r_s = (3/4\ r_n^2 h)^{1/3}$, h being the cylinder length. Thus, the settling factor K is defined as:

$$K = \frac{U_c}{U_s} = \frac{(r_s/r_m)}{\lambda} \tag{3.8}$$

When representing a cylinder by N touching oblate spheroids the following geometrical equalities exist:

$h = 2(N-2)a + 4a_e$

$r_n = b$

a_e = minor radius of end spheroids

a = minor radius of central spheroids

b = major radius of all spheroids

Finally, Happel & Brenner (1) present an empirical correlation for calculating the settling rates based on experimental results obtained for a number of axisymmetric bodies, i.e.,

$$\text{Log}_{10} K = \text{Log}_{10}\left[\frac{r_s}{r_m}\sqrt{\Psi}\right] - 0.25\sqrt{\Psi}\frac{r_s}{r_m}\left[\frac{r_s}{r_m} - 1\right] \tag{3.9}$$

where Ψ, *the sphericity, is defined as the ratio of the area of a sphere of the same volume as the particle to the area of the particle itself.*

As a first approximation to the creeping motion flows past short finite cylinders, end effects will be neglected and the cylinders will be represented by varying numbers of oblate spheroids of equal aspect ratio and the boundary conditions will be satisfied at only the $\eta = \pi/2$ point on the generating arc of each spheroid. The results obtained are compared in Table 3.1 with both the experimental results of Heiss and Coull (29) and the empirical predictions of equation (3.9)

Table 3.1

Comparison of Settling Factors for Short Cylinders Utilizing Only the $\eta = \pi/2$ Point on Each Spheroid with Experimental Results of Heiss & Coul (29) and Empirical Results of Happel & Brenner (Eqn. (3.9)

$\frac{\text{Length}}{\text{Diameter}} = \frac{h}{2r_n}$	Number of Spheroids = N	Aspect Ratio = a/b	K This Work	K Heiss & Coull	K Equation (3.9)
0.25	2	0.125	0.776	0.762	0.759
	3	0.083	0.759		
	5	0.050	0.746		
	7	0.036	0.742		
	9	0.028	0.738		
0.50	2	0.250	0.918	0.864	0.881
	3	0.167	0.892		
	5	0.100	0.869		
	7	0.071	0.857		
	9	0.056	0.856		
1.00	3	0.333	1.038	0.958	0.976
	5	0.200	1.000		
	7	0.143	0.974		
	9	0.111	0.950		
	11	0.091	0.945		
2.00	3	0.667	1.057	0.975	1.009
	5	0.400	1.020		
	7	0.286	1.004		
	9	0.222	0.994		
	11	0.183	0.986		
	13	0.154	0.983		
3.0	5	0.600	1.01	0.958	0.989
	7	0.429	0.996		
	9	0.333	0.986		
	11	0.273	0.979		
	13	0.231	0.974		
	15	0.200	0.970		
4.0	5	0.800	0.989	0.929	0.961
	7	0.571	0.973		
	9	0.444	0.964		
	11	0.364	0.956		
	13	0.308	0.951		
	15	0.267	0.947		

These results show that although the settling factor calculated using this first approximation is in reasonable agreement with the experimental and empirical settling results, convergence is not obtained as the number of spheroids is increased. This inability to converge is due to the poor end representations that result when the no-slip boundary conditions are not adequately satisfied near the cylinder ends. The gross distortion of the ends of the cylinder are apparent from Figure 3.6 which is a plot of the zero streamline obtained when 11 oblate spheroids are used to represent a cylinder having a length to diameter ratio of 1.0. This figure demonstrates graphically that the horizontal boundary of the cylinder is closely approximated by using only the two lowest order multipoles for central spheroids but that major end distortions will result unless higher order multipoles are used to represent the sharp turning of the zero streamline required at the ends of the cylinder.

The data in Table 3.1 are plotted in Figure 3.7 where the theoretical values of K are based on the largest value of N for each cylinder. Interestingly, the settling rates based on even this first crude use of the multipole truncation technique are in closer agreement with experimental data than the empirical predictions of equation (3.9). It should be pointed out, however, that the experimental results were not obtained in a fluid of infinite extent. Heiss and Coull (29) utilized certain empirical techniques to correct their raw data for wall effects but no conclusion can be drawn as to how satisfactory these correction methods are.

The second series of numerical experiments reported in Table 3.2 are designed to refine the representation of the ends of the cylinder by

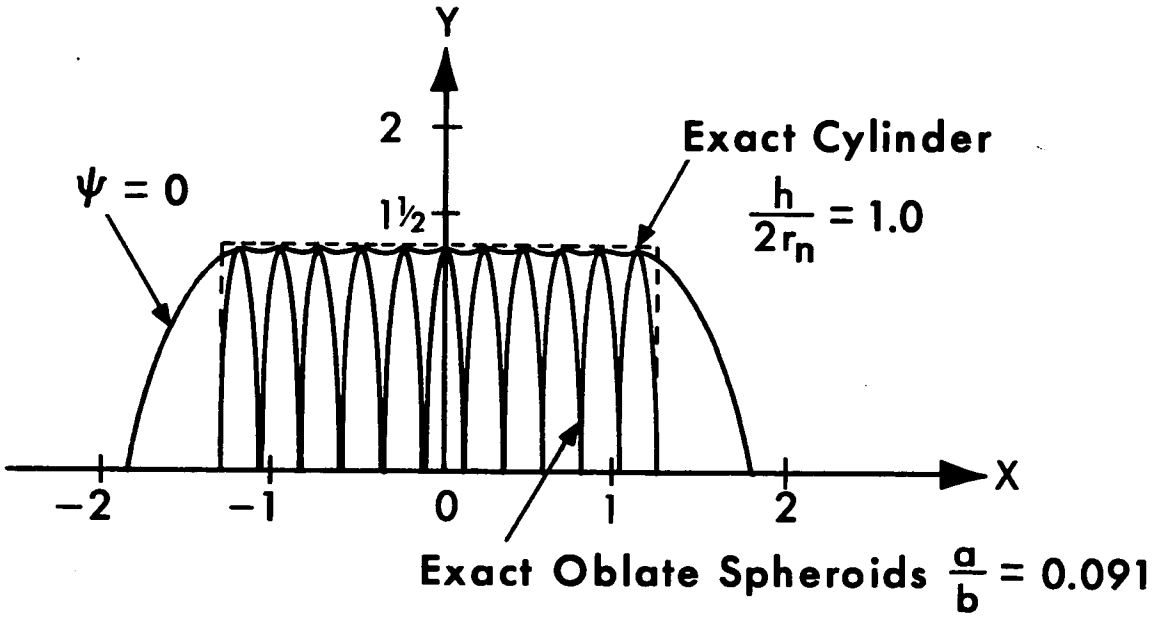

Figure 3.6 - ZERO STREAMLINE FOR CYLINDER ($M_e = 1.0$)

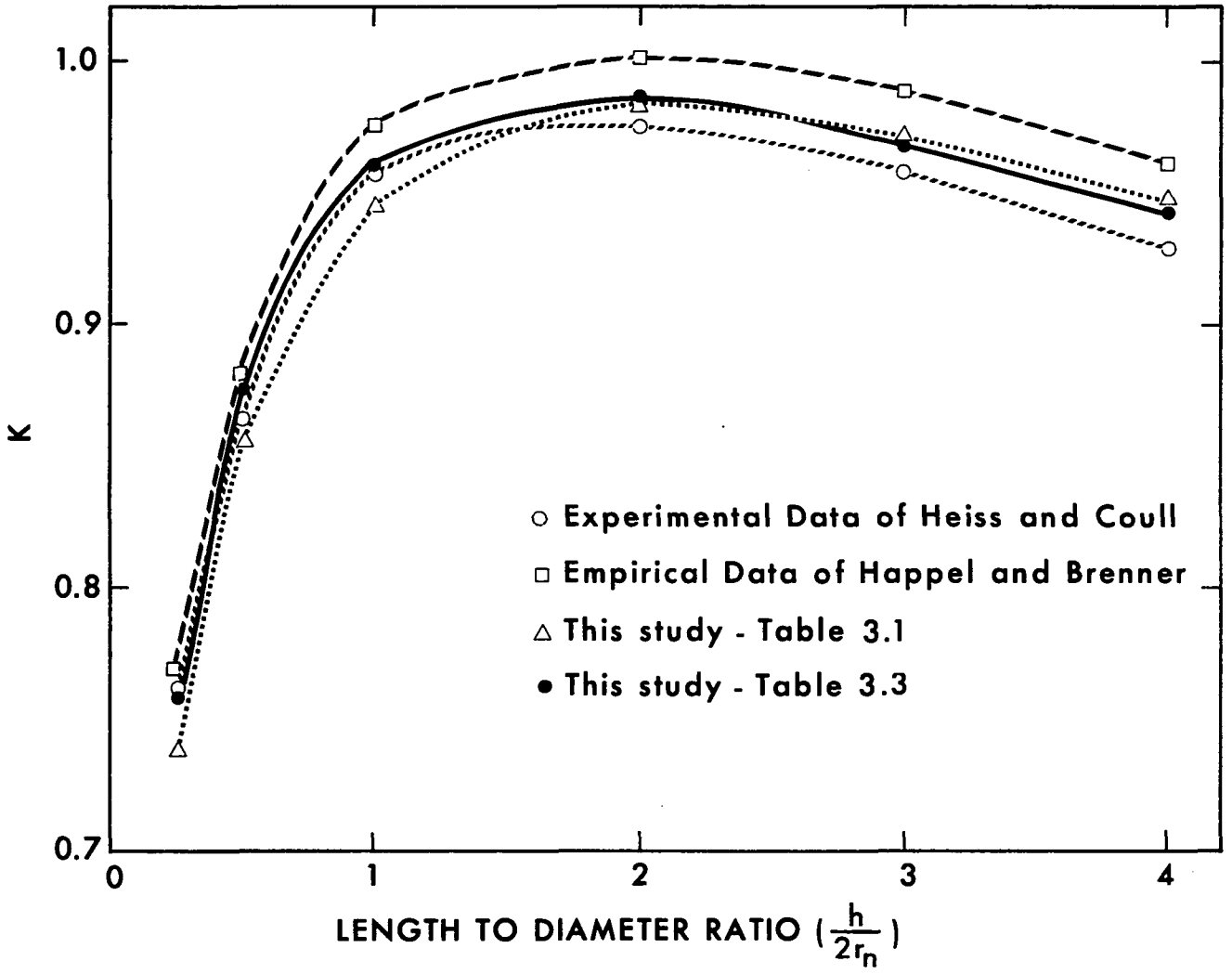

Figure 3.7 - SETTLING FACTOR K VS. $h/2r_n$ FOR SHORT CYLINDERS

utilizing higher order multipoles to satisfy the no-slip boundary conditions at increasing numbers of points on the generating curves of the end spheroids. A cylinder having a fixed length to diameter ratio of 0.5 was chosen and three sets of calculations performed. The number (N) of oblate spheroids ($3 \leq N \leq 11$) was varied, the aspect ratio (a_e/b) of the end spheroids was varied and finally, the no-slip boundary conditions were satisfied at varying numbers of points M_e ($1 \leq M_e \leq 13$) on each of the end spheroids but only at the $\eta = \pi/2$ point on each central spheroid.

As the first set of results in Table 3.2 show, convergence to three significant figures is obtained when the no-slip boundary conditions are satisfied at only 5 approximately equally spaced points on the boundary of each end spheroid. One would also conclude from these results that the effect of the higher order multipoles is localized and does not significantly alter the solution for interior spheroids. This rapid convergence of the solution to a desired boundary shape provided the boundary points conform to some natural coordinate system was also exhibited by the multisphere and spheroid solutions. This behavior suggests that improved end representations should be obtained not by satisfying boundary conditions at more points along the generating arc of the end spheroids, since the solution has converged in this sense, but by choosing end spheroids whose aspect ratio corresponds more closely to the geometry of the cylinder ends. The second set of calculations shown in Table 3.2 shows the effect of decreasing the aspect ratio of the end spheroids from 0.15 to 0.005. It is evident from these results that end spheroids with an aspect ratio of 0.01 or less yield drag results that have converged to roughly 0.1% and should, therefore, accurately represent the cylinder ends.

Table 3.2

Settling Factors for Short Cylinders ($h/2r_n = 0.5$)

Utilizing Higher Order Multipoles for the Ends

Number of Spheroids = N	End Aspect Ratio = a_e/b	Central Aspect Ratio = a/b	No. of Points on End Spheroids = M_e	K
5	0.05	0.133	1	0.852
5	0.05	0.133	3	0.894
5	0.05	0.133	5	0.890
5	0.05	0.133	7	0.890
5	0.05	0.133	9	0.890
5	0.05	0.133	11	0.890
5	0.05	0.133	13	0.890
5	0.15	0.067	5	0.913
5	0.10	0.100	5	0.903
5	0.05	0.133	5	0.890
5	0.03	0.147	5	0.887
5	0.01	0.160	5	0.881
5	0.005	0.163	5	0.880
3	0.05	0.400	5	0.896
5	0.05	0.133	5	0.890
7	0.05	0.080	5	0.890
9	0.05	0.057	5	0.888
11	0.05	0.044	5	0.887

The third set of results in Table 3.2 show the effect of increasing the number of central spheroids for a fixed end representation. For reasons already mentioned in the previous section and to be elaborated on shortly, it is not necessary to satisfy the no-slip boundary conditions at points other than the $\eta_j = \pi/2$ point on the generating arc of central spheroids. The results show that the convergence of the solution in the interior region as N increases is also satisfactory and provides drag results accurate to roughly 0.5% for aspect ratios of 0.2 or less on central spheroids.

Figure 3.8 is a plot of the streamline pattern for the flow past the cylinder as described in Table 3.2. The construction is based on $N = 5$, $a_e/b = 0.05$, $a/b = 0.133$, $M_e = 13$ for the end spheroids and $M = 1$ for the interior spheroids, the $\eta_j = \pi/2$ point. Both the manner in which the oblate spheroid representation converges as the aspect ratio of the elemental spheroids used in the cylinder construction decreases and the reason higher order multipoles and additional boundary points are not required for interior spheroids are evident from an analysis of this figure. The important feature of the solution is the existence of interior recirculation regions between adjacent spheroids. The width and amplitude of these entrained eddies must obviously shrink to zero in the limit as the aspect ratios of the elemental oblate spheroids vanish. While it is not possible, for the reasons discussed in the last section, to satisfy the no-slip boundary conditions at intermediate points along the cylinder surface between adjacent spheroids, one could satisfy these conditions at additional points along the boundary of each interior oblate spheroid as was done for the end spheroids. However, this would be of little value since the principal effect would be only to force the

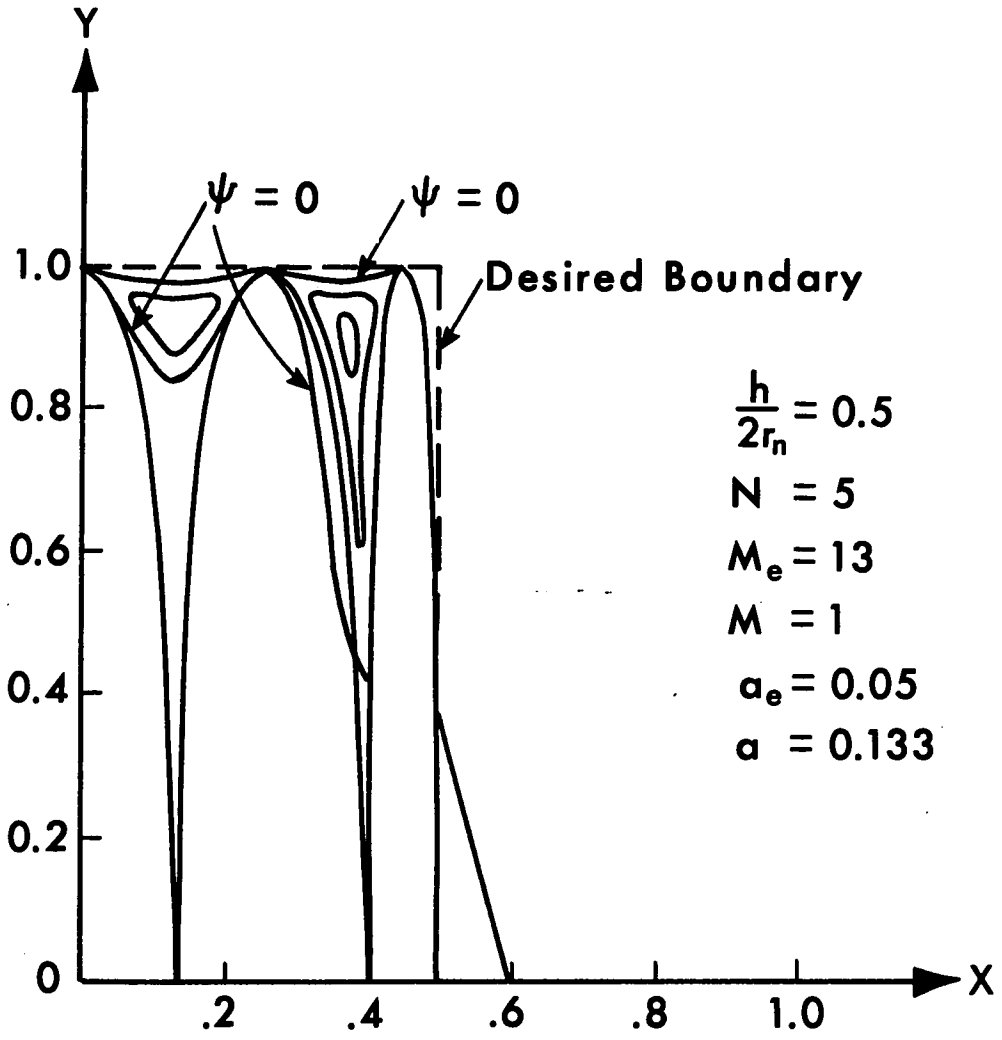

Figure 3.8 - STREAMLINE PATTERN FOR FLOW PAST A CYLINDER (M_e = 13)

entrained eddies to conform more closely to the interior boundaries of the oblate spheroids used in the construction. This behavior is apparent from a comparison of the entrained eddies between the first and second and second and third spheroids. When only the $\eta_j = \pi/2$ boundary point is used the entrained eddies are shallow and of small amplitude. The shape of the $\Psi = 0$ or separation streamline is changed negligibly by the addition of higher order multipoles.

A related result is that the drag or thrust forces associated with the entrained end eddies will influence the final drag to a greater extent than the entrained eddies between interior spheroids. This finding coupled with the previous discussion of the degree of error introduced by the existence of interior eddies indicates that the accuracy of the computed drag will be more sensitive to the aspect ratio of the end spheroids than to the aspect ratios of the interior spheroids. Some measure of the magnitudes of the thrust forces resulting from the entrained eddies between the two end spheroids of the cylinder is obtained from the second set of results in Table 3.2 where the change in K with decreasing aspect ratio of the end spheroid is shown. The settling factor K decreases indicating an increase in the total drag. The relatively minor effects of the entrained eddies in the central section of the chain are demonstrated by the third set of results giving K vs. N which show a much smaller relative increase in drag as N increases.

Finally, Table 3.3 presents data for flow past short cylinders of various length to diameter ratios and compares settling factors with those of Heiss and Coull (29). It can be seen that as the number of spheroids used to represent each cylinder is increased the settling factor appears to asymptote to a value that is in excellent agreement

Table 3.3

Settling Factors for Short Cylinders ($0.25 \leq h/2r_n \leq 4.0$)

Utilizing Higher Order Multipoles for the Ends

Length Diameter $h/2r_n$	Number of Spheroids N	End Aspect Ratio (a_e/b)	Central Aspect Ratio (a/b)	No. of Points on End Spheroids M_e	K This Work	K Heiss and Coull (29)
0.25	3	0.05	0.150	5	0.775	0.762
	7	0.05	0.030	5	0.773	
	11	0.05	0.017	5	0.772	
	3	0.005	0.240	5	0.764	
	7	0.005	0.048	5	0.760	
	11	0.005	0.027	5	0.759	
0.5	3	0.05	0.400	5	0.896	0.864
	7	0.05	0.080	5	0.890	
	11	0.05	0.044	5	0.887	
	3	0.005	0.490	5	0.884	
	7	0.005	0.098	5	0.878	
	11	0.005	0.054	5	0.877	
1.0	5	0.05	0.300	5	0.975	0.958
	9	0.05	0.129	5	0.971	
	11	0.05	0.100	5	0.969	
	5	0.005	0.330	5	0.967	
	9	0.005	0.141	5	0.961	
	11	0.005	0.110	5	0.960	
2.0	5	0.05	0.633	5	1.002	0.975
	9	0.05	0.271	5	0.994	
	11	0.05	0.211	5	0.993	
	5	0.005	0.663	5	0.997	
	9	0.005	0.284	5	0.988	
	11	0.005	0.221	5	0.986	
3.0	7	0.05	0.580	5	0.979	0.958
	9	0.05	0.414	5	0.976	
	11	0.05	0.322	5	0.961	
	7	0.005	0.598	5	0.974	
	9	0.005	0.427	5	0.971	
	11	0.005	0.332	5	0.969	
4.0	7	0.05	0.780	5	0.952	0.929
	9	0.05	0.557	5	0.949	
	11	0.05	0.433	5	0.947	
	7	0.005	0.798	5	0.948	
	9	0.005	0.570	5	0.945	
	11	0.005	0.443	5	0.943	

with the experimentally measured values of K. Some of the improved results from Table 3.3 which include the cylinder end corrections have been plotted in Figure 3.7. These results are in better agreement with the experimental data at the low length to diameter ratios than are the previous settling factors presented in Table 3.1. This improvement is in accord with the fact that the end corrections become increasingly important as the length to diameter ratio of the cylinder decreases. It is also noted that settling factors calculated using the multipole representation technique are in general slightly higher than the experimental results. This apparent reduction in drag might be attributed to the approximate procedure developed in section 3.2 for computing the drag.

As an example of an analytic body of revolution whose generating curve is a function of axial distance the creeping flow past a right circular cone of apex angle θ is considered. The geometry of the system is shown in Figure 3.9. The solution technique employed is similar to that used to represent short cylinders. The end (or base) of the cone is represented by an oblate spheroid of low aspect ratio (a_e/b_e) and the no-slip boundary conditions are satisfied at a number of points on the generating curve of this spheroid. This permits the higher order multipoles to produce an accurate representation of the base of the cone that will converge to the true planar shape as the aspect ratio of the spheroid approaches zero. The rest of the cone interior is divided into N sections of equal axial distance.

The section closest to the apex cannot contain an oblate spheroid due to the geometry and is, therefore, left blank. If a refined representation of the apex is desired this first section can easily be divided into smaller sections. The boundary conditions are to be satisfied at

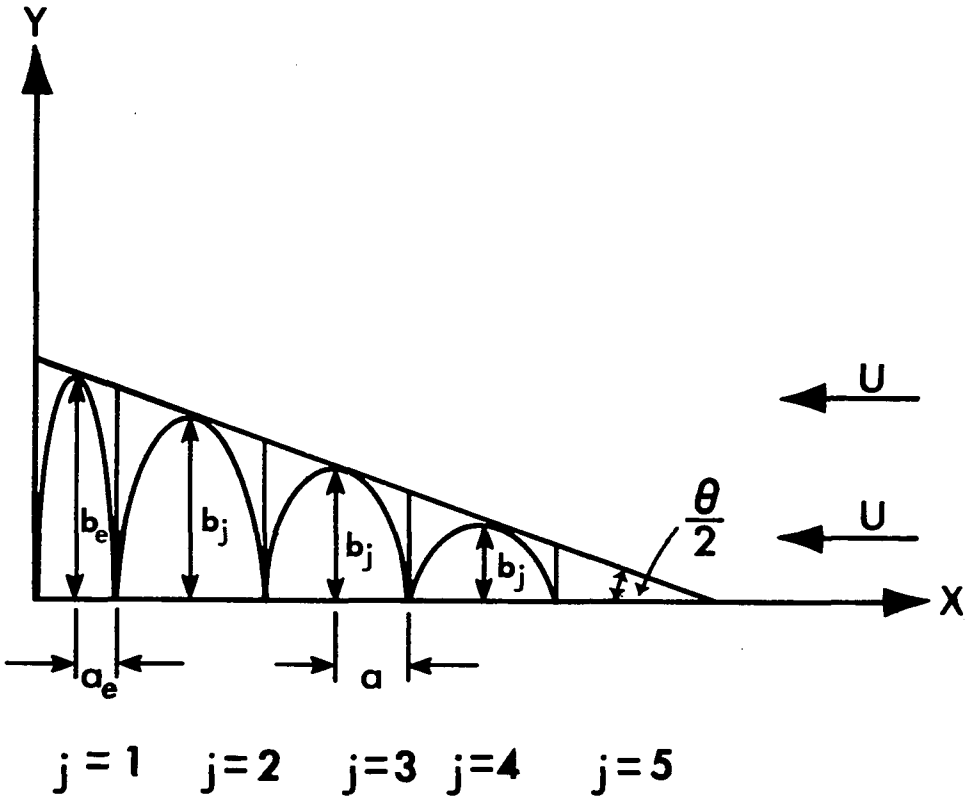

Figure 3.9 - GEOMETRY FOR OBLATE SPHEROIDAL REPRESENTATION OF A CONE

only the $\vartheta = \pi/2$ point on each of the generating surfaces except for the j = 1 spheroid. Convergence to the exact conical boundaries can be expected as the number of spheroids approaches infinity using the same arguments presented in the discussion of the cylinder.

Drag results will be presented for flow past a 30 degree half angle cone represented by N oblate spheroids ($3 \leq N \leq 15$) when the no-slip boundary conditions are satisfied at M_e points ($1 \leq M_e \leq 13$) on the generating arc of the spheroid closest to the base of the cone and at only the tangent point to the cone surface on the remaining N - 1 spheroids. These results will be reported in a terminology consistent with that used for the case of flow past cylinders.

The drag force on the cone F_o will be represented as follows:

$$F_o = \sum_{j=1}^{N} F_j \tag{3.10}$$

where F_j is the drag force on each of the j oblate spheroids used to represent the disturbance due to the cone. Equation (3.10) contains the same approximations as were detailed for the case of equation (3.4).

It has been shown that for the flow parallel to a chain of submerged oblate spheroids, the drag force on any spheroid in the chain can be represented by:

$$F_j = \frac{4\pi\mu D_{2,j}}{C_j} \tag{3.11}$$

where $D_{2,j}$ is a constant in equation (2.40).

C_j is the distance between the foci of the j^{th} spheroid

From (3.10) and (3.11) the total drag force on the cone is:

$$F_o = 4\pi\mu \sum_{j=1}^{N} \frac{D_{2,j}}{C_j} \tag{3.12}$$

The drag force on the cone can be related to the Stokes drag on a sphere having the same diameter as the cone (at its base) by introducing a multiplicative factor λ

$$F_o = 6\pi\mu U r_n \lambda \tag{3.13}$$

where r_n is the radius of the base of the cone. Equating (3.12) and (3.13) one obtains the following expression for λ:

$$\lambda = \frac{1}{1.5 U r_n} \sum_{j=1}^{N} \frac{D_{2,j}}{C_j} \tag{3.14}$$

Some of the results for flow past a 60 degree cone are presented in Table 3.4. Three sets of numerical experiments were performed to show the dependence of the accuracy of the solution on (a) the number of spheroids used; (b) the aspect ratio of the end spheroid; and (c) the number of points on the generating arc of the end spheroid at which the exact no-slip boundary conditions are satisfied. The trends of the results shown in Table 3.3 are similar to those discussed in Table 3.2 for the cylinder. Other factors held constant, λ converges to four significant digits when the no-slip boundary conditions are satisfied at 7 approximately equally spaced points along the generating arc of the end spheroid. λ is a sensitive function of the aspect ratio of the end spheroid. If the results of the second set of calculations are linearly extrapolated to $a_e = 0$ one obtains a value for λ of 0.895. Finally,

Table 3.4

Drag Correction Factor λ (3.14) for a 60 Degree Cone $r_n = 1$

Number of Spheroids N	Minor Axis of End Spheroid a_e	Minor Axes of Other Spheroids a	No. of Points on End Spheroid M_e	λ
15	.05	.0544	1	0.8774
15	.05	.0544	3	0.8666
15	.05	.0544	5	0.8710
15	.05	.0544	7	0.8712
15	.05	.0544	9	0.8713
15	.05	.0544	11	0.8713
9	.005	.0957	7	0.8925
9	.01	.0951	7	0.8899
9	.03	.0929	7	0.8801
9	.10	.0851	7	0.8466
9	.15	.0796	7	0.8234
9	.20	.0740	7	0.8010
3	.005	.2870	7	0.8877
5	.005	.1722	7	0.8908
7	.005	.1230	7	0.8923
9	.005	.0957	7	0.8925
11	.005	.0783	7	0.8926
13	.005	.0662	7	0.8928
15	.005	.0574	7	0.8931

increasing N beyond 7 produces changes in λ that are of the order 0.1% or less.

Figures 3.10a and b present plots of the streamlines when the boundary conditions are satisfied at 1 and 13 points on the generating arc of the end spheroid $a_e = .05$. When only 1 point on the generating arc of the end spheroid is used to satisfy the no-slip boundary conditions major distortions of the zero streamline in the vicinity of the base of the cone are observed. However, the rest of the conical surface is well approximated by the zero streamline. When 13 points along the generating surface of the end spheroid are used to satisfy the no-slip boundary conditions the zero streamline is a vastly improved approximation to the base of the cone except in the vicinity of the axis. These results are in close agreement with the results obtained earlier for the flow past a short cylinder. Finally, by comparing the relative shape and magnitude of the stationary eddies for these two cases, the same conclusions can be drawn as were described for the case of flow past a short cylinder.

3.4 APPROXIMATIONS FOR LONG FINITE CYLINDERS

In theory, the elemental oblate spheroid construction technique described in the previous section can be applied to the creeping flow past an arbitrary body of revolution. A practical limitation exists, however, for bodies of high aspect ratio. If one wishes to minimize the error in the drag computed from (3.12) which results for these bodies from the thrust forces associated with the entrained eddies between each oblate spheroid, a large number of oblate spheroids of low aspect ratio would be required for the representation. For example, to represent a cylinder having a length to diameter ratio of 40 using elemental oblate

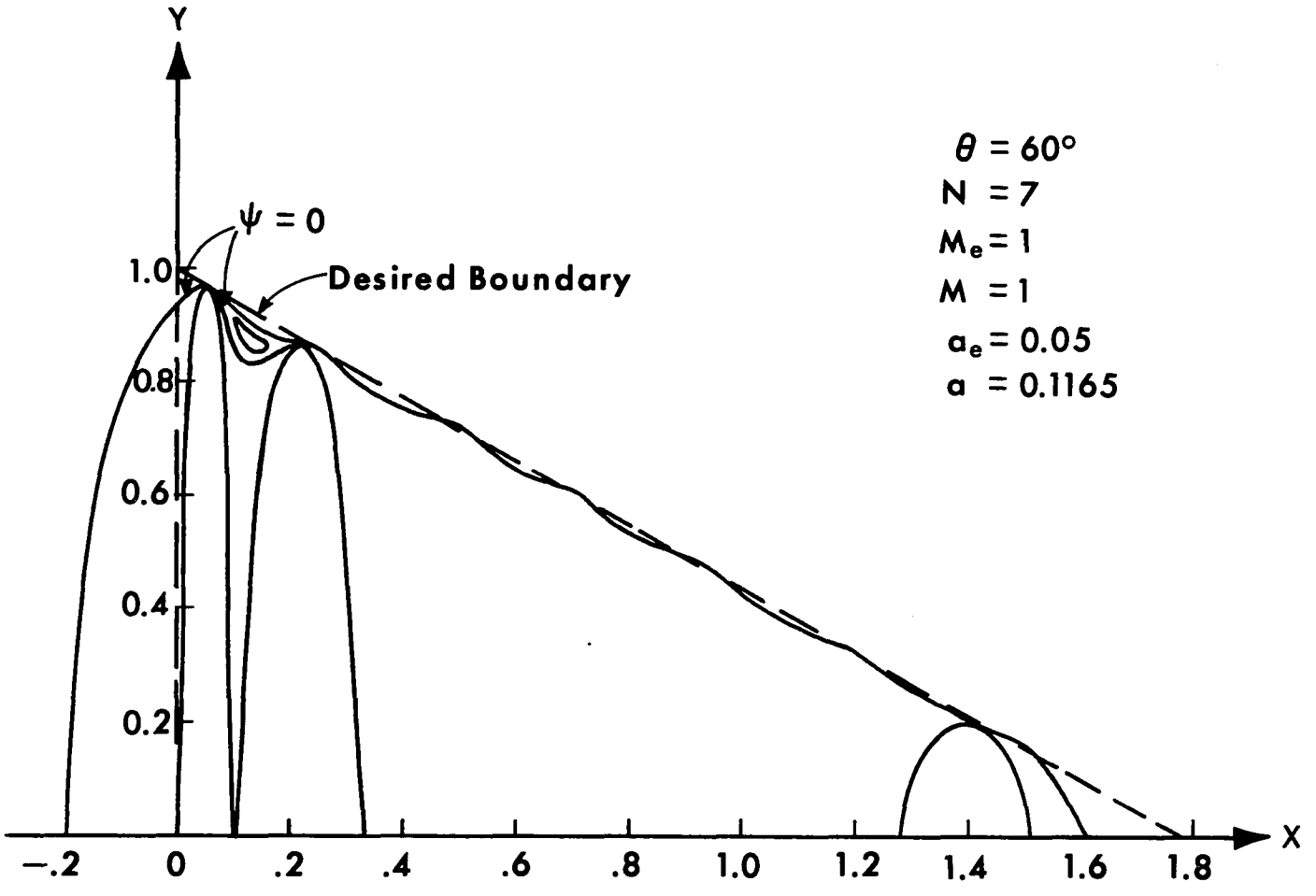

Figure 3.10a - STREAMLINE PATTERN FOR FLOW PAST A 60° CONE ($M_e = 1$)

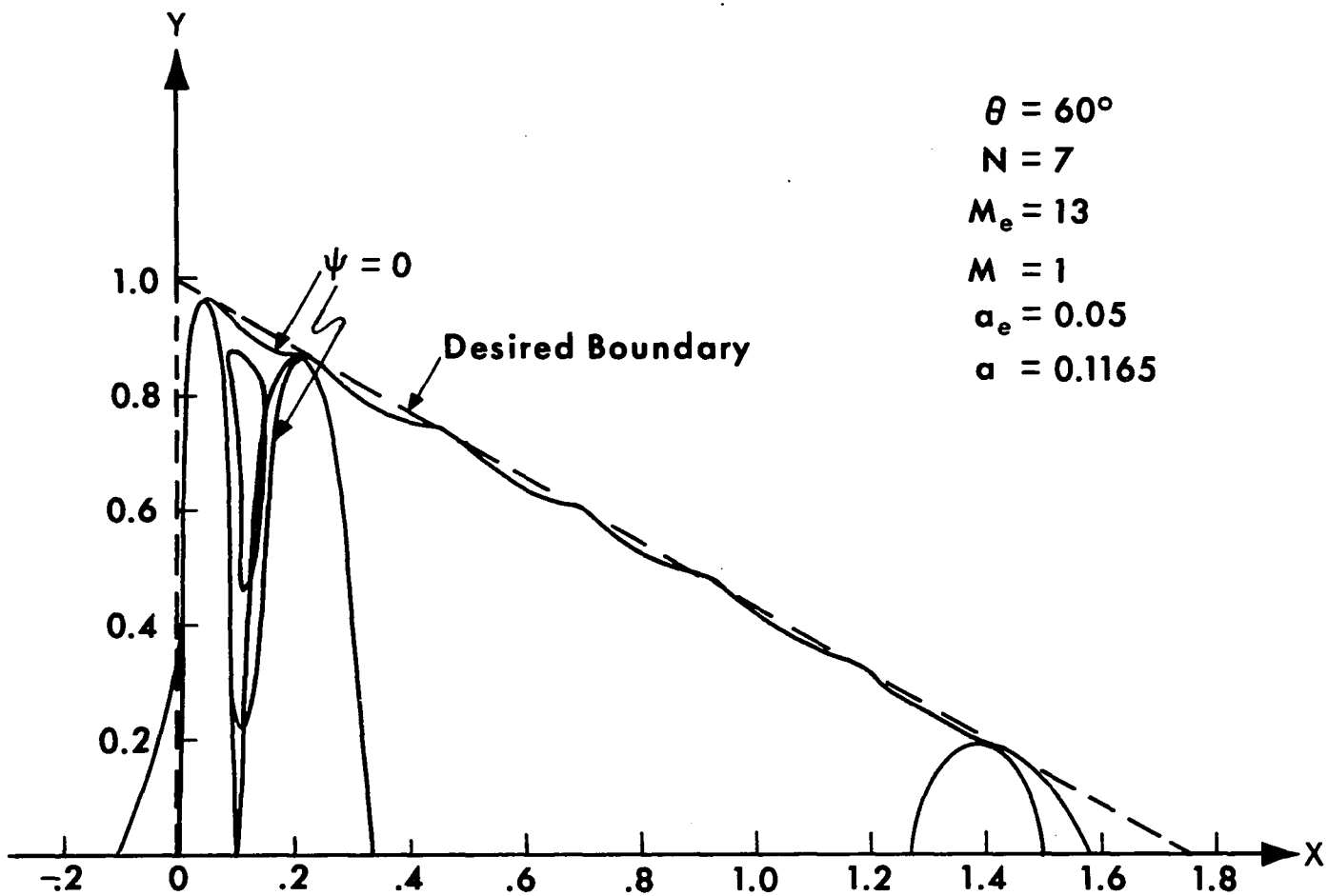

Figure 3.10b - STREAMLINE PATTERN FOR FLOW PAST A 60° CONE (M_e = 13)

spheroids of aspect ratio 0.05 would require 800 spheroids. To determine the coefficients of the two lowest order multipoles for each spheroid would involve the solution of 3200 linear simultaneous algebraic equations.

A simple yet good engineering approximation to the flow past high aspect ratio bodies will now be developed and applied to long finite cylinders. It will be shown that the drag on such elongated objects can be well approximated by one or more touching prolate spheroids. The details of the solution for the stream function for flow past multiple prolate spheroids is given in Chapter 2. The basic solution is equation (2.40) now modified so that p_j and q_j apply to prolate spheroidal co-ordinates:

$$p_j = \cosh \xi_j = \frac{R_{1j} + R_{2j}}{2c} \quad ; \quad q_j = \cos \eta_j = \frac{R_{2j} - R_{1j}}{2c}$$
$$R_{1j} = [(x - 2jd - c)^2 + y^2]^{1/2} \quad ; \quad R_{2j} = [(x - 2jd + c)^2 + y^2]^{1/2} \qquad (2.41)$$

This representation technique for long cylinders is an approximate one. Convergence cannot be expected since the limiting aspect ratio of the prolate spheroids is unity or that of a sphere. Thus, the entrained flow between adjacent prolate spheroids cannot be made to vanish nor can the ends of the object be accurately represented. The errors due to end effects, however, should be unimportant for long objects. Drag correction factors for long cylinders based on prolate spheroidal representation are compared with Burgers' approximate solution

$$F_c = \frac{2\pi \mu U_c h}{L_n\left(\frac{h}{r_a}\right) - 0.72} \qquad (3.15)$$

based on the point force technique in Table 3.5. From the definition of λ the force on the cylinder can be represented by:

Table 3.5

Comparison of Drag Correction Factors for Long Cylinders Calculated from the Multipole Technique, with Approximation of Burgers

Length Diameter $h/2r_n$	Number of Spheroids N	Aspect Ratio a/b	λ This Work	λ Equation (3.17)
10.0	1	10.0	2.647	2.929
	2	5.0	2.815	
	3	3.3333	2.883	
	5	2.0	2.946	
20.0	1	20.0	4.172	4.490
	2	10.0	4.384	
	3	6.6667	4.469	
	5	4.0	4.548	
	9	2.2222	4.611	
	15	1.3333	4.651	
40.0	1	40.0	6.859	7.280
	2	20.0	7.150	
	3	13.3333	7.265	
	5	8.0	7.370	
	9	4.4444	7.450	
	15	2.6667	7.496	

$$F_c = 6\pi\mu U_c r_m \lambda \tag{3.16}$$

Equating (3.15) and (3.16)

$$\lambda = \frac{h}{3r_m\left[L_n\left(\frac{h}{r_m}\right) - 0.72\right]} \tag{3.17}$$

Table 3.5 demonstrates that good approximations to the drag on long cylinders can be achieved by this technique. It can be seen that convergence is not achieved using any reasonable number of prolate spheroids. This is due to the inability of this technique to produce good representations of the ends of the cylinder. The results of Table 3.5 are presented graphically in Figure 3.11. It can be seen that the closest approximation to Burgers' results always seem to occur when the cylinder is represented by between three and five prolate spheroids. The most accurate solution is probably that corresponding to the largest value of N. The zero streamline for the case of five prolate spheroids representing a cylinder having a length to diameter ratio of 10 is shown in Figure 3.12. One observes that the zero streamline (for the case where the boundary conditions are satisfied at only the $\eta = \pi/2$ point on each spheroid) deviates minimally from the horizontal surface of the desired cylinder. Also, as was the case for short cylinders, when the no-slip boundary conditions were satisfied at only $\eta_j = \pi/2$ point on the end spheroids, the end representations are poor.

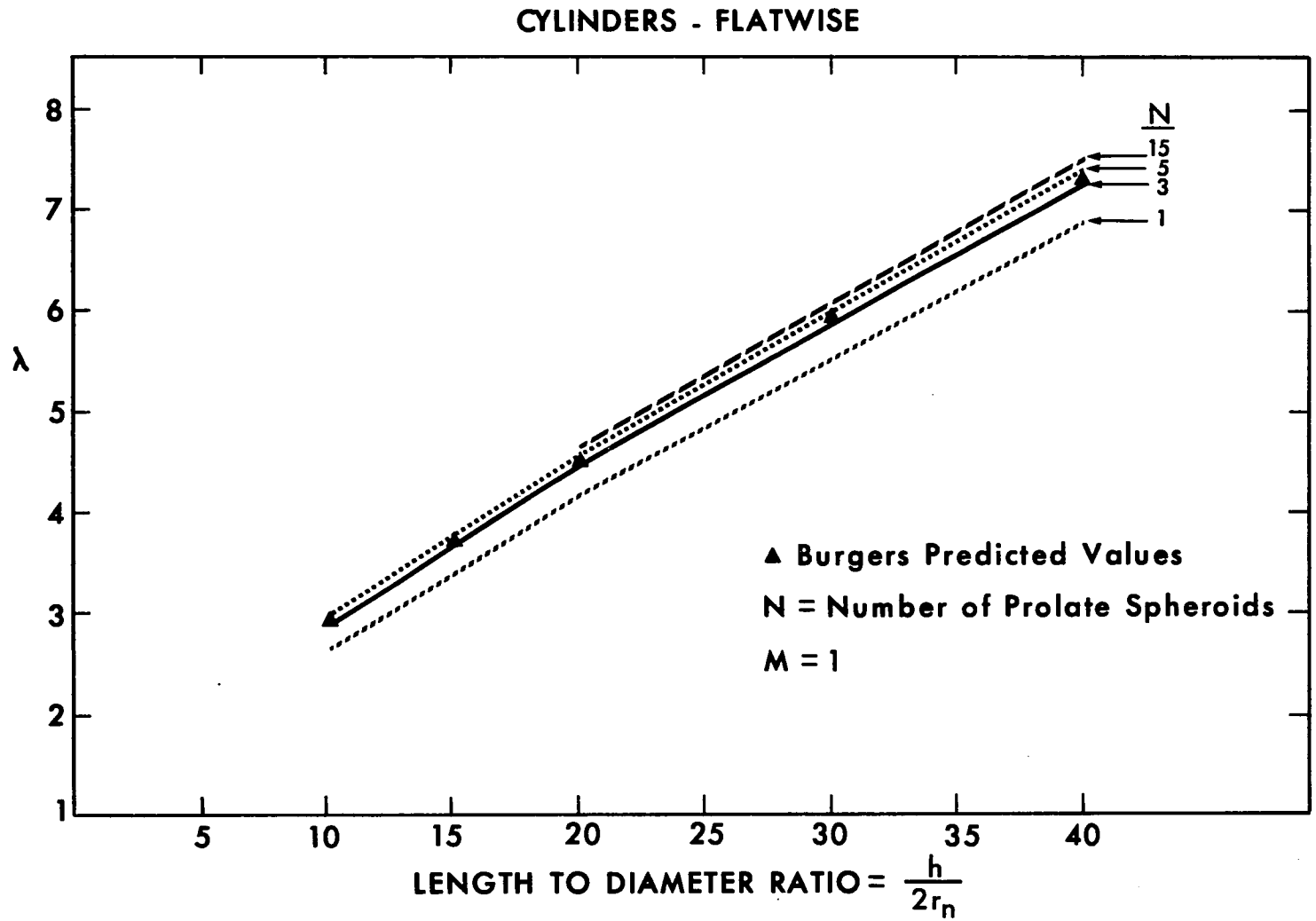

Figure 3.11 - λ VS. $h/2r_n$ FOR LONG CYLINDERS

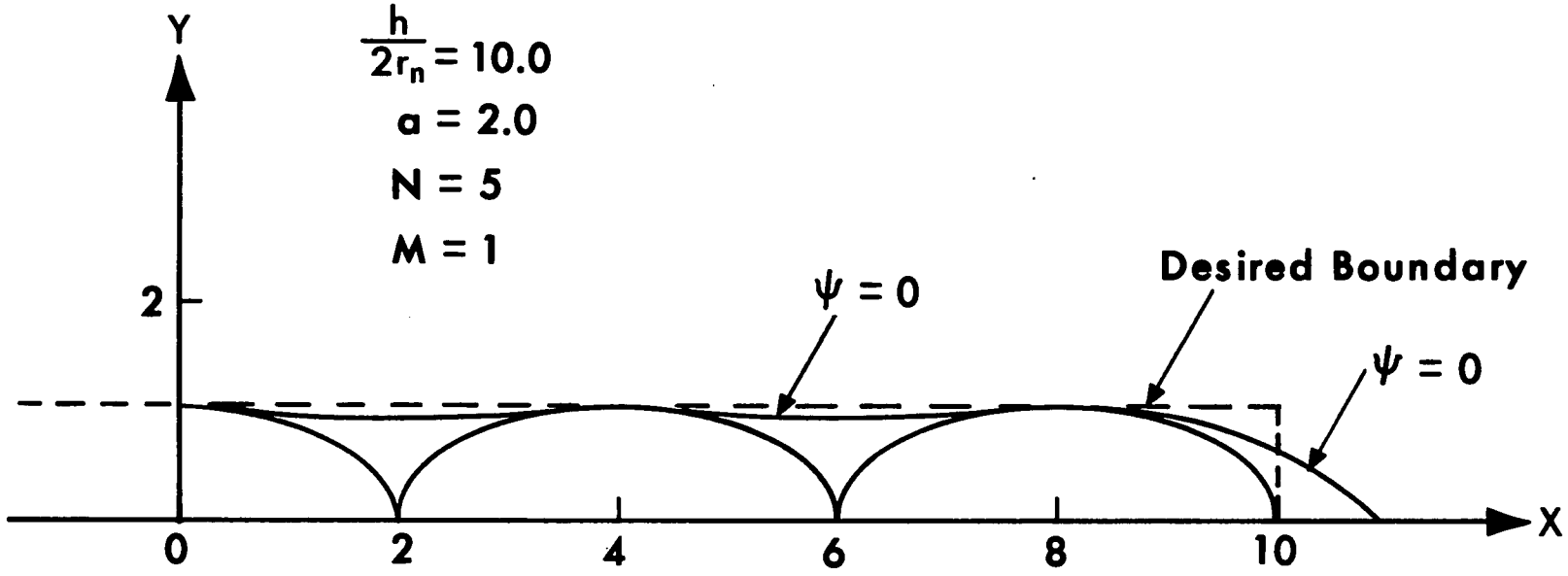

Figure 3.12 - ZERO STREAMLINE FOR LONG CYLINDERS

CHAPTER 4

THREE SPHERES FALLING ALONG THEIR LINE OF CENTERS IN A VISCOUS FLUID

4.1 INTRODUCTION

The steady state problem of two equal spheres falling along their line of centers in a viscous, incompressible, unbounded fluid has been solved analytically for the Stokes flow regime $Re \ll 1$ by Stimson and Jeffery (7), Happel and Brenner (1), and others. Experimental work on this problem by Bart (30), Eveson (31), and Happel and Pfeffer (32) shows excellent agreement with the theoretical results at low Reynolds Numbers ($Re < 0.1$). The related problem of three spheres falling along their line of centers in an unbounded viscous fluid however, has received no previous theoretical treatment.

The fundamental difference between the two flow situations is that the two sphere problem at very low Re is (after the initial transient disturbance has died out) a stable flow configuration in which the sphere spacing does not change since the Stokes quasi-steady state drag on each sphere is the same. In contrast, the three sphere problem has no stable steady state configuration even after the initial quasi-steady settling velocity is achieved since the quasi-steady state Stokes drag on each sphere continues to vary because of multiparticle interaction effects that continually change as a function of particle spacing and velocity. At very low Reynolds Number $Re \ll 1$ two distinct time scales exist in the problem, a short time characteristic of the time required to achieve the initial settling velocity and a long time characteristic of the time over which the sphere spacing changes significantly due to multiparticle interaction effects. As

Re increases the short time scale increases until it no longer can be considered small compared to the larger time scale. The theoretical analysis developed herein describes all the basic physical features of the three sphere system including the Reynolds Number effect on the evolvement of the two time scales for the range $0 < Re \leq 10$.

The qualitative behavior of the three sphere problem has been investigated experimentally by Happel and Pfeffer (32). These investigators found that if three spheres, 1, 2, and 3 were released from rest in a fluid as shown in Figure 4.1a, 1 and 2 would fall as a doublet initially and would therefore travel at a greater velocity than 3 (two spheres touching one another will settle at a velocity that is 55% greater than the settling velocity of an isolated sphere of the same diameter, the drag on each sphere in the doublet being 0.645 that of the isolated sphere). The flow configuration shown in Figure 4.1a, therefore, does not persist. Also, as spheres 1 and 2 approach sphere 3, sphere 2 will start to accelerate due to its combined interaction with spheres 1 and 3. Thus, sphere 2 progressively moves away from sphere 1 as shown in Figure 4.1b. Finally, as sphere 2 approaches sphere 3, 2 and 3 form a doublet having a settling velocity greater than sphere 1 (see Figure 4.1c). This doublet will continue to move away from sphere 1 as long as the spheres are allowed to settle without approaching or impinging on any boundaries.

Unlike the two sphere problem, where the bipolar coordinate transformation allows one to determine relatively easily the flow field and drag on each sphere as a function of sphere spacing, quasi-steady state particle interaction effects are much more difficult to treat for more than two spheres particularly at close sphere spacings. The

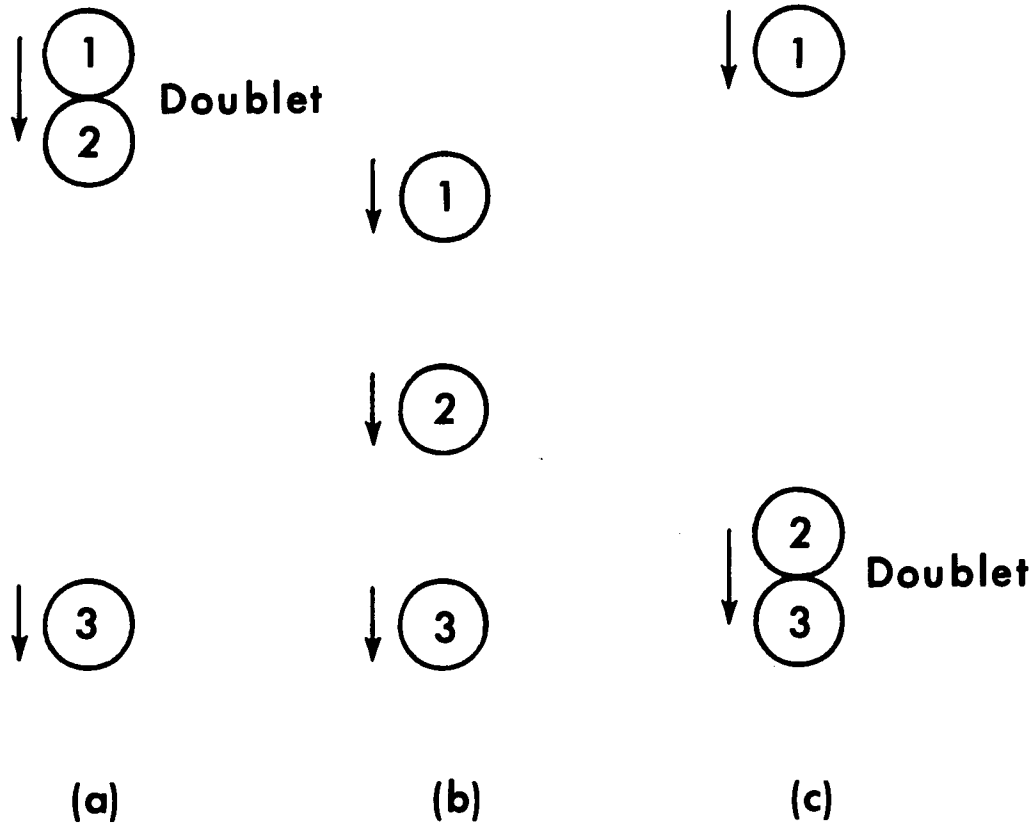

Figure 4.1 - GRAVITY SETTLING OF THREE SPHERES

three sphere interaction problem at very low Re can in principle be treated by the method of reflections developed by Smoluchowksi (2) or the point force technique of Burgers (4). The first technique has important practical limitations, since it is an iterative series solution generated by the solution for the flow past a single sphere and converges very slowly when the sphere spacing is small. The method of reflections is also extremely tedious to apply when more than two objects are present.

The second method the point force technique is only a useful approximation for dilute systems. In this method one approximates the no slip boundary conditions by requiring that the average velocity over the surface vanish rather than requiring that the no slip conditions be satisfied over the entire surface.

The multipole truncation procedure, detailed in Chapters 2 and 3, is ideal for handling this three sphere interaction problem as it is almost as efficient to use when the spheres are touching as when they are far apart. A detailed description of the application of this procedure to the three sphere problem will be presented later in this chapter.

4.2 FORMULATION AND SOLUTION OF THE EQUATIONS OF MOTION

A. DYNAMIC EQUATIONS OF MOTION FOR ONE SPHERE

The unstady creeping motion momentum equations are derived from the Navier-Stokes equations neglecting the inertial terms:

$$\frac{\partial \bar{V}}{\partial t} = \frac{-1}{\rho} \nabla p + \nu \nabla^2 \bar{V} \tag{4.1}$$

To eliminate the pressure one takes the curl of (4.1)

$$\frac{\partial (\text{curl } \bar{V})}{\partial t} = \nu \nabla^2 (\text{curl } \bar{V}) \tag{4.2}$$

Landau and Lifshitz (33) present an elegant analysis of equation (4.2) and solve it for the case of a single sphere moving slowly with velocity U(t) in a viscous fluid. The solution is found by representing the velocity U(t) as a Fourier integral.

$$U(t) = \int_{-\infty}^{\infty} U_w e^{-iwt} dw \tag{4.3}$$

where U_w is the solution to (4.1) for a sphere oscillating with frequency w. The expression for the drag force F on the sphere is given in terms of U(t) as

$$F = 6\pi\mu Ua + \frac{2}{3}\pi\rho a^3 \frac{dU}{dt} + 6\pi\mu a^2 \frac{1}{\sqrt{\pi\nu}} \int_0^t \frac{dU}{d\tau} \frac{d\tau}{\sqrt{t-\tau}} \tag{4.4}$$

Equation (4.4) shows that there are three basic contributions to the drag force on a sphere undergoing an arbitrary slow motion in a viscous fluid. The first term in equation (4.4) represents the steady state component of the drag force, or Stokes drag term due to viscous dissipation. The remaining two terms in (4.4) represent unsteady contributions to the drag force. The first of these two terms is the virtual or hydrodynamic mass contribution. This term is also present for an ideal fluid and is related to the kinetic energy associated with the fluid that is displaced by the sphere. Since this energy is distributed throughout the entire flow field whereas viscous effects are confined to a localized region near boundaries this term is the same as the inertial force that appears in the unsteady potential flow past a sphere, see Darwin (34) and Milne-Thomson (35). The last term in equation (4.4) has been identified as the Basset force after Basset (36). This force is attributed to the unsteady inertial term in (4.1) and its importance will be discussed in a later section.

The complete equation of motion for the unsteady settling of a single sphere at low Re in an unbounded viscous fluid is obtained by adding the static or gravity forces to the three dynamic forces in (4.4) and equating these forces to the acceleration force of the sphere.

$$M\frac{dU}{dt} = Mg - M'g - F_D - F_{V.M} - F_B \qquad (4.5)$$

where
- M = mass of sphere
- M' = mass of displaced fluid
- F_D = Stokes drag force
- $F_{V.M}$ = retarding force due to the energy of the displaced fluid
- F_B = Basset force

For a single sphere, (4.5) can be written as follows:

$$\frac{4}{3}\pi a^3 \rho_s \frac{dU}{dt} = \frac{4}{3}\pi a^3(\rho_s-\rho)g - 6\pi\mu Ua - \frac{2}{3}\pi a^3\rho\frac{dU}{dt} - 6\pi\mu a^2\frac{1}{\sqrt{\pi\nu}}\int_0^t \frac{dU}{d\tau}\frac{d\tau}{\sqrt{t-\tau}} \qquad (4.6)$$

where
- a = sphere radius
- ρ_s = sphere density
- ρ = fluid density
- μ = fluid viscosity
- ν = kinematic viscosity

The terminal settling velocity U_t is found from (4.6) by setting $\frac{dU}{dt} = 0$

i.e.
$$U_t = \frac{2a^2(\rho_s-\rho)g}{9\mu} \qquad (4.7)$$

To apply (4.5) to a flow system with more than one sphere each of the dynamic force contributions must be modified to take into account particle interaction effects. Each dynamic force correction will be considered separately in the next three sections.

B. STOKES DRAG FORCE, F_D

The well documented Stokes drag force on a single sphere settling in an unbounded viscous fluid for Re $\ll$ 1 is

$$F_D = 6\pi\mu U a \tag{4.8}$$

Since the drag force due to viscous dissipation is still proportional to the instantaneous velocity of the test sphere when more than one sphere is present in the system, equation (4.8) for the drag force can be simply modified to account for particle interaction effects on the drag force on each sphere by introducing an interaction parameter

$$F_{D_j} = 6\pi\mu U_j a \lambda_j \tag{4.9}$$

where λ_j is the ratio of the drag on a sphere in an assemblage of particles to the drag on a single sphere of the same diameter and is a strong function of sphere orientation and sphere spacing.

As has been pointed out earlier, the computation of λ has been the subject of extensive work (see Happel and Brenner (1) and Chapter 2). Until recently only two techniques -- the method of reflections and the point force method -- have been available for treating multiple particle interaction problems. For the reasons stated in the introduction neither is suitable for describing the quasi-steady state three sphere interaction problem as the sphere spacing decreases. The multipole truncation technique developed and described in detail in Chapters 2 and 3 is, however, ideally suited for this purpose for the reasons stated earlier.

The geometry being considered is shown in Figure 4.2. The exact solution for the stream function, see equation (2.15), is given by the

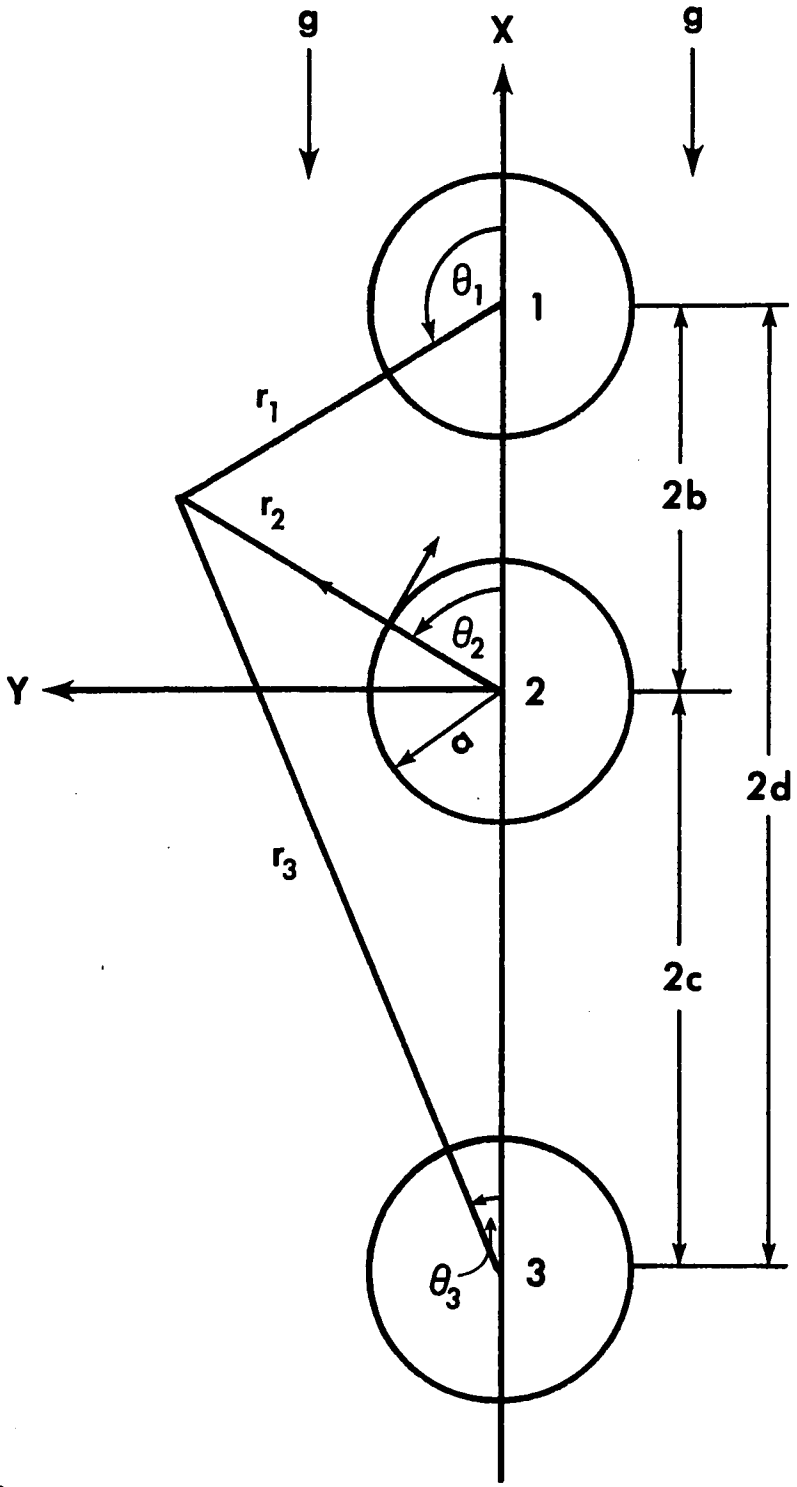

Figure 4.2 - GEOMETRY OF THREE SPHERE SYSTEM

superposition of three infinite series representing the disturbance produced by each of the three spheres.

$$\psi = \sum_{j=1}^{3} \sum_{n=2}^{\infty} \left[B_{nj}\, r_j^{-n+1} + D_{nj}\, r_j^{-n+2} \right] I_n(\xi_j) \qquad (4.10)$$

where: $I_n(\xi_j)$ = Gegenbauer functions of the first kind

$$\begin{aligned} \xi_j &= \cos\theta_j \\ r_1 &= \left[(x-2b)^2 + y^2\right]^{1/2} \;; \quad \xi_1 = \frac{(x-2b)}{r_1} \\ r_2 &= \left[x^2 + y^2\right]^{1/2} \;; \quad \xi_2 = \frac{x}{r_2} \\ r_3 &= \left[(x+2c)^2 + y^2\right]^{1/2} \;; \quad \xi_3 = \frac{(x+2c)}{r_3} \end{aligned} \qquad (4.11)$$

Each term in the inner summation termed a multipole contains an amplitude function shown in brackets and a multilobular Gegenbauer function $I_n(\xi_j)$. The B_{nj} and D_{nj} constant coefficients which fix the strength of the multipole are determined by satisfying the no slip boundary conditions over the generating arc of all spheres simultaneously; i.e.,

$$\begin{aligned} V_{rj} &= U_j \cos\theta_j = -\frac{1}{r_j^2 \sin^2\theta_j} \frac{\partial\psi}{\partial\theta_j} \\ V_{\theta j} &= U_j \sin\theta_j = \frac{1}{r_j \sin\theta_j} \frac{\partial\psi}{\partial r_j} \end{aligned} \qquad (4.12)$$

where the U_j represent the velocities of each sphere. To satisfy the boundary conditions (4.12) exactly along the entire boundary of each sphere would require the solution of a triply infinite array of unknown

coefficients. However, it has been shown that solutions to any desired accuracy can be obtained by a uniform truncation of each of the infinite multipole series. The two unknown coefficients in each multipole permit one to satisfy the exact no-slip boundary conditions (4.12) at one discrete point on the generating arc of each sphere. Thus, if a spherical boundary is to be approximated by satisfying conditions (4.12) at M discrete points on its generating arc M terms are retained in the multipole expansion for each sphere.

The no-slip boundary conditions (4.12) at any point m on the generating arc of the jth sphere can be represented as follows:

$$V_{r_{jm}} = \sum_{q=1}^{3} \sum_{n=2}^{M+1} \left[B'_{nqm} B_{nq} + D'_{nqm} D_{nq} \right] = U_j \cos\theta_{jm}$$

$$V_{\theta_{jm}} = \sum_{q=1}^{3} \sum_{n=2}^{M+1} \left[B''_{nqm} B_{nq} + D''_{nqm} D_{nq} \right] = U_j \sin\theta_{jm} \quad (4.13a)$$

for $1 \le m \le M$

$$B'_{nqm} = \frac{1}{r_{jm}^2 \sin\theta_{jm}} \left[(n-1) r_{qm}^{-n} \frac{\partial r_{qm}}{\partial \theta_{jm}} I_n(\beta_{qm}) + r_{qm}^{-n+1} P_{n-1}(\beta_{qm}) \frac{\partial \beta_{qm}}{\partial \theta_{jm}} \right]$$

$$D'_{nqm} = \frac{1}{r_{jm}^2 \sin\theta_{jm}} \left[(n-3) r_{qm}^{-n+2} \frac{\partial r_{qm}}{\partial \theta_{jm}} I_n(\beta_{qm}) + r_{qm}^{-n+3} P_{n-1}(\beta_{qm}) \frac{\partial \beta_{qm}}{\partial \theta_{jm}} \right]$$

$$B''_{nqm} = \frac{1}{r_{jm} \sin\theta_{jm}} \left[(-n+1) r_{qm}^{-n} \frac{\partial r_{qm}}{\partial r_{jm}} I_n(\beta_{qm}) - r_{qm}^{-n+1} P_{n-1}(\beta_{qm}) \frac{\partial \beta_{qm}}{\partial r_{jm}} \right] \quad (4.13b)$$

$$D''_{nqm} = \frac{1}{r_{jm} \sin\theta_{jm}} \left[(-n+3) r_{qm}^{-n+2} \frac{\partial r_{qm}}{\partial r_{jm}} I_n(\beta_{qm}) - r_{qm}^{-n+3} P_{n-1}(\beta_{qm}) \frac{\partial \beta_{qm}}{\partial r_{jm}} \right]$$

Equation (4.13a) when written in matrix form becomes:

$$\begin{vmatrix} B'_{2,1,1} & D'_{2,1,1} & B'_{3,1,1} & \cdots & D'_{M+1,3,1} \\ \vdots & \vdots & \vdots & & \vdots \\ B''_{2,1,M} & D''_{2,1,M} & B''_{3,1,M} & \cdots & D_{M+1,3,M} \end{vmatrix} \begin{vmatrix} B_{2,1} \\ \vdots \\ D_{M+1,3} \end{vmatrix} = \begin{vmatrix} U_1 \cos\theta_{1,1} \\ \vdots \\ U_3 \sin\theta_{3,M} \end{vmatrix} \quad (4.13c)$$

This linear set of simultaneous algebraic equations can be solved to yield the B_{nj} and D_{nj} constants required in (4.10) by any of the standard matrix reduction techniques.

Experience has shown that the most accurate lowest order truncation solution for the viscous drag is obtained by choosing $\theta_j = \frac{\pi}{2}$ since this point controls the projected area of the boundary shape approximating the sphere. Additional points are selected as mirror image pairs about the line $\theta_j = \frac{\pi}{2}$ in order to preserve the geometric symmetry of the spherical boundary shape about this line. A detailed discussion of the role and importance of the higher order multipoles as well as the convergence properties of the multipole truncation technique is given in Chapters 2 and 3.

The correction to the Stokes drag for a sphere in an assemblage (λ_j) is given by:

$$\lambda_j = \frac{D_{2,1}}{1.5\, U_j\, a} \qquad (2.24)$$

It can be surmised by an examination of (4.12) and (2.24) that the λ_j are only functions of the distances between spheres and their relative velocities.

An examination of the λ_j for three spheres moving at the same velocity for various sphere spacings provides the basic physical insight into the experimental observations of Happel and Pfeffer (32) shown in Figure 4.1. In the actual solution of the problem, of course, the different instantaneous values of the velocity for the three spheres must be taken into account in computing the instantaneous value of λ_j. Curves of λ_j versus a spacing parameter $\frac{b}{b+c}$ for two values of the overall spacing (b+c) are shown in Figure 4.3. As (b+c) decreases, it

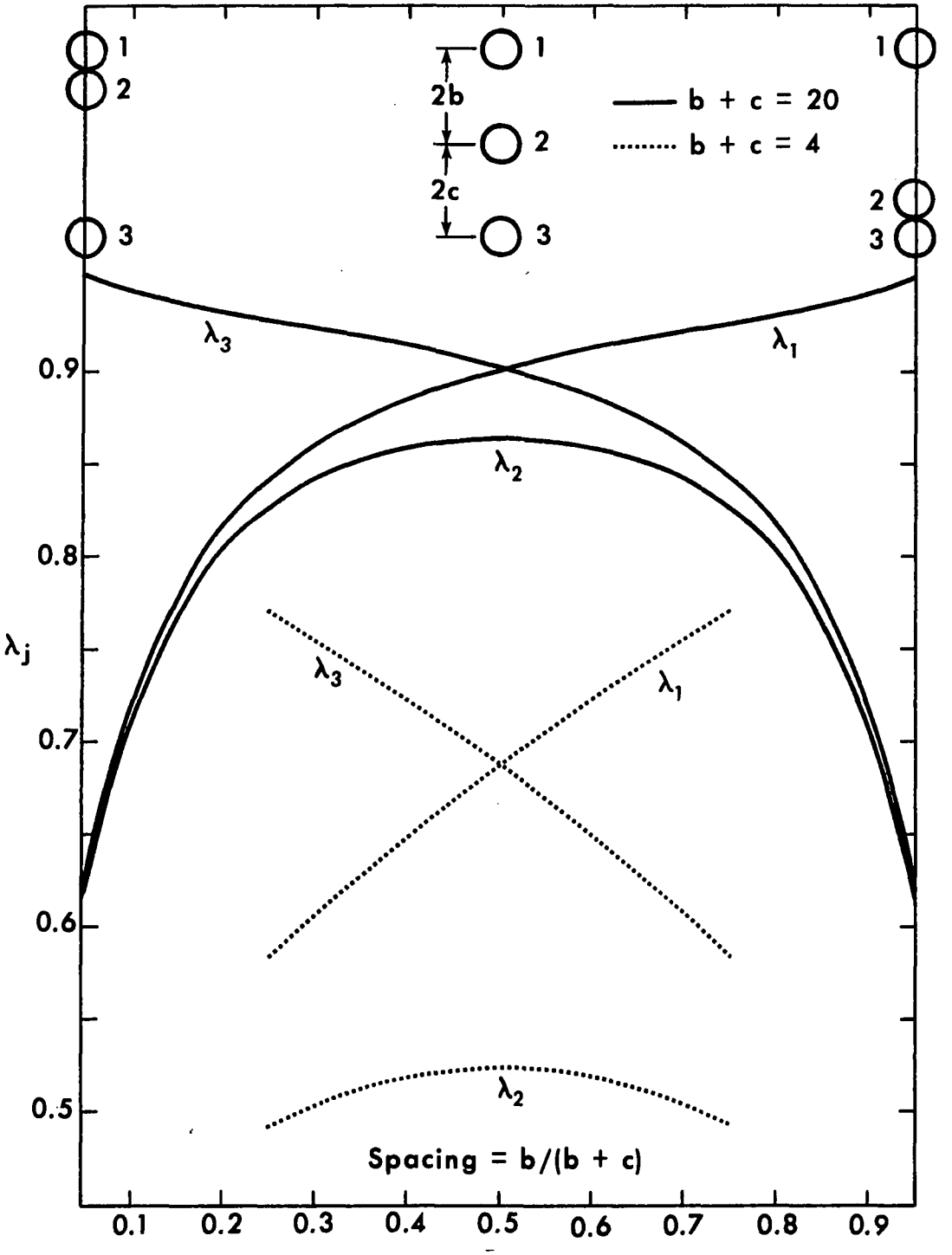

Figure 4.3 - λ_j VS. SPACING FOR THREE SPHERES

can be seen that the λ_j decrease showing that drag reduction effects increase as the spheres approach one another.

A number of other interesting features emerge from an examination of Figure 4.3. First, the drag on the center sphere is always less than the drag on either of the outer spheres. This is due to the fact that the central sphere is being acted on directly by both outer spheres, whereas an outer sphere is being acted on directly only by the central sphere and indirectly by the far sphere. This suggests that whatever the starting position of the three spheres may be, if they are allowed to settle for a long enough time, the central sphere will eventually approach sphere 3. Spheres 2 and 3 will then settle as a doublet having a higher terminal velocity than the single sphere 1 and will continue to move away from 1. Therefore, for any initial value of $\frac{b}{b+c}$ one should always move to the right along the $\frac{b}{b+c}$ axis as time progresses, due to the lower drag on the central sphere. Finally, it is of interest to note that as spheres 2 and 3 move away from the single sphere 1, λ_1 will approach the isolated sphere value of 1.0 and λ_2 and λ_3 will approach the exact value of λ for two touching spheres of 0.645. This indicates that for $b \gg 1$, the doublet will be settling at a velocity that is 55% greater than the terminal velocity of sphere 1.

C. F_D AS A FUNCTION OF Re

It has been stated in the introduction that the temporal behavior of the solution is dependent on Re, and that for very low Re two distinct time scales were present; a short scale characteristic of the time to achieve the initial settling velocity and a long time scale characteristic of the time over which changes in sphere velocity occur due to sphere interaction effects.

A qualitative insight into the Re dependence of the short time scale can be obtained by integrating the equation of motion for a single sphere (4.6), where as a rough approximation F_D has been represented by its Stokes value (4.8). If the Basset force is neglected the solution of (4.6) is

$$t = \frac{(\tilde{\rho}+\frac{1}{2})Re^{1/2}}{18\sqrt{2(\tilde{\rho}-1)}} \ln\left[\frac{1}{1-\frac{U}{U_t}}\right] \tag{4.14}$$

where $\tilde{\rho} = \rho_s/\rho$

U = velocity

U_t = terminal settling velocity (4.7)

At Re=0.1 and $\tilde{\rho}$=5.0, the time required to achieve 99% of U_t is t=0.236 whereas at Re=10.0 albeit far beyond the range where (4.8) and hence (4.14) is valid, this time is increased by a factor of 10 to t=2.36.

Many attempts have been made in the past to determine the influence of inertial effects at low Re and to extend the range of validity of the Stokes drag formula, e.g. the classic work of Oseen (37) and more recently Proudman and Pearson (38). The latter authors using a theory of matched inner and outer expansions obtained the following expression for the drag coefficient C_D for a single sphere

$$C_D = \frac{24}{Re}\left[1 + \frac{3}{16}Re + \frac{9}{160}Re^2 \ln(Re) + O(Re^2)\right] \tag{4.15}$$

This solution agrees with experimental data up to Re≈1.

Theoretical attempts to significantly extend the Re range of validity of the above expression for C_D have been notably unsuccessful. This difficulty is probably due to the inability of the linearized solutions of the Navier-Stokes equations to properly describe the viscous layer separation and incipient wake formation that occurs at

higher Re. For this reason a purely empirical approach has been adopted to extend this analysis to higher Reynolds Numbers. The data of Lapple and Shepherd (39) for a single isolated sphere were utilized to fit the drag force to a power series in Re.

$$\frac{F_D}{F_{D_{stokes}}} = \left[1 + 0.06951\,Re + 0.01905\,Re^2 - 0.00296\,Re^3 + 0.987\times10^{-4}\,Re^4 - 0.13\times10^{-8}\,Re^5\right] \tag{4.16}$$

which is applicable in the range $Re \leq 20$.

It is evident that there is no rational procedure by which (4.16) can be modified to take into account the effect of sphere interactions when more than one sphere is present. For very low values of Reynolds Number ($Re \ll 1$) these interaction effects can be accurately accounted for by (4.9) where the interaction parameter λ_j is given by (2.24). To extend (4.9) to include inertial effects even in an approximate manner some semi-empirical approach must be adopted. The simplifying assumption that is made is that the inertial and sphere interaction effects are essentially independent of one another provided Re is not large enough for the character of the flow to change significantly, that is for separation to move forward of the rear stagnation point and a wake bubble form. Taneda's (40) extrapolated experimental results as well as numerical solutions of the Navier-Stokes equations predict that the incipient separation Re for a single sphere is between 17 and 24. Therefore, the range of application of the proposed approximate formula

$$F_{D_j} = 6\pi\mu U_j a \lambda_j f(Re_j) \tag{4.17}$$

where f (Re_j) is the viscous drag on a single sphere from (4.16) will

be confined to values of $Re_j < 20$. It is assumed that λ_j is given by its Stokes slow flow expression (2.24) independent of Re and that the Re dependence of the inertial terms is unaffected by the presence of the other spheres and hence given by the empirical expression for a single sphere.

It is seen that equation (4.17) reduces to the correct limit when $Re_j \ll 1$ for any sphere spacings and to (4.16) when the spheres are far apart. For the broad range of conditions between these limiting cases it is expected that (4.17) will provide a reasonable description of the drag force. This will enable a study to be made of the Re dependence of the two time scales in the region where Re is no longer $\ll 1$.

D. VIRTUAL MASS TERM, $F_{V.M}$

Virtual mass has been defined by Darwin (34) as follows: "When a solid body moves through an incompressible fluid, it induces a drift in the fluid, such that the final positions of the particles are further on than those from which they started. The drift volume enclosed between the initial and final positions is equal to the volume corresponding to the hydrodynamic mass, that is, the mass of fluid to be added to that of the solid in calculating its kinetic energy." All existing calculations of the virtual mass of an object using either the drift volume concept or the kinetic energy of the flow field have been based on inviscid potential flow theory.

Although a rigorous treatment of the virtual mass of an object moving in a viscous fluid has not been presented the arguments and examples in Landau and Lifshitz (33) provide valuable insight into its approximate calculation. At high Re viscous effects are confined to

the thin region near the boundaries of an object and its wake. The contribution to the kinetic energy of the fluid by these viscous regions is therefore a very small portion of the total kinetic energy of the flow field and the use of potential flow theory to compute the virtual mass is thus justified. At very low Re Landau and Lifshitz have shown that for the case of a single sphere moving with an arbitrary velocity U(t) in a real fluid the virtual mass is identical to that for the given sphere moving in a potential flow with the same velocity. Since the Stokes flow equation (4.1) is linear the solution can be treated as the superposition of a potential solution which satisfies the same boundary condition on the normal velocity component as the given sphere in an ideal fluid plus a rotational solution which satisfies the no-slip boundary condition on the tangential velocity component. This rotational solution contributes to the viscous work performed on the fluid in increasing its internal energy but does not affect the kinetic energy of the flow field and therefore its virtual mass.

At intermediate Re where non-linear inertial effects are important and viscous effects are not confined to thin layers a rigorous treatment of the virtual mass effect is considerably more difficult. However, physically plausible arguments can be advanced which suggest that an appropriate potential flow analysis is still a reasonable approximation. As the results in section 4.3 will show, the force due to the virtual mass of the fluid is a significant fraction of the buoyancy force only for the initial portion of the short time scale after the spheres are released when the accelerations are very large. The penetration of viscous effects during this initial phase of large accelerations is confined to a thin layer whose thickness is of order $\sqrt{\nu t}$.

Thus the arguments for using a potential flow analysis for calculating the virtual mass are essentially the same as for high Re potential flow. As the numerical solutions in the next section will shown the virtual mass force is but a few percent of the buoyancy force for the accelerations typical of the long time scale and therefore need not be accurately represented on the time scale during which particle interaction effects are important and the thickness of the viscous layer is large.

In light of the above discussion it is a reasonable approximation to calculate the virtual mass for the entire range of conditions encountered in this study using potential flow theory. This is still a formidable task because of particle interaction effects and has not previously been performed for a finite assemblage of more than two spheres, Milne-Thomson (35). In general, the virtual mass V.M. of an object is given by

$$V.M. = kM' \tag{4.18}$$

where M' is the mass of the fluid displaced by the object and k is a configuration parameter depending on the object shape and the interaction effects that arise from the presence of other boundaries. For a single sphere in an infinite medium $k=\frac{1}{2}$.

One can show using Green's theorem, e.g. Milne-Thomson (35), that when the motion is irrotational the kinetic energy of the fluid can be represented by:

$$T = -\tfrac{1}{2} P \oint \phi \frac{\partial \phi}{\partial n} dA \tag{4.19}$$

where

ϕ = velocity potential
dn = element of normal drawn into the fluid at the element dA of surface

and the integral is performed in a clockwise sense about the boundaries of all objects in the flow field. A steam function ψ_p can be defined in spherical coordinates such that

$$\frac{\partial \phi}{\partial s} = \frac{1}{r \sin\theta} \frac{\partial \psi_p}{\partial n} \quad ; \quad \frac{\partial \phi}{\partial n} = -\frac{1}{r \sin\theta} \frac{\partial \psi_p}{\partial s} \tag{4.20}$$

where $ds = dA/[2\pi r \sin\theta]$ is an arc length. Using the above relationships, the kinetic energy of an irrotational fluid can be defined as follows

$$T = -\pi \rho \oint \frac{\psi}{r \sin\theta} \frac{\partial \psi}{\partial n} ds \tag{4.21}$$

For a single sphere moving with velocity U in an unbounded medium one finds that the total kinetic energy of the solid of mass M plus liquid is:

$$T = \tfrac{1}{2}[M + \tfrac{1}{2}M']U^2 \tag{4.22}$$

The constant k in (4.17) is obtained by equating the time rate of change of kinetic energy of the fluid to the work done by the external force F applied to the moving sphere; i.e.,

$$FU = \frac{dT}{dt} = (M + \tfrac{1}{2}M')U \frac{dU}{dt}$$

$$F = (M + \tfrac{1}{2}M')\frac{dU}{dt} \tag{4.23}$$

The virtual mass is therefore $\frac{1}{2}M'$ and from (4.17) $k=\frac{1}{2}$. By using the method of images, Milne-Thomson (35) has shown that for the case of 2 spheres 1 and 2 having a center-to-center distance of c and radii a and b moving with velocities U and V along their lines of centers, the kinetic energy of the fluid correct to the term in c^{-3} is:

$$T = \tfrac{1}{4}M_1'U^2 + \frac{2\pi a^3 b^3 \rho}{c^3} UV + \tfrac{1}{4}M_2'V^2 \tag{4.24}$$

One now wishes to evaluate the integral (4.21) for the flow kinetic energy for a three sphere system. The governing equation for the stream function in spherical polar coordinates for axially symmetric potential flow is:

$$\frac{\partial^2 \psi_p}{\partial r^2} + \frac{\sin\theta}{r^2} \frac{\partial}{\partial \theta}\left[\frac{1}{\sin\theta} \frac{\partial \psi_p}{\partial \theta}\right] = 0 \tag{4.25}$$

The general solution to (4.25) is of the form:

$$\psi_p = \sum_{n=2}^{\infty} B_n r^{-n+1} I_n(\mu) \tag{4.26}$$

Following a similar line of development to that presented in Chapter 2 for flow past multiple spheres and applied in the previous subsection for the viscous flow along the line of centers of three spheres it can be shown that the solution for the axisymmetric potential flow for the three sphere system is

$$\psi_p = \sum_{j=1}^{3} \sum_{n=2}^{\infty} B_{nj} r_j^{-n+1} I_n(\mu_j) \tag{4.27}$$

where the r_j and Θ_j coordinates are shown in Figure 4.2. Choosing as a reference a stationary fluid at infinity, the boundary conditions become

$$r_j = a\,; \quad V_{rj} = U_j \cos\theta_j = -\frac{1}{r_j^2 \sin\theta_j} \frac{\partial \psi_p}{\partial \theta_j} \tag{4.28}$$

Using the following relationships:

$$dn = dr\,; \quad ds_j = \frac{a}{\sin\theta_j} d\cos\theta_j$$

it can be shown that the contribution to the kinetic energy integral (4.21) from each sphere is

$$T_j = \pi\rho \int_0^{\pi} \frac{a\,\psi_p}{r_j \sin\theta_j} \frac{\partial \psi_p}{\partial r_j} d\theta_j \tag{4.29}$$

Substituting for ψ_p in (4.29) from (4.27) yields

$$T_k = -\pi \rho \frac{a}{r_k} \int_0^{\pi} \frac{1}{\sin^2\theta_k} \sum_{j=1}^{3} \sum_{n=2}^{\infty} \left\{ \left[r_j^{-n+1} I_n(\beta_j) B_{nj} \right] \times \right.$$

$$\left\langle \left[(-n+1) r_j^{-n} I_n(\beta_j) B_{nj} \frac{\partial r_j}{\partial r_k} \right] - \right.$$

$$\left. \left. \left[r_j^{-n+1} P_{n-1}(\beta_j) B_{nj} \frac{\partial \beta_j}{\partial r_k} \right] \right\rangle \right\} d\theta_j \qquad (4.30)$$

To evaluate (4.30) one truncates the infinite series solution (4.27) in the same manner as the viscous flow solution (4.10). One anticipates an even faster convergence of the solution procedure because of the reduced order of the equation than for slow viscous flow. In the latter case a maximum error of 2.5% was obtained in the computed drag coefficient for the most severe case of two spheres touching by taking only the leading term of the infinite series solution. With this in mind only the lowest order approximation to (4.30) will be obtained by retaining only the first multipole (n=2) in the series solution (4.26) for ψ_p . Even with the help of this truncation procedure the integration of (4.30) presents major difficulties due to the complicated variation of r_j when points along the boundary of one sphere are given in terms of a position vector measured from an origin that is at the center of another sphere.

A further simplifying approximation is therefore introduced by replacing r_j in the denominators of each term in the expression for T_k when $j \neq k$ by the distance between the sphere centers and when $j=k$ letting $r_j=a$. The justification for this approximation is the fact that the occurrence of r_j in the denominator of any term represents an average effect of sphere spacing taken at all points along the boundary

of the test sphere. As the spacing increases; i.e. $c \gg a$ and $d \gg a$, the first order effects of sphere spacing will essentially become constant over the entire surface of the test sphere.

Utilizing the above approximation procedures and carrying out the integration indicated by (4.30) yields the following expression for T_k.

$$T_k = -\pi\rho\left[\frac{B_{2,k}^2}{3a^3} + \frac{B_{2,k}B_{2,k-1}}{96c^5} - \frac{B_{2,k}B_{2,k-1}}{12c^3} + \frac{B_{2,k}B_{2,k-2}}{96d^5} - \frac{B_{2,k}B_{2,k-2}}{12d^3} + \frac{B_{2,k}B_{2,k-1}}{24c^3} + \frac{B_{2,k-1}^2}{768c^8} - \frac{B_{2,k-1}^2}{96c^6} + \frac{B_{2,k-1}B_{2,k-2}}{768c^5d^5} - \frac{B_{2,k-1}B_{2,k-2}}{96c^3d^3} + \frac{B_{2,k-2}B_{2,k}}{24d^3} + \frac{B_{2,k-2}B_{2,k-1}}{768c^5d^3} - \frac{B_{2,k-2}B_{2,k-1}}{96d^3c^3} + \frac{B_{2,k-2}^2}{768d^8} - \frac{B_{2,k-2}^2}{96d^6}\right] \tag{4.31}$$

where a rotating index notation has been used; i.e. $1 \to 2 \to 3 \to 1 \to \ldots$, e.g. for k=1, k-1=3 and k-2=2. Also, c represents the spacing between spheres k and k-1 and d represents the spacing between spheres k and k-2. The first term in (4.31) represents the result for a single sphere translating at velocity U, that is $\frac{\pi\rho}{3a^3}B_{2,k}^2 = \frac{1}{4}M'U_k^2$. One also notes that when $c \ll d$ and terms smaller than c^{-3} are dropped (4.31) reduces to the two sphere result obtained previously by Milne-Thomson.

From the definition (4.17)

$$T_j = \tfrac{1}{2}(k_j M_j')U_j^2 \tag{4.32}$$

hence

$$k_j = \frac{2T_j}{M_j'U_j^2} = \frac{3T_j}{2\pi\rho a_j^3 U_j^2} \tag{4.33}$$

For the three sphere problem under consideration, the radii (a_j) of all spheres are equal and have been normalized. The $B_{2,j}$ constants occurring

in equation (4.31) have been evaluated using (4.26) satisfying the boundary condition at five points on the generating arc of each sphere.

The values of k_3 have been determined from (4.33) and (4.31) over a range of two spacing parameters

$$1 \leq b \leq 8; \quad 1 \leq c \leq 8.$$

and are plotted in Figure 4.4 for the case where all three spheres have the same velocity. This figure indicates that the maximum deviation from the single sphere value k=½ occurs as would be expected when the three spheres are touching. As the distance between spheres 3 and 2 increases, k_3 rapidly asymptotes to the single sphere value of ½. The greatest deviation exhibited by k_3 from the value of ½ is approximately 9%. This deviation occurs only when the two spheres (3 and 2) are touching and drops off rapidly to approximately 1½% when these spheres are two diameters apart. This exercise demonstrates that in a three sphere system, particle interaction effects influence the virtual mass associated with each sphere to a relatively minor extent -- even when the spheres are close together. Since, it will be demonstrated in the next section, that the forces due to the virtual mass effects are either very small due to small accelerations or are significant only for very short periods of time (except perhaps for the Re=10 cases), the values of k_j used were considered to be constant and equal to ½. The error introduced by this assumption should be small while the assumption itself allows computing times to be reduced substantially.

E. BASSET FORCE F_B

The Basset force exerted on a sphere moving with an arbitrary velocity U(t) can be constructed as a superposition integral in which the unit velocity impulsive motion of the sphere is treated as

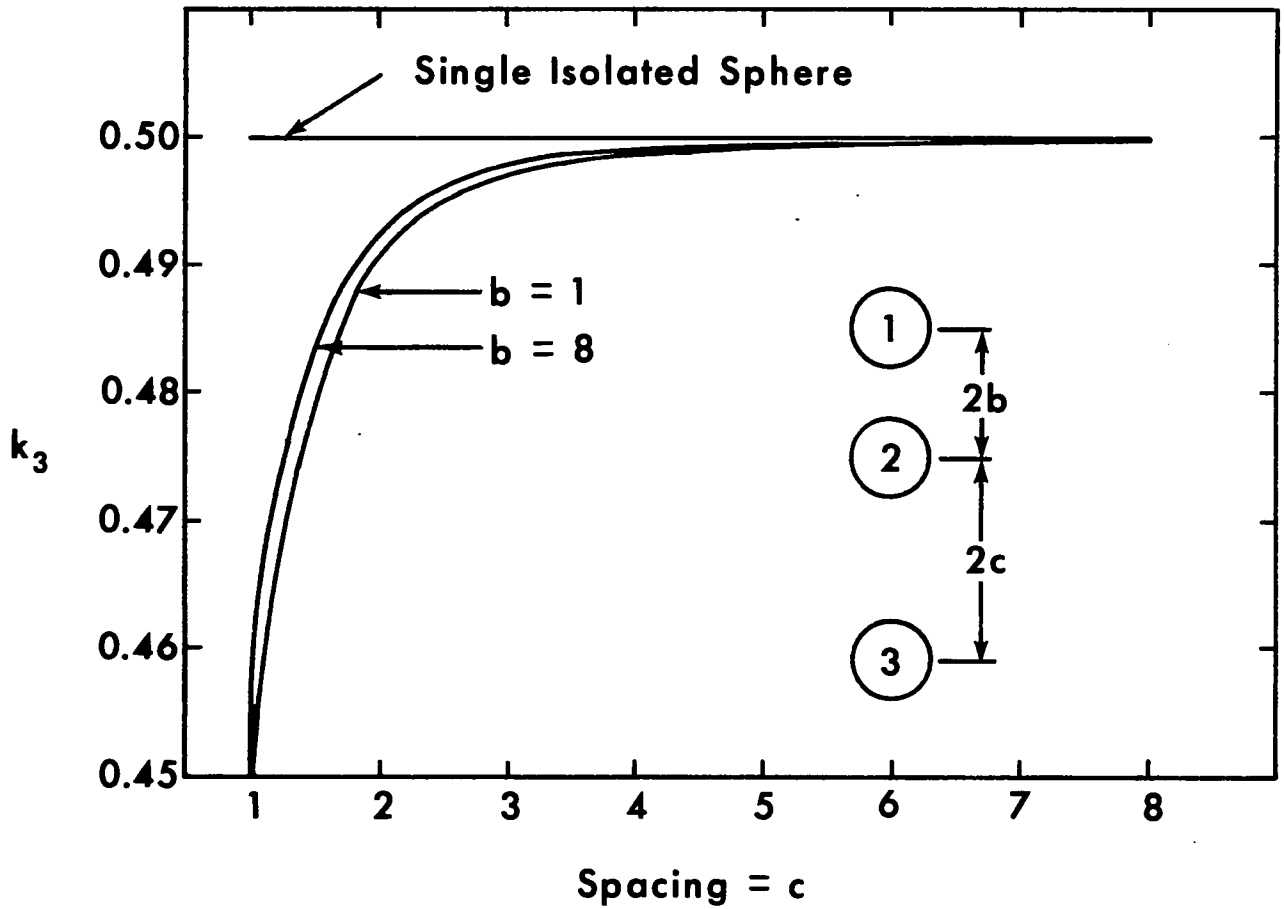

Figure 4.4 - DEVIATION IN VIRTUAL MASS PARAMETER k_3 VS. SYSTEM GEOMETRY

the basic solution. A precise treatment of this force for a multi-sphere problem would require that this basic unit solution takes into account the boundaries of the other spheres. However, an examination of the behavior of the unit solution for a single sphere shows that the Basset force is negligible on the long time scale and a small fraction of the total force over most of the short time scale. The accuracy obtained by considering sphere interaction effects is therefore unwarranted and we shall assume that the unit solution is sufficiently well approximated by the unit solution for a single sphere. Thus, we approximate F_{Bj} by the analogous expression to that given in (4.6).

$$F_{Bj} = 6\pi\mu a^2 \frac{1}{\sqrt{\pi\nu}} \int_0^t \frac{dU_j}{d\tau} \frac{d\tau}{\sqrt{t-\tau}} \tag{4.34}$$

The Basset force is a transient phenomenon associated with the diffusion of vorticity away from solid boundaries. In the basic solution each segment of solid boundary is treated locally as a Rayleigh problem for the impulsive motion of a flat plate. Unless the boundary continues to accelerate and generate vorticity the Basset force will decay as $\frac{1}{\sqrt{t}}$ on the short time scale, the total amount of vorticity being conserved but redistributed throughout the flow field. For continuous, as opposed to impulsive, accelerations the Basset force is a measure of the departure of the wall shear stress from its steady state Stokes value.

Further insight into the physical significance of this force can be gained by analogy with a situation involving unsteady heat conduction in a finite incompressible medium. Consider the boundary plane of the medium to be x=0. The temperature T on the plane x=0 is a given function of time; i.e.,

$$T = T_0(t) \text{ for } x=0 \; ; \quad T=0 \text{ for } -\infty < t \leq 0$$

The heat flux $q=-k\frac{\partial T}{\partial x}$ through the boundary plane x=0 is found to be, see Landau and Lifshitz (33):

$$q(t) = \frac{k}{\sqrt{\pi\alpha}} \int_{-\infty}^{t} \frac{dT_0(\tau)}{d\tau} \frac{d\tau}{\sqrt{t-\tau}} \tag{4.35}$$

where:

k = thermal conductivity

$\alpha = \frac{k}{\rho c_p}$ = thermal diffusivity

It can be seen that (4.35) is very similar to (4.34). Equation (4.35) describes the effect of time on the diffusion of heat from a prescribed boundary having a time dependent temperature T_0 (t). By analogy, equation (4.34) for the Basset force is representative of a force resulting from the effects of time on the diffusion of vorticity away from a boundary having a time dependent velocity U(t). A better feeling for the effects of different types of acceleration on the Basset force can be obtained by solving a few elementary problems.

Consider a sphere which at time t=0 begins to move with a uniform acceleration $U=\alpha t$. The Basset force resulting from this type of motion would be:

$$F_B = 12\pi\mu a^2 \sqrt{\frac{t}{\pi\nu}} \tag{4.36}$$

It can be seen for this case that as time increases the Basset force will increase as $t^{\frac{1}{2}}$ and will become very large for large time. This is due to the fact that the sphere is accelerating all the time and therefore generating ever increasing amounts of vorticity at the surface which must diffuse into the far flow field.

The second situation to be considered is that of a sphere brought instantaneously into uniform motion; i.e.,

$$U=0 \text{ for } t<0 \; ; \quad U=U_0 \text{ for } t>0$$

$\frac{dU}{dt}$ is therefore represented by the Dirac delta function $\delta(t)$ and the Basset force for this case becomes:

$$F_B = 6\pi\mu a^2 U_0 \frac{1}{\sqrt{\pi\nu t}} \tag{4.37}$$

In this instance, the force F_B varies as $t^{-\frac{1}{2}}$. When t=0 the force is infinitely large as a large amount of vorticity has been generated but has had no time to diffuse into the fluid. The relative magnitude and therefore the importance of the Basset force will be examined in the following sections.

4.3 EQUATIONS OF MOTION FOR THREE SPHERES

Based on the discussions presented in section 4.2, the equations of motion for any sphere j in the three sphere chain can be represented using equations (4.5), (4.6), (4.16) as:

$$\rho_s \frac{dU_j}{dt} = (\rho_s - \rho) g - \frac{9\mu}{2a^2} U_j \lambda_j f(Re_j) - \tfrac{1}{2}\rho \frac{dU_j}{dt} - \frac{9\mu}{2a}\sqrt{\frac{1}{\pi\nu}} \int_0^t \frac{dU_j}{d\tau} \frac{d\tau}{\sqrt{t-\tau}} \quad \text{for } j = 1,2,3 \tag{4.38}$$

where Re_j is based on the instantaneous velocity. In accord with the previous analysis sphere interaction effects in the three equations (4.38) are described by the λ_j factors applied to each Stokes drag term whereas both the virtual mass and Basset forces are approximated by their single sphere expressions.

In order to determine the relative magnitude of each of the terms appearing in (4.38) all the variables in (4.38) will be made dimensionless by introducing characteristic reference quantities. (The subscript j will be dropped since the analysis is identical for each of

the equations (4.38)). Denoting dimensionless variables by a tilda,

$$\tilde{U} = \frac{U}{U_t} \qquad \tilde{\nu} = \frac{\nu}{U_t a} = \frac{1}{Re_\infty}$$

$$\tilde{t} = \frac{t U_t}{a} \qquad \tilde{g} = \frac{g a^2}{\nu U_t} = \frac{Re_\infty}{Fr^2}$$

$$\tilde{\rho} = \frac{\rho_s}{\rho} \tag{4.39}$$

where the Froude number $F_r = \frac{U_t}{\sqrt{ga}}$ and the characteristic velocity U_t is based on the terminal settling velocity of a single sphere. Applying (4.39) to (4.38) results in

$$Re_\infty \frac{d\tilde{U}}{d\tilde{t}} = \left(1 - 1/\tilde{\rho}\right) \frac{Re_\infty}{Fr^2} - \frac{9\tilde{U}\lambda f(Re)}{\tilde{\rho}} - \frac{Re_\infty}{2\tilde{\rho}} \frac{d\tilde{U}}{d\tilde{t}}$$

$$- \frac{9 Re_\infty^{1/2}}{2\sqrt{\pi}\tilde{\rho}} \int_0^{\tilde{t}} \frac{d\tilde{U}}{d\tilde{\tau}} \frac{d\tilde{\tau}}{\sqrt{\tilde{t}-\tilde{\tau}}} \tag{4.40}$$

where Re in the expression for f (4.17) is a Reynolds Number based on instantaneous velocity; hence $Re = Re_\infty \tilde{U}$.

At first appearance (4.40) seems to depend on three fundamental dimensionless groups Re_∞, $\tilde{\rho}$, and Fr. However, if U_t for a single sphere is evaluated from (4.38) by setting $\frac{dU}{dt}=0$, $\lambda = 1$ and neglecting the Basset force

$$U_t = \frac{2a(\tilde{\rho}-1)g}{9\nu f(Re)} \tag{4.41}$$

Also $Re_\infty = \frac{2aU_t}{\nu}$ and $Fr = \frac{U_t}{\sqrt{ga}}$ thus $Fr = \left[\frac{(\tilde{\rho}-1)Re_\infty}{9f(Re)}\right]^{1/2}$ (4.42)

Equation (4.42) indicates that only two of the three dimensionless groups in (4.40) are independent. Therefore, any one group can be eliminated and it has been decided to retain the Reynolds Number Re_∞ and the density ratio $\tilde{\rho} = \frac{\rho_s}{\rho}$. Introducing the expression (4.42)

for Fr in (4.40) and regrouping terms, one has

$$Re_\infty \left(\tilde{\rho}+\tfrac{1}{2}\right)\frac{d\tilde{U}}{d\tilde{t}} = 9f(Re)(1-\tilde{U}\lambda) - \frac{9Re_\infty^{1/2}}{2\sqrt{\pi}}\int_0^{\tilde{t}} \frac{d\tilde{U}}{d\tilde{\tau}}\,\frac{d\tilde{\tau}}{\sqrt{\tilde{t}-\tilde{\tau}}} \tag{4.43}$$

As expected, one observes from (4.43) that for $Re_\infty \ll 1$ all acceleration terms are small. For higher Re_∞ the Basset force increases as $Re_\infty^{\frac{1}{2}}$ whereas the virtual mass force increases as Re_∞ itself. During the initial portion of the short time scale $\tilde{U}\lambda \ll 1$. Therefore, the Stokes drag term in (4.43) (term containing λ) is unimportant and the gravity forces are balanced principally by the acceleration forces. For larger times the behavior depends on the relative magnitudes of the short, $\tilde{t}_s$, and long, $\tilde{t}_\infty$, time scales. $\tilde{t}_s$ is defined as the time required for a sphere to achieve a prescribed percentage of an initial quasi-steady state settling velocity based on its initial value of λ, whereas $\tilde{t}_\infty$ is defined as a time characteristic of the length of the experiment, that is the time required for the second sphere to overtake and collide with the lead sphere. λ the interaction parameter undergoes changes of O(1) on this long time scale. Thus, one can obtain distinctly different behavior depending on whether λ is slowly or rapidly varying on the time scale during which the acceleration forces are large.

When $\tilde{t}_s \ll \tilde{t}_\infty$ λ can be treated as a constant on the short time scale $\tilde{t}_s$. The quasi-steady settling velocity is determined by the value of λ characteristic of the short time scale. Treated as a two time scale problem the quasi-steady state solution for $\tilde{U}$ as $\tilde{t}_s \to \infty$ for the inner problem, defined by $\tilde{U}_s$ is simply given from (4.43) by:

$$1 - \tilde{U}_s\lambda = 0 \tag{4.44}$$

or $\tilde{U}_s = \frac{1}{\lambda}$. Thus, the gravity-viscous force balance as $\tilde{t} \to \infty$ shows that the terminal settling velocity for an isolated sphere can be simply corrected for sphere interaction effects by using the value of λ based on the initial sphere spacing. An analytical approximation to $\tilde{t}_s$ can be obtained by integrating (4.43) neglecting the Basset force term

$$\tilde{t} = \frac{Re_\infty}{9}\left(\tilde{\rho} + \tfrac{1}{2}\right)\int_0^{\tilde{U}} \frac{d\tilde{U}}{f(1-\tilde{U}\lambda)} \tag{4.45}$$

The integral in (4.45) has a simple evaluation only if $Re_\infty \ll 1$ in which case $f \approx 1$. The solution, approximating λ by its initial value λ_0 which satisfied (4.44) is

$$\tilde{t} = -\frac{Re_\infty}{9\lambda_0}\left(\tilde{\rho} + \tfrac{1}{2}\right) L_n\left(1 - \frac{\tilde{U}}{\tilde{U}_s}\right) \tag{4.46}$$

$\tilde{t}_s$ is defined as the value of $\tilde{t}$ for which $\frac{\tilde{U}}{\tilde{U}_s} = 0.99$ then

$$\tilde{t}_s = 0.512\ \frac{Re_\infty}{\lambda_0}\left(\tilde{\rho} + \tfrac{1}{2}\right) \tag{4.47}$$

When $Re_\infty \gtrsim O(1)$ $\tilde{t}_s$ can still be obtained from (4.45) except that the integral, whose upper limit is now 0.99 U_s, must be evaluated numerically unless some simplifying expression for f (Re) is used. When $\tilde{t}_s$ is not small compared to $\tilde{t}_\infty$ λ cannot be treated as a constant on the short time scale and a quasi-steady state solution in the sense of (4.44) does not exist. One can, nevertheless, define a $\tilde{t}_s$ based on the initial value of λ and use this value of $\tilde{t}_s$ as a measure of the dimensionless time in which large accelerations will occur.

An approximate value for the long time scale, the time to collision, can be obtained by dividing the initial spacing 2d between the

two outer spheres by some characteristic relative velocity between the lead and middle spheres. A qualitative measure of the latter velocity can be had by taking the difference between the terminal settling velocity U_t of the isolated sphere and the initial quasi-steady state settling velocity U_s defined by equation (4.44). Thus,

$$\tilde{t}_\infty = \frac{2d}{U_s - U_t}\left(\frac{U_t}{a}\right) = \left(\frac{2d}{a}\right)\left(\frac{\lambda_o}{1-\lambda_o}\right) \tag{4.48}$$

From (4.45) and (4.48) a suitable measure of the ratio of the short to long time scale is given by

$$\frac{\tilde{t}_s}{\tilde{t}_\infty} = Re_\infty\left(\tilde{\rho}+\tfrac{1}{2}\right)\left(\frac{a}{2d}\right)\left(\frac{1-\lambda_o}{9\lambda_o^2}\right)\int_0^{.99\tilde{U}_s}\frac{d\tilde{U}}{f\left(\frac{1}{\lambda_o}-\tilde{U}\right)} \tag{4.49}$$

When $Re_\infty \ll 1$ the integral in (4.49) has the value 4.605. The initial conditions for the numerical experiments conducted in the present study were $\frac{2d}{a} = 42$ and $\tilde{U}_j = 0$. For spheres 1 and 2 initially touching this yields a value for λ_o for sphere 2 of 0.645. Some estimates of $\frac{\tilde{t}_s}{\tilde{t}_\infty}$ based on (4.49) for various values of Re_∞ and $\tilde{\rho}$ are given in Table 4.1.

Table 4.1

Values of $\frac{\tilde{t}_s}{\tilde{t}_\infty}$ for Different $\tilde{\rho}$ and Re_∞

Re_∞	1.01	1.10	2.00	5.00	10.00
0.01	0.00016	0.00017	0.00026	0.00057	0.00109
0.10	0.00156	0.00165	0.00258	0.00567	0.01082
0.50	0.00748	0.00793	0.01239	0.02725	0.05203
1.00	0.01417	0.01501	0.02346	0.05160	0.09852
5.00	0.05099	0.05403	0.08443	0.18574	0.35459
10.00	0.11146	0.11810	0.18454	0.40598	0.77505

These estimates are a valuable guide in choosing the range of Re_∞ and $\tilde{\rho}$ for which the experiments were run. In essence, one wishes to examine the transition in behavior as $\tilde{t}_0/\tilde{t}_\infty$ increases from values approaching zero to values approaching unity.

In choosing a technique for integrating (4.43) for each sphere it must be kept in mind that (4.43) are non-linear due to the Re dependence of the Stokes drag force. Therefore, lower order numerical integration schemes offer a high risk of instability due to local truncation errors. Of the fourth order procedures available, the Runge-Kutta (R-K) and Predictor-Corrector (P-C) techniques are most widely used due to their stability and accuracy, see Ralston (41). As the evaluation of the right hand sides of equations (4.43) is quite tedious, Hamming's modification of Milne's P-C method was chosen instead of an equivalent fourth order R-K technique, see Ralston and Wilf (42). This choice is based on the fact that the P-C method requires evaluation of the right hand side of (4.43) twice for each increment whereas a R-K technique requires each right hand side to be evaluated four times for each increment. Use of the P-C method will therefore halve the required computing time. Also P-C methods allow for a simple estimation of the per-step error which is not possible when using a R-K method. Therefore a less conservative choice of step size can be made using the P-C method while still ensuring stability of the solution. On the other hand, the P-C technique is not self-starting and therefore a fourth order R-K technique was employed to start the integration procedure. The P-C technique used allowed for eleven halvings of the initially chosen step size in order to enable a specified maximum error per step to be met.

Finally, it should be pointed out that numerical experiments at low Re and $\tilde{\rho} = 1$ consume excessive amounts of computing time since $\tilde{t}_s \ll \tilde{t}_\infty$ and that at each step, new values of λ_j need to be determined. If the no-slip boundary conditions are to be satisfied at 5 points on each generating arc, this would require that 36 simultaneous equations be solved to accurately determine λ_j at as many as 1,000 to 20,000 steps. Therefore, in order to conserve computational time, the λ_j were not evaluated at each step for the low Re low $\tilde{\rho}$ experiments. Since the spacing parameters b and c as well as changes in U_j per step are extremely small in these experiments after the initial period $\tilde{t}_s$ of rapid variation, the λ_j were evaluated at only every P steps between $\tilde{t}_s$ and the end of the experiment where P is an arbitrarily chosen integer. However, if it were found that λ_j varied by more than 0.1% in P steps, the value of P was halved and the computations repeated. If on the other hand it was found that λ_j varied by less than 0.01% in P steps, the value of P was doubled before proceding with the computation.

4.4 RESULTS

Before presenting the results of the numerical experiments conducted, the general conditions for these experiments will be outlined. Three values of Re_∞ were chosen (Re_∞ =0.1, 1.0, and 10.0). Each of these Reynolds Numbers was examined at two values of $\tilde{\rho}$ ($\tilde{\rho}$ =1.1 and 5.0) resulting in six experiments in all. All of the experiments were started with the same initial conditions: at t=0; U_j=0; b_o=1.0; c_o=20.0.

Each of the above six experiments was terminated when the following condition was achieved: $t=t_\infty$ when $c=c_\infty$ =1.0. The condition c_∞ =1.0 was chosen because when sphere 2 touches sphere 3 the equations of

motion used do not contain a term to describe the impact force and therefore do not apply to the system when c=1.0.

Table 4.2 presents a listing of the basic parameters and final values of some of the more important variables determined at the conclusion of each experiment. It is interesting to note that one of the effects of increasing Re was to decrease the spacing (b_∞) between spheres 1 and 2 at the end of the experiment. This result can be explained by the fact that as the Reynolds Number increases the forces due to particle acceleration become large compared to the drag forces. The major effect produced by decreasing $\tilde{\rho}$ was to substantially decrease the magnitude of all forces acting on each sphere thereby decreasing their relative velocities and substantially increasing the total time of the experiments.

The two time scales that exist in this quasi-steady state problem have been described and defined in previous sections. The initial unsteady portion t_s of each experiment as defined in section 4.3 is only an approximate value for $Re \geq 1$ as it is based on λ_o which depends only on the initial sphere spacing. For this reason a second experimental short time parameter t_s^* will be defined to include the effect of variations in λ during the short time scale.

Thus t_s^* is defined as the time required for the force due to the virtual mass of sphere 1 to decrease to less than 1% of the buoyancy force. In non-dimensional form:

$$\tilde{t}_s^* = \frac{U_t t_s^*}{a} \tag{4.50}$$

Similarly, an experimental long time scale is defined t_∞^* as the time

Table 4.2

Parameters and Final Values for the Six Numerical Experiments

Re_∞		$\tilde{\rho} = 5.0$	$\tilde{\rho} = 1.1$
	F_r = Froude No. = $\frac{U_t}{(ga)^{\frac{1}{2}}}$	0.2098	0.0332
	U_t = Terminal Velocity of 1 Sphere, ft/sec.	1.1883	0.1879
	B = Buoyancy Force = $(1-1/\tilde{\rho})$ g, ft/sec^2	25.600	2.9091
0.1	t_∞ = Time to end of Experiment, secs.	137.11	1005.8
	b_∞ = Spacing at end of Experiment, ft.	13.360	19.297
	X_∞ = Distance moved by Sphere 3, ft.	217.53	258.06
	Number of time steps used	9987	22,292
	F_r = Froude No. = $\frac{U_t}{(ga)^{\frac{1}{2}}}$	0.6395	0.1011
	U_t = Terminal Velocity of 1 Sphere, ft/sec.	3.6193	0.5723
	B = Buoyancy Force = $(1-1/\tilde{\rho})$ g, ft/sec^2	25.600	2.9091
1.0	t_∞ = Time to end of Experiment, secs.	43.09	303.14
	b_∞ = Spacing at end of Experiment, ft.	7.4475	10.719
	X_∞ = Distance moved by Sphere 3, ft.	191.44	218.12
	Number of time steps used	1490	2580
	F_r = Froude No. = $\frac{U_t}{(ga)^{\frac{1}{2}}}$	1.6500	0.2608
	U_t = Terminal Velocity of 1 Sphere, ft/sec.	9.3426	1.4772
	B = Buoyancy Force = $(1-1/\tilde{\rho})$ g, ft/sec^2	25.600	2.9091
10.0	t_∞ = Time to end of Experiment, secs.	9.9874	69.000
	b_∞ = Spacing at end of Experiment, ft.	1.8977	3.2146
	X_∞ = Distance moved by Sphere 3, ft.	105.00	130.67
	Number of time steps used	250	350

taken for impact between spheres 2 and 3 to be achieved; i.e.

$$\tilde{t}^*_\infty = \frac{U_t\, t^*_\infty}{a} \tag{4.51}$$

The short and long time scales for each of the six experiments are presented in Table 4.3. It is interesting to note that as Re_∞ increases, the ratio $\tilde{t}_s/\tilde{t}_\infty$ or $\tilde{t}^*_s/\tilde{t}^*_\infty$ increases from a negligibly small fraction at Re=0.1

Table 4.3

Various Time Scales for the Six Experiments

	$\tilde{\rho}$ = 5.0			$\tilde{\rho}$ = 1.1		
Re	0.1	1.0	10.0	0.1	1.0	10.0
t^*_s secs	0.335	0.938	3.275	0.613	1.667	5.730
t^*_∞ secs	137.114	43.092	9.987	1005.854	303.135	69.000
$\tilde{t}^*_s$	0.403	3.393	30.581	0.115	0.954	8.452
$\tilde{t}^*_\infty$	163.002	156.104	93.261	189.100	173.451	101.938
$\tilde{t}_s/\tilde{t}_\infty$	0.005	0.051	0.406	0.0016	0.015	0.118
$\tilde{t}^*_s/\tilde{t}^*_\infty$	0.002	0.021	0.328	0.0006	0.005	0.083

to a significantly large fraction at Re=10.0, especially as the density ratio $\tilde{\rho}$ is increased. It can be seen from Table 4.3 that even at moderately low Re; i.e., O(10) and $\tilde{\rho}$ of O(10), the short time scale $\tilde{t}_s$ or $\tilde{t}^*_s$ becomes of the same order as the long time scale $\tilde{t}_\infty$ or $\tilde{t}^*_\infty$. Figures 4.5a - 4.5f present curves of $\frac{U_k}{U_t}$ versus t/t_∞ for each experiment. The effects of Re and $\tilde{\rho}$ on $\tilde{t}^*_s$ described above are clearly shown in these six figures. In general, Figures 4.5a - 4.5f indicate similar trends in the velocity -- time profiles for each of the three spheres. After the initial unsteady period, spheres 1 and 2 possess

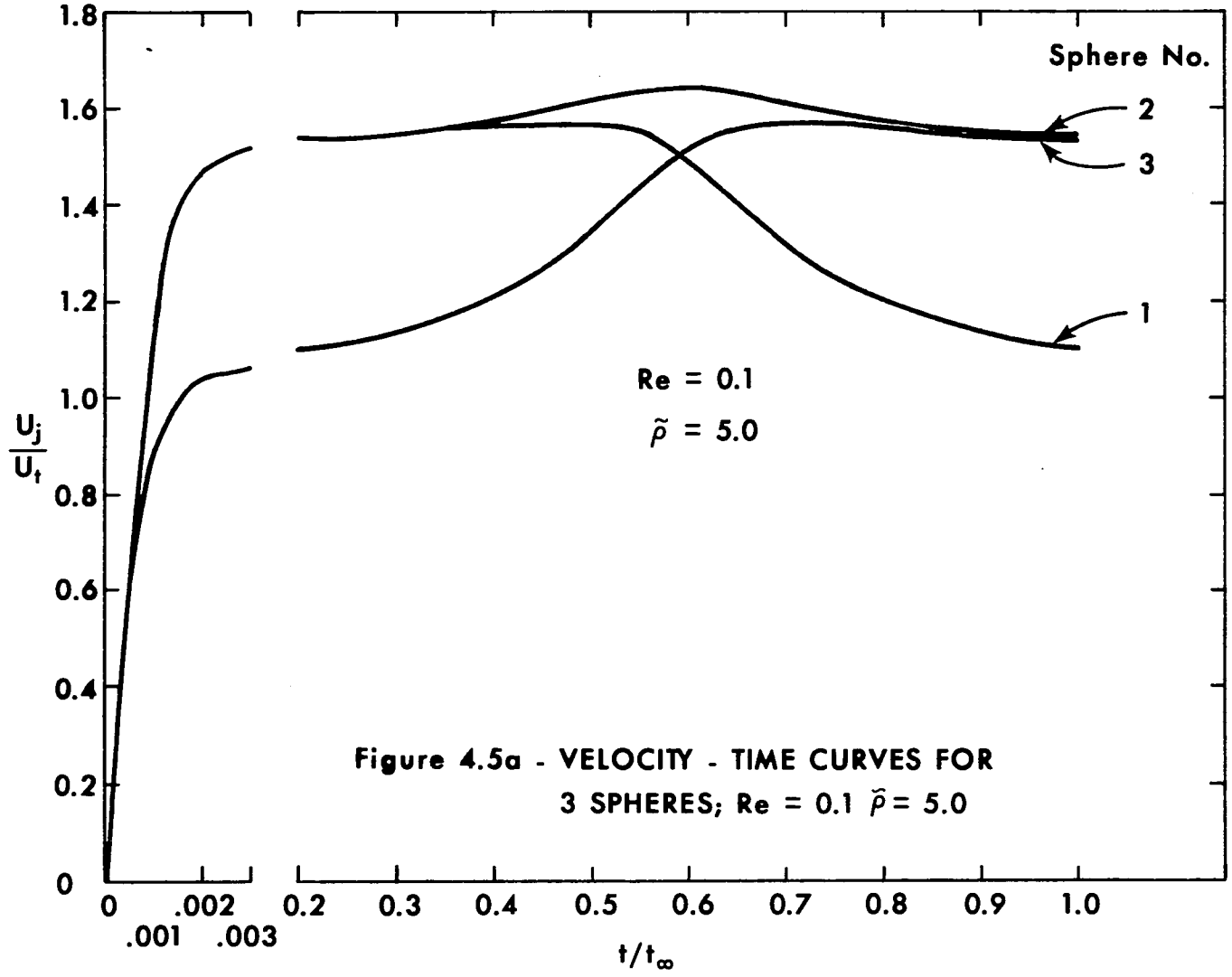

Figure 4.5a - VELOCITY - TIME CURVES FOR 3 SPHERES; Re = 0.1 $\tilde{\rho}$ = 5.0

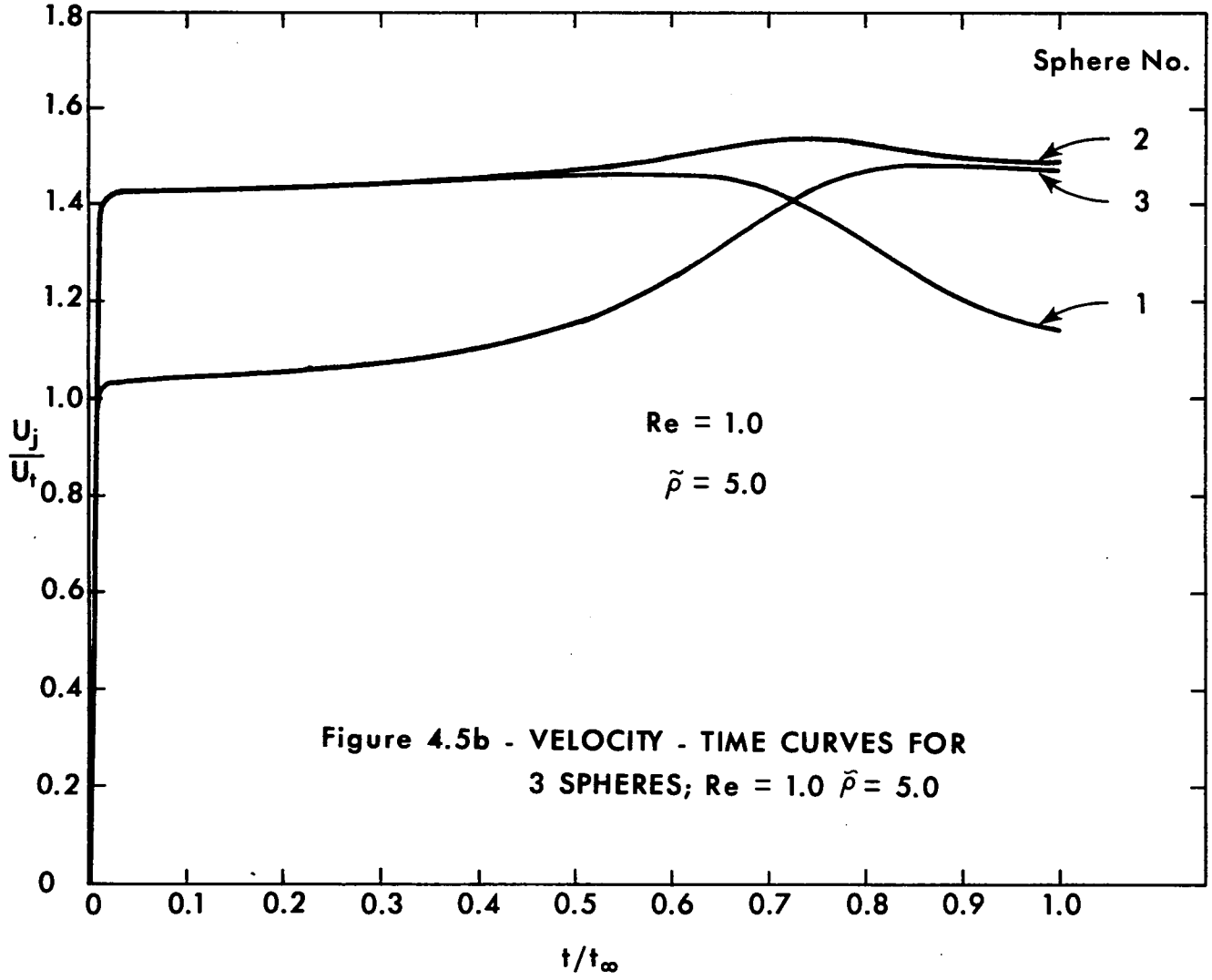

Figure 4.5b - VELOCITY - TIME CURVES FOR 3 SPHERES; Re = 1.0 $\tilde{\rho}$ = 5.0

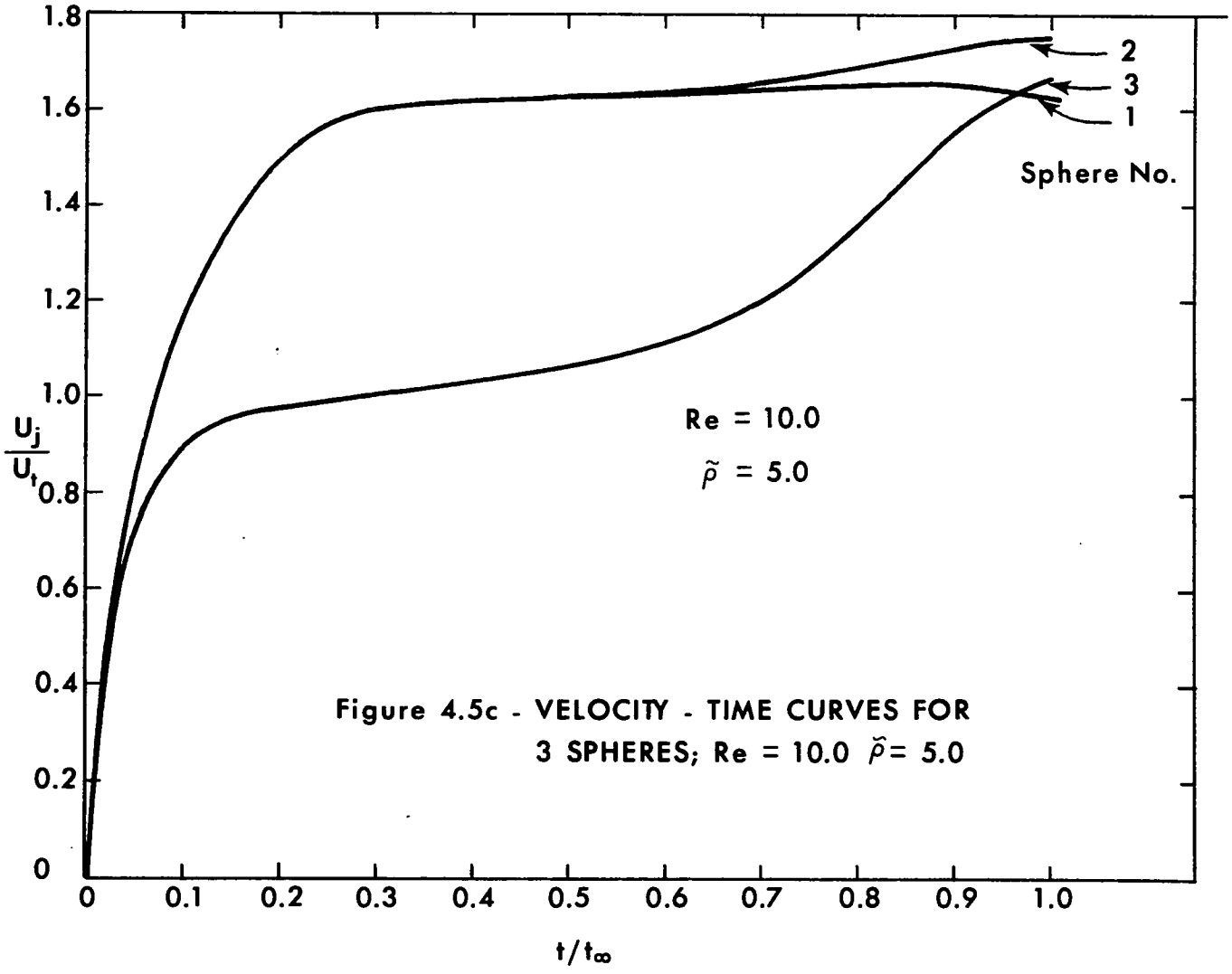

Figure 4.5c - VELOCITY - TIME CURVES FOR 3 SPHERES; Re = 10.0 $\tilde{\rho}$= 5.0

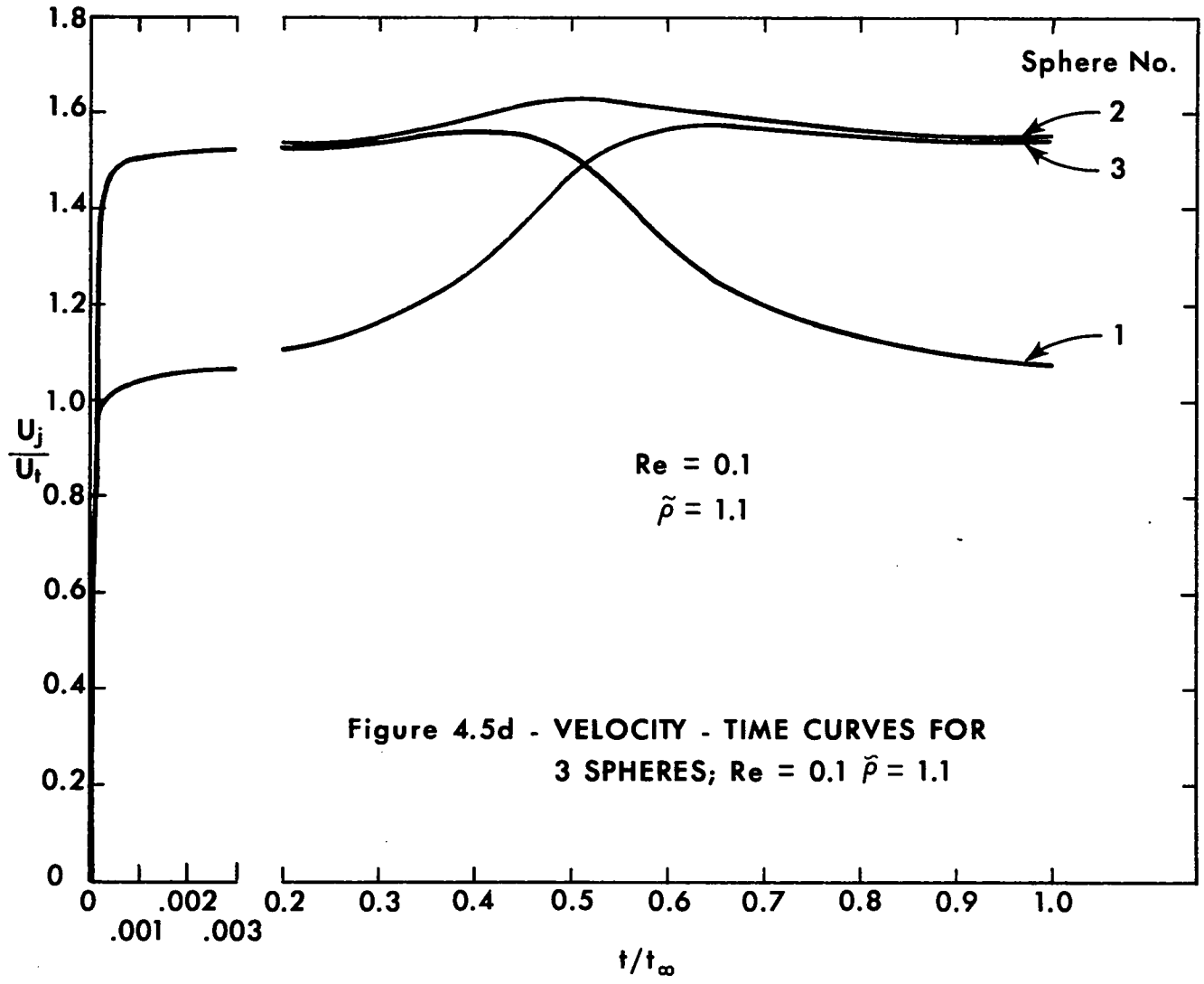

Figure 4.5d - VELOCITY - TIME CURVES FOR 3 SPHERES; Re = 0.1 $\tilde{\rho}$ = 1.1

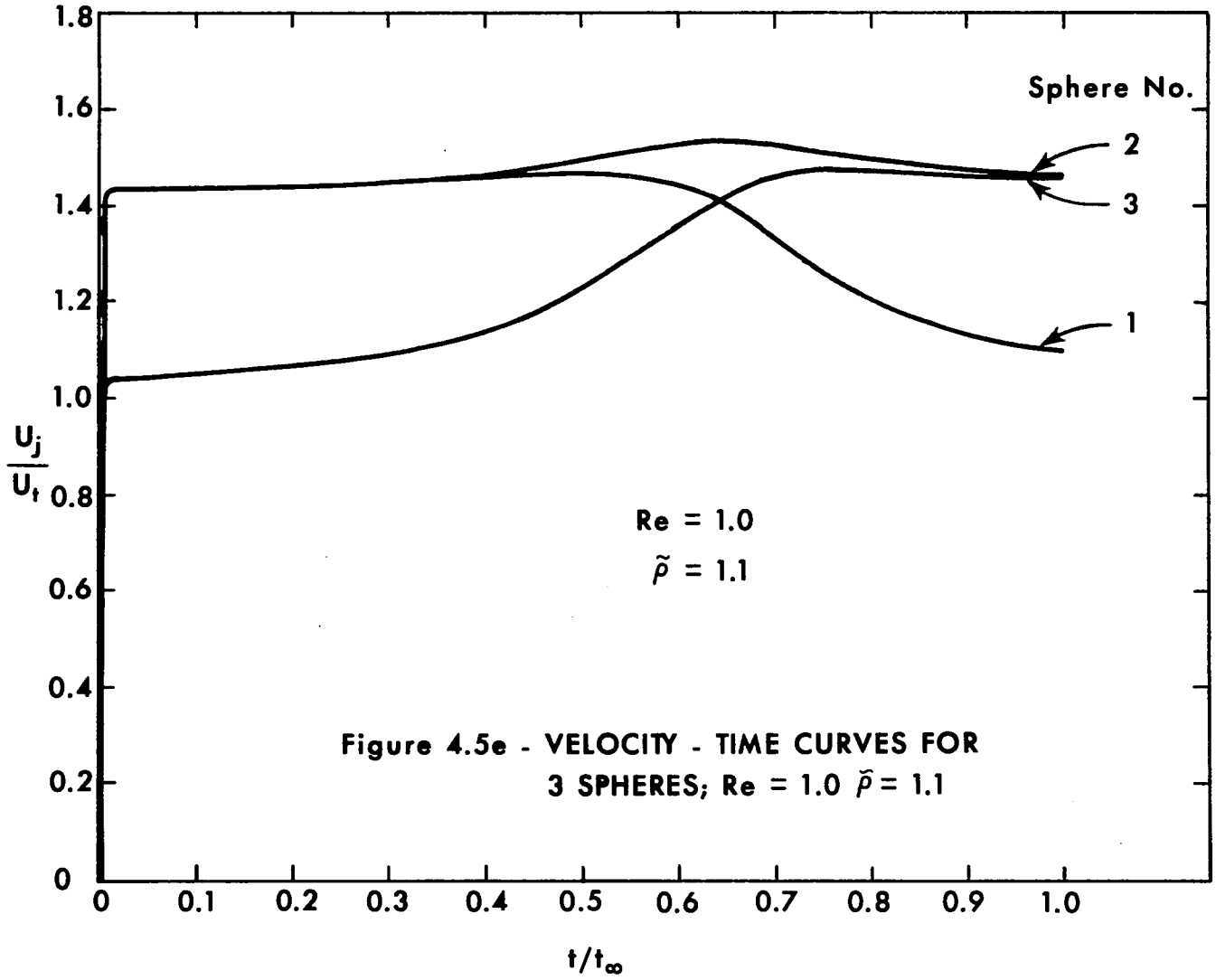

Figure 4.5e - VELOCITY - TIME CURVES FOR 3 SPHERES; Re = 1.0 $\tilde{\rho}$ = 1.1

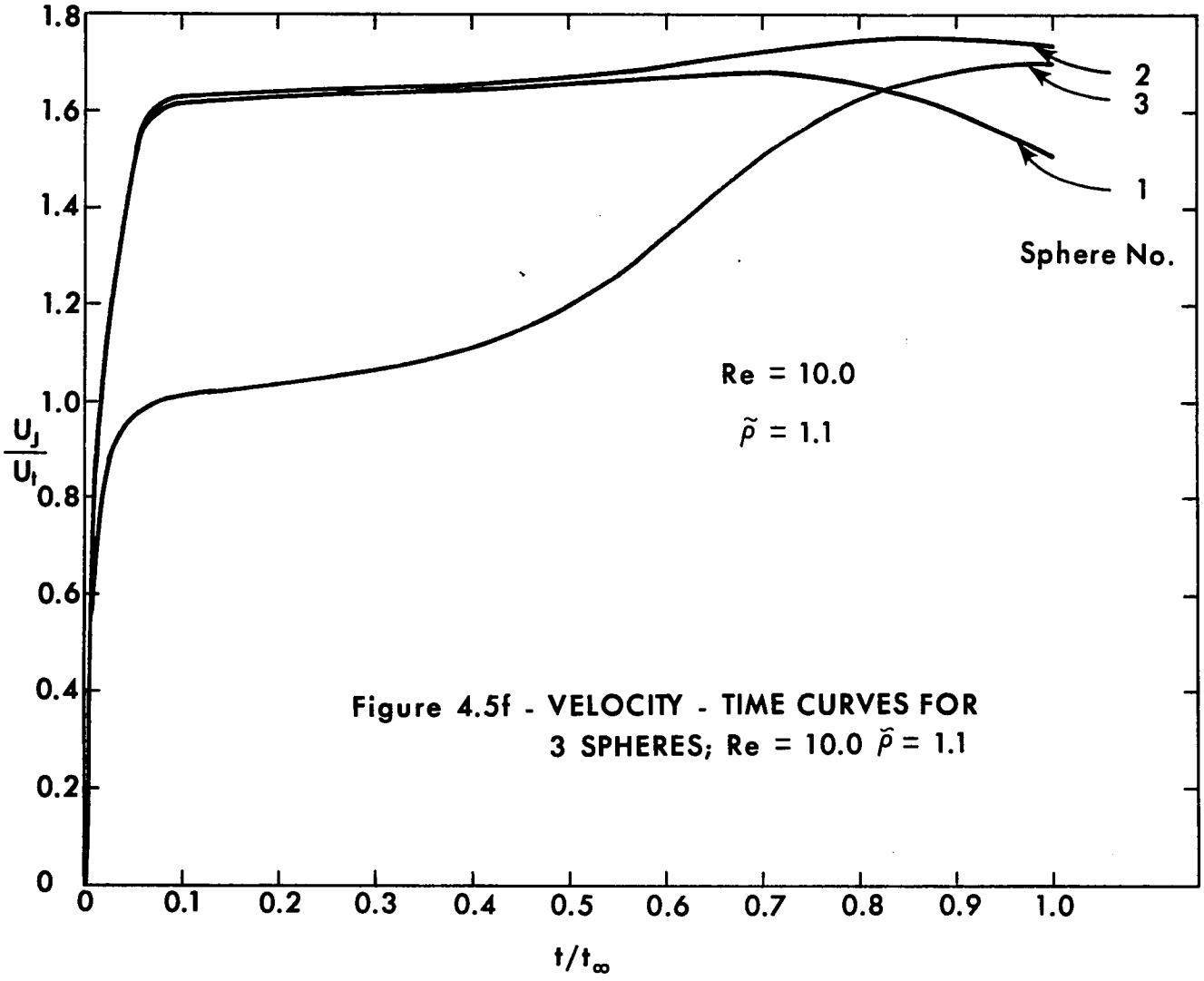

Figure 4.5f - VELOCITY - TIME CURVES FOR 3 SPHERES; Re = 10.0 $\tilde{\rho}$ = 1.1

essentially the same velocities which are between 50% and 70% greater than the velocity of sphere 3. The velocity of sphere 2 does not vary greatly from this point to the end of the experiment. Sphere 3, however, begins to accelerate due to the reduction in its drag created by the approach of the doublet consisting of spheres 1 and 2. At the same time, sphere 1 begins to decelerate due to the decrease in the drag reduction effect produced by sphere 2 separating and moving away from sphere 1. At some point in time, spheres 1 and 3 will have the same velocity indicating that the spacing parameters b and c are equal. From that point on the velocities of spheres 2 and 3 will approach each other while that of sphere 1 will decrease and asymptote to a value of $\frac{U_1}{U_t}$ =1.0; i.e., the terminal settling velocity of a single isolated sphere.

Figure 4.6 shows particle trajectories as a plot of position X_j versus t/t_∞ for Re=0.1 and Re=10.0 and $\tilde{\rho}$=5.0. Changing $\tilde{\rho}$ from 5.0 to 1.1 results in no noticable change in the particle trajectories.

Certain interesting conclusions concerning the magnitudes of the different forces acting on the three sphere system can be drawn from the data of Tables 4.4 and 4.5. These tables present the magnitudes of the drag force (F_D), the force due to virtual mass effects ($F_{V.M.}$) and the Basset force (F_B) related to the buoyancy force (B) on each sphere of the three sphere system. Table 4.4 contains data from the three experiments conducted for $\tilde{\rho}$=5.0 and Table 4.5 contains similar data for $\tilde{\rho}$=1.1. It can be seen from these tables that increasing the Reynolds Number decreases the relative contribution of the drag force and increases the importance of the Basset force. Changing Re from 0.1 to 10.0 has the effect of increasing F_B/B from 1% to approximately

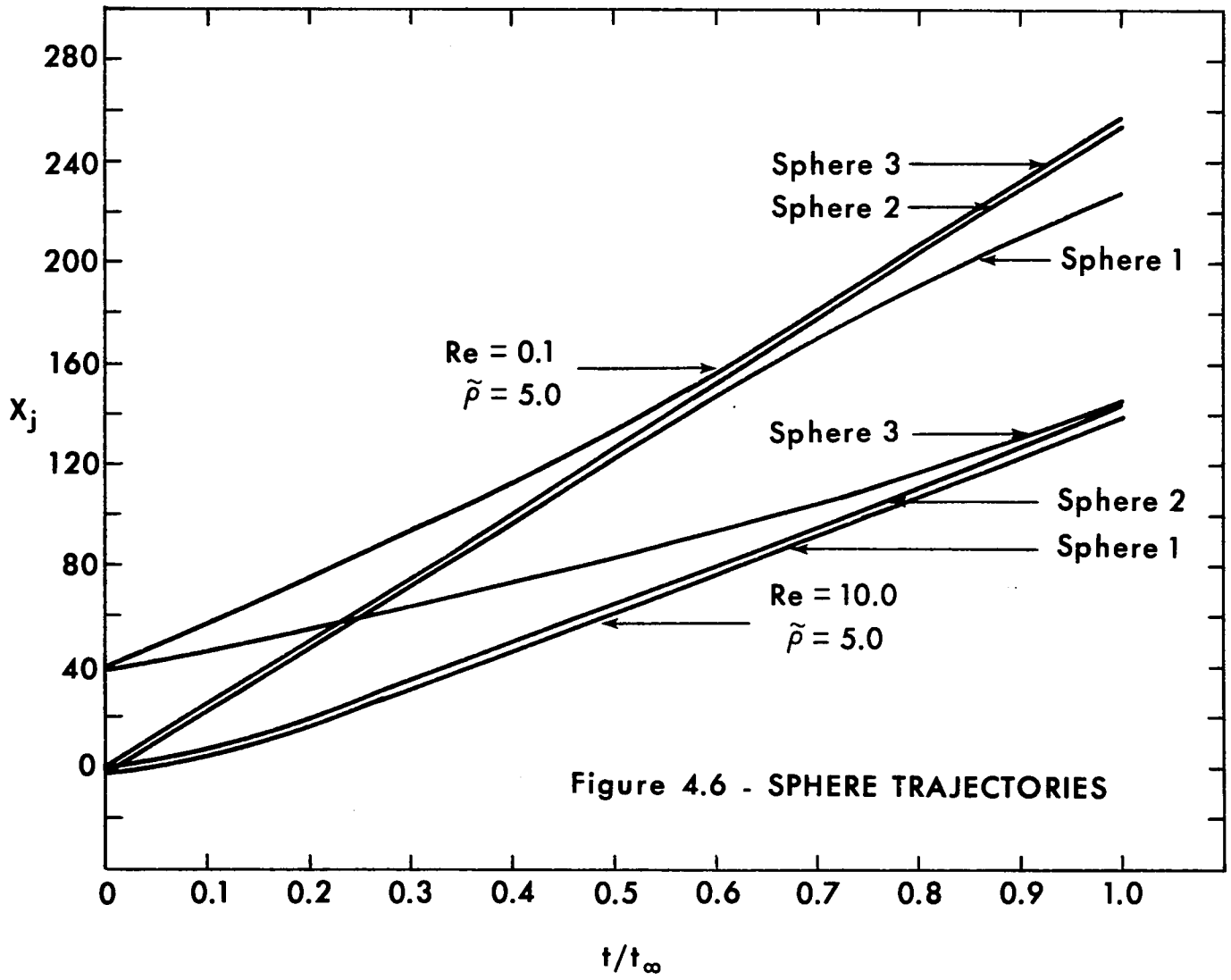

Figure 4.6 - SPHERE TRAJECTORIES

Table 4.4

Forces Acting on 3 Sphere System for $\tilde{\rho} = 5.0$

Re_∞	t/t_∞	F_D/B			$F_{V.M.}/B$			F_B/B		
		Sphere 1	Sphere 2	Sphere 3	Sphere 1	Sphere 2	Sphere 3	Sphere 1	Sphere 2	Sphere 3
0.1	.0005	.71328	.71275	.83610	.27723	.27776	.15629	.00948	.00949	.00761
	.005	.98619	.98716	.99069	.00077	.00020	.00021	.01304	.01304	.00910
	.05	.98811	.98573	.99079	-.00115	.00119	.00005	.01304	.01308	.00916
	.50	.98164	.99150	.98585	.00507	-.00541	.00226	.01347	.01392	.01190
	1.00	.99263	.98384	.98912	-.00009	.00320	-.00312	.00746	.01296	.01399
1.0	.0005	.07887	.07857	.11502	.91767	.91798	.88160	.00345	.00345	.00338
	.005	.58110	.58066	.71537	.39514	.39556	.26448	.02376	.02378	.02015
	.05	.96242	.96241	.97246	.00017	.00015	.00040	.03741	.03744	.02715
	.50	.96176	.95956	.96572	.00001	.00180	.00336	.03823	.03864	.03091
	1.00	.97190	.96525	.95553	-.00310	-.00372	.00205	.02400	.03847	.04242
10.0	.0005	.00492	.00490	.00732	.99408	.99411	.99168	.00099	.00099	.00099
	.005	.05250	.05228	.07705	.93781	.93803	.91339	.00969	.00969	.00956
	.05	.54510	.54456	.68568	.38768	.38817	.25629	.06722	.06727	.05803
	.50	.86171	.86067	.89587	.00234	.00302	.01518	.13595	.13632	.08896
	1.00	.88970	.83717	.76045	-.01452	.00151	.02126	.12482	.16132	.21829

Table 4.5

Forces Acting on 3 Sphere System for $\tilde{\rho} = 1.1$

Re_∞	t/t_∞	F_D/B			$F_{V.M.}/B$			F_B/B		
		Sphere 1	Sphere 2	Sphere 3	Sphere 1	Sphere 2	Sphere 3	Sphere 1	Sphere 2	Sphere 3
0.1	.0005	.95549	.95522	.98151	.03098	.03123	.00899	.01353	.01355	.00951
	.005	.98594	.98604	.98990	.00023	.00010	.00013	.01383	.01386	.00997
	.05	.98537	.98701	.98988	.00071	-.00091	.00008	.01392	.01390	.01004
	.50	.98396	.98258	.98629	.00112	.00216	.00084	.01492	.01526	.01287
	1.00	.99121	.98523	.98367	-.00017	.00081	.00036	.00896	.01396	.01597
1.0	.0005	.27524	.27461	.37851	.71408	.71470	.61156	.01068	.01068	.00994
	.005	.94631	.94618	.97119	.02011	.02020	.00447	.03357	.03361	.02435
	.05	.96476	.96672	.97497	.00112	-.00086	.00026	.03412	.03414	.02477
	.50	.96507	.96397	.96944	.0000	.00045	.00105	.03493	.03558	.02951
	1.00	.97848	.96591	.96290	-.00010	-.00015	.00011	.02162	.03424	.03699
10.0	.0005	.01880	.01871	.02786	.97791	.97800	.96886	.00329	.00329	.00328
	.005	.22988	.22927	.31839	.74094	.74154	.65394	.02918	.02919	.02767
	.05	.79622	.79666	.90558	.09680	.09625	.02486	.10698	.10709	.06957
	.50	.87900	.87742	.89932	.00125	.00204	.01196	.11976	.12053	.08872
	1.00	.91528	.87475	.85335	-.01093	-.00183	.00085	.09565	.12708	.14580

20%. The effects of changing $\tilde{\rho}$ from 5.0 to 1.1 can be seen by comparing data at the same Re between Table 4.4 and Table 4.5. At Re=0.1, decreasing $\tilde{\rho}$ tends to increase the relative importance of the Basset force; i.e., from 1.3% to 1.5%. At Re=10.0, however, decreasing $\tilde{\rho}$ tends to decrease the relative importance of the Basset force from 20% to 14%.

CHAPTER 5

BOUNDARY LAYER FLOW AT INTERMEDIATE REYNOLDS NUMBERS

5.1 INTRODUCTION

One promising approach to modelling flow problems in multiparticle systems such as packed beds had been the "free surface" model suggested by Happel (43, 44) and Pfeffer and Happel (45). This idealized model is based on the concept that an assemblage of particles can be divided into a number of identical unit cells, each cell consisting of a single particle and a fluid envelope having a "free surface", i.e., zero tangential stress surrounding the particle. The size of the outer envelope is so chosen that the porosity of the cell is identical to that of the actual assemblage of particles.

One particularly intriguing feature of the "free surface" model is that the predicted pressure drop and heat and mass transfer coefficients using the model were found to agree quite well with experimental drag data up to a Reynolds Number of about 50 depending on the porosity of the multiparticle system. This was surprizing since the model is based on the creeping motion equations which are known to lead to large errors in predicting the drag force on a single particle for $Re \geq 1$.

In order to investigate this and related phenomena it is necessary to develop a mathematically tractable system for examining flow past objects in the intermediate Reynolds number range, i.e., $0 < Re < 200$ without the necessity of having to solve the complete Navier Stokes equations of motion. A great deal of effort based on Oseen's (63) classic work has been directed toward determining the flow past objects at Reynolds numbers in the vicinity of unity. Proudman and Pearson (38), using a technique of inner and outer expansions, attempted to determine

corrections to the Stokes drag on a sphere at higher Reynolds numbers. Their predicted results begin to deviate from experimentally determined drag coefficients for $Re > 0.6$.

Another notable attempt has been the development of a higher order boundary layer theory by Van Dyke (48) and Kaplun (49), also using the method of inner and outer expansions. The lowest order inner solution is based on the pressure distribution from the inviscid solution about the original body. The first correction to the outer solution is based on the displacement effect of the lowest order inner solution. The solution procedure is thus an iterative one and will converge very slowly (if at all) if the lowest order outer solution is far removed from the actual solution for the outer flow. It is important to note that the error in the lowest order outer solution is cumulative and becomes progressively worse as one proceeds away from the forward stagnation point.

Appropriate solutions to flows at very high Reynolds numbers can be obtained by the methods of traditional boundary layer theory developed by Prandtl and adapted to the problems of flow past two dimensional and axisymmetric bodies by Pohlhausen (46) and Holstein and Bohlen (47). This theory, however does not apply in the intermediate Re range due to a restrictive fundamental assumption, viz; the thickness of the boundary layer or viscous flow region must be very much smaller than the radius of curvature of the object in the flow field. This constraint immediately limits the application of these theories to flows at very high Re. Incipient wake formation from spheres and cylinders occurs in the range $1 \lesssim Re \lesssim 25$ thereby precluding the use of conventional boundary layer theories.

A modified boundary layer theory has, therefore, been developed to enable the prediction of wake formation at intermediate Reynolds Numbers for flow past blunt bodies. The basis for the new theory is a systematic correction to the effective shape of the body as seen by the inviscid flow as one proceeds downstream by using the information gained from the solution up to the given point. This type of systematic correction at each point is achieved by applying a technique of local streamwise coordinate straining which has the effect of a) accounting for the effects of boundary layer displacement thickness on the inviscid flow solution, and b) modifying the Prandtl boundary layer hypothesis so as to take account in some mean sense for the variation in the pressure gradient across the viscous layer. It is thus important to note that the major simplifying assumptions of regular boundary layer theories (i.e. thin boundary layers as well as $\partial p/\partial y = 0$ are not necessary for the application of the new theory.

5.2 COORDINATE STRAINING TECHNIQUE

As in the case of conventional boundary layer theory, the natural coordinate system will be used for both two-dimensional and axisymmetric flow (see Schlichting (50)) as shown in Figure 5.1. The new theory assumes as hypothesis a) that a boundary layer traversing a distance dx_o along the original body, behaves as if it has traversed the same distance dx^* (where $dx^* = dx_o$) along some larger surface corresponding to the displacement arc generated by the interaction between the inner and outer fluid streams of the flow past the original body. Thus,

$$\int_0^{x^*} dx^* = \int_0^{x_o} dx_o \quad \text{or} \quad x^* = x_o \tag{5.1}$$

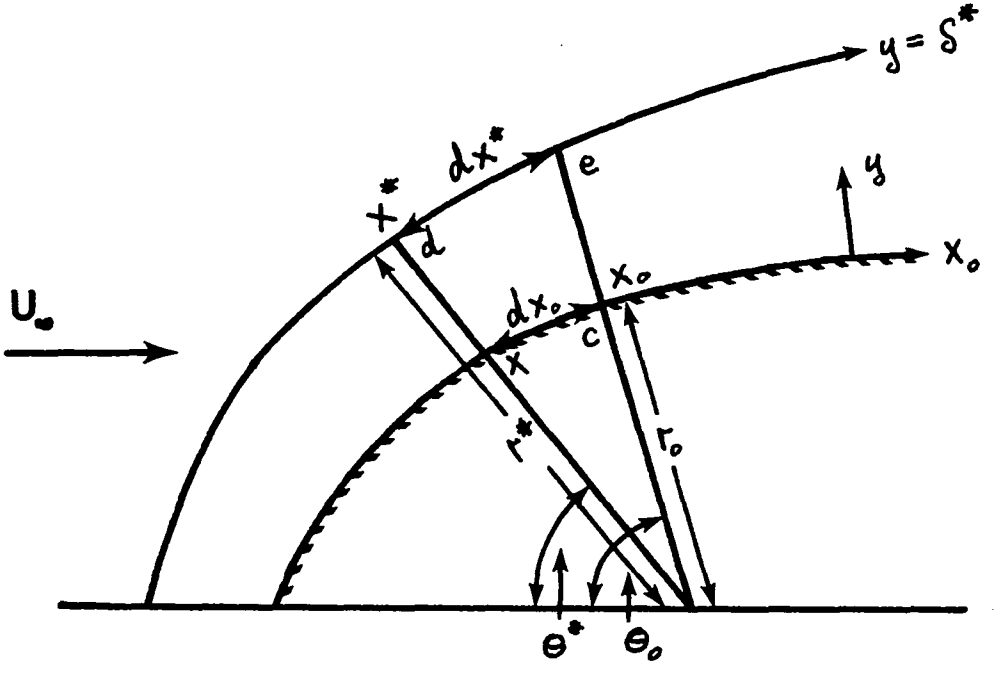

Figure 5.1 - BOUNDARY LAYER COORDINATE SYSTEM

As stated earlier, for thick boundary layers the assumption of $dp/dy = 0$ in the viscous layer is incorrect and leads to large errors. Therefore, it must be assumed that the pressures at stations c and e along the original body and displacement arc respectively are not equal. As no simple technique has been developed for determining pressures in the viscous layer a second hypothesis needs to be made concerning the variation in pressure between the body and the edge of the boundary layer. Thus, hypothesis (b) assumes that the average pressure gradient in the x_o direction between the body and the edge of the boundary layer (i.e. $\int_0^\delta \frac{\partial p}{\partial x_o}\, dy$) is represented by the gradient of an average pressure p^* taken upstream at x^* along the displacement thickness of the body, i.e.

$$\int_0^\delta \frac{\partial p}{\partial x_o}\, dy = \frac{d p^*}{d x_o} \tag{5.2}$$

Thus, implicit in the new theory is recognition of the fact that the pressure gradient is not constant across the viscous layer, but is given by an average value measured along the displacement arc at an earlier station. This concept of an average pressure gradient is fundamental to the development of the new theory and will be discussed more fully in following sections.

To determine the exact inviscid pressure distribution for the flow past the displacement arc, one would need to know its shape a priori. However, it has already been stated that the boundary layer thickness at a certain point along the actual body is determined from conditions existing at a point along the displacement arc which is upstream of the point on the body. Thus, the displacement arc is actually known downstream of where one is presently performing the boundary layer calculation. Since it would be a large task to determine the exact inviscid flow past

each updated displacement arc, some approximation must be introduced. A convenient simplification is to assume that the flow past each segment of the displacement arc can be represented by some enlarged object having a shape that is geometrically similar to the original body and a concentric but locally enlarged radius of curvature. Based on the above simplification and equation (5.1) the following transformations between regular and stretched coordinates can be defined

$$
\begin{aligned}
&r_o\theta_o = r^*\theta^* \quad \text{or} \quad \theta^* = \frac{r_o}{r^*}\theta_o \\
&r^* = r_o + \delta^* \\
&x = r_o\theta^* \quad \text{or} \quad x = \frac{r_o}{r^*}x_o \\
&\frac{\partial}{\partial x_o} = \frac{\partial}{\partial x^*} = \frac{r_o}{r^*}\frac{\partial}{\partial x} = \frac{1}{r^*}\frac{\partial}{\partial \theta^*}
\end{aligned}
\tag{5.3}
$$

The relationships (5.1) and (5.3) will be used to determine inviscid pressure gradients required in later sections.

5.3 INTEGRAL EQUATION OF MOTION - TWO-DIMENSIONAL FLOW

The control volume concept will be used to develop the integral equation for two-dimensional flow over a curved surface. Referring to Figure 5.2a, the continuity equation can be written as follows:

$$\rho V_e dx' = \rho U_e \frac{d\delta}{dx_o} dx_o - \frac{\partial}{\partial x_o}\int_0^\delta \rho u dy dx_o \tag{5.4}$$

$$V_e dx' = U_e \frac{d\delta}{dx_o} dx_o - \frac{\partial}{\partial x_o}\int_0^\delta u dy dx_o \tag{5.5}$$

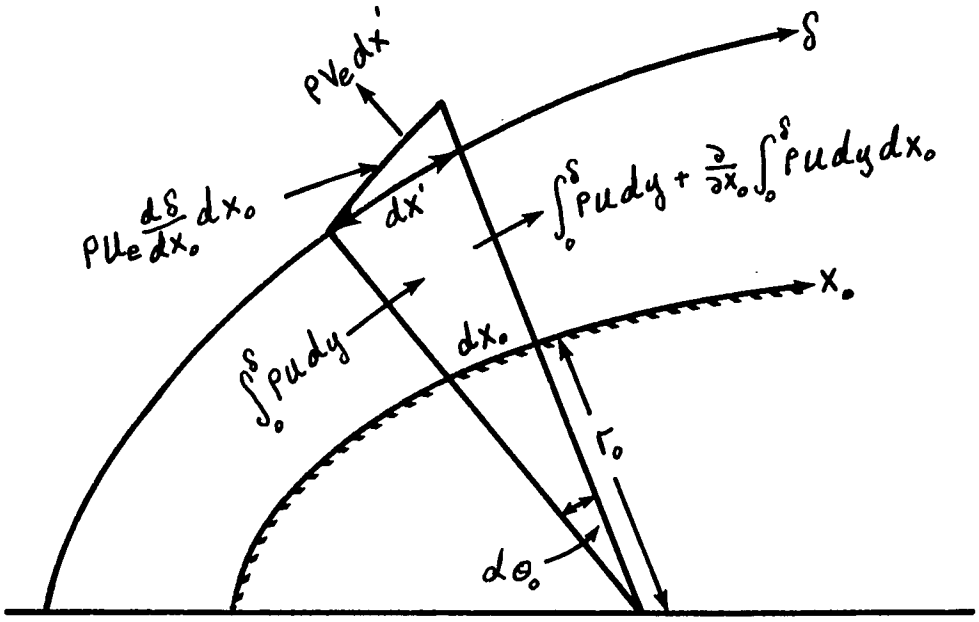

Figure 5.2a - CONTINUITY DIAGRAM FOR 2 - D SYSTEM

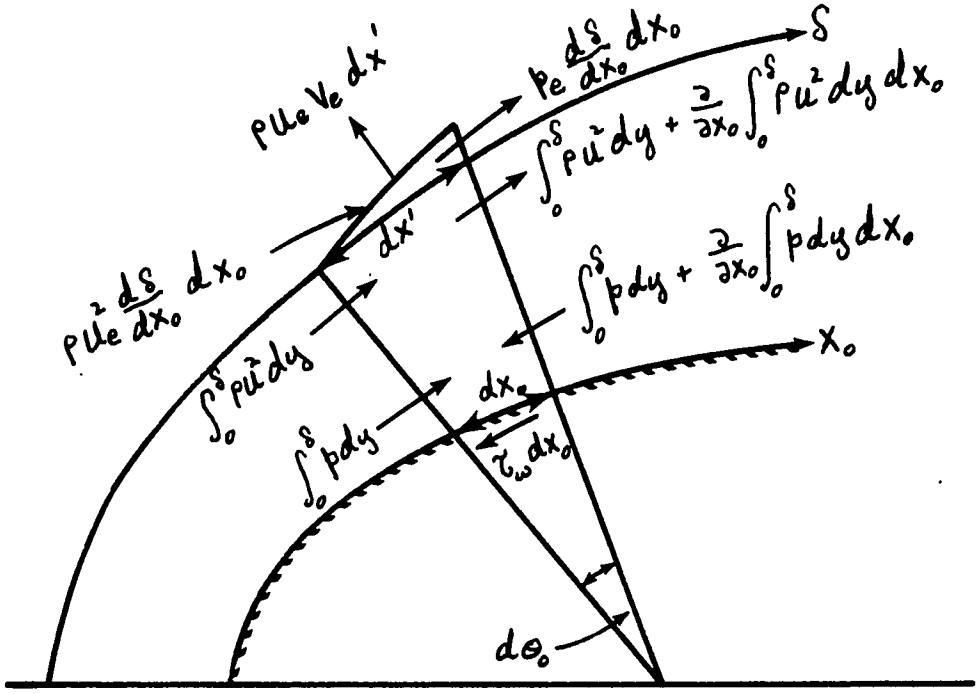

Figure 5.2b - FORCE DIAGRAM FOR 2 - D SYSTEM

where x_o is measured along the body, x' along the boundary layer thickness, δ and U_e is the external potential flow velocity in the usual boundary layer sense.

The integral momentum equation is developed with reference to Figure 5.2b as:

$$-\tau_\omega\, dx_o - \frac{\partial}{\partial x_o}\int_0^\delta p\, dy\, dx_o + p_e \frac{d\delta}{dx_o}\, dx_o = \frac{\partial}{\partial x_o}\int_0^\delta \rho u^2\, dy\, dx_o - \rho U_e^2 \frac{d\delta}{dx_o}\, dx_o + \rho U_e V_e\, dx' \tag{5.6}$$

Dividing by ρdx_o and substituting for Vedx' from equation (5.5) gives

$$-\frac{\tau_\omega}{\rho} - \frac{\partial}{\partial x_o}\int_0^\delta \frac{p}{\rho}\, dy + \frac{p_e}{\rho}\frac{d\delta}{dx_o} = \frac{\partial}{\partial x_o}\int_0^\delta u^2\, dy - U_e^2 \frac{d\delta}{dx_o} + U_e^2 \frac{d\delta}{dx_o} - U_e \frac{\partial}{\partial x_o}\int_0^\delta u\, dy \tag{5.7}$$

Applying Leibnitz's Rule to (5.7), we obtain

$$-\frac{\tau_\omega}{\rho} - \int_0^\delta \frac{1}{\rho}\frac{\partial p}{\partial x_o}\, dy - \frac{p_e}{\rho}\frac{d\delta}{dx_o} + \frac{p_e}{\rho}\frac{d\delta}{dx_o} = \int_0^\delta \frac{\partial}{\partial x_o}(u^2)\, dy + U_e^2 \frac{d\delta}{dx_o} - U_e\int_0^\delta \frac{\partial}{\partial x_o} u\, dy - U_e^2 \frac{d\delta}{dx_o} \tag{5.8}$$

or

$$-\frac{\tau_\omega}{\rho} - \int_0^\delta \frac{1}{\rho}\frac{\partial p}{\partial x_o}\, dy = \int_0^\delta \frac{\partial}{\partial x_o}(u^2)\, dy - U_e\int_0^\delta \frac{\partial}{\partial x_o} u\, dy \tag{5.9}$$

At first glance equation (5.9) appears to be identical with the von Karman, Pohlhausen integral equation. There are, however, two

subtle and important differences. The first can be seen in the second term on the left of equation (5.9) containing $\int_0^\delta \frac{\partial p}{\partial x_o} dy$. Pohlhausen (46) utilized the total derivative of the pressure, as his y momentum equation indicated that $\partial p/\partial y = 0$ or $p = p(x_o)$ for $\delta \ll r_o$. Equation (5.9) recognizes the fact that $p = p(x_o, y)$ and does not require that $\delta \ll r_o$. As was explained in section 5.2, hypothesis (b) states that the average value of the pressure gradient in the x_o direction can be replaced by the gradient of an average pressure p* measured along the displacement arc that is upstream of the point x_o along the original body.

$$\int_0^\delta \frac{\partial p}{\partial x_o} dy = \frac{dp^*}{dx_o} \tag{5.3}$$

The second difference between equation (5.9) and Pohlhausen's equation is in the definition of the inviscid velocity U_e. Pohlhausen defines U_e as the inviscid velocity in the x_o direction measured along the surface of the original body. In equation (5.9) U_e is defined by hypothesis (c) as the inviscid velocity in the x_o direction measured in the scaled coordinate system along the displacement or enlarged surface, i.e. Pohlhausen's $U_e = U_e(\theta_o)$ whereas the new $U_e = U_e(\theta^*)$.

From Bernoulli's theorem:

$$\frac{1}{\rho} \frac{dp^*}{dx_o} = - U_e \frac{dU_e}{dx_o} \tag{5.10}$$

substituting (5.2) and (5.10) in (5.9) yields

$$\frac{\tau_w}{\rho} = \int_0^\delta \left[U_e \frac{dU_e}{dx_o} - \frac{\partial}{\partial x_o}(u^2) + U_e \frac{\partial u}{\partial x_o} \right] dy \tag{5.11}$$

However

$$\frac{\partial}{\partial x_o}[U_e u] = U_e \frac{\partial u}{\partial x_o} + u \frac{dU_e}{dx_o} \tag{5.12}$$

and substituting (5.12) in (5.11) shows

$$\frac{\tau_\omega}{\rho} = \int_0^\delta \left[U_e \frac{dU_e}{dx_o} - \frac{\partial}{\partial x_o}(u^2) + \frac{\partial}{\partial x_o}(U_e u) - u \frac{dU_e}{dx_o}\right] dy \tag{5.13}$$

Applying Leibnitz's Rule to (5.13) and rearranging gives:

$$\frac{\tau_\omega}{\rho} = \frac{\partial}{\partial x_o}\int_0^\delta u(U_e - u)\,dy + \frac{dU_e}{dx_o}\int_0^\delta (U_e - u)\,dy \tag{5.14}$$

Conventional momentum and displacement thicknesses are defined as:

displacement thickness: $$\delta^*(x_o) = \frac{1}{U_e}\int_0^\delta (U_e - u)\,dy \tag{5.15}$$

momentum thickness: $$\theta(x_o) = \frac{1}{U_e^2}\int_0^\delta u(U_e - u)\,dy \tag{5.16}$$

Substituting (5.15) and (5.16) in (5.14) results in:

$$\frac{\tau_\omega}{\rho} = \frac{d}{dx_o}(\theta U_e^2) + \delta^* U_e \frac{dU_e}{dx_o} \tag{5.17}$$

The velocity in the viscous layer (u) is determined using Pohlhausen's (46) profile, i.e.

$$\frac{u}{U_e} = e\left(\frac{y}{\delta}\right) + f\left(\frac{y}{\delta}\right)^2 + g\left(\frac{y}{\delta}\right)^3 + h\left(\frac{y}{\delta}\right)^4 \tag{5.18}$$

with the following boundary conditions:

$$\begin{aligned} &y=0: \quad u=0 \; ; \quad \nu \frac{\partial^2 u}{\partial y^2} = \frac{1}{\rho}\frac{dp^*}{dx_o} = -U_e \frac{dU_e}{dx_o} \\ &y=\delta: \quad u=U_e \; ; \quad \frac{\partial u}{\partial y} = 0 \; ; \quad \frac{\partial^2 u}{\partial y^2} = 0 \end{aligned} \tag{5.19}$$

Although conditions (5.19) assume the same form as those employed by Pohlhausen, the condition involving the pressure gradient has a different meaning in this case. By hypotheses (b) and (c) the wall boundary condition is considered in terms of the enlarged body as represented by the displacement arc upstream of the station x_o along the original body. Therefore, dp^*/dx_o represents a wall pressure gradient measured along the enlarged surface.

If a shape factor Λ is defined as:

$$\Lambda = \frac{\delta^2}{\nu}\frac{dU_e}{dx_o} \tag{5.20}$$

then using (5.18), (5.19) and (5.20) it can be seen that

$$\begin{aligned} &e = 2 + \frac{\Lambda}{6} \quad ; \quad f = -\frac{\Lambda}{2} \\ &g = -2 + \frac{\Lambda}{2} \quad ; \quad h = 1 - \frac{\Lambda}{6} \end{aligned} \tag{5.21}$$

Also, since $\tau_w = \mu \left(\frac{\partial u}{\partial y}\right)_{y=0}$

$$\frac{\tau_w}{\rho} = \frac{e \nu U_e}{\delta} \tag{5.22}$$

substituting (5.22) in (5.17)

$$\frac{e \nu U_e}{\delta} = 2\theta U_e \frac{dU_e}{dx_0} + U_e^2 \frac{d\theta}{dx_0} + \delta^* U_e \frac{dU_e}{dx_0} \tag{5.23}$$

and dividing (5.23) by $U_e \frac{dU_e}{dx_0} \delta$ gives

$$\frac{e}{\Lambda} = 2\frac{\theta}{\delta} + \frac{U_e}{\delta \frac{dU_e}{dx_0}} \frac{d\theta}{dx_0} + \frac{\delta^*}{\delta} \tag{5.24}$$

Rearranging (5.24) and replacing e and δ from (5.21) and (5.20) finally yields

$$\frac{d\theta}{dx_0} = \frac{\left(\Lambda \nu \frac{dU_e}{dx_0}\right)^{1/2}}{U_e} \left\{ \frac{2}{\Lambda} + \frac{1}{6} - 2\frac{\theta}{\delta} - \frac{\delta^*}{\delta} \right\} \tag{5.25}$$

Pohlhausen has shown that θ/δ and δ^*/δ can be expressed as the following simple functions of Λ by performing the integrations indicated by (5.15) and (5.16) and utilizing the results of (5.18) $\longrightarrow$ (5.21).

$$\frac{\theta}{\delta} = \left[\frac{37}{315} - \frac{\Lambda}{945} - \frac{\Lambda^2}{9072}\right]$$

$$\frac{\delta^*}{\delta} = \left[\frac{3}{10} - \frac{\Lambda}{120}\right] \tag{5.26}$$

Equations (5.25) and (5.26) constitute a non-linear first order differential equation for the momentum thickness in terms of the local shape factor Λ as well as the local inviscid velocity and acceleration.

For flow past a single cylinder, the inviscid velocity is given by (see Milne-Thomson (25)):

$$U_e = 2 U_\infty \sin \theta^* \tag{5.27}$$

where the stretched coordinate θ^* (see Figure 5.1) is used for reasons given above. Using (5.27) and (5.3) it can be shown that:

$$\frac{dU_e}{dx_o} = \frac{2U_e}{r^*} \cos \theta^* \tag{5.28}$$

5.4 INTEGRAL EQUATION OF MOTION - AXISYMMETRIC FLOW

An analogous development for axisymmetric flow to that presented above for two-dimensional flow is presented in the appendix section A.2.

The resulting boundary layer equation for axisymmetric flow is given by equation (A.49), i.e.

$$\frac{d\theta}{dx_o} = \frac{(\Lambda \nu U_e')^{1/2}}{U_e} \left[\frac{2}{\Lambda} + \frac{1}{6} - 2\frac{\theta}{\delta} - \frac{\delta^*}{\delta} - \right.$$

$$\left. \frac{R_o'}{R_o} \frac{U_e}{U_e'} \frac{\theta}{\delta} - \frac{\gamma F_1}{R_o U_e (\Lambda \nu U_e')^{1/2}} - \frac{\gamma' F_2}{R_o U_e (\Lambda \nu U_e')^{1/2}} \right] \tag{5.29}$$

where primes denote differentiation with respect to x_o and U_e and U_e' have the same definitions as for the two-dimensional case, i.e. they are developed in terms of the stretched coordinate system. All variables

that occur in both equations (5.29) and (5.25) have the same definitions. Other quantities appearing in equation (5.29) above are derived in the appendix section A.2. These quantities are:

$$F_1 = \left\{ \frac{d}{dx_o}\left[(A_2 - A_1) U_e^2 \delta^2\right] + \left(\frac{1}{2} - A_2\right) U_e U_e' \delta^2 \right\}$$

$$F_2 = (A_2 - A_1) U_e^2 \delta^2 \qquad \text{(A.45)}$$

$$A_2 = A_2[e, f, g, h] = A_2(\Lambda)$$

$$A_1 = A_1[e, f, g, h] = A_1(\Lambda) \qquad \text{(A.43)}$$

R_o = vertical distance from point on the boundary to the axis of rotation defined in Figures A.3 and A.4

$$\gamma = \cos\varepsilon = \left[1 - \left(\frac{d R_o}{dx_o}\right)^2\right]^{1/2} \qquad \text{(A.36)}$$

For flow past a single sphere the inviscid velocity is given by (see Milne-Thomson (35)):

$$U_e = \tfrac{3}{2} U_\infty \sin\theta^* \qquad (5.30)$$

where the stretched coordinate θ^* (see Figure 5.1) is used for the same reasons as were discussed for the two-dimensional case. Using (5.30) and (5.3) it can be shown that:

$$\frac{dU_e}{dx_o} = \frac{3U_e}{2r^*}\cos\theta^* \qquad (5.31)$$

5.5 SOLUTION PROCEDURES AND NUMERICAL TECHNIQUES

The solution of the boundary layer equations using the coordinate straining technique described above obtained for flow past both a single

cylinder and a single sphere and separation angles so obtained will be compared with those available in the literature from solutions of the Navier-Stokes equations. The solution procedures adopted for the two-dimensional and axisymmetric situations are very similar and will be briefly outlined below. The equations of motion (5.25) and (5.29) for the two-dimensional and axisymmetric cases respectively, are first order non-linear differential equations and are well behaved in the regions of interest except at the forward stagnation point where a singularity exists in each case. Therefore, if the forward stagnation point is considered separately, the equations can be integrated using a simple finite difference technique. The step size is determined by trial and error by running the same problem at various increments and noting the convergence characteristics of the final solution. It was found in all cases examined that the relative error between the use of 1000 and 5000 increments over the generating arc of the test object was less than 0.1%. Therefore, a standard of 1000 increments was used.

The method of solution utilized for each problem is outlined below - first for the two-dimensional case and then for axisymmetric flow:

(i) Two-Dimensional Flow

(a) The potential velocity U_e at the forward stagnation point is zero. The acceleration U_e' is determined by trial and error as it can be seen from equation (5.3) that $\frac{dU_e}{dx_o} = \frac{1}{r^*}\frac{dU_e}{d\theta^*}$, i.e. U_e' depends on δ^*, ($r^* = r_o + \delta^*$). It was found that the solution for U_e' converged to 0.1% in less than five iterations when a direct iteration scheme was employed, i.e. $U_{e'}^{n+1}_{assumed} = U_{e'}^{n}_{calculated}$.

(b) Conditions at the forward stagnation point (especially the value of the shape factor defined by equation (5.20)) can be determined as shown in the appendix section A.4. It is shown that for the two-dimensional case, the value of Λ at the forward stagnation point is independent of Reynolds Number and is always 7.052 which is the same as the value obtained by Pohlhausen and von Karman.

(c) Knowing Λ , U_e and U_e' enables the computation of all boundary layer quantities at the forward stagnation point to be made.

(d) With the initial conditions obtained above, the integration procedure can commence. It must be kept in mind that although equation (5.25) is developed in terms of dx_o along the original body, it is exactly equivalent to a development in terms of dx* along the enlarged body by (5.3), i.e. $d/dx_o = d/dx^*$ (hypothesis (a)).

(e) The stepwise integration described in (d) is now repeated for the next incremental step along x*.

(f) At each point along x*, the value of τ_w is checked by using equation (5.22). Separation is considered to have been achieved when the value of $\tau_w = 0$.

(ii) Axisymmetric Flow

(a) As for the two-dimensional case U_e at the forward stagnation point is zero. The acceleration U_e' at the forward stagnation point is determined by trial and error for the same reason as described for two-

dimensional flow.

(b) The computation of the shape factor Λ at the forward stagnation point is a trial and error procedure as outlined in the appendix section A.4. This value of Λ for the axisymmetric case is a function of Reynolds Number which makes it different from the two-dimensional case as well as from the axisymmetric solution of Pohlhausen and von Karman for thin boundary layers. The reason for the dependence of Λ on Re at the forward stagnation point is the occurrence of the curvature factor κ defined by equation (A.36) in the equation of motion (5.29). A direct iteration procedure using Pohlhausen's universal initial value of $\Lambda = 4.716$ results in convergence to 0.2% in under 10 iterations, i.e. $\Lambda^{n+1}_{assumed} = \Lambda^{n}_{calculated}$. This interesting dependence of Λ on Re for axisymmetric flow has not been considered in any previous developments. For this reason values of Λ for flow past a single sphere at various Reynolds Numbers are presented in Table 5.1.

Table 5.1

Variation of Λ with Reynolds Number

Re	Λ
∞	4.716
130	4.310
100	4.260
80	4.213
60	4.148
40	4.034
20	3.807
10	3.530
8	3.436

(c) From this point on the solution procedure is identical to that outlined for the two-dimensional case steps (c) through (f) substituting equation (5.29) for equation (5.25).

5.6 RESULTS

In order to test the precision of the newly developed boundary layer theory the two problems investigated were the prediction of separation angles from a single two-dimensional cylinder and a single sphere as functions of Re. These two problems were chosen for comparative purposes as experimental data and numerical Navier-Stokes solutions exist in the literature for each case. The two-dimensional case was investigated in the range $0 < Re \leq 60$. For $Re > 60$, the behavior of the wake becomes unstable due to oscillation of the vortex street (see Batchelor (51)).

Separation angles from the rear stagnation point of the cylinder calculated from this new theory are compared with the numerical results of Kawaguti (52), Apelt (53), Kawaguti and Jain (54), Takami and Keller (12) and Son and Hanratty (55) and with experimental results of Taneda (56) in Figure 5.3. This figure demonstrates that the present results are in remarkable agreement with experimental and numerical solutions in the range $5 \leq Re \leq 60$. The maximum deviation between these results and numerical solutions in the above Re range is less than 6^{o} whereas it can be seen that at Re = 40 differences in numerical solutions themselves are of the order of 4^{o}. Taneda (56) observed initial boundary layer separation at Re = 5. The new theory predicts initial separation at Re = 5.1.

Examination of hypotheses (a), (b) and (c) together with the equation of motion indicates that although this new theory provides a

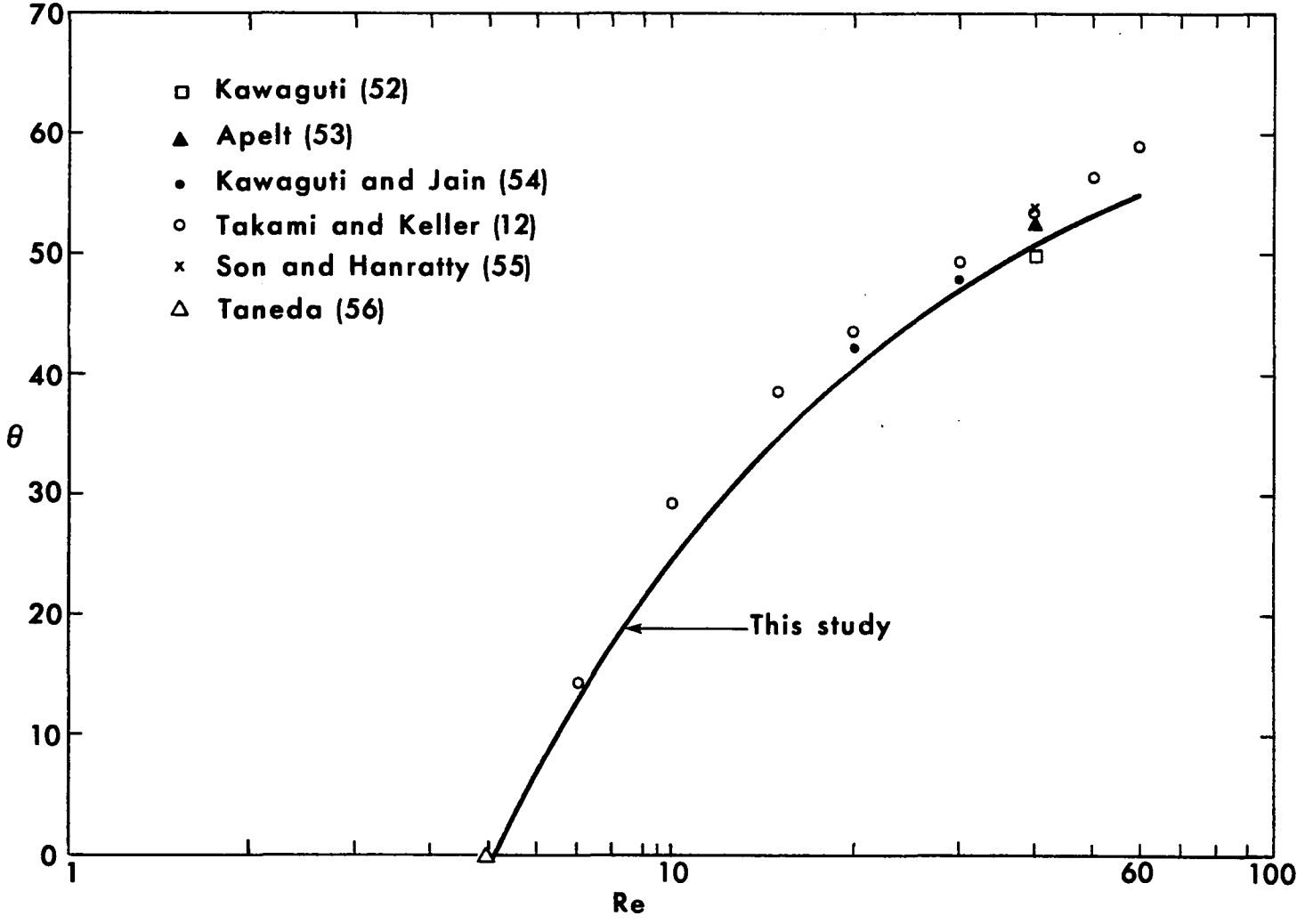

Figure 5.3 - SEPARATION ANGLE VS. Re FOR A CYLINDER

technique for determining average boundary layer properties, it does not provide an obvious technique for calculating point pressures on the surface of the actual body. Extension of this technique to calculate the actual surface pressures will be the subject of future work in this area.

For the case of axisymmetric flow past a single sphere, the wake becomes unstable at approximately Re = 130 (see Batchelor (51)) and therefore the new theory was applied in the range Re $\leq$ 130. Separation angles from the rear stagnation point of the sphere calculated from this new theory are compared with the numerical results of Jenson (57) and Rimon and Cheng (11) and the experimental results of Nisi and Porter (58) and Taneda (40) in Figure 5.4. It can be seen that separation angles predicted by this theory differ by less than 10^{o} in the worst case from the numerical results of Rimon and Cheng (11). It is apparent from the various results in Figure 5.4 that the Reynolds Number for initial separation from a sphere varies considerably. Experimentally observed initial Re vary between 8 and 24. Numerically, Jenson (57) found the critical Re to be 17 whereas Rimon and Cheng (11) found a separation angle of 13^{o} at Re = 10. The present theory indicates a critical Re = 6.

These first two problems have demonstrated that the proposed boundary layer approximation for both two-dimensional and axisymmetric flow produces results that are in good agreement with experimental data and numerical results for flows past single objects. Utilizing this new technique, the effect on boundary layer separation of interactions resulting from other objects on the test object will be discussed in the following chapter.

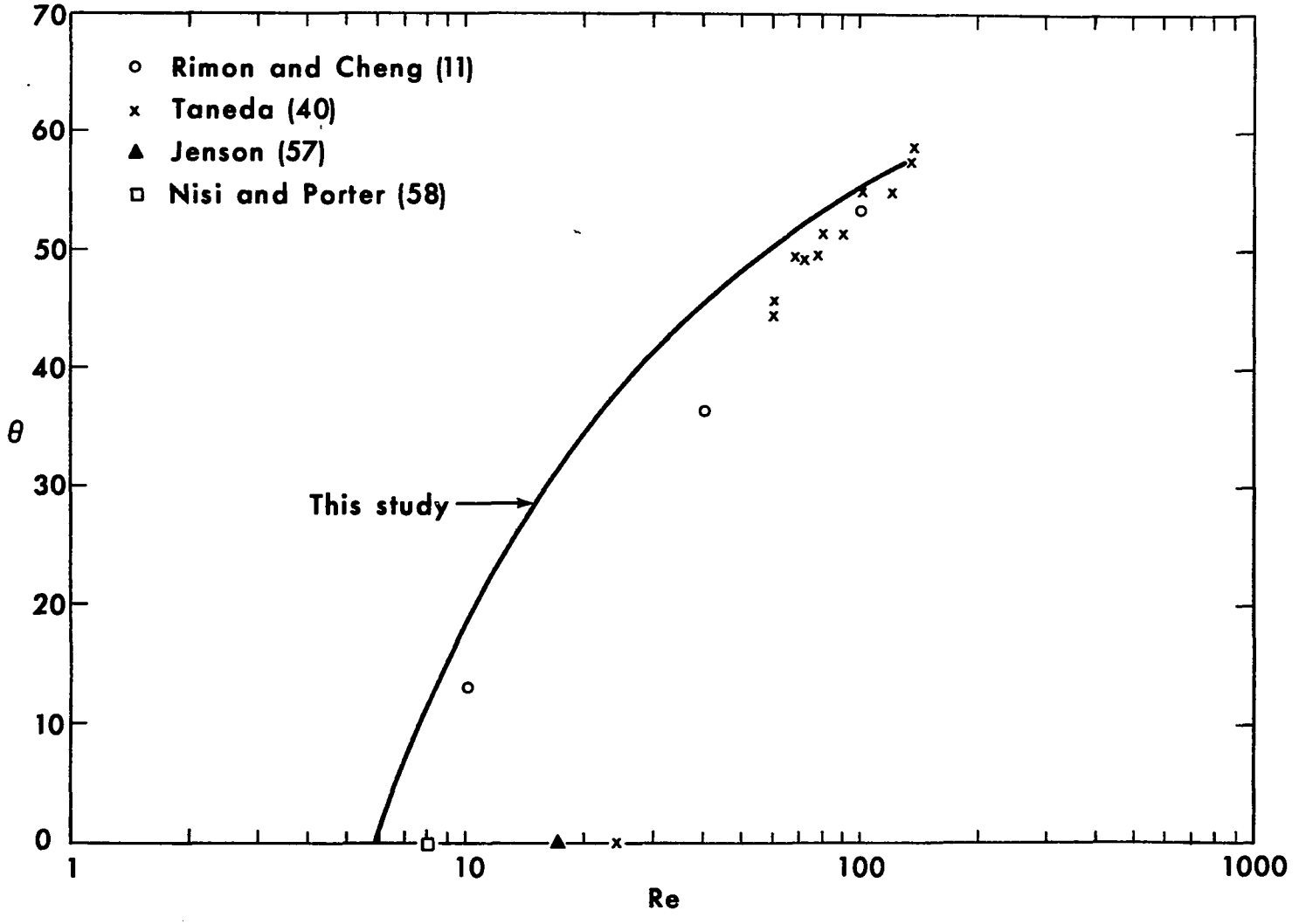

Figure 5.4 - SEPARATION ANGLE VS. Re FOR A SPHERE

CHAPTER 6

INTERMEDIATE REYNOLDS NUMBER FLOW IN MULTIPARTICLE SYSTEMS

6.1 INTRODUCTION

It has been stated in the introduction to Chapter 5 that the motivation for the development of an intermediate Re range boundary layer theory was the interesting success exhibited by the "free surface" model for predicting pressure drops as well as heat and mass transfer coefficients in packed beds in the range $0 < Re \leq 50$. Leclair and Hamielec (13) applied the "zero vorticity" model, i.e., zero vorticity is assumed along the outer fluid envelope to a multiple system of spheres. Using the complete Navier-Stokes equations to represent the fluid motion in the concentric shell, these authors have shown that as the void volume of the system decreases, the flow separation point moves closer and closer to the rear stagnation point, i.e., wake formation appears to be delayed to higher Re as the porosity decreases. While these numerical solutions indicate a trend, they cannot be used as a rigorous demonstration of wake suppression as a function of porosity due to the uncertainty associated with the use of the "outer envelope" boundary conditions.

By using the boundary layer techniques developed in Chapter 5 it is now possible in a semi-quantitative manner to examine the effects of particle interactions on boundary layer separation and subsequent wake formation from a test particle.

6.2 PROBLEM IDENTIFICATION AND SOLUTION PROCEDURES

Basically, three problems of boundary layer separation will be investigated, i.e., (a) separation from the lead cylinder in a finite chain of cylinders with the flow parallel to the line of centers; (b)

separation from the lead sphere in a two sphere system with the flow parallel to the line of centers and (c) separation from the central cylinder in an odd numbered chain of cylinders with the flow normal to the line of centers. These three flow configurations are depicted in Figure 6.1.

The following general comments apply to all three flow situations. In all cases, separation from the lead (or central) object will be the only separation investigated. The other objects in each array will only be considered to the extent that they modify the inviscid flow field in the vicinity of the test object. Interaction effects of the second object on the test object do include the effect of an enlarged second object due to growth of the viscous layer around the second object. This growth around the second object is not calculated directly, but is assumed to be identical to the growth of the boundary layer about the test object. This assumption is not strictly correct due to the different free stream conditions facing the second object resulting from the disturbance due to the test object. However, it was deemed sufficient to indicate any significant trend in separation from the test object resulting from interactions with the second object. For this reason, the closest particle spacing examined in all of these studies was that spacing for which the enlarged objects (i.e., radius equal to actual particle radius plus displacement thickness) were considered to be touching one another. Therefore, results presented for arrays containing more than one object must be considered to be first order approximations indicating relative behavior only.

In order to determine the effects on separation arising from multiple particle interactions, it is necessary to obtain a solution to the

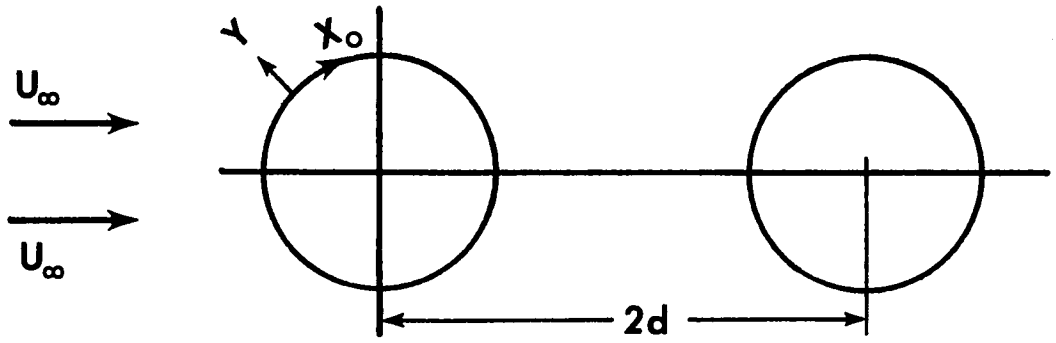

2-D and Axisymmetric Flow (a and b)

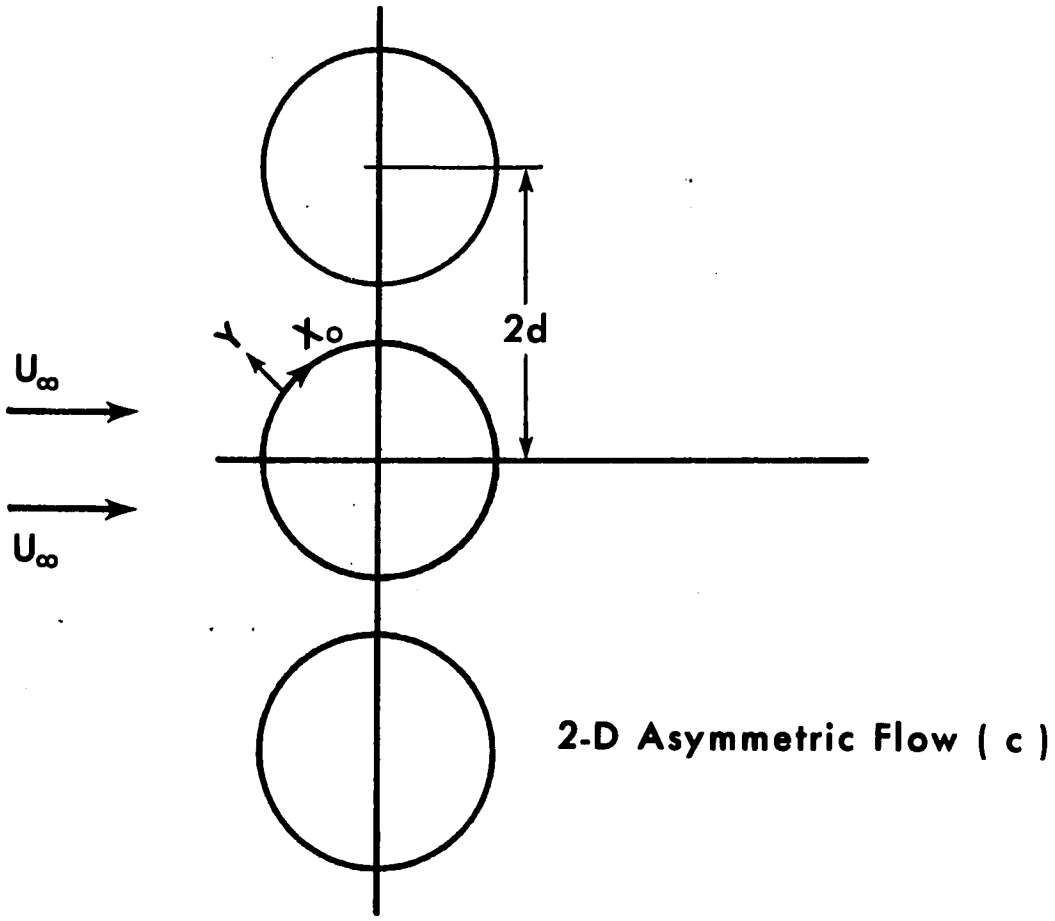

2-D Asymmetric Flow (c)

Figure 6.1 - GEOMETRY FOR 2 - D AND AXISYMMETRIC FLOW SYSTEMS

potential flow field about the entire array. For the two two-dimensional situations, i.e., flow along the line of centers of a chain of two or more cylinders and flow normal to the line of centers of a chain of three or more cylinders, the potential flow solutions are developed in the Appendix, section A.1. The solution procedure is an approximate one based on summing the contributions of a number of equally spaced doublets of equal strength. Potential flow solutions for streaming motion parallel to the line of centers of more than two spheres do not exist in the current literature. Milne-Thomson solved the two sphere problem using the method of images which is an approximate technique that loses accuracy as the sphere spacing decreases. Solutions for irrotational flow along the line of centers of two spheres are developed in the Appendix, section A.3. The solution technique is based on the multipole truncation procedure developed in detail for viscous flow past finite chains of spheres and spheroids in Chapter 2. The results obtained are preferred over Milne-Thomson's results as any desired degree of accuracy is attainable using the multipole truncation procedure.

The solution procedures for both the two-dimensional and the axisymmetric multiparticle flow configurations presented below are identical in concept to the procedures detailed in Chapter 5 for flow past single objects. The only difference exists in the determination of the inviscid velocity U_e. In Chapter 5 the single particle U_e was used whereas in this chapter the multiparticle U_e developed in the Appendix, sections A.1 and A.3 is utilized.

6.3 RESULTS

The first multiparticle system investigated consists of two spheres,

one behind the other as shown in Figure 6.1 (a). This system was investigated in the range Re $\leq$ 130 at a number of different sphere spacings (d/a). The results are shown in Figure 6.2. This figure demonstrates an interesting effect of particle interactions on separation from the test sphere. As the trailing sphere approaches the lead sphere, the critical Re required for the onset of separation appears to be decreased and when the spheres are 1.5 diameters apart the onset of boundary layer separation is advanced from Re = 6 for an isolated sphere to Re = 5.4. Although this effect is small, it is contrary to the expected result; that of wake suppression.

One possible explanation for this phenomenon might be the fact that as the spheres approach one another the fluid volume between the spheres is a region of very small flow, and is almost stagnant. This low flow condition near the point of maximum velocity results in abnormally large negative velocity gradients and, therefore, adverse pressure gradients that are larger than those existing in the case of an isolated sphere. It must be kept in mind, however, that these separation angle changes are relatively small, approximately 3 degrees between spheres that are 1.5 diameters apart compared to a single sphere. These changes are of the same order as the probable accuracy of the solution procedure and should, therefore, not be considered as being conclusive.

Similar results were found for the case of flow past two cylinders one behind the other as is evident from the results plotted in Figure 6.3. Again wake advancement is shown but the effect is minimal. When the cylinders are 1.5 diameters apart, the onset of separation is advanced from Re = 5.1 for an isolated cylinder to Re = 4.6. When the cylinders are 4 diameters apart, the value of the critical Re = 5.0. It is inter-

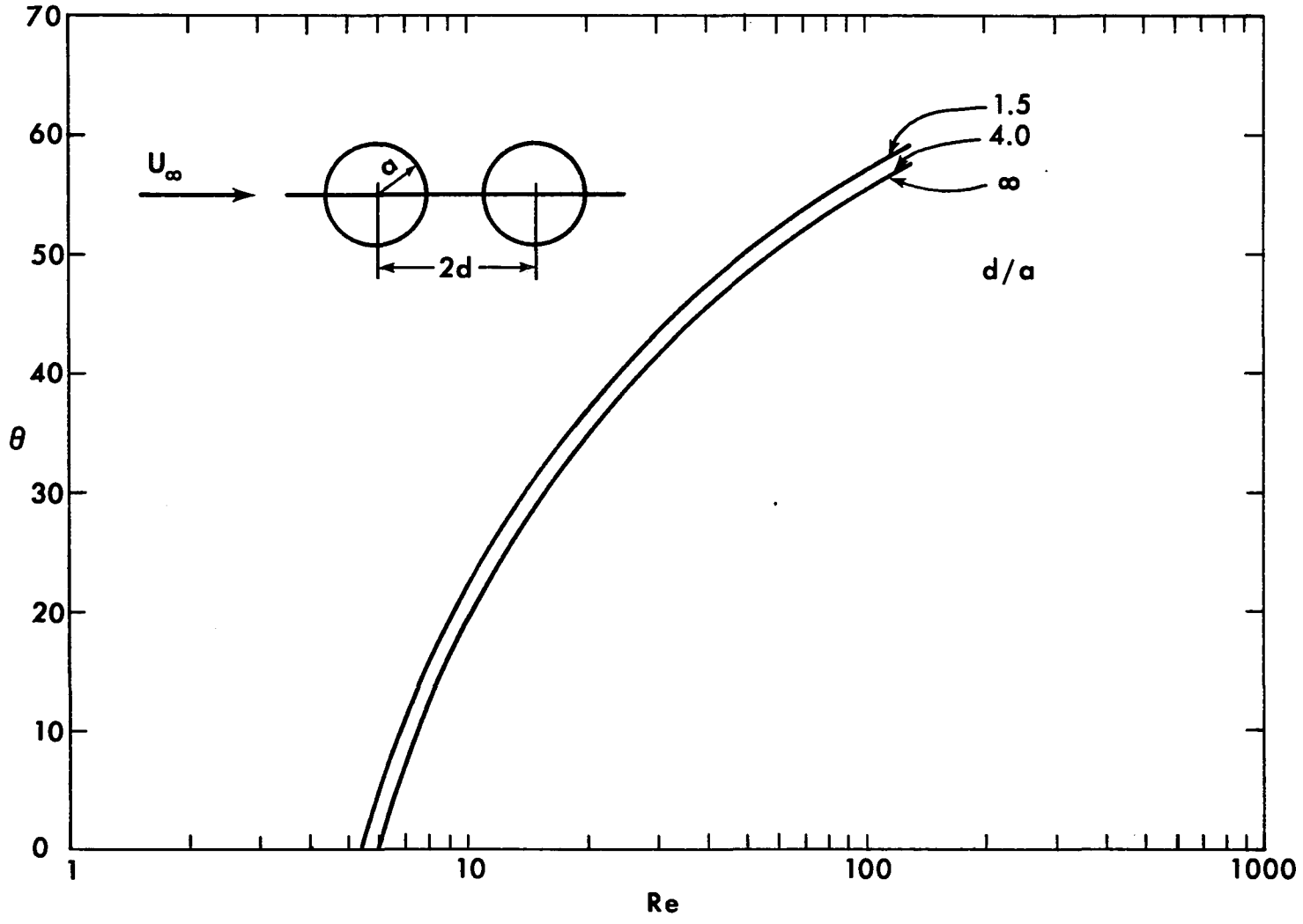

Figure 6.2 - SEPARATION ANGLE VS. Re FOR 2 SPHERES

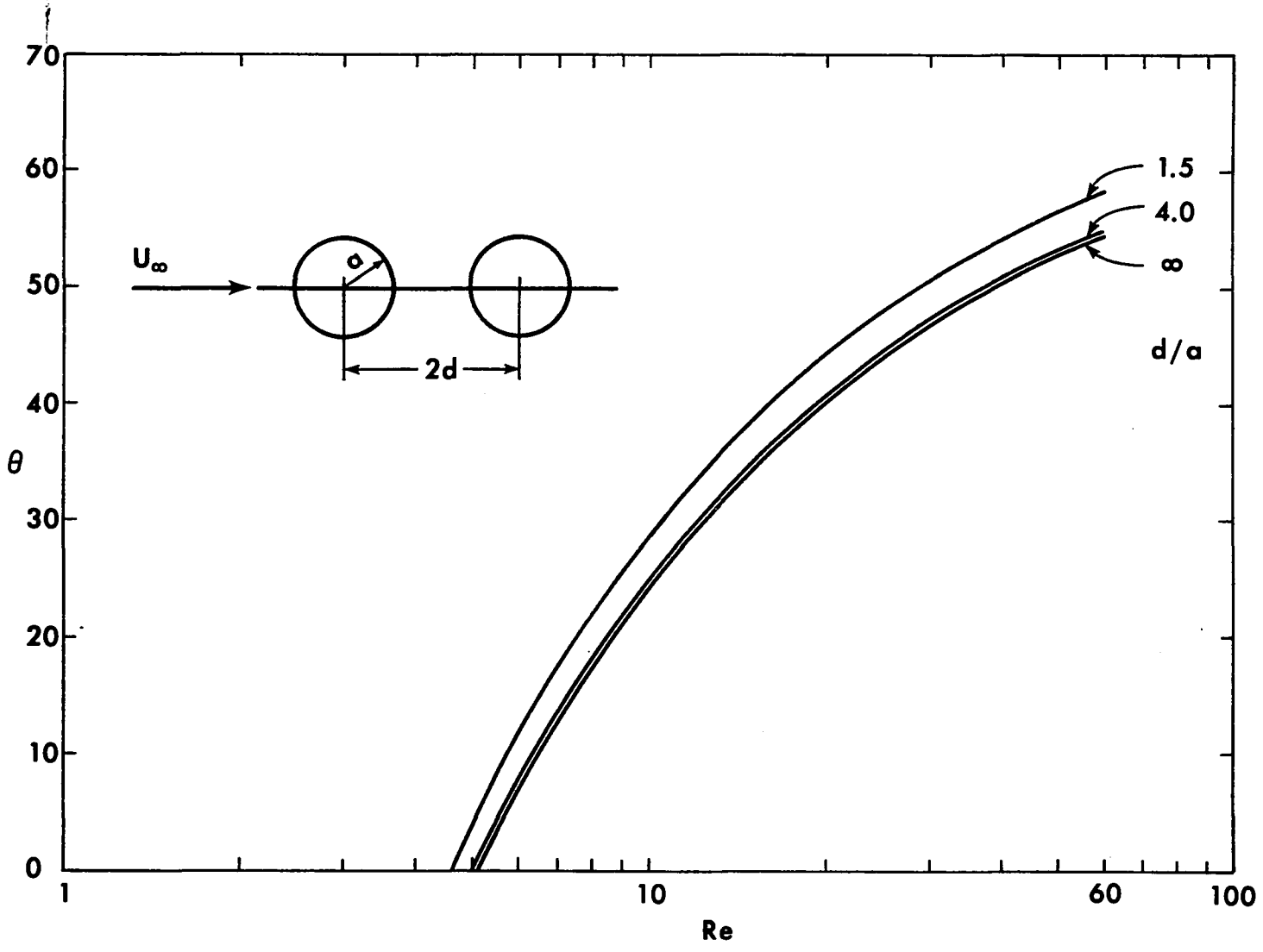

Figure 6.3 - SEPARATION ANGLE VS. Re FOR 2 HORIZONTAL CYLINDERS

esting to note that adding more cylinders behind the second one does not appreciably change the separation angle on the test cylinder. These results are shown in Table 6.1.

Table 6.1

Effect of Number of Cylinders in the Chain on the Separation Angle from the Test Cylinder

Re	Spacing (d/a)	Number of Cylinders (N)	Separation Angle
10	1.5	2	28.7°
		3	28.9°
		10	29.0°
		50	29.0°
40	1.5	2	54.1°
		3	54.2°
		10	54.4°
		50	54.4°

It is believed that this phenomenon is due to the fact that effects from the potential flow solutions are not transmitted to any appreciable extent along a long chain of objects.

The results of these first two multiparticle experiments indicate that the effects on wake formation of chains of particles with their line of centers parallel to the flow are very small.

The last experiment conducted was to investigate the effects of

placing a number of cylinders above and below the test cylinder with line of centers normal to the flow as shown in Figure 6.1(c). Before presenting the results of these trials, the Re needs to be defined more precisely. In all of the previous experiments, the Reynolds number used has been based on particle diameter and free stream velocity, i.e.,

$$Re = \frac{2a\,U_\infty}{\nu} \tag{6.1}$$

However, in this last experiment, a new characteristic length (particle spacing d/a) has been introduced that will obviously effect the fluid velocity in the region of interest and, therefore, the Re (for example, if the cylinders are touching, the fluid behind the test cylinder will be essentially stagnant).

Thus, when the cylinders are very close together, the fluid velocity past the $\theta = \pi/2$ station of the test cylinder will be very large resulting in a high local Re. As separation is directly related to the local velocity and local velocity gradient, it is apparent that separation should be related to the local Re as well as the free stream Re for this particular case. The Reynolds number ($Re_{l\infty}$) at the $\theta = \pi/2$ station of a single isolated cylinder is defined as:

$$Re_{l\infty} = \frac{2a\,U_{l\infty}}{\nu} \tag{6.2}$$

where $U_{l\infty} = 2U_\infty$ for a single cylinder at very large Re. (6.3)

A new local Re will now be defined for flow through the space between two cylinders (spacing d/a) at the $\theta = \pi/2$ station, i.e.,

$$Re_\ell = \frac{L U_\ell}{\nu} \tag{6.4}$$

where U_ℓ = local velocity at $\theta = \pi/2$ station

L = porosity function

The porosity function L must satisfy the requirement that:

$$\begin{aligned} &\text{for } d/a = \infty, \quad L = 2a \\ &\text{as } d/a \to 1, \quad L \gg 2a \end{aligned} \tag{6.5}$$

Consistent with (6.5) it is possible to define L as follows:

$$L = \frac{2a(d/a)}{(d/a - 1)} \tag{6.6}$$

Using (6.1), (6.2), (6.4) and (6.6) the local Reynolds number Re_ℓ can be simply related to the free stream Reynolds number Re:

$$Re_\ell = Re \frac{U_\ell}{U_\infty} \frac{(d/a)}{[(d/a) - 1]} \tag{6.7}$$

Based on the above definition of Re_ℓ, the wake suppression effects of placing a cylinder above and below the test cylinder (line of centers normal to the flow) will be investigated as a function of Re_ℓ and spacing (d/a). The results of this study are plotted in Figure 6.4. This figure demonstrates the relatively dramatic effects of cylinder spacing on wake suppression from the test cylinder. At a cylinder spacing of 1.2 diameters the onset of boundary layer separation is retarded from the single cylinder value of Re = 5.1 to a new critical value of Re = 16.4. These results explain in

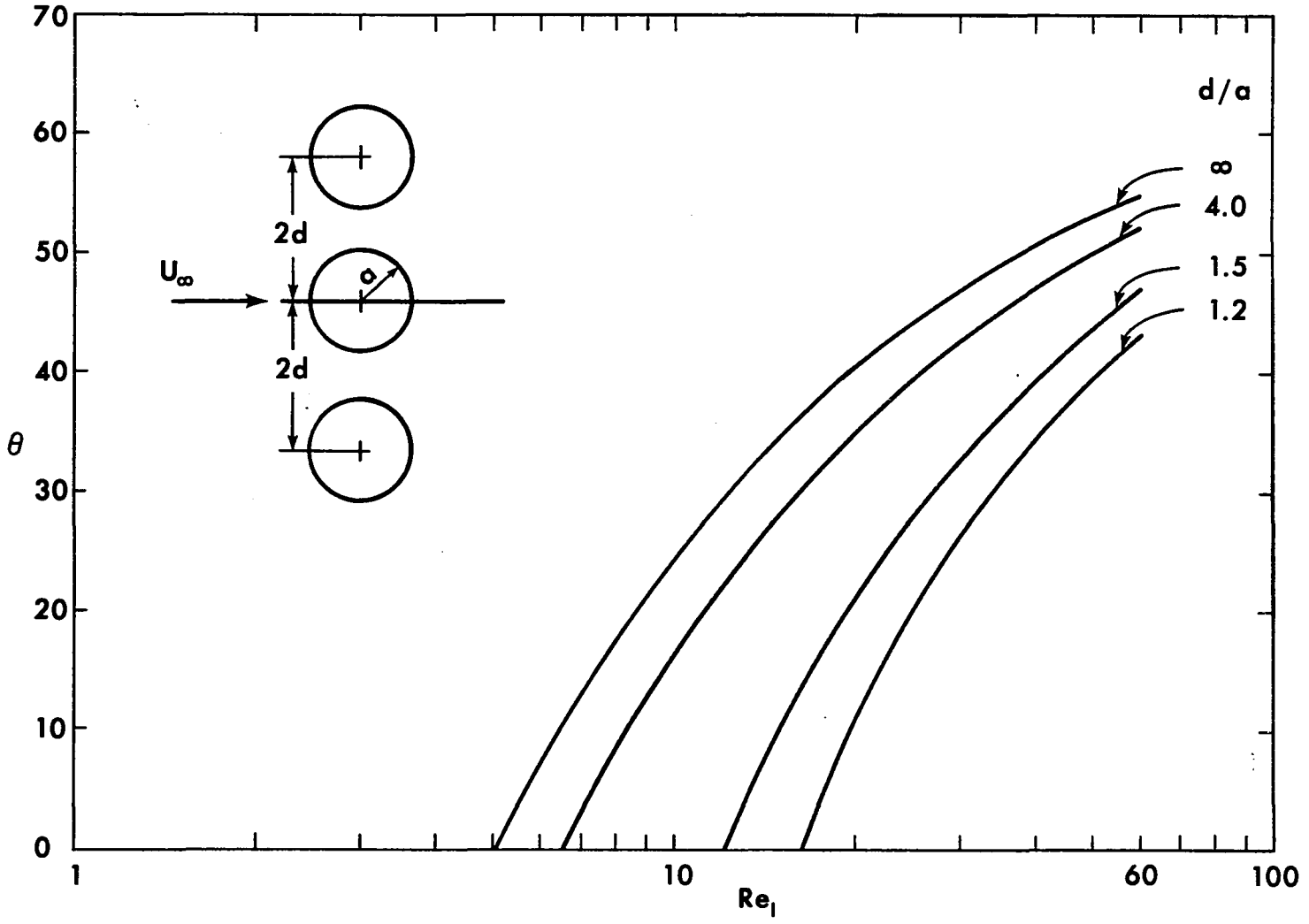

Figure 6.4 - SEPARATION ANGLE VS. Re FOR 3 VERTICAL CYLINDERS

a semi-quantitative manner the effects described in section 5.1, i.e., the ability of the creeping motion equations to determine drag coefficients in packed beds at intermediate Reynolds numbers. They also agree, qualitatively with the numerical results of Leclair and Hamielec (13) for flow through assemblages of spheres. The most interesting feature of the results presented in this section is the fact that the major wake suppression effects are produced by objects normal to the flow direction rather than those parallel to the direction of flow.

CHAPTER 7

SUMMARY AND CONCLUSIONS

The first goal of this work has been to develop a consistent and simply applied technique for treating creeping motion flows relative to finite axisymmetric chains of objects having natural coordinate systems (such as spheres and spheroids) and then to extend the theory to include flows past axisymmetric bodies of revolution of arbitrary shape. It has been shown that any object having a natural coordinate system in a single or multiple flow configuration can be represented by an infinite series of multilobular disturbances emanating from the geometric center of the object. It has further been illustrated that approximate representations can be obtained by truncating the infinite multipole series; the accuracy of the representations being systematically improved by the addition of higher order multipoles.

The rapid convergence of the multipole truncation procedure has been demonstrated for creeping motion flows relative to arrays of two spheres, two prolate spheroids and two oblate spheroids. In all of the above cases it was found that five figure accuracy could be obtained by retaining at most the first nine multipoles in the series even for the cases of objects touching one another. In addition, comparison of the two sphere results with the exact solution of Stimson and Jeffery (7) demonstrated that the converged solution was in actual fact the correct solution.

The flexibility and ease of use of this procedure has been graphically demonstrated by its application to flow configurations involving long finite chains of axisymmetric objects, i.e. chains containing up to 101 spheres or 15 prolate or oblate spheroids. None of these problems have been attempted in the past due to the practical inability of the method

of reflections to account for a large number of interactions of closely spaced objects. Drag results for creeping flow past long finite chains of equally spaced spheres or spheroids indicate that the forces on the objects in the central section of the chain are considerably smaller than the forces on the end objects. These shielding effects are greatest for low aspect ratio objects (e.g. oblate spheroids) and reduce in magnitude as the aspect ratio of the objects in the chain increases.

It has also been demonstrated that the truncated multipole representation technique provides a powerful tool for representing creeping motion axisymmetric flow relative to bodies of revolution of arbitrary shape. Constructing the flow past complex shapes using elemental touching oblate spheroids is equivalent in the limit of vanishing aspect ratio to representing the desired shape by a line source of multilobular disturbances continuously distributed along the axis of rotation of the desired body. It has been found to be sufficient in regions of small boundary curvature to satisfy the exact no slip boundary conditions at only the polar point on the generating arc of each spheroid. It has also been demonstrated that in regions of large boundary curvature such as a cone base or cylinder ends, accurate representations can be achieved by introducing higher order multipoles to satisfy the no slip boundary conditions at a number of points along the generating arc of an oblate spheroid of very low aspect ratio. Qualitative evidence has been presented to show that in the limit of vanishing aspect ratio, the entrained eddies between adjacent spheroids will become vanishingly small, thereby resulting in an exact representation of the desired boundary shape.

Drag calculations for short cylinders and cones have been presented as illustrative examples of the application of the above techniques to

complex bodies of revolution. The predicted results are in remarkably good agreement with experimental data where available. Theoretical data could not be found in the literature indicating that problems of this degree of complexity have not been successfully attempted in the past.

All of the results of this study have indicated that the multipole truncation procedure is an extremely powerful tool for handling multiparticle interaction problems in axisymmetric creeping flow. Extension of these procedures to asymmetric flow configurations would provide a powerful technique for all creeping motion problems relative to finite assemblages of particles of arbitrary shape.

In order to illustrate the application of the multipole procedure to a physically real and previously unsolved multiparticle interaction problem, the settling of three spheres along their line of centers in a gravitational field was investigated for the range $0 < Re \leq 10$. It was found that the final sphere spacings after settling for some time were independent of the initial spacings. Thus, if enough time were allowed in the experiment, the final configuration would consist of the bottom two spheres touching one another and settling as a doublet at a greater velocity than the third sphere which would be left behind. These results are in agreement with qualitative experimental observations.

This quasi-steady state three-body interaction problem exhibited the interesting feature of having two distinct time scales: a short time scale characteristic of the time required for a sphere to approach its quasi-steady terminal settling velocity and a long time scale over which forces due to particle interaction effects dominate the motion due to large changes in sphere spacing. It was found that at low Re the ratio of short to long time scales was very small indicating this type of motion to be dominated except for very small times by the

quasi-steady drag forces. For the higher Re range, however, it was found that the ratio of short to long time scales approached unity, indicating the increase in importance of the unsteady forces associated with sphere accelerations.

The second goal of this work was aimed at developing a procedure for investigating the effects of higher Re flow on boundary layer separation and wake formation for submerged two-dimensional and axisymmetric bodies. In the range of interest ($0 < Re \leq 200$) conventional boundary layer theory does not apply due to the restrictive constraint requiring the boundary layer thickness to be very much smaller than the radius of curvature of the object. Solutions to problems in this Re range have, therefore, only been achieved by the tedious and costly process of numerically solving the complete Navier-Stokes equations of motion.

A new coordinate stretching procedure has been developed along the lines of conventional boundary layer theory that does not require the assumption of thin boundary layers and thus zero pressure gradient in the normal coordinate direction. This new approach is based on the hypothesis that the outer inviscid flow "sees" an object that is larger than the actual object by an amount that is equal to the thickness of the layer of concentrated vorticity along the surface of the submerged body.

Application of this new approach to determine the relationship between Re and separation angle for flow past a two-dimensional cylinder in the range $1 \leq Re \leq 60$ showed remarkable agreement with Navier-Stokes solutions and experimental observations. The onset of separation has been experimentally observed at Re = 5.0. Application of this new procedure predicts incipient wake formation to take place at Re = 5.1. Similar agreement with experimental and numerical solutions was found

when this technique was applied to flow past a single sphere.

Application of this new procedure to flows past two spheres or two cylinder along their lines of centers indicated that the influence of the second object was to slightly decrease the Re required for incipient separation to occur. These effects were found to be small and died out very rapidly as the particle spacing was increased. This was felt to be due to the relatively short range effects attributable to potential or irrotational interactions.

For flow normal to the line of centers of three equally spaced cylinders, approximate determinations of separation from the central cylinder indicated a wake suppression effect at any particular Re that was a strong function of object spacing. This result is in agreement with the semi-quantitative findings of Leclair and Hamielec (13) for flow through beds of spheres.

Therefore, it can be concluded that the proposed coordinate stretching procedure provides for the first time an approximate theory for examining flows past submerged objects in the intermediate Re range without having to solve the exact equations of motion which for many cases of interest is extremely difficult even with presently available high speed computers.

APPENDIX

A.1 POTENTIAL FLOW SOLUTIONS PAST MULTIPLE TWO-DIMENSIONAL CYLINDERS

In 1965 Collins (59) solved the problem of inviscid flow normal to an infinite chain of equally spaced cylinders. The flow geometry is shown in Figure A.1. The approach taken by Collins was as follows. The solution to the two-dimensional irrotational flow problem reduces to solving Laplace's equation.

$$\nabla^2 \phi = 0 \qquad \nabla^2 \psi = 0 \tag{A.1}$$

where the complex potential function is defined by:

$$\omega = \phi + i\psi \tag{A.2}$$

Consider an array of doublets of equal strength spaced uniformly on the imaginary axis in the complex plane. For a doublet of strength $2\pi m\, U_\infty a^2$ the complex potential becomes:

$$\omega = U_\infty \left[z + \frac{ma^2}{z} + \frac{ma^2}{z-2id} + \frac{ma^2}{z+2id} + \frac{ma^2}{z-4id} + \frac{ma^2}{z+4id} + \cdots \right] \tag{A.3}$$

As doublets of equal strength instead of actual cylinders are used for the representation it is apparent from the viscous flow results presented in Chapters 2 and 3 that the boundaries of the submerged objects will not be exactly circular, but will be distorted to some degree based on the object spacing and the position in the chain. These distortions will be smaller in magnitude than those presented for viscous flow due to the relatively short range influence of irrotational as opposed to rotational effects. For flow normal to an infinite chain of doublets having a center to center spacing of two diameters, the elongation

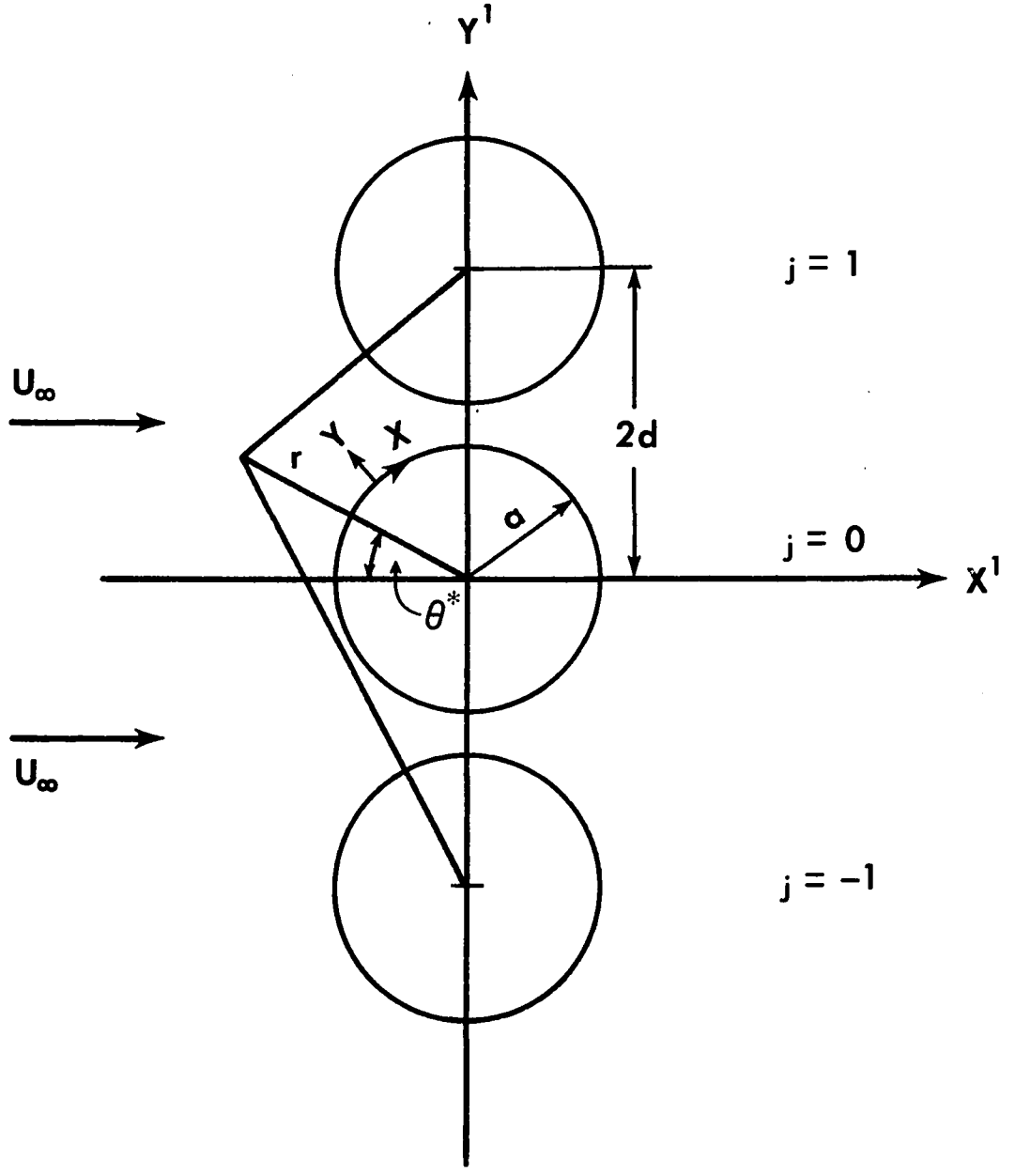

Figure A.1 - GEOMETRY FOR VERTICAL CYLINDER SYSTEM

along the x axis is approximately 2%. Therefore, within the limits of accuracy associated with the boundary layer theory for which these computations are to be used, the small deviations from the cylindrical shape were considered to negligibly small.

For flow past N cylinders (A.3) reduces to:

$$\omega = U_\infty z + m a^2 U_\infty \sum_{j=\frac{-(N-1)}{2}}^{\frac{(N-1)}{2}} \left\{ \frac{1}{z - 2ijd} \right\} \tag{A.4}$$

The stream function (the imaginary part of the complex potential) is determined from (A.4) as:

$$\psi = U_\infty y' - m a^2 U_\infty \sum_j \left\{ \frac{y' - 2jd}{x'^2 + (y' - 2jd)^2} \right\} \tag{A.5}$$

Equation (A.5) can be transformed to polar coordinates using

$$y' = r \sin\theta^* \qquad x' = r \cos\theta^* \tag{A.6}$$

Applying (A.6) to (A.5):

$$\psi = U_\infty r \sin\theta^* - m a^2 U_\infty \sum_j \left[\frac{r \sin\theta^* - 2jd}{r^2 - 4jdr \sin\theta^* + 4j^2 d^2} \right] \tag{A.7}$$

The constant m which determines the doublet strength is determined from the boundary condition:

$$\text{for } r = a \text{ and } \theta^* = \pi/2, \quad \psi = 0 \tag{A.8}$$

Substituting (A.8) in (A.7) yields:

$$m = \frac{1}{a \sum_j \left[\frac{1}{a - 2jd}\right]} \tag{A.9}$$

To determine the required potential velocity U_e along the surface of the cylinder, a further transformation to regular boundary layer coordinates (x, y) is required (see Figure A.1). Letting

$$y = r - a \; ; \; x = a\theta^* \tag{A.10}$$

and since

$$U_e(x) = \frac{\partial \psi}{\partial y} = \frac{\partial \psi}{\partial r} \tag{A.11}$$

and applying (A.11) to (A.7)

$$U_e(x) = U_\infty \sin\theta^* - U_\infty m a^2 \sum_j \left\{ \frac{(r^2 - 4jdr\sin\theta^* + 4j^2d^2)\sin\theta^*}{(r^2 - 4jdr\sin\theta^* + 4j^2d^2)^2} \right.$$

$$\left. - \frac{(r\sin\theta^* - 2jd)(2r - 4jd\sin\theta^*)}{(r^2 - 4jdr\sin\theta^* + 4j^2d^2)^2} \right\} \tag{A.12}$$

Equation (A.12) evaluated at r = a gives

$$U_e(x) = U_\infty \sin\theta^* - U_\infty m a^2 \sum_j \left[\frac{4jda - 4j^2d^2\sin\theta^* - a^2\sin\theta^*}{(a^2 - 4jda\sin\theta^* + 4j^2d^2)^2} \right] \tag{A.13}$$

If only one cylinder is present j = 0 and m = 1.0 from (A.9), and (A.13) reduces to the familiar solution for inviscid flow past a cylinder, i.e.

$$U_e(x) = 2U_\infty \sin\theta^*$$

The acceleration tangent to the cylinder can be found from (A.10) and (A.13), i.e.

$$\frac{d}{dx}\left[U_e(x)\right] = \frac{1}{a}\,\frac{dU_e(x)}{d\theta^*}$$

$$\frac{dU_e}{dx} = \frac{U_\infty}{a}\left[\cos\theta^* - ma^2\sum_j\left\{\frac{(a^2-4jda\sin\theta^*+4j^2d^2)^2(-4j^2d^2\cos\theta^*-a^2\cos\theta^*)}{(a^2-4jda\sin\theta^*+4j^2d^2)^4}\right.\right. \tag{A.14}$$

$$\left.\left. + \frac{(4jda-4j^2d^2\sin\theta^*-a^2\sin\theta^*)(a^2-4jda\sin\theta^*+4j^2d^2)(8jda\cos\theta^*)}{(a^2-4jda\sin\theta^*+4j^2d^2)^4}\right\}\right]$$

(A.14) can be simplified to:

$$\frac{dU_e}{dx} = \frac{U_\infty}{a}\left[\cos\theta^* - ma^2\sum_j\left\{\frac{(a^2-4jda\sin\theta^*+4j^2d^2)(-4j^2d^2\cos\theta^*-a^2\cos\theta^*)}{(a^2-4jda\sin\theta^*+4j^2d^2)^3}\right.\right. \tag{A.15}$$

$$\left.\left. + \frac{(4jda-4j^2d^2\sin\theta^*-a^2\sin\theta^*)(8jda\cos\theta^*)}{(a^2-4jda\sin\theta^*+4j^2d^2)^3}\right\}\right]$$

For a single cylinder, (A.15) reduces to the familiar irrotational relationship:

$$\frac{dU_e}{dx} = \frac{2U_\infty}{a}\cos\theta^*$$

The above development represents flow normal to a chain of equally spaced doublets. A similar development is possible for the case of irrotational flow parallel to the line of centers of a chain of equally spaced cylinders. In 1969 Gabor (60) simply extended Collins' solution to that of flow parallel to an infinite chain of equally spaced doublets of strength $2\pi mU_\infty a^2$ (see Figure A.2). Gabor's solution

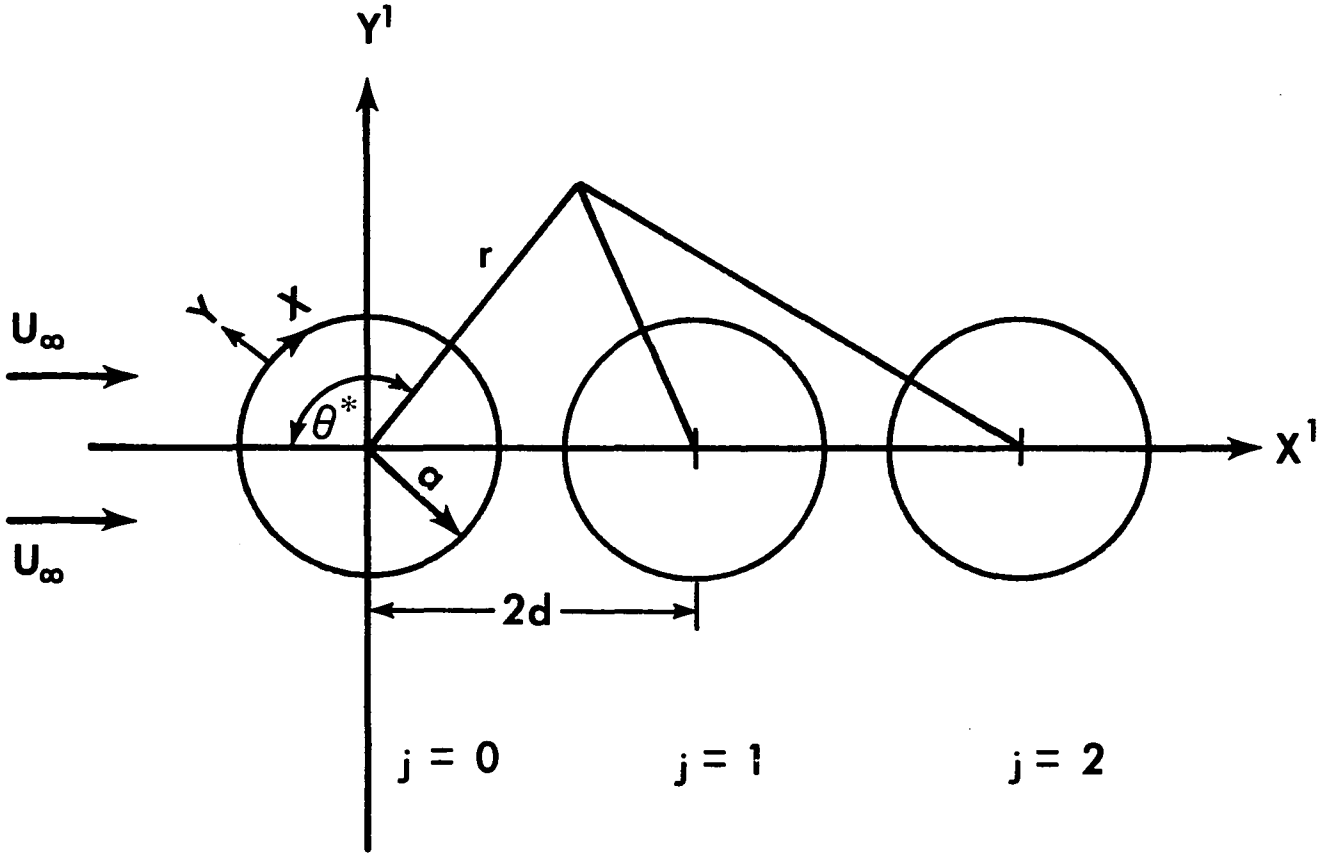

Figure A.2 - GEOMETRY FOR HORIZONTAL CYLINDER SYSTEM

technique will be utilized to determine the stream function for flow past a finite chain of N equally spaced doublets of equal strength resulting in similar distortions to those described previously.

Solving equation (A.1) results in the following expression for the complex potential:

$$\omega = U_\infty \left[z + m a^2 \sum_{j=0}^{N-1} \left\{ \frac{1}{z - 2jd} \right\} \right] \tag{A.16}$$

The stream function (the imaginary part of the complex potential) is determined from (A.16) as:

$$\psi = U_\infty y' - m a^2 U_\infty \sum_j \left[\frac{y'}{(x' - 2jd)^2 + y'^2} \right] \tag{A.17}$$

Equation (A.17) is transformed to polar coordinates by using (A.6) to give

$$\psi = U_\infty r \sin\theta^* - m a^2 U_\infty \sum_j \left[\frac{r \sin\theta^*}{r^2 + 4jdr\cos\theta^* + 4j^2 d^2} \right] \tag{A.18}$$

The constant m is determined from (A.8) and (A.18) so that

$$m = \frac{1}{a^2 \sum_j \left[\frac{1}{a^2 + 4j^2 d^2} \right]} \tag{A.19}$$

To determine the required potential velocity U_e along the surface of the cylinder, a further transformation to regular boundary layer coordinates (x, y) defined by equation (A.10) is required (see Figure A.2). Applying (A.11) to (A.17) results in:

$$U_e(x) = \frac{\partial \psi}{\partial r} = U_\infty \sin\theta^* - m a^2 U_\infty \sum_j \left\{ \frac{(r^2 + 4jdr\cos\theta^* + 4j^2d^2)\sin\theta^*}{(r^2 + 4jdr\cos\theta^* + 4j^2d^2)^2} \right.$$

$$\left. - \frac{r\sin\theta^*(2r + 4jd\cos\theta^*)}{(r^2 + 4jdr\cos\theta^* + 4j^2d^2)^2} \right\} \qquad \text{(A.20)}$$

Equation (A.20) evaluated at r = a yields:

$$U_e(x) = U_\infty \sin\theta^* - m a^2 U_\infty \sum_j \left[\frac{4j^2d^2\sin\theta^* - a^2\sin\theta^*}{(a^2 + 4jda\cos\theta^* + 4j^2d^2)^2} \right] \qquad \text{(A.21)}$$

The acceleration tangent to the cylinder can be found from (A.10) and (A.21).

$$\frac{dU_e}{dx} = \frac{U_\infty}{a} \left\{ \cos\theta^* - m a^2 \sum_j \left[\frac{(a^2 + 4jda\cos\theta^* + 4j^2d^2)^2(-a^2\cos\theta^* + 4j^2d^2\cos\theta^*)}{(a^2 + 4jda\cos\theta^* + 4j^2d^2)^4} \right.\right.$$

$$\left.\left. + \frac{(-a^2\sin\theta^* + 4j^2d^2\sin\theta^*)(a^2 + 4jda\cos\theta^* + 4j^2d^2)(8jda\sin\theta^*)}{(a^2 + 4jda\cos\theta^* + 4j^2d^2)^4} \right] \right\} \qquad \text{(A.22)}$$

Equation (A.22) can be simplified to:

$$\frac{dU_e}{dx} = \frac{U_\infty}{a} \left\{ \cos\theta^* - m a^2 \sum_j \left[\frac{(a^2 + 4jda\cos\theta^* + 4j^2d^2)(-a^2\cos\theta^* + 4j^2d^2\cos\theta^*)}{(a^2 + 4jda\cos\theta^* + 4j^2d^2)^3} \right.\right.$$

$$\left.\left. + \frac{(4j^2d^2\sin\theta^* - a^2\sin\theta^*)(8jda\sin\theta^*)}{(a^2 + 4jda\cos\theta^* + 4j^2d^2)^3} \right] \right\} \qquad \text{(A.23)}$$

A.2 INTEGRAL EQUATION OF MOTION FOR AXISYMMETRIC FLOW

As for the two-dimensional case, the control volume concept will be used to develop the integral equation of motion for flow past an axisymmetric body of revolution. Referring to Figure A.3 the continuity equation can be written as follows:

$$\rho V_e 2\pi R_e dx = \rho U_e \frac{d}{dx_o}(2\pi R_e \delta) dx_o - \frac{\partial}{\partial x_o}\int_o^\delta \rho u 2\pi R dy dx_o \qquad (A.24)$$

or

$$V_e R_e dx = U_e R_e \frac{d\delta}{dx_o} dx_o + U_e \delta \frac{dR_e}{dx_o} dx_o - \frac{\partial}{\partial x_o}\int_o^\delta u R dy dx_o \qquad (A.25)$$

where U_e is defined in the same way that it was for the two-dimensional case in Chapter 5 by hypothesis (c).

The integral momentum equation is developed with reference to Figure A.4 as:

$$-\tau_\omega 2\pi R_o dx_o - \frac{\partial}{\partial x_o}\int_o^\delta p 2\pi R dy dx_o + p_e \frac{\partial}{\partial x_o}\int_o^\delta 2\pi R dy dx_o =$$
$$\frac{\partial}{\partial x_o}\int_o^\delta \rho u^2 2\pi R dy dx_o - \rho U_e^2 \frac{d}{dx_o}(2\pi R_e \delta) dx_o + \rho U_e V_e 2\pi R_e dx \qquad (A.26)$$

Dividing (A.26) by $2\pi\rho\, dx_o$ and substituting for $V_e R_e dx$ from (A.25):

$$-\frac{\tau_\omega}{\rho} R_o - \frac{\partial}{\partial x_o}\int_o^\delta \frac{p}{\rho} R dy + \frac{p_e}{\rho}\frac{\partial}{\partial x_o}\int_o^\delta R dy = \frac{\partial}{\partial x_o}\int_o^\delta u^2 R dy$$
$$-U_e^2 \delta \frac{dR_e}{dx_o} - U_e^2 R_e \frac{d\delta}{dx_o} + U_e^2 R_e \frac{d\delta}{dx_o} + U_e^2 \delta \frac{dR_e}{dx_o} - U_e \frac{\partial}{\partial x_o}\int_o^\delta u R dy \qquad (A.27)$$

Applying Leibnitz's Rule to (A.27):

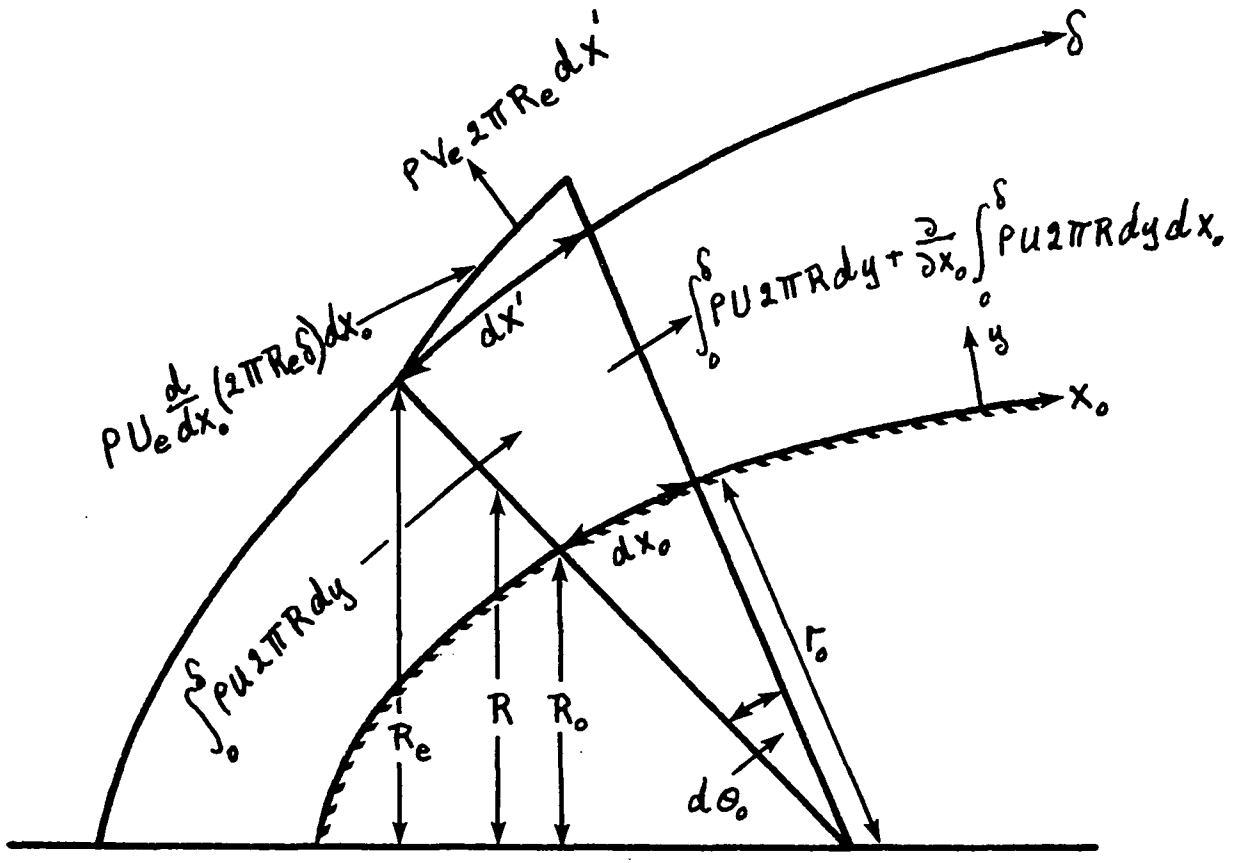

Figure A.3 - CONTINUITY DIAGRAM FOR AXISYMMETRIC BODY

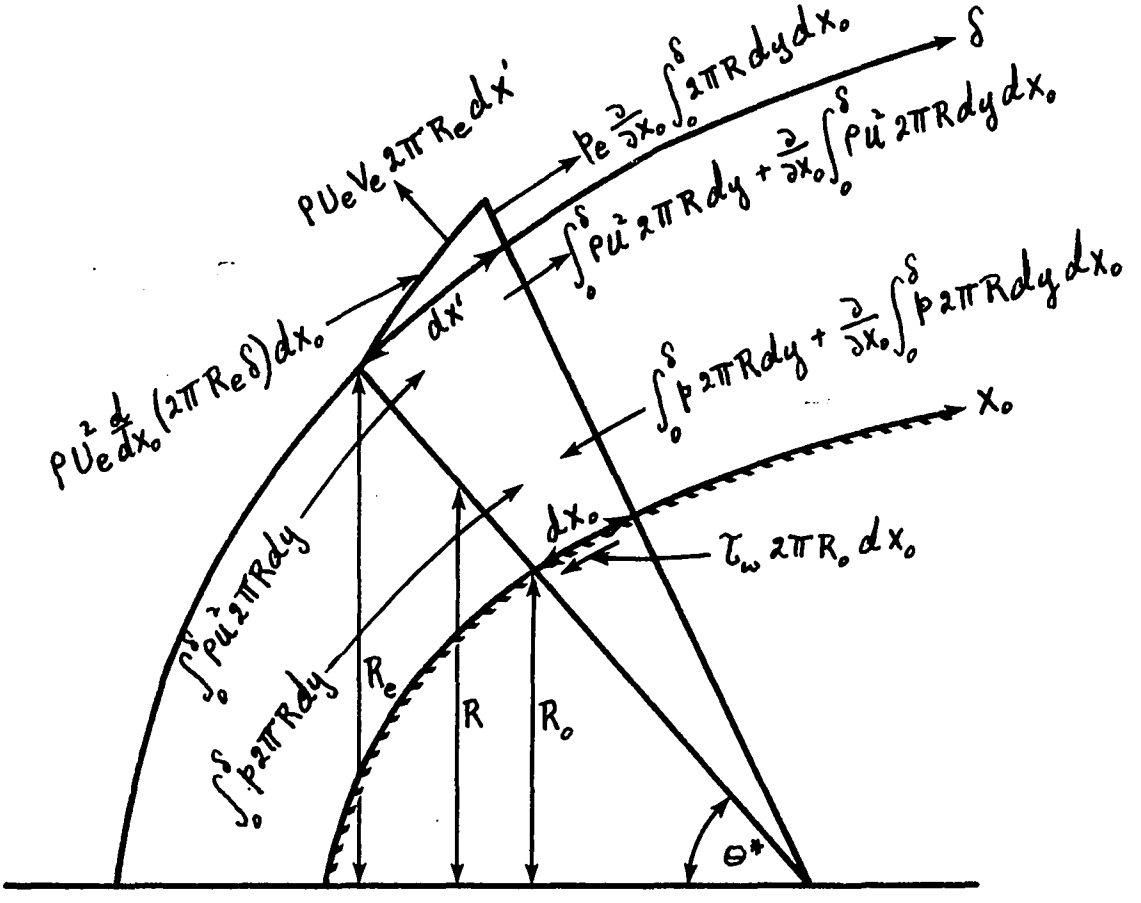

Figure A.4 - FORCE DIAGRAM FOR AXISYMMETRIC BODY

$$-\frac{\tau_w}{\rho}R_o - \int_0^\delta \frac{1}{\rho}\frac{\partial}{\partial x_o}(pR)\,dy - \frac{p_e}{\rho}R_e\frac{d\delta}{dx_o} + \frac{p_e}{\rho}\int_0^\delta \frac{\partial R}{\partial x_o}\,dy + \frac{p_e}{\rho}R_e\frac{d\delta}{dx_o} =$$

$$\int_0^\delta \frac{\partial}{\partial x_o}(u^2R)\,dy + U_e^2R_e\frac{d\delta}{dx_o} - U_e\int_0^\delta \frac{\partial}{\partial x_o}(uR)\,dy - U_e^2R_e\frac{d\delta}{dx_o} \qquad \text{(A.28)}$$

As was explained in Chapter 5, the pressure p in the second term on the left of (A.28) is not constant across the viscous layer if $\delta = 0(r_o)$. Therefore, hypothesis (b) must be invoked and equation 5.2 used, i.e.

$$\int_0^\delta \frac{\partial p}{\partial x_o}\,dy = \frac{dp^*}{dx_o} \qquad \text{(5.2)}$$

Equation (5.2) implies that

$$p_e = p^* \qquad \text{(A.29)}$$

Applying (5.2) and (A.29) to the second term on the left of (A.28)

$$-\int_0^\delta \frac{1}{\rho}\frac{\partial}{\partial x_o}(pR)\,dy = -\int_0^\delta \frac{1}{\rho}R\frac{dp^*}{dx_o}\,dy - \frac{p_e}{\rho}\int_0^\delta \frac{\partial R}{\partial x_o}\,dy \qquad \text{(A.30)}$$

Substituting (A.30) in (A.28) gives

$$-\frac{\tau_w}{\rho}R_o - \int_0^\delta \frac{1}{\rho}R\frac{dp^*}{dx_o}\,dy - \frac{p_e}{\rho}\int_0^\delta \frac{\partial R}{\partial x_o}\,dy + \frac{p_e}{\rho}\int_0^\delta \frac{\partial R}{\partial x_o}\,dy =$$

$$\int_0^\delta \frac{\partial}{\partial x_o}(u^2R)\,dy - U_e\int_0^\delta \frac{\partial}{\partial x_o}(uR)\,dy \qquad \text{(A.31)}$$

Also, from Bernoulli's theorem

$$\frac{1}{\rho}\frac{dp^*}{dx_o} = -U_e\frac{dU_e}{dx_o} \qquad \text{(A.32)}$$

Substituting (A.32) in (A.31) and rearranging, gives

$$\frac{\tau_\omega}{\rho} = \frac{1}{R_o} U_e \frac{dU_e}{dx_o}\int_0^\delta R\,dy - \frac{1}{R_o}\int_0^\delta \frac{\partial}{\partial x_o}(u^2 R)\,dy + \frac{1}{R_o} U_e \int_0^\delta \frac{\partial}{\partial x_o}(uR)\,dy \qquad \text{(A.32a)}$$

Expanding (A.32a) and letting differentiation with respect to x_o be represented by a prime:

$$\frac{\tau_\omega}{\rho} = \int_0^\delta \left\{ \frac{R}{R_o} U_e U_e' - \frac{R}{R_o}\frac{\partial}{\partial x_o}(u^2) - \frac{R'}{R_o}u^2 + \frac{R}{R_o}U_e\frac{\partial u}{\partial x_o} + \frac{R'}{R_o}U_e u \right\} dy \qquad \text{(A.33)}$$

But

$$U_e \frac{\partial u}{\partial x_o} = \frac{\partial}{\partial x_o}\left[U_e u\right] - u U_e' \qquad \text{(A.34)}$$

Therefore:

$$\frac{\tau_\omega}{\rho} = \int_0^\delta \left\{ \frac{R}{R_o} U_e U_e' - \frac{R}{R_o}\frac{\partial}{\partial x_o}(u^2) - \frac{R'}{R_o}u^2 + \frac{R}{R_o}\frac{\partial}{\partial x_o}(U_e u) \right. \qquad \text{(A.35)}$$

$$\left. - \frac{R}{R_o} u U_e' + \frac{R'}{R_o} U_e u \right\} dy$$

At this point the variable R will be expressed in terms of R_o and a local boundary slope with the aid of Figure A.5

$$R = R_o + y\cos\varepsilon \qquad \text{(A.36)}$$

But

$$\cos\varepsilon = \left[1 - \left(\frac{dR_o}{dx_o}\right)^2\right]^{1/2} \qquad \text{(A.36a)}$$

so that

$$R = R_o + \gamma y \qquad \text{(A.37)}$$

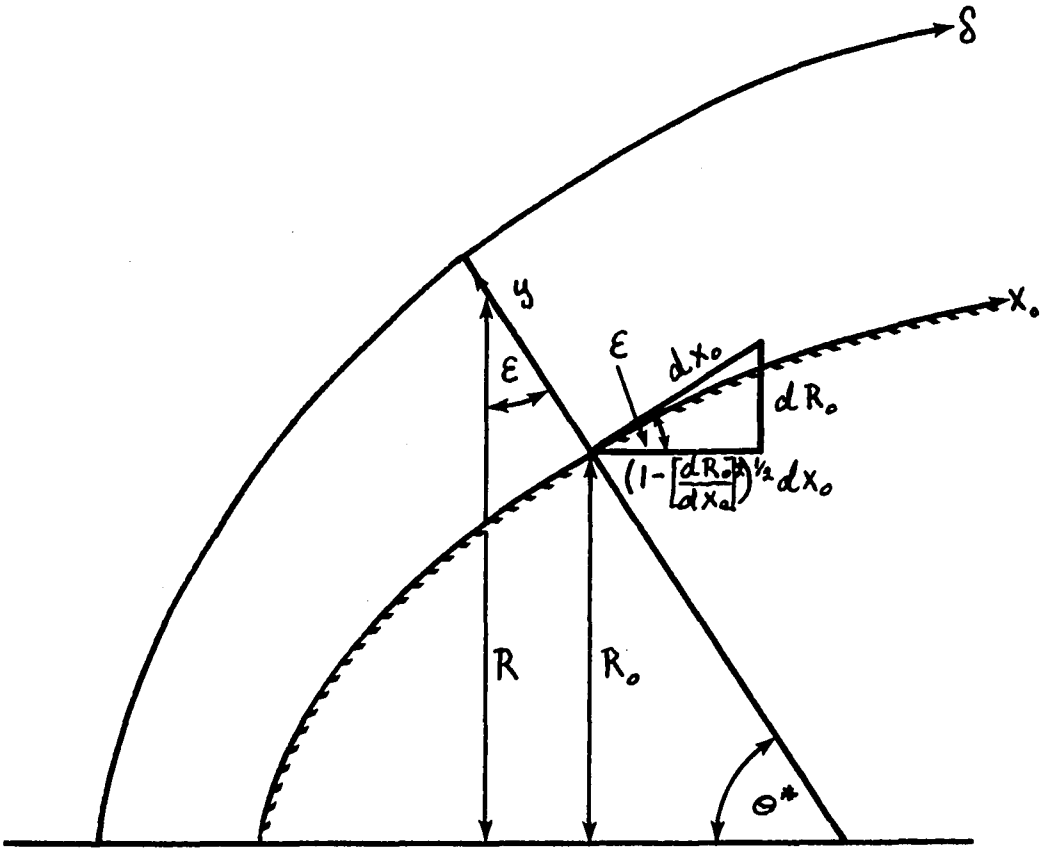

Figure A.5 - AXISYMMETRIC SHAPE FACTOR DIAGRAM

Equation (A.37) in (A.35) gives

$$\frac{\tau_w}{\rho} = \int_0^\delta \Big\{ U_e U_e' + \frac{\gamma}{R_o} y U_e U_e' - \frac{\partial u^2}{\partial x_o} - \frac{\gamma}{R_o} y \frac{\partial u^2}{\partial x_o} - \frac{R_o'}{R_o} u^2$$

$$- \frac{\gamma'}{R_o} y u^2 + \frac{\partial}{\partial x_o}(U_e u) + \frac{\gamma}{R_o} y \frac{\partial}{\partial x_o}(U_e u) - u U_e' \qquad \text{(A.38)}$$

$$- \frac{\gamma}{R_o} y u U_e' + \frac{R_o'}{R_o} u U_e + \frac{\gamma'}{R_o} y u U_e \Big\} dy$$

Rearranging (A.38)

$$\frac{\tau_w}{\rho} = \int_0^\delta \frac{\partial}{\partial x_o} u(U_e - u) dy + U_e' \int_0^\delta (U_e - u) dy + \frac{R_o'}{R_o} \int_0^\delta u(U_e - u) dy$$

$$+ \frac{\gamma}{R_o} \Big[\int_0^\delta \frac{\partial}{\partial x_o} u(U_e - u) y dy + U_e' \int_0^\delta (U_e - u) y dy \Big] + \frac{\gamma'}{R_o} \int_0^\delta u(U_e - u) y dy \qquad \text{(A.39)}$$

and applying Leibnitz's Rule to (A.39)

$$\frac{\tau_w}{\rho} = \frac{\partial}{\partial x_o} \int_0^\delta u(U_e - u) dy + U_e' \int_0^\delta (U_e - u) dy + \frac{R_o'}{R_o} \int_0^\delta u(U_e - u) dy$$

$$+ \frac{\gamma}{R_o} \Big\{ \frac{\partial}{\partial x_o} \int_0^\delta [u U_e y - u^2 y] dy + U_e' \int_0^\delta [U_e y - u y] dy \Big\} + \frac{\gamma'}{R_o} \int_0^\delta [u U_e y - u^2 y] dy \qquad \text{(A.40)}$$

It is of extreme interest to note that equation (A.40) is identical to the equation of motion developed by Millikan (61) by integrating the axisymmetric boundary layer equations without the assumption that for $\delta \ll r_o$, $R \approx R_o$.

Utilizing the conventional definitions for the displacement and momentum thickness from equations (5.15) and (5.16) in (A.40)

$$\frac{\tau_w}{\rho} = \frac{d}{dx_o}(\theta U_e^2) + \delta^* U_e U_e' + \frac{R_o'}{R_o} U_e' \theta$$

$$+ \frac{\gamma}{R_o} \Big\{ \frac{\partial}{\partial x_o} \int_0^\delta [u U_e y - u^2 y] dy + U_e' \int_0^\delta [U_e y - u y] dy \Big\} + \frac{\gamma'}{R_o} \int_0^\delta [u U_e y - u^2 y] dy \qquad \text{(A.41)}$$

The first three terms on the right of equation (A.41) will be recognized as being identical to the terms occurring in the conventional axisymmetric boundary layer equation. The remaining terms on the right of equation (A.41) represent effects of boundary curvature which cannot be neglected if $\delta = O(r_o)$. These curvature terms can only be evaluated after a velocity profile is chosen for the viscous flow region.

As for the two-dimensional case, the Pohlhausen profile will be used, i.e.

$$\frac{u}{U_e} = e\left(\frac{y}{\delta}\right) + f\left(\frac{y}{\delta}\right)^2 + g\left(\frac{y}{\delta}\right)^3 + h\left(\frac{y}{\delta}\right)^4 \tag{5.18}$$

The integrals in the curvature terms of equation (A.41) that need to be evaluated are:

$$\int_0^\delta u y\,dy \quad \text{and} \quad \int_0^\delta u^2 y\,dy$$

These terms can be directly obtained by substituting for u from equation (5.18) and integrating. Recognizing that:

$$u^2 = U_e^2\left[e^2\left(\frac{y}{\delta}\right)^2 + 2ef\left(\frac{y}{\delta}\right)^3 + (f^2+2eg)\left(\frac{y}{\delta}\right)^4 + 2(eh+fg)\left(\frac{y}{\delta}\right)^5 + (g^2+2fh)\left(\frac{y}{\delta}\right)^6 + 2gh\left(\frac{y}{\delta}\right)^7 + h^2\left(\frac{y}{\delta}\right)^8\right] \tag{A.42}$$

it can be seen that:

$$\int_0^\delta u^2 y\,dy = A_1 U_e^2 \delta^2 \quad \text{and} \quad \int_0^\delta u y\,dy = A_2 U_e \delta^2$$

$$A_1 = \left[\frac{e^2}{4} + \frac{2ef}{5} + \frac{(f^2+2eg)}{6} + \frac{2(eh+fg)}{7} + \frac{(g^2+2fh)}{8} + \frac{2gh}{9} + \frac{h^2}{10}\right] \tag{A.43}$$

$$A_2 = \frac{e}{3} + \frac{f}{4} + \frac{g}{5} + \frac{h}{6}$$

Substituting (A.43) in (A.41) gives

$$\frac{\tau_w}{\rho} = \frac{d}{dx_0}(\theta U_e^2) + \delta^* U_e U_e' + \frac{R_0'}{R_0} U_e^2 \theta$$
$$+ \frac{\gamma}{R_0}\left\{\frac{d}{dx_0}\left[(A_2 - A_1) U_e^2 \delta^2\right] + \left(\tfrac{1}{2} - A_2\right) U_e U_e' \delta^2\right\} + \frac{\gamma'}{R_0}(A_2 - A_1) U_e^2 \delta^2 \qquad \text{(A.44)}$$

Using the following definitions from Chapter 5:

$$\Lambda = \frac{\delta^2}{\nu} U_e' \qquad (5.20)$$

$$e = 2 + \frac{\Lambda}{6} \qquad (5.21)$$

$$\frac{\tau_w}{\rho} = \frac{e \nu U_e}{\delta} \qquad (5.22)$$

and putting

$$F_1 = \left\{\frac{d}{dx_0}\left[(A_2 - A_1) U_e^2 \delta^2\right] + \left(\tfrac{1}{2} - A_2\right) U_e U_e' \delta^2\right\}$$
$$F_2 = (A_2 - A_1) U_e^2 \delta^2 \qquad \text{(A.45)}$$

equation (A.44) reduces to:

$$\frac{e \nu U_e}{\delta} = U_e^2 \frac{d\theta}{dx_0} + 2\theta U_e U_e' + \delta^* U_e U_e' + \frac{R_0'}{R_0} U_e^2 \theta$$
$$+ \frac{\gamma}{R_0} F_1 + \frac{\gamma'}{R_0} F_2 \qquad \text{(A.46)}$$

Dividing equation (A.46) by $U_e U_e' \delta$:

$$\frac{e}{\Lambda} = \frac{U_e}{U_e' \delta} \frac{d\theta}{dx_0} + 2\frac{\theta}{\delta} + \frac{\delta^*}{\delta} + \frac{R_0'}{R_0} \frac{U_e}{U_e'} \frac{\theta}{\delta}$$
$$+ \frac{\gamma F_1}{R_0 U_e U_e' \delta} + \frac{\gamma' F_2}{R_0 U_e U_e' \delta} \qquad \text{(A.47)}$$

Rearranging equation (A.47) results in:

$$\frac{d\theta}{dx_o} = \frac{(\Lambda \nu U_e')^{1/2}}{U_e}\left[\frac{2}{\Lambda} + \frac{1}{6} - 2\frac{\theta}{\delta} - \frac{\delta^*}{\delta} - \frac{R_e'}{R_o}\frac{U_e}{U_e'}\frac{\theta}{\delta}\right.$$
$$\left. - \frac{\gamma F_1}{R_o U_e U_e' \delta} - \frac{\gamma' F_2}{R_o U_e U_e' \delta}\right] \qquad \text{(A.48)}$$

The variable δ can be replaced in the last two terms of (A.48) using equation (5.20)

$$\frac{d\theta}{dx_o} = \frac{(\Lambda \nu U_e')^{1/2}}{U_e}\left[\frac{2}{\Lambda} + \frac{1}{6} - 2\frac{\theta}{\delta} - \frac{\delta^*}{\delta} - \frac{R_e'}{R_o}\frac{U_e}{U_e'}\frac{\theta}{\delta}\right.$$
$$\left. - \frac{\gamma F_1}{R_o U_e (\Lambda \nu U_e')^{1/2}} - \frac{\gamma' F_2}{R_o U_e (\Lambda \nu U_e')^{1/2}}\right] \qquad \text{(A.49)}$$

A.3 POTENTIAL FLOW SOLUTIONS PAST TWO SPHERES

The solution to the problem of irrotational flow reduces to finding an appropriate solution to Laplace's equation, i.e. Milne-Thomson (35) and Sampson (22), i.e.

$$\nabla^2 \Psi = 0 \qquad \text{(A.50)}$$

in spherical coordinates

$$\nabla^2 = \frac{\partial^2}{\partial r^2} + \frac{(1-\mu^2)}{r^2}\frac{\partial^2}{\partial \mu^2} \qquad \text{(A.51)}$$

and $\mu = \cos\theta^*$ where the stream function Ψ is defined as:

$$V_r = -\frac{1}{r^2 \sin\theta^*}\frac{\partial \Psi}{\partial \theta^*} \qquad V_\theta = \frac{1}{r \sin\theta^*}\frac{\partial \Psi}{\partial r} \qquad \text{(A.52)}$$

Sampson (22) has shown that the general solution in spherical coordinates to (A.50) for flow past a sphere can be written as:

$$\psi = \tfrac{1}{2} U_\infty r^2 \sin^2\theta^* + \sum_{n=2}^{\infty} \left[B_n r^{-n+1}\right] I_n(\beta) \qquad \text{(A.53)}$$

where B_n = constants

$I_n(\beta)$ = Gegenbauer functions of the first kind defined in Chapter 2 by equation (2.6).

The linearity of (A.50) allows solutions for flow past more than one sphere to be achieved by superimposing individual solutions utilizing exactly the same procedures as described in Chapter 2 for the rotational flow problem. Therefore, referring to Figure A.6, the solution to the stream function for irrotational flow past two spheres is:

$$\psi = \tfrac{1}{2} U_\infty r^2 \sin^2\theta^* + \sum_{n=2}^{\infty} \left[B_n r^{-n+1} I_n(\cos\theta^*) + B_n' r_1^{-n+1} I_n(\cos\theta_1^*)\right] \qquad \text{(A.54)}$$

The r_1 and θ_1^* coordinates can be related to the r, θ^* coordinates by:

$$r_1 = (r^2 + 4d^2 + 4rd\cos\theta^*)^{1/2}$$
$$\sin\theta_1^* = \frac{r}{r_1}\sin\theta^* \qquad \text{(A.55)}$$

The Gegenbauer functions in (A.54) represent multilobular disturbances emanating from the center of each sphere as described in Chapter 2. The B_n and B_n' constants in each term in the infinite series in (A.54) control the strength of each multipole and are determined by satisfying the zero normal velocity boundary conditions over the entire generating arc of each sphere such that

$$\text{on } r = a \qquad \psi = 0$$
$$\text{and, on } r_1 = a \qquad \psi = 0 \qquad \text{(A.56)}$$

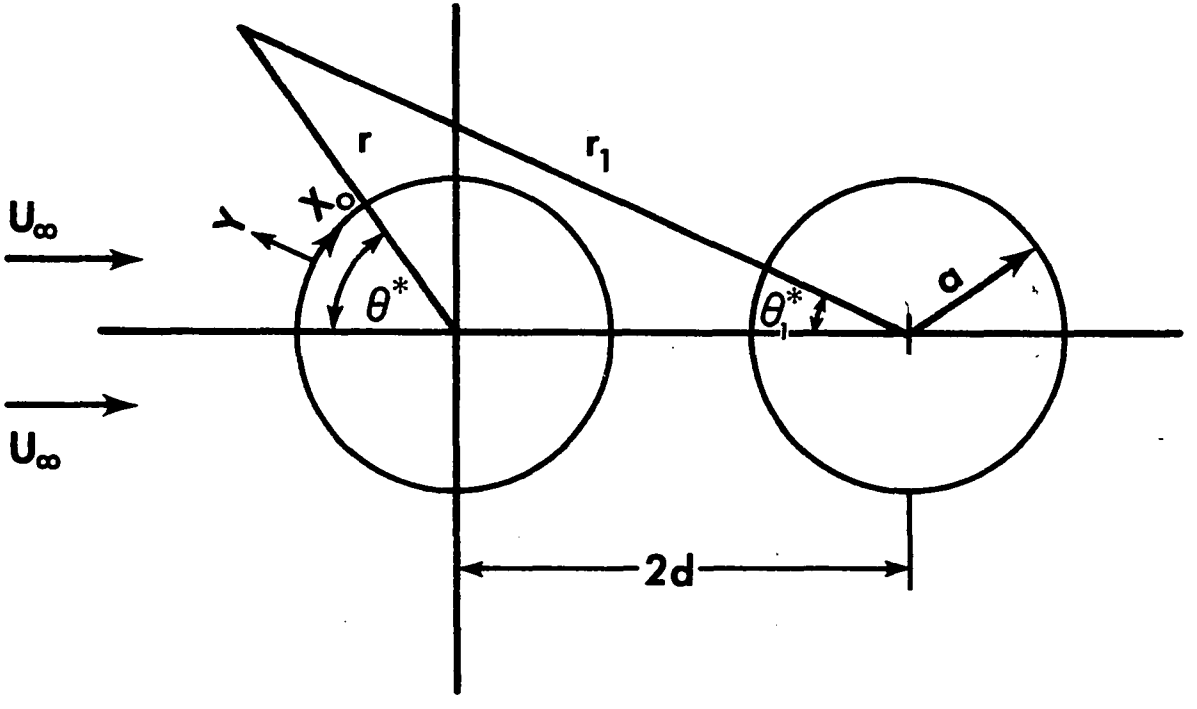

Figure A.6 - GEOMETRY FOR 2 SPHERE SYSTEM

The infinite series in equation (A.54) can be truncated by satisfying conditions (A.56) at a discrete number of points along the generating arc of each sphere. These procedures have already been described in detail in Chapter 2.

To determine the required velocity U_e along the surface of the sphere, a transformation to regular boundary layer coordinates (x, y) is required (see Figure A.6).

$$x = a\theta^* \; ; \; y = r - a \tag{A.57}$$

It has been shown by Happel and Brenner (1) that:

$$U_e(x) = \frac{1}{r \sin\theta^*} \frac{\partial \Psi}{\partial y} = \frac{1}{r \sin\theta^*} \frac{\partial \Psi}{\partial r} \tag{A.58}$$

Applying (A.58) to (A.54)

$$U_e(x) = \frac{1}{r \sin\theta^*} \left\{ U_\infty r \sin^2\theta^* + \sum_{n=2}^{\infty} \left[(-n+1) B_n r^{-n} I_n(\cos\theta^*) \right.\right.$$

$$\left.\left. + B_n' r_1^{-n+1} \left[-P_{n-1}(\cos\theta_1^*) \right] \frac{\partial \cos\theta_1^*}{\partial r} + B_n' (-n+1) I_n(\cos\theta_1^*) r_1^{-n} \frac{\partial r_1}{\partial r} \right] \right\} \tag{A.59}$$

where $P_{n-1}(\cos\theta_1^*)$ is a Legendre function of the first kind.

From (A.55) it can be shown that:

$$\frac{\partial \cos\theta_1^*}{\partial r} = \frac{-2d \sin^2\theta_1^*}{r r_1^2 \cos\theta_1^*} \left[r \cos\theta^* + 2d \right]$$

$$\frac{\partial r_1}{\partial r} = \frac{r + 2d \cos\theta^*}{r_1} \tag{A.60}$$

Rewriting (A.59) yields the following expression for $U_e(x)$:

$$U_e(x) = U_\infty \sin\theta^* + \sum_{n=2}^{\infty} \left\{ (-n+1) B_n r^{-n-1} \frac{I_n(\cos\theta^*)}{\sin\theta^*} \right.$$

$$\left. - B_n' \frac{r_1^{-n+1}}{r \sin\theta^*} P_{n-1}(\cos\theta_1^*) \frac{\partial \cos\theta_1^*}{\partial r} + (-n+1) B_n' \frac{r_1^{-n}}{r \sin\theta^*} I_n(\cos\theta_1^*) \frac{\partial r_1}{\partial r} \right\} \tag{A.61}$$

If only one sphere is present so that $B_n' = 0$, it can be shown that:

$$B_2 = -U_\infty a^3 \; ; \; B_3 = B_4 = ... \; B_n = 0 \qquad (A.62)$$

Equation (A.62) in (A.61) and the result evaluated at r = a produces the familiar expression for the tangential velocity past a single sphere, i.e.

$$U_e(x) = 3/2 \; U_\infty \sin\theta^*$$

A.4 FORWARD STAGNATION POINT ANALYSIS

(i) Two-Dimensional Flow

The equation of motion for two-dimensional flow is given by equation (5.25)

$$\frac{d\theta}{dx_o} = \frac{(\Lambda \nu U_e')^{1/2}}{U_e}\left[\frac{2}{\Lambda} + \frac{1}{6} - 2\frac{\theta}{\delta} - \frac{\delta^*}{\delta}\right] \qquad (5.25)$$

At the forward stagnation point $U_e = 0$ and U_e' is finite and different from zero for a cylinder. The initial slope of the integral curve $d\theta/dx_o$ would become infinite if the term in parenthesis in equation (5.25) did not vanish at the forward stagnation point so that

$$\frac{2}{\Lambda} + \frac{1}{6} - 2\frac{\theta}{\delta} - \frac{\delta^*}{\delta} = 0 \qquad (A.63)$$

Both θ/δ and δ^*/δ are functions of Λ (see equation (5.26)) and therefore equation (A.63) can be solved for Λ at the forward stagnation point to give

$$\Lambda_{f.s.p.} = 7.052$$

(ii) Axisymmetric Flow

The equation of motion for axisymmetric flow is given by equation (A.48)

$$\frac{d\theta}{dx_0} = \frac{(\Lambda \nu U_e')^{1/2}}{U_e}\left[\frac{2}{\Lambda} + \frac{1}{6} - 2\frac{\theta}{\delta} - \frac{\delta^*}{\delta} - \frac{R_e'}{R_0}\frac{U_e}{U_e'}\frac{\theta}{\delta} - \frac{\gamma F_1}{R_0 U_e U_e' \delta} - \frac{\gamma' F_2}{R_0 U_e U_e' \delta}\right] \tag{A.48}$$

For the same reasons given in (i) the term in parenthesis in (A.48) must be zero at the forward stagnation point so that

$$\frac{2}{\Lambda} + \frac{1}{6} - 2\frac{\theta}{\delta} - \frac{\delta^*}{\delta} - \frac{R_0'}{R_0}\frac{U_e}{U_e'}\frac{\theta}{\delta} - \frac{\gamma F_1}{R_0 U_e U_e' \delta} - \frac{\gamma' F_2}{R_0 U_e U_e' \delta} = 0 \tag{A.64}$$

Before equation (A.64) can be solved, the last three terms on the right need to be analyzed. These terms will be investigated for flow past a single sphere due to the simplicity of the expressions for U_e and U_e' for that case. If more than one sphere is present it has not been shown that the following results for the forward stagnation point will be exact due to the complexity of the multiple sphere expression for U_e'. However, even if the following results are not exact for the multiple sphere case they will provide a good estimate of the stagnation point conditions due to the very small effect of particle interactions on U_e' at the forward stagnation point.

For a single sphere the quantities required for equation (A.64) are defined below with reference to Figure A.5.

$$
\begin{aligned}
U_e &= \tfrac{3}{2} U_\infty \sin\theta^* \\
U_e' &= \tfrac{3}{2} \frac{U_\infty}{r_0} \cos\theta^* \\
R_0 &= r_0 \sin\theta^* \\
R_0' &= \cos\theta^* \\
\gamma &= \sin\theta^* \\
\gamma' &= \frac{1}{r_0} \cos\theta^*
\end{aligned}
\tag{A.65}
$$

Consider $\frac{R_0'}{R_0} \frac{U_e}{U_e'} \frac{\theta}{\delta}$ at the forward stagnation point:

$$
\frac{R_0'}{R_0} \frac{U_e}{U_e'} \frac{\theta}{\delta} = \frac{1}{r_0} \frac{\theta}{\delta} \tag{A.66}
$$

Now considering $\gamma F_1 / R_0 U_e U_e' \delta$ and substituting for F_1 from equation (A.45) gives

$$
\frac{\gamma}{R_0 U_0 U_e' \delta} \left[\frac{d}{dx_0} \left\{ (A_2 - A_1) U_e^2 \delta^2 \right\} + \left(\tfrac{1}{2} - A_2\right) U_e U_e' \delta^2 \right] =
$$

$$
\begin{aligned}
&\frac{\gamma}{R_0 U_0 U_e' \delta} \Big[U_e^2 \delta^2 \frac{d}{dx_0} (A_2 - A_1) + 2(A_2 - A_1) \delta^2 U_e U_e' \\
&\quad + 2(A_2 - A_1) \delta U_e^2 \frac{d\delta}{dx_0} + \left(\tfrac{1}{2} - A_2\right) U_e U_e' \delta^2 \Big]
\end{aligned}
\tag{A.67}
$$

so that

$$
\begin{aligned}
\frac{\gamma F_1}{R_0 U_e U_e' \delta} &= \frac{\gamma U_e \delta \frac{d}{dx_0} (A_2 - A_1)}{R_0 U_e'} + \frac{2\gamma (A_2 - A_1) \delta}{R_0} \\
&\quad + \frac{2\gamma (A_2 - A_1) U_e \frac{d\delta}{dx_0}}{R_0 U_e'} + \frac{\gamma \left(\tfrac{1}{2} - A_2\right) \delta}{R_0}
\end{aligned}
\tag{A.68}
$$

The first and third terms on the right of (A.68) are zero at the forward stagnation point due to the appearance of U_e in

the numerator. Therefore, (A.68) with the use of equations (A.65) reduces to:

$$\frac{\gamma F_1}{R_o U_e U_e' \delta} = \frac{\delta}{r_o}\left[A_2 - 2A_1 + \tfrac{1}{2}\right] \tag{A.69}$$

Finally expanding F_2 in $\gamma' F_2 / R_o\, U_e\, U_e' \delta$ by means of equation (A.45) gives:

$$\frac{\gamma' F_2}{R_o U_e U_e' \delta} = \frac{\gamma'}{R_o U_e U_e' \delta}\left[(A_2 - A_1) U_e^2 \delta^2\right] = \frac{\gamma'(A_2 - A_1) U_e \delta}{R_o U_e'} \tag{A.70}$$

Simplifying (A.70) using equations (A.65):

$$\frac{\gamma' F_2}{R_o U_e U_e' \delta} = \frac{\delta}{r_o}\left[A_2 - A_1\right] \tag{A.71}$$

Equations (A.66), (A.69) and (A.71) substituted in (A.64) gives the final relationship for the forward stagnation point:

$$\Lambda_{f.s.p} = \frac{2}{\left(2 + \frac{1}{r_o}\right)\frac{\theta}{\delta} + \frac{\delta^*}{\delta} + \frac{\delta}{r_o}\left[2A_2 - 3A_1 + \frac{1}{2}\right] - \frac{1}{6}} \tag{A.72}$$

It can be seen that equation (A.72) is an implicit equation for $\Lambda_{f.s.p.}$ as the functions θ/δ, δ^*/δ, A_2 and A_1 are all themselves functions of Λ (defined by equations (5.26) and (A.43)). The Reynolds Number dependence results from the third term in the denominator of (A.72) requiring a trial and error solution for $\Lambda_{f.s.p.}$ for each value of Re.

BIBLIOGRAPHY

1. Happel, J. and Brenner, H., "Low Reynolds Number Hydrodynamics", Prentice-Hall, Inc. (1965).
2. Smoluchowski, M, Bull, Inter. Acad. Polonaise Sci. Lett. IA, 28 (1911).
3. Smoluchowski, M., Proc. 5th Intern. Congr. Math. 2, 192 (1912).
4. Burgers, J. M., "Second Report on Viscosity and Plasticity", Amsterdam, North Holland Publishing Company (1938).
5. Burgers, J. M., Proc. Konigl. Akad. Wetenschap. (Amsterdam) 44, 1045 (1941).
6. Burgers, J. M., Proc. Konigl. Akad. Wetenschap. (Amsterdam) 45, 9 (1942).
7. Stimson, M. and Jeffery, O. B., Proc. Royal Soc. (London), A111, 110 (1926).
8. Wang, H. and Skalak, R., J. Fluid Mech. 38, Part 1, 75 (1969).
9. Wakiya, S., J. Phys. Soc. Japan, 20, (8), 1502 (1965).
10. Rosenhead, L., "Laminar Boundary Layers", Oxford University Press, (1966).
11. Rimon, Y. and Cheng, S. I., Phys. of Fluids, 12 , 949 (1969).
12. Takami, H. and Keller, H. B., Phys. of Fluids Suppl. 2, Vol. 12, No. 12, 51 (1969).
13. Leclair, B. P. and Hamielec, A. E., I. and E. C. Fund. 7, 542 (1968).
14. Burgers, J. M., Proc. Konigl. Akad. Wetenschap. (Amsterdam), 43, 425 and 646 (1940).
15. Kynch, G. J., J. Fluid Mech. 5, 193 (1959).

BIBLIOGRAPHY (continued)

16. McNown, J. S. and Lin, P. N., Proc. 2nd Midwestern Conf. Fluid Mech. Reprint in Eng. 109, Iowa State University (1952).

17. Tchen, C., J. Appl. Phys. 25, 463 (1954).

18. Broersma, S., J. Chem. Phys. 32, 1632 (1960).

19. Dean, W. R. and O'Neill, M. E. Mathematika 10, 13 (1963).

20. Goldman, A. J., Cox, R. G. and Brenner, H., Chem. Eng. Sci. 21, 1151 (1966).

21. Davis, M. H., Chem. Eng. Sci. 24, 1769 (1969).

22. Sampson, R. A., Phil. Trans. Royal Soc. A182, 449 (1891).

23. Savic, P., Rept. No. MT-22, Nat. Res. Council Canada (Ottawa) (1953).

24. Haberman, W. L. and Sayre, R. M., David W. Taylor Model Basin Report No. 1143, Washington, D.C. (1958).

25. Faxen, H. (with Appendix by Dahl), Arkiv. Mat. Astron. Fys. 19A, No. 13, (1925).

26. Faxen, H., Z. Angew. Math. Mech. 7, 79 (1927).

27. Slack, G. W. and Matthews, H. W., Porton Tech. Paper No. 797 Chem. Defence Exptl. Establishment, Porton, Wilts., England (1961).

28. Payne, L. E. And Pell, W. H., J. Fluid Mech. 7, 529 (1960).

29. Heiss, J. F. and Coull, J., Chem. Eng. Prog. 48, 133 (1952).

30. Bart, E., M.Ch.E. Thesis, New York University (1959).

31. Eveson, G. F., Hall, E. W. and Ward, S. G., Brit. J. of Appl. Phys. 10, 43 (1959).

32. Happel, J. and Pfeffer, R., A.I.Ch.E. Jour. 6, 129 (1960).

33. Landau, L. D. and Lifshitz, E. M., Vol. 6 of "Course of Theoretical Physics", Addison - Wesley Series in Advanced Physics (1959).

34. Darwin, C., Proc. Cambridge Phil. Soc. 49, 342 (1953).

BIBLIOGRAPHY (continued)

35. Milne - Thomson, L. M., "Theoretical Hydrodynamics", 4th ed., The MacMillan Company (1960).

36. Basset, A. B., "Hydrodynamics", Deighton Bell, Cambridge (1888), Dover, New York (1961).

37. Oseen, C. W., Ark. Mat. Astr. Fys. 6, No. 29 (1910).

38. Proudman, I. and Pearson, J.R.A., J. Fluid Mech. 2, 237 (1957).

39. Lapple, C. E. and Shepherd, C. B., I. and E. C. 32, 605 (1940).

40. Taneda, S., Rept. Res. Inst. Appl. Mech. Kyushu University, 4, 99 (1956).

41. Ralston, A. "A First Course in Numerical Analysis", McGraw Hill Book Company (1965).

42. Ralston, A. and Wilf, H. S., "Mathematical Methods for Digital Computers", Wiley, New York (1960).

43. Happel, J., A.I.Ch.E. Jour. 4, 197 (1958).

44. Happel, J., A.I.Ch.E. Jour. 5, 174 (1959).

45. Pfeffer, R. and Happel, J., A.I.Ch.E. Jour. 10, 605, (1964).

46. Pöhlhausen, K., ZAMM. 1, 252 (1921).

47. Holstein, H. and Bohlen, T., Lilienthal-Berichts 10, 5 (1940).

48. Van Dyke, M., J. Fluid Mech. 14, 161 (1962).

49. Kaplun, S., Z. Angew. Math. Mech. 5, 111 (1954).

50. Schlichting, H., "Boundary Layer Theory", 4th ed., McGraw Hill (1960).

51. Batchelor, G. K., "Fluid Dynamics", Cambridge University Press (1967).

52. Kawaguti, M., J. Phys. Soc. Japan 8, 747 (1953).

53. Apelt, C. J., Aero. Res. Council Rep. and Mem. No. 3175 (1961).

54. Kawaguti, M. and Jain, P., J. Phys. Soc. Japan 21, 2055 (1966).

55. Son, J. S. and Hanratty, T. J., J. Fluid Mech. 35, 369 (1969).

BIBLIOGRAPHY (continued)

56. Taneda, S., J. Phys. Soc. Japan 11, 302 (1956).

57. Jenson, V. G., Proc. Royal Soc., London 249A, 346 (1959).

58. Nisi, H. and Porter, A. W., Phil. Mag. 46, 754 (1926).

59. Collins, R., Chem. Eng. Sci. 20, 747 (1965).

60. Gabor, J. D., I. and E. C. Fund. 8, 34 (1969).

61. Millikan, C. B., Trans. A.S.M.E. Appl. Mech. 54, 29 (1932).

62. Stokes, G. G., Trans. Cambridge Phil. Soc. 9, Part II, 8 (1851).

63. Oseen, C. W. "Hydrodynamik", Leipzig (1927).

VITA

Michael John Gluckman was born in Johannesburg, South Africa on October 12, 1937. He received his elementary and high school education at local institutes. Following his freshman year at the University of the Witwatersrand, Johannesburg, he transferred to the University of Cape Town, Cape Town, South Africa where he received his Bachelor's Degree in Chemical Engineering (December 1958, with second class honors). He joined the Kwikbrite Detergent Company, Johannesburg, South Africa in 1959 and worked there as Chief Chemical Engineer until 1962. In 1962 Michael Gluckman came to the United States and joined the St. Regis Paper Company where he is a Senior Process Engineer. In 1966 he enrolled in the graduate program at New York University and transferred to the graduate division of The City University of New York in September, 1968. Since January 1970, he has been engaged in Doctoral research. The author is married and lives with his wife, Janet, and two daughters, Deborah and Stefanie, in New City, New York.